

國立交通大學

電子物理研究所

博士論文

超導鐵磁薄膜系統的界面電阻與臨近效應

Interface Resistance and Proximity effect in the Singlet  
Superconductor and Ferromagnet Layered System

研究生：黃斯衍

指導教授：許世英

李尚凡

中華民國九十八年六月

超導鐵磁薄膜系統的界面電阻與臨近效應

Interface Resistance and Proximity effect in the Singlet  
Superconductor and Ferromagnet Layered System

研究生：黃斯衍

Student : Ssu Yen Huang

指導教授：許世英

Advisor : Shih-Ying Hsu

李尚凡

Shang-Fan Lee



A Dissertation  
Submitted to Department of Electrophysics  
College of Science  
National Chiao Tung University  
in Partial Fulfillment of the Requirements  
for the Degree of  
Doctor of Philosophy  
in  
Electrophysics  
June 2009  
Hsinchu, Taiwan, Republic of China

中華民國九十八年七月

# 超導鐵磁薄膜系統的界面電阻與臨近效應

學生：黃斯衍

指導教授：許世英博士  
李尚凡博士

國立交通大學電子物理研究所

## 摘 要

鐵磁與超導這兩種材料都是自旋有序的相轉變系統，然而鐵磁有序驅使電子自旋同向排列，超導體的庫珀電子對則是傾向自旋電子以相反方向來互相配對，因此彼此之間交互作用引發出許多有趣的物理現象。而最直接和最有系統的研究方式來探討這互相競爭的有序參數，是利用製作鐵磁與超導層狀結構( $F/S$ )並進一步量測其傳輸性質例如超導臨界溫度，臨界磁場，和臨界電流，在層狀結構中超導的波函數會滲透過鐵磁層，並受到鐵磁物質中多數自旋與少數自旋能量不同的影響，而作空間上的修正，因此鐵磁與超導界面的臨近效應會誘導庫珀電子對波函數在進入鐵磁性物質時產生振盪的行為。此量子效應吻合實驗上所量測到的統計行為，這些因為鐵磁與超導的交互作用所引發的物理現象其實都是發生在  $F/S$  的邊界。由於在實驗上層狀結構的界面相當的複雜甚至會影響所觀察到的物理特性，因此在本論文中，我們主要以電流垂直膜面的量測技術定量的分析出塊材與界面的個別貢獻，這個重要且基礎的傳輸參數，在了解與設定鐵磁超導臨近效應的邊界條件中扮演舉足輕重的角色。

我們將所有系列的樣品區分三組，這三組樣品的臨界溫度與臨界磁場對超導膜厚的行為，都經由電流平行膜面的四點探針分式來量測得知，根據鐵磁超導臨近效應的理論分析，我們得出每一系列樣品的臨界厚度，低於此厚度，超導特性會不存在。臨界磁場與溫度行為的量測中，可以得知樣品維度的轉換行為與磁力線的釘扎機制。藉由電流垂直膜面的量測搭配電阻串聯模型，我們可以經由超導膜厚的改變，定量分析出鐵磁超導在正常態與超導態的界面電阻。在第一組樣品中我們量測與分析鐵磁物質鈷 Co 和不同比例的鈮鈦合金( $Nb_xTi_{1-x}$ , with  $x = 1, 0.6$ , and  $0.4$ )之界面電阻，並將界面傳輸透明度的物理量，以界面電阻和其它物理參數來表達並作系統性的分析與討論，我們的結果發現超導態的界面電阻會受到超導體的散射中心和滲透到超導體逐漸消失的電子波函數的影響。第二組樣品，我們藉由製備鐵/鈮，鈷/鈮，鎳/鈮[Fe/Nb (bcc/bcc), Co/Nb (hex/bcc), Ni/Nb (fcc/bcc)]層狀結構，利用不同結構和材料的強鐵磁性物質，來研究其與超導的臨近效應，從結果發現鐵磁與超導的晶格常數匹配程度會影響其界

面電阻。第三組樣品則是研究弱磁性銅鎳合金與超導鈮的臨界效應，藉由分析超導臨界溫度對鐵磁與超導厚度的行為，我們發現其界面擁有高的傳輸透明度，這樣好的界面會造成弱的鐵磁性擁有強的拆散效應，並影響臨界磁場對溫度的空間維度轉換厚度，進一步在電流垂直膜面量測中，我們證明界面電阻和傳輸透明度有高度的相依性。



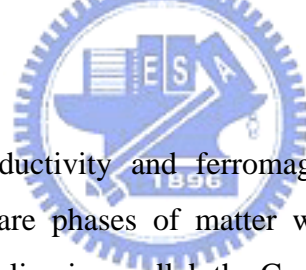
# Interface Resistance and Proximity effect in the Singlet Superconductor and Ferromagnet Layered System

student : Ssu-Yen Huang

Advisors: Dr. Shang-Fan Lee  
Shih-Ying Hsu

Department of Electrophysics  
National Chiao Tung University  
Hsinchu 300, Taiwan

## Abstract



The interplay between superconductivity and ferromagnetism results in many interesting physical phenomena. Both materials are phases of matter with ordered electronic spins. While ferromagnetic order forces the spins to align in parallel, the Cooper pairs in singlet superconductivity prefer an antiparallel spin orientation with total spin zero. The most straightforward way to study the competition of the two order parameters is to fabricate ferromagnet/superconductor ( $F/S$ ) layered structure and to measure the transport properties such as critical temperature, critical field, and critical current in the superconducting state. The superconducting wavefunction penetrating inside the  $F$  is modulated by the energy difference between the minority and majority spin bands. Thus, the proximity effect at  $F/S$  interface would induce damped oscillatory behavior of the Cooper pair wavefunction within the ferromagnetic material. These physical phenomena of the proximity effect are related to the interplay between superconductivity and magnetism and occur at the boundary of  $F/S$  structures. However the character of the real interface in the  $F/S$  systems complicates the physical situation considerably. In this dissertation, we use current perpendicular measurement technique to quantitatively separate the interface and bulk contribution. The fundamental information of the transport properties given by this useful tool plays a dominant role in the boundary condition of the microscopic model within the proximity effect.

We divide a series of samples into three groups. The behaviors of superconducting transition temperature  $T_c$  and upper critical field  $H_{c2}$  as a function of different superconductor thicknesses have been investigated in all groups with current flowing in the plane by a standard four-probe technique. We deduce superconductor critical thicknesses, below which superconductivity vanishes, by analyzing the data in terms of the proximity effect theory. The temperature dependence of  $H_{c2}$  measurement reveals the spatial dimensional crossover and the flux pinning mechanism in the superconductor. Using the current perpendicular to plane measurements (CPP) with a series resistor model, we can, by varying the thickness of  $S$ , extract the unit area resistance for one pair of  $F/S$  interface when  $S$  is in the superconducting and normal states. In Group 1, the quantitative interface resistance between polycrystalline ferromagnetic Co and  $Nb_xTi_{1-x}$ , with  $x = 1, 0.6,$  and  $0.4,$  are measured and analyzed. The interface transparencies in terms of the ratio between interface resistance and various physical quantities are discussed. Our results show that the superconducting state interface resistance is influenced by the scattering centers and the penetration depths of the electron evanescent wave into the superconductors according to the Pippard model. In Group 2, we study the proximity in Fe/Nb (bcc/bcc), Co/Nb (hex/bcc), and Ni/Nb (fcc/bcc) with a sputtered layered system. The influence of lattice mismatch on interface resistance is found to be important. In Group 3, we report the proximity effect between a weak ferromagnet  $Cu_{0.5}Ni_{0.5}$  and a superconductor Nb. High interfacial transparency is derived from the behavior of the superconducting critical temperature as a function of the  $S$  and  $F$  layer thicknesses. A strong pair-breaking effect as a result of the high interface quality influences the spatial dimensional crossover in the temperature dependence of the upper critical magnetic field. Here, by using the CPP measurement with a series resistor model, a close correlation between the interfacial transparency and the interface resistance is demonstrated.

## 致謝

對我來說，論文的最後一個部份便是致謝，其重要性絕不亞於論文主體。這本著作絕對不是我一人可以獨立完成的。從碩士到國防役助理再到攻讀博士學位，不知不覺也快過了十年寒窗。我不是一個很會讀書的人，也沒有聰明的頭腦，但在李尚凡老師的指導與支持之下，以自己的步伐與堅持，一步一腳印努力地突破每一道關卡。因此，非常感謝李老師給我進修的機會並願意培養我獨立研究的能力；交大的許世英老師讓我了解到作科學研究應保持樂觀且嚴謹的態度；亦師亦友的輔大梁君致老師除了在模擬程式中不辭辛勞的協助外，影響我最深的便是其求知的熱忱。另外中研院姚永德老師、劉鏞老師的鼓勵與意見，交大林俊源老師更總是在我每年的物理年會報告中丟給我很多頭痛卻又很重要的物理問題，此外論文口試委員交大吳光雄老師、莊振益老師、林俊源老師以及清大牟中瑜老師、齊正中老師、和郭瑞年老師在口試時提供的建議，讓我了解到自己還是有不少知識未能融會貫通。有了老師們的想法和建議，我才能使更嚴謹的寫出這本論文。

本論文有許多內容建立在之前碩士班學弟的基礎研究上。由於黃建成、游駿毅、林明賢和邱昱哲同學的努力與貢獻才能使這個研究有更深入與完整的結果；經由彼此討論與爭辯所引起的火花，與對實驗結果的興奮，是不易被取代的。此外和實驗室的博士後于淳學長及一起奮鬥的歐敏男與徐豐麒學長天馬行空地討論物理也是我最快樂與收穫良多的時刻；當然也要感謝小圭、典蔚、再昌、凱文、延松、東呈還有後來加入的正凱、宗展——有了他們的幫忙才能讓研究時的瓶頸一一突破。他們的歡笑讓枯燥的實驗也能充滿歡樂。還有許多共事過的碩士班學弟、研究助理、大專專題生、與其他實驗室的好朋友，請原諒我沒有一一唱名，十年時間畢竟不短，但我真的非常感謝有他們的參與。當然，有了中央研究院物理所的高級設備與一流的行政、技術人員的協助，斯衍才能完成此學位。

最後最大的感謝要獻給我的父母，謝謝他們的支持與體諒，還有被強迫要校正我破英文的妹妹，愛護我的外公、外婆、叔叔、嬸嬸、姑姑、姑爹以及情同手足的堂弟、堂妹和兩個表妹。還有我的女友亦欣，雖然我們分隔地球兩地，但她的信任與陪伴，給我勇氣克服每一次的挑戰。最後，我要將此論文獻給天上的爺爺和奶奶。我的家人永遠在我無助時給我一盞明燈，謝謝你們。

# Contents

Abstract (in Chinese)	.....	i
Abstract (in English)	.....	iii
Acknowledgement (in Chinese)	.....	v
Contents	.....	vi
List of Tables	.....	ix
List of Figures	.....	x
<b>1</b>	<b>Introduction</b> .....	<b>1</b>
References	.....	9
<b>2</b>	<b>General Background and Previous Work</b> .....	<b>12</b>
2.1	The length scale of Superconductivity and Ferromagnetism.....	12
2.2	The coexistence of Superconductivity and Ferromagnetism in the LOFF state.....	17
2.3	General phenomenon in proximity effect.....	20
2.4	Oscillatory superconducting temperature in <i>F/S</i> layered structure.....	24
2.5	Superconductor-Ferromagnet-Superconductor $\pi$ junction.....	35
2.6	Density of states oscillations.....	37
2.7	Ferromagnet-Superconductor-Ferromagnet spin-valve sandwiches.....	39
References	.....	43
<b>3</b>	<b>Experimental Techniques and Measurement System</b> .....	<b>47</b>
3.1	The sputtering system.....	47
3.2	Magnetic property measurement (SQUID).....	50
3.2.1	Josephson Effect: SQUID.....	50
3.2.2	Magnetic measurement.....	55
3.3	CPP with low resistance measurement.....	57
3.4	Electric property measurement with CIP structure.....	63
References	.....	64



<b>4</b>	<b>Theoretical Description for Data Analysis</b> .....	66
4.1	Radovic's Theory: single-mode approximation .....	67
4.2	Tagirov's Theory.....	73
4.3	Fominov's Theory: single-mode and multi-mode solution.....	74
4.3.1	single-model solution.....	75
4.3.2	multi-mode solution-method of fundamental solution.....	77
4.4	Global Fit.....	83
4.5	Andreev reflection and the Blonder, Tinkham, and Klapwijk model.....	85
References	.....	91
<b>5</b>	<b>Results and Discussion-Conventional Ferromagnet:</b>	
	<b>Co/Nb<sub>x</sub>Ti<sub>1-x</sub> System</b> .....	93
5.1	Thickness dependence of superconducting transition temperature in Co/S trilayers with $S = \text{Nb}, \text{Nb}_{0.4}\text{Ti}_{0.6}, \text{and } \text{Nb}_{0.6}\text{Ti}_{0.4}$ .....	94
5.2	Theoretical fitting in term of Radovic's model.....	97
5.3	The behavior of upper critical field for Co/Nb multilayers.....	103
5.4	The result of CPP measurement for Co/Nb <sub>x</sub> Ti <sub>1-x</sub> multilayers.....	106
5.4.1	Two parameters Global Fit for Co/Nb multilayers.....	109
5.4.2	Two parameters Global Fit for Co/Nb <sub>0.4</sub> Ti <sub>0.6</sub> and Co/Nb <sub>0.6</sub> Ti <sub>0.4</sub> multilayers	112
5.4.3	Four parameters Global Fit for Co/Nb multilayers.....	115
5.5	The result of CPP measurement for Co/Nb <sub>0.4</sub> Ti <sub>0.6</sub> and Co/Nb <sub>0.6</sub> Ti <sub>0.4</sub> multilayers with four parameter Global Fit and comparison.....	119
5.6	Interface transparency.....	127
5.7	Pippard model.....	130
References	.....	135
<b>6</b>	<b>Results and Discussion-Conventional Ferromagnet:</b>	
	<b>Fe/Nb and Ni/Nb System as Compared with Co/Nb System</b> .....	139
6.1	Fe/Nb system.....	139
6.1.1	The behavior of critical temperature for Fe/Nb trilayers.....	140
6.1.2	The behavior of upper critical field for Fe/Nb multilayers.....	143
6.1.3	Fe/Nb interface resistance by CPP measurement.....	146

6.2	Ni/Nb system.....	153
6.2.1	The behavior of critical temperature for Ni/Nb trilayers.....	153
6.2.2	The behavior of upper critical field for Ni/Nb multilayers.....	155
6.2.3	Ni/Nb interface resistance by CPP measurement.....	157
6.3	Co/Nb, Fe/Nb, and Ni/Nb interface resistance calculated by First-Principle calculation.....	162
6.4	Transport polarization.....	164
References	.....	166
<b>7</b>	<b>Results and Discussion-Weak Ferromagnet: Cu<sub>0.5</sub>Ni<sub>0.5</sub>/Nb System...</b>	<b>170</b>
7.1	The behavior of critical temperature fitted by Radovic's model.....	173
7.2	Fitted by Fominov's model in terms of interface transparency.....	175
7.3	Pair breaking ratio by upper critical magnetic field measurement.....	184
7.4	Interface resistance by CPP measurement.....	189
References	.....	197
<b>8</b>	<b>Summary.....</b>	<b>200</b>
<b>A</b>	<b>Calculating <math>T_C</math>.....</b>	<b>204</b>
A.1	Rodivic's model: $T_C(d_S)$ .....	196
A.2	Fominov's model: $T_C(d_F)$ .....	201
A.3	Fominov's model: $T_C(d_S)$ .....	208
<b>B</b>	<b>The Activation Energy in Ni/Nb Layered System.....</b>	<b>222</b>
	List of Publications which have resulted from this Work.....	224



# List of Tables

4.1	Transmission and reflection coefficients. $A$ gives the probability of Andreev reflection, $B$ of normal reflection probability, $C$ of transmission probability without branch crossing, $D$ of transmission probability with branch crossing.....	89
5.1	Linear least-square fits to the two sets of data in Figure 5.10. The fits are independent of the model.....	109
5.2	Linear least-square fits to the two sets of data in Figure 5.11 and Figure 5.12. The fits are independent of the model.....	113
5.3	The derived values and parameters of different fitting procedures for the Co/Nb $x$ Ti $1-x$ multilayers with $x=1, 0.6,$ and $0.4$ .....	124
5.4	The best derived values (two global fit) and parameters for the Co/Nb, Co/Nb $_{40}$ Ti $_{60}$ , and Co/Nb $_{60}$ Ti $_{40}$ multilayers.....	131
6.1	The best derived values and parameters for the Fe/Nb multilayers.....	152
6.2	The dimension crossover thickness for Co/Nb, Fe/Nb and Ni/Nb.....	157
6.3	The interface resistance in superconducting and normal state for the Fe/Nb, Co/Nb, , and Ni/Nb.....	162
6.4	The interface resistance of Nb/Co by <i>ab initio</i> calculation.....	163
6.5	The transport polarization of Co, Fe and Ni extracted from interface resistance.....	165

# List of Figures

2.1	Overview of the $F/S$ heterostructure in different regime.....	13
2.2	Cooper pair in superconductor and ferromagnet. $\Delta p = \hbar/v_F$ .....	19
2.3	Schematic behavior of the superconducting order parameter near the (a) superconductor-normal metal and (b) superconductor-ferromagnet interfaces The continuity of the order parameter at the interface implies the absence of the potential barrier.....	21
2.4	Spatial dependence of the magnetization in the $F/S$ system. Inset: Schematic view of the inverse proximity effect in a $F/S$ system.....	24
2.5	Multilayered $F/S$ systems that have been studied in experiments: bilayers, trilayers and superlattices.....	25
2.6	Transition temperature for glass-Pb-Fe sandwiches with a constant iron film thickness of 100 nm. The solid line represents a fit ignored the fact that the used metals are ferromagnetic. The effective electron-electron interaction for Fe has been taken into account in the dashed line. In the lower curve the proximity effect is combined with the Abrikosov-Gor'kov theory and is in fair agreement with the data.....	26
2.7	Superconducting transition temperature of $V_mFe_n$ superlattices.....	27
2.8	Resistively determined transition temperature $T_C$ as a function of $dGd$ in several series of MBE triple Nb/Gd layers that have been prepared in a single evaporation run.....	28
2.9	Superconducting transition temperature $T_C$ versus $dGd$ in sputtered Nb/Gd multilayers with (a) $d_{Nb} = 60$ nm and (b) 50 nm. Different symbols correspond to different sample series. Dashed line in (a) is a fit by Radovic's theory.....	29
2.10	Superconducting transition temperature $T_C$ as a function of $d_{Fe}$ as determined by ac susceptibility solid symbols and resistivity opened symbols measurements. The triangles, circles, and squares correspond to different sample sets. The dashed lines are guide for the eyes.....	30
2.11	Superconducting transition temperature $T_C$ versus $d_{Fe}$ for three series of samples. The broken lines are guides for the eye.....	31
2.12	Dependence of the superconducting transition temperature on the thickness of the Fe layer as determined by resistivity measurements. The dashed and solid lines are the best fits using the theory by Radovic' <i>et al.</i> and the theory by Tagirov, respectively.....	32
2.13	$T_C$ of Nb (26 nm)/ $Co_{60}Fe_{40}$ bilayers as a function of $d_{CoFe}$ . The different	

	symbols mean two different sets of data. The solid line is a fit.....	33
2.14	Critical temperature $T_C$ versus PdNi thickness $d_{\text{PdNi}}$ in Nb/Pd <sub>0.81</sub> Ni <sub>0.19</sub> bilayers with constant Nb thickness $d_{\text{Nb}}=14$ nm. Different lines are the theoretical fit in the single-mode approximation for different values of $\gamma_b$ . Inset: comparison between the single-mode and the multimode calculations.....	34
2.15	Nonmonotonous $T_C(d_F)$ dependence for Nb/Cu <sub>41</sub> Ni <sub>59</sub> bilayers: (a) $d_{\text{Nb}} = 8.3$ nm; (b) $d_{\text{Nb}} = 7.3$ nm. The solid and dashed lines are theoretical curves for the clean and dirty cases, respectively. The inset shows $T_C(d_{\text{Nb}})$ for a top layer Cu <sub>41</sub> Ni <sub>59</sub> of constant thickness with the solid line calculated for the clean case.....	34
2.16	Critical current $I_C$ as a function of temperature for Cu <sub>0.48</sub> Ni <sub>0.52</sub> junctions with different $F$ layer thicknesses $2d_F$ . The temperature mediated transition between the 0 and $\pi$ phase occurs when the thickness of the $F$ layer is 27 nm..	36
2.17	Critical current $I_C$ at T=4.2 K of Cu <sub>0.47</sub> Ni <sub>0.53</sub> junctions as a function of the $F$ layer thickness. Two 0- $\pi$ transitions are revealed. The solid line is theoretical fit taking into account the presence of magnetic scattering. The inset shows the temperature mediated 0- $\pi$ transition for a $F$ layer thickness of 11 nm.....	37
2.18	The differential conductance for two Al/Al <sub>2</sub> O <sub>3</sub> /PdNi/Nb junctions with two different thicknesses ferromagnetic PdNi. Tunnel junction areas were defined by the 50 nm thick SiO <sub>2</sub> evaporated through masks.....	39
2.19	Schematic structure of a $F/S/F/AF$ proximity switch device.....	40
2.20	Resistance vs temperature for the P and AP states of a $d_s = 17$ nm sample measured in 100 Oe. Two distinct transitions are observed, with $\Delta T_C = 28$ mK. Inset: Resistance vs applied field at T= 0.51 K (dotted line in main graph).....	41
2.21	(a) Superconducting spin valve effect in the structure (in nm): MgO (10)/Fe(6)/V(40)/Fe(6)/CoO, and the sample is fully submerged in superfluid He4 which has infinitely thermal conductivity to avoid heating complications. (b) Superconducting transition of the same sample in its spin P and AP configurations. Inset: Thickness dependence of the $S$ spin valve effect; solid line is only for visual guidance. Example of the MR loop with 50 nm V is also shown.....	42
3.1	The schematic view of the sputtering system.....	47
3.2	Metal mask of CIP-type sample to produce a 4-terminal device for transport measurements and a rectangular film for magnetization measurement.....	48
3.3	(a) Top view of CPP samples plate (b) Bottom view of CPP masks plate.....	49
3.4	Geometry of a current perpendicular to plane sample on a substrate. The middle part of the circular shape is the multilayer.....	50

3.5	Tunnel Josephson junction in a magnetic field $H$ . The distribution of the screening supercurrent is shown by lines with arrows.....	52
3.6	Superconducting interferometer with two Josephson junctions, a and b, are connected in parallel. The interior of the SQUID loop is threaded by a magnetic flux $\Phi$ .....	53
3.7	Dependence of the maximum supercurrent through the two-junction interferometer on the total magnetic flux through its interior.....	54
3.8	(a) V-I characteristic curve of dc SQUID with integer and half integer flux quantum, $\Phi$ , of applied flux. (b) To bias the SQUID above the critical current with applying an external flux results in a sinusoidal behavior of the $V$ s versus $\Phi$ .....	54
3.9	The superconducting pick-up coil couples the external flux to the input terminal of the SQUID.....	55
3.10	Voltage signal profile when a magnetic sample is moved through a detection pick-up coils.....	56
3.11	Cross section of a CIP and CPP structure with current traveling in the plane and perpendicular to the plane, respectively.....	58
3.12	Simplified circuit for the precision measurement with SQUID based picovolt meter.....	60
3.13	CPP sample measured by by a superconducting quantum interference device (SQUID) based picovolt meter at 4.2 K.....	61
3.14	Interface resistance representing the sample area $A$ times the boundary resistance $R_b$ in the CPP sample.....	62
3.15	A 4-terminal device for transport measurement in the CIP sample.....	63
4.1	The reduced transition temperature as a function of the reduced (a) S film thickness and (b) F film thickness for $\varepsilon=10$ . The tricritical points $T^*/T_{CS}$ are shown as thin curves. Dashed cures show solutions that are physically unstable.....	70
4.2	The calculation for the phase difference $\varphi=0$ , dot-dashed line, and $\varphi=\pi$ , dashed line. The ground state oscillations where $0<\varphi<\pi$ , solid line. Inset: groune state $\varphi$ vs $d_F/\zeta_F$ .....	71
4.3	Spatial variation of the real part of the pairing function near the interface in the models by Radovic' <i>et al</i> with $d_{pb}=730$ Å and $d_{Fe}=4$ Å (a), 9 Å (b), and 20 Å (c) with the parameters $\zeta_S=170$ Å, $\zeta_F=16$ Å, and $\varepsilon=3.4$ .....	72
4.4	Spatial variation of the real part of the pairing function near the interface in the model by Tagirov with $d_{pb}=730$ Å and $d_{Fe}=4$ Å (a), 9 Å (b), and 20 Å (c) with the parameters $\zeta_S=170$ Å, $\zeta_F=7.7$ Å, $l_F=15$ Å, $N_{FVF}/N_SvF_S=1.3$ and $T_m=0.4$ .....	73

4.5	<i>SF</i> bilayer. The <i>F</i> and <i>S</i> layers occupy the regions $-d_f < x < 0$ and $0 < x < d_s$ , respectively.....	75
4.6	Comparison between single- and multimode methods. Generally speaking, the results of the single-mode and multimode methods are close: (a) and (f). However, at some parameters are different: (b), (c), (c), (d), and (e).....	80
4.7	Four types of trajectories contributing in the sense of Feynman's path integral to the anomalous wave function of correlated quasiparticles in the ferromagnetic region. The solid lines correspond to electrons, and the dashed lines to holes; the arrows indicate the direction of the velocity.....	81
4.8	(a) Schematic diagram of energy versus momentum of a normal metal-superconductor contact (b) the conductance versus voltage for metallic contact (down) and tunnel junction (up) in <i>NM/F</i> structure.....	85
4.9	Schematic diagram of energy vs momentum at an <i>NM-S</i> interface. The open circles denote holes, the closed circles electrons, and the arrow point in the direction of the group velocity. The figure in the right hand side simply describes the process of transmitted and reflected electron at <i>F/S</i> interface.....	87
4.10	(a) Schematic diagram of energy versus momentum of a ferromagnet-superconductor contact (b) the conductance versus voltage for metallic contact with different polarization of ferromagnet in <i>F/S</i> structure.....	90
5.1	Dependence of the superconducting transition temperature on the thickness of the (a) Nb,(b) Nb <sub>40</sub> Ti <sub>60</sub> and (c) Nb <sub>60</sub> Ti <sub>40</sub> contained layers. The solid curves are obtained by fitting Eq. (1).....	96
5.2	The variation in $H_{c2}$ at 4.2 K, $T_C$ and resistivity are plotted as a function of the mass fraction of Ti across the binary Nb-Ti alloy system. $H_{c2}$ is defined as the linear extrapolation of the high field pinning force to zero.....	100
5.3	(a) Variation in resistivity as a function of Ti content in Nb-Ti films for 300 K and 10 K, respectively. (b) Variation in resistivity ratios with Ti content in Nb-Ti films for 300K/77K and 300K/10K, respectively. (c) Variation in $T_C$ with Ti content in Nb-Ti films.....	100
5.4	A hybrid equilibrium phase diagram for Nb-Ti combining the experimentally determined high temperature phase boundaries of Hansen et al with the calculated low temperature phase boundaries of Kaufman and Bernstein modified by Moffat and Kattner. Also shown is the martensite transformation curve (Ms) of Moffat and Larbalestier.....	102
5.5	Upper critical field, $H_{c2  }$ , versus reduced temperature for series of multilayers [Co(20nm)/Nb( $d_s$ )] <sub>6</sub> /Co(20nm), with $d_s$ = 135, 145, 160, and 185 nm.....	104

5.6	Upper critical field, $H_{c2  }$ , versus reduced temperature for series of multilayers $[\text{Co}(d_F)/\text{Nb}(60)]_{10}/\text{Co}(d_F)$ , with $d_F = 0.6, 2, \text{ and } 4 \text{ nm}$ .....	104
5.7	Angular dependence of upper critical field of a series of samples.....	105
5.8	Hysteresis curves measured at 10 K of $[\text{Co}(20)/\text{Nb}(30)/\text{Co}(2)/\text{Nb}(30)]_5/\text{Co}(20)$ multilayers with all numbers in nm.....	107
5.9	CPP resistance vs magnetic field of two samples $[\text{Co}(20)/\text{Nb}(t)/\text{Co}(2)/\text{Nb}(t)]_{10}/\text{Co}(20)$ with Nb thicknesses of 20 and 80 nm, respectively.....	107
5.10	Unit area resistance, $AR_T$ vs $N$ number of bilayers for two sets of samples with Nb thicknesses fixed at 20 and 80 nm, respectively. The dashed lines are linear least-square fits to individual sets. The solid lines are global fits to two sets of data simultaneously.....	111
5.11	Unit area resistance, $AR_T$ versus bilayer number $N$ of two sets of samples with $\text{Nb}_{0.4}\text{Ti}_{0.6}$ thicknesses fixed at 8nm and 80nm, respectively. The dashed lines are linear least square fits to individual sets. Solid lines are global fit to two sets of data simultaneously.....	114
5.12	Unit area resistance, $AR_T$ versus bilayer number $N$ of two sets of samples with $\text{Nb}_{0.6}\text{Ti}_{0.4}$ thicknesses fixed at 15nm and 80nm, respectively. The dashed lines are linear least square fits to individual sets. Solid lines are global fit to two sets of data simultaneously.....	114
5.13	(a) Specific resistance $AR_T$ vs bilayers number $N$ of two sets of samples with Nb thicknesses fixed at 15 and 80 nm, respectively. The dot lines and solid lines are global fit for two and four parameters, respectively.....	117
	(b) Specific resistance $AR_T$ vs Co thickness with Nb thickness fixed at 15 nm and $N = 6$ . The dot lines and solid lines are global fit for four parameters.....	118
	(c) Specific resistance $AR_T$ vs Nb thickness with Co thickness fixed at 20 nm and $N = 6$ . The dot lines are linear least squares fit to individual sets. The solid lines are global fit for four parameters to the data simultaneously. The dot-dashed lines used the bulk CIP resistivities as the slope and the two interface resistances from two- and four-parameter fits as upper and lower limits, respectively.....	118
5.14	Data for $\text{Co}/\text{Nb}_{0.4}\text{Ti}_{0.6}$ multilayers. (a) Unit area resistance, $AR_T$ , plotted against bilayer number $N$ of two sets of samples with $\text{Nb}_{0.4}\text{Ti}_{0.6}$ thickness fixed at 8 nm and 80 nm, respectively. The dot lines are fits for two parameters. (b) $AR_T$ versus Co thickness with $\text{Nb}_{0.4}\text{Ti}_{0.6}$ thickness fixed at 8 nm and $N = 6$ . The dashed lines are linear least square fits to individual sets. The solid lines in (a) and (b) are global fits for four parameters to the data simultaneously.....	120



	(c) $AR_T$ versus $Nb_{0.4}Ti_{0.6}$ thickness with Co thickness fixed at 20 nm and $N = 6$ . The dashed lines are linear least square fits to individual sets. The dot-dashed lines used the bulk CIP resistivities as the slope and the two interface resistances from two- and four-parameter fits as upper and lower limits, respectively. The solid lines in (c) are global fits for four parameters to the data simultaneously.....	121
5.15	Data for $Co/Nb_{0.6}Ti_{0.4}$ multilayers. (a) Unit area resistance, $AR_T$ , plotted against bilayer number $N$ of two sets of samples with $Nb_{0.6}Ti_{0.4}$ thickness fixed at 15 nm and 80 nm, respectively. The dot lines are fits for two parameters. (b) $AR_T$ versus Co thickness with $Nb_{0.6}Ti_{0.4}$ thickness fixed at 15 nm and $N = 6$ . The solid lines in (a) and (b) are global fits for four parameters to the data simultaneously.....	122
	(c) $AR_T$ versus $Nb_{0.6}Ti_{0.4}$ thickness with Co thickness fixed at 20 nm and $N = 6$ . The dashed lines are linear least square fits to individual sets. The dot-dashed lines used the bulk CIP resistivities as the slope and the two interface resistances from two- and four-parameters fits as upper and lower limits, respectively. The solid lines in (c) are global fits for four parameters to the data simultaneously.....	123
5.16	Unit area resistance, $AR_{F/S(S)}$ , plotted against $\rho_S \xi_S$ for alloy $Nb_xTi_{1-x}$ superconductor with $x=1, 0.6, \text{ and } 0.4$ . The solid line is linear least squares fit to the results of two-parameter fits.....	133
6.1	TEM image of a $[Fe(20 \text{ nm})/Nb(50 \text{ nm})]_6/Fe(20 \text{ nm})$ multilayer sample.....	140
6.2	High-angle x-ray diffraction of $[Fe(0.2 \text{ nm})/Nb(0.3 \text{ nm})]_{60}$ multilayer. Satellite peaks around Nb (110) are indicated by arrows.....	141
6.3	Dependence of the superconducting transition temperature on the thickness of the Nb layer, the solid line is the best fit with Eq. (4.12).....	142
6.4	$H_{c2}$ versus reduced temperature $t$ for $[Fe(20 \text{ nm})/Nb(d_{Nb})]_6/Fe(20 \text{ nm})$ multilayers with $d_{Nb} = 100$ (a), 120 (b) and 140 nm (c).....	145
6.5	Specific resistance, $AR_T$ , versus bilayer number $N$ of two sets of samples with Nb thicknesses fixed at 15 nm and 80 nm, respectively. The dashed lines are linear least square fits to individual sets. The solid lines are global fit for two parameters and dash dot lines are global fit for four parameters to two sets of data simultaneously.....	150
6.6	(a) Specific resistance, $AR_T$ , versus Fe thickness with Nb thickness fixed at 15 nm and $N=6$ . (b) Specific resistance, $AR_T$ , versus Nb thickness with Fe thickness fixed at 20 nm and $N=12$ . The dashed lines are linear least square fits to individual sets. The solid lines are global fit for four parameters to the data simultaneously.....	151

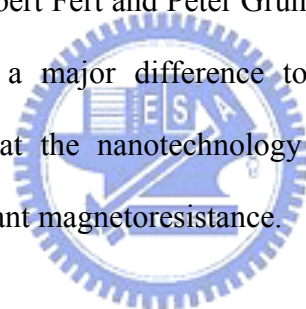
6.7	The superconducting critical temperatures for Ni/Nb/Ni trilayers as a function of $d_{\text{Nb}}$ . The solid line is obtained from the theoretical fitting with parameters of $\xi_S = 19$ nm, and $\gamma = 0.1$ . Inset: thickness dependence of the low temperature resistivity as a function of the single Ni layer fitted by the Fuchs-Sondheimer relation.....	154
6.8	Temperature dependence of the parallel (open circles, triangles, squares, and stars) and perpendicular (filled stars) upper critical fields for Ni/Nb multilayers with $d_{\text{Nb}} = 60, 80, 100,$ and $130$ nm. Data for the $d_{\text{Nb}} = 60,$ and $80$ are shifted to the left by $T/T_C = 0.1$ and $0.2$ ; $d_{\text{Nb}} = 130$ nm are shifted to the right by $T/T_C = 0.1$ for clarity. The lines are least-square fit to describe the 3D to 2D crossover using the Gizburg-Landau relation.....	156
6.9	Unit area resistance, $AR_T$ , versus bilayer number $N$ measured at 4.2 K. The two sets of samples have Nb thickness fixed at 12 nm and 108 nm, respectively. The solid lines are global fits for four parameters to the data. Inset: the top view geometry of the current perpendicular to plane (CPP) configuration. Sample is sandwiched between the two circular Nb electrodes. The top and bottom Nb strips are used for the four-point measurement.....	160
6.10	Unit area resistance, $AR_T$ , versus Ni thickness with Nb thickness fixed at 27 nm and $N = 7$ measured at 4.2 K. The dashed-line is linear least-square fit. The solid line is global fit for four parameters to the data.....	161
6.11	Unit area resistance, $AR_T$ , versus Nb thickness with Ni thickness fixed at 78 nm and $N = 7$ measured at 4.2 K. The dashed-line is linear least-square fit. The solid line is global fit for four parameters to the data.....	161
7.1	Superconducting critical temperatures for $\text{Cu}_{0.5}\text{Ni}_{0.5}/\text{Nb}/\text{Cu}_{0.5}\text{Ni}_{0.5}$ trilayers as a function of $d_{\text{Nb}}$ . The solid line is obtained from the theoretical fitting with parameters $\xi_S = 16$ nm, $\gamma = 0.1$ , and $T_{c0} = 8.7$ K.....	174
7.2	Curie temperature versus $\text{Cu}_{0.5}\text{Ni}_{0.5}$ layer thickness. The solid line is meant to guide the eye. Inset (right): magnetic hysteresis loop for $\text{Cu}_{0.5}\text{Ni}_{0.5}$ thickness of 300 nm at $T = 5$ K. Inset (left): the cross-section TEM image of a $[\text{Cu}_{0.5}\text{Ni}_{0.5} 20 \text{ nm}/\text{Nb} 100 \text{ nm}]_6/[\text{Cu}_{0.5}\text{Ni}_{0.5} 20 \text{ nm}]$ multilayer sample.....	176
7.3	The superconducting critical temperature versus $\text{Cu}_{0.5}\text{Ni}_{0.5}$ thickness for $\text{Cu}_{0.5}\text{Ni}_{0.5}/\text{Nb}/\text{Cu}_{0.5}\text{Ni}_{0.5}$ trilayers with constant Nb thickness $d_{\text{Nb}} = 37$ nm: (a) different lines are the results of theoretical fit for different values of $E_{ex}$ and for $\gamma_b = 0.3$ , (b) different lines are the results of theoretical fit for different values of $\gamma_b$ and for $E_{ex} = 120$ K.....	180
7.4	The superconducting critical temperatures as a function of $d_{\text{Nb}}$ for $\text{Cu}_{0.5}\text{Ni}_{0.5}/\text{Nb}/\text{Cu}_{0.5}\text{Ni}_{0.5}$ trilayers with constant $\text{Cu}_{0.5}\text{Ni}_{0.5}$ thickness $d_{\text{CuNi}} = 50$ nm. The solid red line is the theoretical fitting with high interfacial	

	transparency assumption. The other different lines are the results of the theoretical calculation for different values of $\gamma b$ and for $E_{ex}=120$ K obtained in Figure 3. The inset is an enlargement of the region between 40 nm and 160 nm close to the corner.....	183
7.5	The superconductor coherence with 12 nm of Nb dependent on the temperature.....	186
7.6	In the top part, reduced parallel uppercritical fields versus reduced temperature for $\text{Cu}_{0.5}\text{Ni}_{0.5}/\text{Nb}$ multilayers with $d_{\text{Nb}}=140, 160, \text{ and } 180$ nm. Data for the $d_{\text{Nb}} = 160$ and $180$ nm are shifted to the right by $T/T_C=0.05$ and $0.1$ , respectively, for clarity. The solid lines are least-square fit using the Ginzburg-Landau relation. The filled circle symbol is perpendicular upper critical fields for $d_{\text{Nb}}=140$ nm and the dashed line is a linear fit. In the down part is parallel upper critical fields as a function of the reduced temperature for the $\text{Cu}_{0.5}\text{Ni}_{0.5}/\text{Nb}$ multilayers with $d_{\text{Nb}} = 140$ nm. It can be categorized into two groups according to the 3D and 2D behavior as shown the solid line fitted by Tinkham expression.....	188
7.7	Unit area resistance, $AR_T$ , versus bilayer number $N$ measured at 4.2 K. The two sets of samples have Nb thickness fixed at 80 nm and 15 nm, respectively. The dashed-lines are linear least-square fit. The dotted lines and the solid lines are global fits for two and three parameters, respectively, to the data.....	192
7.8	In the top right side part: the linear $I-V$ characteristic as a function of $\text{Cu}_{0.5}\text{Ni}_{0.5}$ thickness for CPP $\text{Cu}_{0.5}\text{Ni}_{0.5}/\text{Nb}$ multilayer. The different lines are linear least-square fit. In the down right side part: the non-linear $I-V$ characteristic as a function of $\text{Cu}_{0.5}\text{Ni}_{0.5}$ thickness for CPP $\text{Cu}_{0.5}\text{Ni}_{0.5}/\text{Nb}$ multilayer. The solid line is meant to guide the eye.....	194
7.9	Unit area resistance, $AR_T$ , versus $\text{Cu}_{0.5}\text{Ni}_{0.5}$ thickness measured at 4.2 K. The dashed line is a linear least-square fit. The solid line is a global fit for three parameters to the data. Inset: the top view geometry of the current perpendicular to plane (CPP) configuration for this series sample. Sample is sandwiched between two superconducting electrodes of Nb stripes used for the four-point measurement.....	196
B.1	Activation energy $U_0$ of flux flow versus parallel and perpendicular applied field for $(\text{Cu}_{50}\text{Ni}_{50}/\text{Nb})_6/\text{Cu}_{50}\text{Ni}_{50}$ multilayer with $d_{\text{Nb}} = 40$ nm and monolayer Nb with $d_{\text{Nb}} = 240$ nm. Open symbols are for monolayer and solid symbols for multilayers. Data for parallel field are in triangles and for perpendicular field in circles.....	223

# Chapter 1

## Introduction

Interest has increased in ferromagnet/superconductor (*F/S*) heterostructures during the last decade. [1–3] This may probably be attributed to advances in experimental fabrication and deposition techniques as well as theoretical works. The main reason to study this kind of heterostructures is that future devices and applications will rely on manipulation of not only the electron charge but also its spin. Lying at the heart of the computer which the most important tool we are using today is a memory retrieval system based on the discoveries for which the 2007 Nobel Prize in Physics was awarded to Albert Fert and Peter Grünberg. They discover that a small magnetic change can make a major difference to an electrical current through sandwiches of metals built at the nanotechnology scale. This is the basis of a responsive sensor that uses giant magnetoresistance.



The phenomenon called magnetoresistance (MR) is the change of resistance in a conductor first observed by W. Thomson [4] when the sample is placed in an external magnetic field. For ferromagnets such as iron, cobalt, and nickel, this property will depend on the direction of the external field relative to the direction of the current through the magnet. This difference in resistance between the parallel and perpendicular cases is called anisotropic magnetoresistance (AMR). [5] It is now known that this property originates from the electron spin-orbit coupling. The magnetoresistance effects are generally very small, at most of the order of a few percent.

Therefore it was surprising when two independent research groups in 1988 both

discovered that magnetic layered structure showed considerably large magnetoresistance by using magnetic fields to evoke much greater increases in electrical resistance in specially constructed stacks made from alternating layers of very thinly spread iron and chromium. The widths of the individual layers were of nanometer size, i.e. only a few atomic layers thick. In the original experiments Peter Grünberg's group [6] used a trilayer system Fe/Cr/Fe, while Albert Fert and his colleagues [7] created multilayers of the form  $(\text{Fe/Cr})_n$  where  $n$  could be as high as 60. The Fert group saw a magnetization-dependent change of resistance of up to 50 percent, whereas the German group saw a 10 percent difference at most, as result of Fert's use of many more layers and interfaces than Grunberg's. However, the basic effect and the physics behind it were identical in both cases. Both groups realized that they had observed a totally new phenomenon. With traditional magnetoresistance, few researchers had registered more than a single percent or so of change in resistance. Albert Fert named it "giant magnetoresistance (GMR)" to describe the new effect, and in his first publication on this topic he pointed out that the discovery could lead to important applications. Peter Grunberg also realized the practical potential of the phenomenon and filed a patent at the same time as he was writing his first scientific publication.

Giant magnetoresistance is essentially a quantum mechanical effect depending on the property of electron spin. Within the magnetic material and especially at the interface between the magnetic and the non-magnetic material, electrons with different spins are scattered differently. With an applied magnetic field which controls the direction of magnetization in different layers, the electrons scatter more if their spin is anti-parallel to the general direction of magnetization than those parallel to the direction of magnetization.

The advantage of obtaining well-behaved metallic multilayers is that the lattice

parameters for the different metallic layers could match each other and the two metals forming the multilayer could have the same crystal structure. This is the case for chromium and iron, where both metals adapt the bcc (body-centred cubic) crystal structure and they have very similar lattice parameters. Moreover, in order to exhibit the GMR effect the length of mean free path for the conduction electrons has to greatly exceed the interlayer separations, so that the electrons can travel through magnetic layers with spin information. The epitaxial layer structure used by both Grunberg and Fert was laborious and costly, better suited for a research laboratory than for a technological process on a larger scale. As a result, it was an important step when Stuart Parkin, [8] demonstrated that it was possible to achieve the same effect using a much simpler technology by sputtering. The GMR-effect actually proved not to depend on very perfect layers. Since this discovery of the GMR effect in metal multilayers in which the current was carried in the plane of the layers (CIP), GMR has also been observed when the current is carried perpendicular to the plane of the layers (CPP). [9] The CPP research area is a useful way to clear the fundamental science in the GMR effect with a quantitative analysis of the interface and bulk contributions. [9-12]

The discovery of the GMR effect may also be regarded as the first step in developing a completely new type of electronics called spintronics. After GMR a similar system in which two ferromagnetic layers are separated by an insulating material has been constructed. If the insulating layer is thin enough, electric current be able to pass through the insulator by a quantum mechanical effect called tunnelling. This new system is called TMR, Tunnelling Magnetoresistance. In TMR system, an even larger difference in resistance can be created by very weak magnetic fields, and the newest generation of read-out heads uses this technology. [13,14]

Based on these discoveries, a new research area known as superspintronics has

emerged, aiming at utilization of charge and spin transport in ferromagnet/superconductor heterostructures. The rich physics of interplay between ferromagnetism and superconductivity has recently attracted much theoretical and experimental attention (see Ref. [1-3] as reviews). The interest continues due to the progress in the preparation of both new materials and high quality heterostructures down to nanometer size. Singlet superconductivity prefers an antiparallel spin orientation of electrons to form the Cooper pairs, while ferromagnetic order forces the spins to align in parallel. In such systems the exchange field in the ferromagnet is expected to break the time-reversal symmetry in the superconductor and suppress singlet superconductivity. Because superconductivity and ferromagnetism are two competing orders, their coexistence is possible only in a narrow interval in phase space by the proximity effect, and their interaction is referred to as the LOFF state, explained by Fulde, Ferrell, Larkin, and Ovchinnikov. [15,16] The LOFF state means that nonzero total momentum pairing could occur when an exchange field  $E_{ex}$  is present in the  $F/S$  layer structure. In recent years, advances in the fabrication of artificial layered structures have enabled the study of this effect from both the fundamental and the applied aspects when the two orders are spatially separated. In artificially fabricated layered systems, the proximity effect between superconductor ( $S$ ) and normal metal ( $NM$ ) manifests itself as exponentially decaying amplitude of the superconducting wavefunction, which penetrates across the interface into  $NM$ . [17] On the other hand, in ferromagnet/superconductor ( $F/S$ ) layered structures, the superconducting order parameter exhibits spatial variation upon entering the ferromagnet, which arises from the energy shift between the quasiparticles of the pair in the presence of the exchange field. As a consequence, the superconducting wavefunction not only decays in the  $F$  layer but also oscillates over a certain length in the direction perpendicular to the interface. The properties of superconducting wave

functions under the influence of exchange field can be studied by changing the relative strengths of the two competing orderings.

A considerable amount of attention has been devoted to the  $F/S$  bilayer in experimental laboratories where the interplay between ferromagnetism and superconductivity can be studied. The two long-range-order phenomena mix close to the interface, giving rise to interesting effects both from a basic physics perspective and from a perspective of potential applications. These effects include induction of unusual superconducting symmetry correlations and a highly nonmonotonic behavior of various physical quantities on the size of the system. This is a result of the nonuniform superconducting correlations that are induced in the ferromagnetic layer by means of the proximity effect. As a natural extension of the  $F/S$  bilayer, research has also focused on  $S/F/S$  systems,  $F/S/F$ , and multilayer systems, where the influence of ferromagnetism on the Josephson current and the critical temperature has been studied, respectively. For instance, the nonmonotonic oscillating superconducting critical temperature ( $T_c$ ) [18, 19] and the critical current ( $I_c$ ) [20-22], depending on the thickness of the  $F$  layer,  $d_F$ , and reentrant superconducting behavior [23, 24] have been experimentally observed. To reliably control  $F$  thickness over a large range for the study of the  $S/F/S$  junction, it is essential to use a weak ferromagnetic metal. [20, 21] In the study of quasiparticle-mediated coupling in the  $F/S/F$  spin valve structure, a thin  $S$  layer is required. [25-27] These phenomena mentioned above are related to the interaction between superconductivity and magnetism and occur around the boundary of the  $F/S$  structures.

In order to study the transport properties, it is important to understand which boundary condition is applicable at the interfaces. The quality of the interface transparency will affect the coupling mechanism between the  $S$  and the  $F$ . Lately, interfacial transparency  $T_{tran}$ , has been included in the analysis of the interfacial



quality and has been considered to play a dominant role in the boundary condition in layered structures. [27-34] While  $T_{tran} = 1$  indicates a perfect interface, the value of  $T_{tran} < 1$  signifies the decrease in the amplitude of the order parameter. It implies that the electrons are apt to be reflected rather than transmitted at the interfaces, which may reduce the strength of the proximity effect. [28, 29] It is known that the reduced transparency results from both extrinsic and intrinsic factors such as interface imperfection, Fermi velocity difference, and band-structures mismatch. By including the interfacial transmission coefficient in the proximity theory, the discrepancy between the experimental results and the theoretical prediction under a perfect interface assumption could be reconciled. It is common to find discussions in the literature that treats interfacial transparency in terms of the ratio of interface resistance to the product of bulk resistivity and the Cooper pair penetration depth in  $NM$ . [29~34] Studies on  $V/V_{1-x}Fe_x$  ( $x = 1 \sim 0.34$ ) multilayers were performed with current in plane measurements by Aarts *et al.* who first discussed and derived different interface transparency from the result of theoretical fitting. [31] Attanasio *et al.* have studied interfacial transparency for different layered structures, which consist of Nb as a superconductor, Cu, Ag, and Pd as normal metals, and PdNi and Fe as ferromagnetic materials, to investigate the effect of the fabrication method on  $T_{tran}$  with sputtering and molecular beam epitaxy. Their results showed that the interfacial transparency was influenced by intrinsic factors related to the microscopic properties of the two metals across the interface rather than by the fabrication method. [30] Although interfacial transparency is important both from the theoretical and experimental points of view, interfacial transparency is usually treated as a fittable parameter due to the great difficulty in direct measurement. [27-34] Thus our motivation is to approach the  $F/S$  proximity effect by studying the transport property at the interface. In this dissertation, we directly and systematically investigate the influence of interface

resistance on the interfacial transparency between  $S$  and  $F$ , both when  $S$  is in the normal state and in the superconducting state, by varying the thickness of  $S$  with current perpendicular to plane (CPP) measurement. This tool is successful to explain the GMR effect by quantitatively analyzing the interface and bulk contributions. [9-12] Since the interface resistance must be considered as areas conduct in parallel, the unit area resistance we are interested in is  $AR$ , total sample area times the sample resistance. We discuss the unit area interface resistance between  $F$  and  $S$  both in the superconducting state and in the normal state with different kinds of superconductor and ferromagnetic materials (from strong to weak ferromagnetic metal) and compare these values to theoretic prediction quantitatively.

The thesis is structured as follows. Chapter 2 gives an overview of the background and previous literatures of the  $F/S$  heterostructures. Chapter 3 outlines the experimental techniques including sample fabrication and measurement. Chapter 4 introduces the theoretical models necessary for understanding the main mechanisms for describing  $F/S$  system. Chapter 5 gives experimental results of  $\text{Co}/\text{Nb}_x\text{Ti}_{1-x}$  systems. By analyzing the data with the proximity effect model with high interface transparency assumption developed by Radovic [35], we can deduce the critical thickness below which superconductivity vanished. A one-band series-resistance model is used to analyze the CPP data. We compare and analyze the interface transparency in terms of the ratio between unit area interface resistance and various physical quantities in the  $\text{Co}/\text{Nb}_x\text{Ti}_{1-x}$  systems. The influence of the interface resistance with strong ferromagnet Co and three superconductors, Nb,  $\text{Nb}_{0.6}\text{Ti}_{0.4}$ , and  $\text{Nb}_{0.4}\text{Ti}_{0.6}$ , which have various superconducting coherence lengths, are also discussed by the Pippard model. [36] In Chapter 6, we study and analyze the proximity effect between Nb and three strong ferromagnets Fe, Co, and Ni. The influence of lattice mismatch and the lattice structure on interface resistance is found to be important as

compared with Fe/Nb (bcc/bcc), Co/Nb (hex/bcc), and Ni/Nb (fcc/bcc) layered systems. The relevant first principle calculation for these systems is discussed. In Chapter 7, we report a systematic investigation in thickness dependence of  $T_c$  for  $\text{Cu}_{0.5}\text{Ni}_{0.5}/\text{Nb}$  layered structures with weak ferromagnet  $\text{Cu}_{0.5}\text{Ni}_{0.5}$ . High interfacial transparency in this system is deduced. According to study of the dimensional crossover, high interfacial transparency also significantly influences the behavior of the temperature dependence of the critical magnetic field,  $H_{c2}$ , through the strong pair-breaking effect. To understand the transport characteristic at the interface, current perpendicular to plane measurement is also employed. The interfacial transparency between the  $S$  and the  $F$  is systematically studied by comparing experimental data with the result derived from the theoretical model developed by Fominov. [29] Eventually, we are able to determine the interfacial transparency quantitatively. Chapter 8 is a summary of all the results.



## References:

1. F. S. Bergeret, A. F. Volkov, and K. B. Efetov, *Rev. Mod. Phys.* **77**, 1321 (2005).
2. A. I. Buzdin, *Rev. Mod. Phys.* **77**, 935 (2005).
3. Yu. A. Izyumov, Yu. N. Proshin, and M. G. Khusainov, *Phys. Usp.* **45**, 109 (2002).
4. W. Thomson, “*On the Electro-Dynamic Qualities of Metals, Proceedings of the Royal Society of London*”, **8**, pp. 546–550 (1856–1857).
5. I. A. Campbell and A. Fert, ed. E.P. Wohlfarth, North-Holland, Amsterdam, Vol. **3**, p. 747 (1982).
6. G. Binasch, P. Grünberg, F. Saurenbach, and W. Zinn, *Phys. Rev. B* **39**, 4828 (1989).
7. M.N. Baibich, J.M. Broto, A. Fert, F. Nguyen van Dau, F. Petroff, P. Eitenne, G. Creuzet, A. Friederich, and J. Chazelas, *Phys. Rev. Lett.* **61**, 2472 (1988).
8. Presentation of the GMR-technique at IBM’s website:  
[www.research.ibm.com/research/gmr.html](http://www.research.ibm.com/research/gmr.html)
9. W.P. Pratt Jr., S.F. Lee, J.M. Slaughter, R. Lolee, P.A. Schroeder, J. Bass, *Rev. Lett.* **66**, 3060 (1991).
10. J. Bass and W. P. Pratt, Jr., *J. Magn. Magn. Mater.* **200**, 274 (1999).
11. T. Valet and A. Fert, *Phys. Rev. B* **48**, 7099 (1993).
12. P. M. Levy, in *Solid State Physics Series*, edited by H. Ehrenreich and D. Turnbull (Academic, New York, 1994), Vol. **47**, p. 367.
13. J. Moodera and G. Mathon, *J. Magn. Magn. Mater.* **200**, 248 (1999).
14. S. S. P. Parkin, C. Kaiser, A. Panchula, P.M. Rice, B. Hughes, M. Samant, and S.-H. Yang, *Nature Materials* **3**, 862 (2004).

15. P. Fulde and R. A. Ferrell, Phys. Rev. **135**, A550 (1964).
16. A. I. Larkin and Y. N. Ovchinnikov, Sov. Phys. JETP. **20**, 762 (1965).
17. P. G. de Gennes, Rev. Mod. Phys. **36**, 225 (1964).
18. J. S. Jiang, D. Davidović, D. H. Reich, and C. L. Chien, Phys. Rev. Lett. **74**, 314 (1995).
19. I. A. Garifullin, J. Magn. Magn. Mater. **240**, 571 (2002).
20. V. V. Ryazanov, V. A. Oboznov, A. Yu. Rusanov, A. V. Veretennikov, A. A. Golubov, and J. Aarts, Phys. Rev. Lett. **86**, 2427 (2001).
21. V. A. Oboznov, V. V. Bol'ginov, A. K. Feofanov, V. V. Ryazanov, and A. I. Buzdin, Phys. Rev. Lett. **96**, 197003 (2006).
22. J. W. A. Robinson, S. Piano, G. Burnell, C. Bell, and M. G. Blamire, Phys. Rev. B **76**, 094522 (2007).
23. I. A. Garifullin, D. A. Tikhonov, N. N. Garif'yanov, L. Lazar, Yu. V. Goryunov, S. Ya. Khlebnikov, L. R. Tagirov, K. Westerholt, and H. Zabel, Phys. Rev. B **66**, 020505(R) (2002).
24. V. Zdravkov, A. Sidorenko, G. Obermeier, S. Gsell, M. Schreck, C. Müller, S. Horn, R. Tidecks, and L. R. Tagirov, Phys. Rev. Lett. **97**, 057004 (2006).
25. L. R. Tagirov, Phys. Rev. Lett. **83**, 2058 (1999).
26. J. Y. Gu, C.-Y. You, J. S. Jiang, J. Pearson, Ya. B. Bazaliy, and S. D. Bader, Phys. Rev. Lett. **89**, 267001 (2002).
27. A. Potenza and C. H. Marrows, Phys. Rev. B **71**, 180503(R) (2005).
28. L. R. Tagirov, Physica C **307**, 145 (1998).
29. Ya. V. Fominov, N. M. Chtchelkatchev, and A. A. Golubov, Phys. Rev. B **66**, 014507 (2002).
30. R. Gross, A. Sidorenko, and L. Tagirov, *Nanoscale Devices-Fundamentals and Applications*, Springer (2004).

31. J. Aarts, J. M. E. Geers, E. Bruck, A. A. Golubov, and R. Coehoorn, Phys. Rev. B **56**, 2779 (1997).
32. C. Cirillo, S. L. Prischepa, M. Salvato, and C. Attanasio, M. Hesselberth, and J. Aarts, Phys. Rev. B **72**, 144511 (2005).
33. J. Kim, Jun Hyung Kwon, K. Char, Hyeonjin Doh, and Han-Yong Choi, Phys. Rev. B **72**, 014518 (2005).
34. J. Kim, Y-J Doh, and K. Char, Phys. Rev. B **71**, 214519 (2005).
35. Z. Radović, M. Ledvij, L. Dobrosavljević-Grujić, A. I. Buzdin, and J. R. Clem, Phys. Rev. B **44**, 759 (1991).
36. A. B. Pippard, Proc. R. Soc. London, Ser. A **391**, 255 (1984).



# Chapter 2

## General Background and Previous Work

### 2.1 The length scale of Superconductivity and

#### Ferromagnetism

There are many new phenomena that do not exist in the constituent materials in isolation. These behaviors come from the proximity of different materials with various functionalities and long-range orderings. For instance, Giant magnetoresistance in heterogeneous structures is due to interlayer coupling between two ferromagnetic layers across a non-magnetic spacer layer. [1.2] The interplay of superconductivity and magnetism is another area where proximity effects are of long-standing interest. Superconducting ordering and magnetic ordering are diametrically different and generally incompatible with each other. To analyze  $F/S$  multilayer structures, we must distinguish several different lengths in  $S$  and  $F$ .

Under the basic assumptions of the Drude model, the molecules of a gas, which move in straight lines until they collide, is treated as identical solid spheres in the kinetic theory. [3] An electron experiences a collision with a probability per unit time  $1/\tau$  and is assumed to achieve thermal equilibrium with its surroundings. According to Ohm's law, the current,  $I$ , flowing in a wire is proportional to the potential drop  $V$  and follow  $V=IR$ . Here, the resistance of the wire,  $R$ , though depends on dimensions, is independent of the magnitude of either the current or potential drop. We can estimate the resistance by the Drude model. [4] The resistivity,  $\rho$ , is defined to be the proportionality constant between the electric field,  $E$ , and the current density,  $j$ , by the equation:

$$E=\rho j. \quad (2.1)$$

If each electron carries a charge  $-e$ , then the total charge crossing area,  $A$ , will be  $-nevAdt$  with velocity,  $v$ , in the time  $dt$ , where  $n$  is electrons per unit volume. Hence the current density is

$$j=I/A=-nev. \quad (2.2)$$

Because of the collision of electrons with impurities, lattice imperfections, and phonons, the displaced sphere may be maintained in a steady state in an electric field. In the presence of a field  $E$ , electrons are moving in an average electronic velocity,  $v$ , which is directed opposite to the field due to negative charge. Therefore

$$v = -\frac{eE\tau}{m}, \quad (2.3)$$

$\tau$  is the relaxation time. So the current density is usually stated in terms of the inverse of the resistivity, the conductivity  $\sigma=1/\rho$ , by

$$j = \frac{ne^2\tau}{m}E; \quad \sigma = \frac{ne^2\tau}{m}. \quad (2.4)$$

The electrical resistivity of most metals is dominated at room temperature by collisions of the conduction electrons with lattice phonons and at low temperature by collisions with impurity atoms and mechanical imperfections in the lattice. Qualitatively, electrons are pictured as moving ballistically between collisions, but making many collisions as they traverse a sample (diffusive transport). The mean free path,  $l$ , measures the average distance an electron travels between collisions associated with the elastic scattering processes. The distance is defined by

$$l = v_F\tau, \quad (2.5)$$

where  $v_F$  is the velocity at Fermi surface, because all collisions involve only electrons near the Fermi surface. For thin films,  $l$  is usually limited by the size of grain boundaries, imperfections, sample roughness and dimensions, the limitation which is related to the finite size effect. [5] We can simply distinguish the diffusive regime from ballistic regime by a comparison between dimension of the system  $L$ , in the direction of transport and  $l$ , as shown in Fig. 2.1

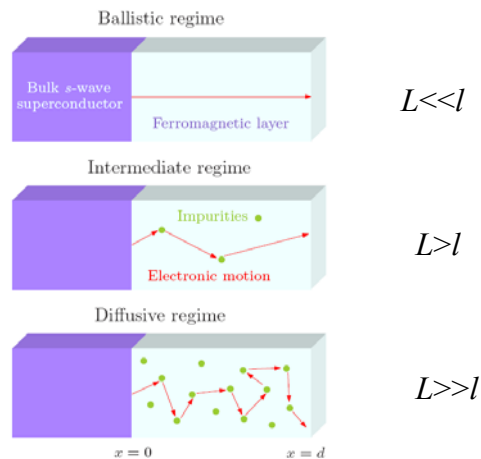


**Figure 2.1:** Overview of the  $F/S$  heterostructure in different regime. [6]



When  $L$  is much larger than  $l$ , an electron will experience several collisions before reaching the boundaries and will undergo random diffusion motion in the sample. Alternately, when the  $L$  of the sample size is smaller, the electron will reach the boundaries of the sample without losing its initial momentum. The ballistic regime is usually referred to the clean limit, whereas a system in which an electron undergoes diffusion motion corresponds to the dirty limit. Moreover, the product of  $\rho$  and  $l$  from Eqs. (2.4) and (2.5) is a constant, and can be obtained by

$$\rho l = \frac{mv_F}{ne^2\tau}. \quad (2.6)$$

Actually, superconductivity and magnetic ordering have very different intrinsic length scales. The coherence length, which is the appropriate correlation length for superconductivity, is of the order of several hundred Å for the low temperature superconductors. However the correlation lengths for the various types of magnetic (M) ordering are much shorter, typically  $\leq 20$  Å. [7] There are two typical characteristic lengths, the London penetration depth and the coherence length in the theoretical and experimental investigations of superconductivity. The London penetration depth refers to the exponentially decaying magnetic field at the surface of a superconductor derived from London Equation. It is related to the density of superconducting electrons in the material, given by [3]

$$\lambda_L = (mc^2 / 4\pi ne^2)^{1/2}, \quad (2.7)$$

for particles of charge,  $e$ , and mass,  $m$ , with superconducting electron density,  $n$ . An independent characteristic length is the coherence length. The coherence length is best introduced into the theory through the Landau-Ginzburg equation. [4] It is related to the Fermi velocity for the material and the energy gap,  $\Delta$ , associated with the condensation to the superconducting state, represented as

$$\xi_0 = 2\hbar v_F / \pi\Delta. \quad (2.8)$$

The coherence length is a measure of the distance within which the superconducting electron concentration cannot change drastically in a spatially-varying magnetic field. The zero-temperature energy gap gives a fundamental formula independent of phenomenological parameters: [8]

$$\Delta(0) = 1.76k_B T_C. \quad (2.9)$$

The elementary theory also predicts that the energy gap will vanish near the critical temperature; the behavior can be described as a function of temperature by

$$\frac{\Delta(T)}{\Delta(0)} = 1.74 \left(1 - \frac{T}{T_C}\right)^{1/2}. \quad (2.10)$$

In  $F/S$  layered system, one of the challenges in the studies of proximity effects is that both layers are near the thin film limit, with thicknesses comparable to their respective correlation lengths. Thus, both are subject to strong "finite-size effects". In general, the correlation length  $\xi_S(T)$  of a superconducting and  $\xi_F(T)$  of a magnetic system with long-range order diverge at  $T_{C,(Curie)}$ , which here denotes the bulk superconducting transition temperature and the bulk magnetic ordering temperature, respectively. Near  $T_{C,(Curie)}$ ,  $\xi_{S,F}(T)$  has a power law temperature dependence [4]

$$\xi_{S,F}(T) = \xi_{S,F}(0) \left(1 - \frac{T}{T_{C,(Curie)}}\right)^{-\alpha}, \quad (2.11)$$

where  $\xi_{S,F}(0)$  is the extrapolated correlation length at 0 K, and  $\alpha$  is the critical exponent for the correlation length. The transition temperature  $T_C(d_{S,F})$  of a function of layer thickness  $d$  is reduced from  $T_{C,(Curie)}$  according to the "finite-size scaling relation [7]

$$T_C(d_{S,F}) = T_{C,(Curie)} \left(1 - \frac{d}{\xi_{S,F}(0)}\right)^{1/\alpha}. \quad (2.12)$$

Thus,  $T_C(d_{S,F})$  is significantly reduced from  $T_{C,(Curie)}$ , when  $d$  is smaller than, or comparable to  $\xi_{S,F}(0)$ . As for low  $T_C$  superconductors, since the values of  $\xi_S(0)$  are long as mentioned above, the  $T_C$  of  $S$  layers for several hundred Å thick is already reduced. Whereas the  $\xi_F(0)$  of magnetic systems is much shorter, no significant reduction of  $T_{Cuire}$  can be observed except in ultrathin layers of thickness  $d < 50$  Å.

The spin-diffusion length  $l_{SF}$  is another important length scale to study  $F/S$  system due to an additional degree of freedom introduced by the spin of electron. The spin coherence can be maintained in an effective travel distance before the orientation of the spin is destructed by spin-orbit interactions and other mechanisms. [9] Moreover, the spin-flip length,  $\lambda_{SF}$ , which is the mean distance between spin-flipping collisions. Defined  $\tau_{SF}$  as the mean time between spin-flipping events gives

$$\lambda_{SF} = v_F \tau_{SF}. \quad (2.13)$$

In contrast, the spin-diffusion length,  $l_{SF}$ , is the mean distance that electrons diffuse between spin-flipping collisions which obeys a diffusion equation. The standard form

is [10]

$$l_{SF} = \sqrt{D\tau_{SF}} = \sqrt{(1/3)lv_F\tau_{SF}} = \sqrt{(1/3)l\lambda_{SF}}, \quad (2.14)$$

where  $D$  is the diffusion constant, and the usual ordering of lengths is  $l < l_{SF} < \lambda_{SF}$ .

We find the thermal conductivity of a Fermi gas,  $K_{el}$ , when taking into consideration the coefficient of electronic specific heat,  $\gamma$ , can be defined as [4]

$$K_{el} = \frac{\pi^2 nk_B T \tau}{3m} = \frac{1}{3} \gamma T v_F l. \quad (2.15)$$

According to the Widmann-Franz law, for metals, the ratio of the thermal conductivity to the electrical conductivity is directly proportional to the temperature by using Eq. (2.4) for  $\sigma$  and Eq. (2.15) for  $K_{el}$ : [3, 4]

$$\frac{K_{el}}{\sigma} = \frac{\pi^2 nk_B T \tau / 3m}{ne^2 \tau / m} = \frac{\pi^2}{3} \left(\frac{k_B}{e}\right)^2 T \quad (2.16)$$

This result supports the picture of an electron gas as the carrier of charge and energy. Furthermore, the diffusion constant is related to low temperature resistivity,  $\rho$ , and the to coefficient of electronic specific heat,  $\gamma$ , following the relationship by considering the Eqs. (2.15) and (2.16)

$$D = v_F l / 3 = \frac{1}{3\gamma\rho} \left(\frac{\pi k_B}{e}\right)^2. \quad (2.17)$$

Thus the diffusion constant can be estimated by measuring the specific heat.

Non-magnetic pure metals, such as  $l_{SF}$  of Cu, Ag, and Al are as long as a few hundred nanometers, whereas the values of ferromagnets like Fe, Ni, and Py, the values are all  $\leq 20$ nm. [9] The early analysis of the current-in-plane (CIP) measurements is relatively complex, in part because the mean free paths,  $l$ , for total scattering of electrons, are fundamental lengths. [11] The currents are mixed by transmission of electrons across interface. The variation of the CIP with layer thickness is mainly dominated by  $l \ll l_{SF}$  usually. In contrast, for the current perpendicular to plane (CPP) measurement [12, 13], currents of electrons with moments *up* or *down* relative to a fixed direction propagate independently through a simple two-current series resistor (2CSR) model, in which this model gives a total

specific resistance (sample area  $A$  times resistance  $R$ ) that is just the sum of effective resistivities times layer thicknesses, plus effective interface specific resistances. For the CPP measurements, we emphasize that the important lengths in this model and the Valet-Fert theory [10] are the layers thicknesses and spin diffusion length,  $l_{SF}$ , since the thickness is usually smaller than or comparable to  $l$ .

It is of great interest how the spin accumulation signal is modified by replacing normal metals with a superconductor. Lately, a study predicts that the spin diffusion length in the superconducting state is the same as that in the normal state. [14] In proximity-effect  $F/S$  systems, effects of spin-flipping in the  $F$  metal have been seen in damped oscillatory behavior of the superconducting correlations. Expected longer-range penetration into the  $F$ -metal of triplet-state superconducting correlations is also predicted [15, 16] Triplet correlations may be affected by spin flipping at the  $F/S$  interfaces. But these predictions have yet to be confirmed and little reliable information is available, especially for an investigation of  $F/S$  interface.

## **2.2 The coexistence of Superconductivity and Ferromagnetism in the LOFF state**

The rich physical phenomenon between ferromagnetic and superconductivity materials has recently attracted much attention due to the great progress in the preparation of high quality heterostructures (see Ref [17], [18] for a review). According to their incompatible nature, singlet superconductivity and ferromagnetic order do not coexist in bulk materials. Ginzburg [19] has first formulated the problem of the coexistence of magnetism and superconductivity considering an orbital mechanism by which superconductivity is suppressed. It then becomes clear that

superconductivity in the singlet state could be destroyed by an exchange mechanism based on the advent of the BCS theory by Bardeen, Cooper, and Schrieffer (1957). The exchange field in a magnetically ordered state tends to align spins of Cooper pairs in the same direction, thus preventing a pair-pairing effect. In early reports, there has been experimental evidence providing the coexistence between the magnetism and superconductivity, such as ternary compounds (RE)Rh<sub>4</sub>B<sub>4</sub> and (RE)Mo<sub>6</sub>X<sub>8</sub> (X=S, Se) [20], and quaternary compounds (RE)Ni<sub>2</sub>B<sub>2</sub>C [21]. However, it has turned out that in many of these systems superconductivity coexists with antiferromagnetic order, and the Néel temperature  $T_N < T_{Curie}$ , the critical temperature. In fact, superconductivity and antiferromagnetism can coexist quite peacefully since, on average, the exchange and orbital fields are zero at distances of the order of the Cooper pair size or superconducting coherence length.

Anderson and Suhl (1959) have predicted that a nonuniform magnetic order would appear at the Curie temperature and the period of this magnetic structure would be smaller than the superconducting coherence length but larger than the interatomic distance. [22] The coexistence phase is a domain like structure with very small period according to this theoretical analysis which takes orbital and exchange mechanisms as well as magnetic anisotropy into account. [23] Recently, UGe<sub>2</sub> [24] and URhGe [25] have first discovered ferromagnetic superconductors but actually these systems have a triplet pairing character which permits the coexistence of superconducting with ferromagnetism. Apparently, the coexistence of singlet superconductivity with ferromagnetism is very unlikely in bulk compounds. Because of their competing nature, singlet superconductivity prefers an antiparallel spin orientation of electrons to form Cooper pairs, while ferromagnetic order forces the spins to align in parallel.

However, the coexistence may be achieved in artificially fabricated layered ferromagnet/superconductor (F/S) systems. The probability of the coexistence of

superconductivity and magnetic order has been studied for several decades. Fulde and Ferrell (1964) [26] and Larkin and Ovchinnikov (1965) [27] have demonstrated that, in a pure ferromagnetic superconductor at low temperature, superconductivity may be nonuniform (FFLO state). In the FFLO state, a superconducting order parameter is generated in the presence of an exchange field, and it turns out that the distribution of the electrons is favorably extended along one of the directions perpendicular to the exchange field than a spherically symmetric distribution. [28] So the Cooper pairs with shifted center of mass momenta appear, and an inhomogeneous distribution function is shown in Fig. 2.2. It means that nonzero total momentum pairing can still occur while an exchange field  $E_{ex}$  is present. However, it is difficult to verify this prediction experimentally due to the incompatibility of ferromagnetism and superconductivity. In the layered system, the Cooper pairs can penetrate into the  $F$  layer and induce superconductivity there. In such a case we have a unique opportunity to study the properties of superconducting electrons under the influence of exchange field. Since we can change the relative strengths of two competing orderings by varying the layer thicknesses, it is possible to study the interplay between superconductivity and magnetism in a controlled manner.

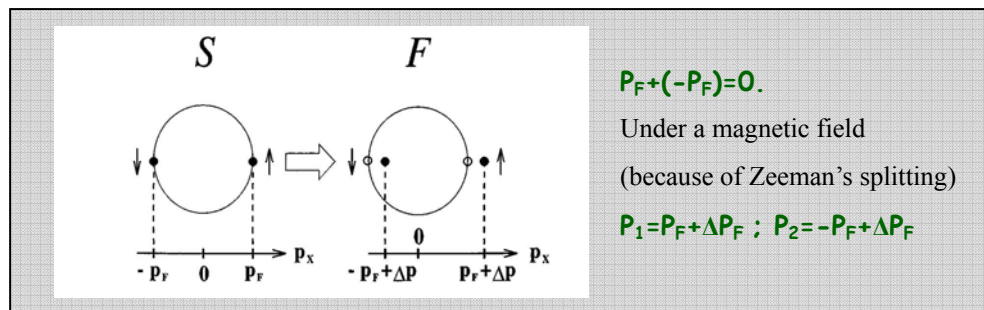


**Figure 2.2:** Cooper pair in superconductor and ferromagnet.  $\Delta p = h/v_F$ . [28]

## 2.3 General phenomenon in proximity effect

As mentioned in Section 2.1, the contact of materials with different range ordering will modify their properties near the interface. Note that the conventional proximity effect is considered in the case of interface between superconductor and normal-metal. When a superconducting layer  $S$  is brought into contact with a normal metallic layer  $NM$ , the superconducting critical temperature  $T_c$  of  $S$  decreases with the thickness of the  $NM$ -layer increasing and the superconducting condensate penetrates into the  $NM$ -layer over a long distance. Therefore, superconducting like properties may be induced in the normal metal, and this phenomenon is called the conventional proximity effect. (see reviews [29], [30]) Thus, attractive electron-electron interaction may be absent in the  $NM$ -layer, and the Cooper pair wave function penetrates into  $NM$  over a distance  $\xi_{NM}$ , much exceeding the interatomic spacing. (See Fig. 2.3 (a) ) In a dirty limit, i.e. in a diffusive metal with an impurity concentration, the correlation length  $\xi_{NM}$  is given by the characteristic rate,  $\xi_{NM} = \sqrt{D/2\pi T}$ , where  $D = v_F l / 3$  is the diffusion coefficient,  $v_F$  is the Fermi velocity and  $l = v_F \tau$  is the mean free path of the conduction electrons, where  $\tau$  is the momentum relaxation time. [31] Meanwhile, the Josephson effect in  $S/NM/S$  junctions is an absolute manifestation of the induced superconductivity in a normal metal. If the thickness of the  $NM$  layer,  $L$ , is the order of the correlation length  $\xi_{NM}$ , the critical current  $j_c$  decays exponentially with  $L$  as  $j_c \sim \exp(-L/\xi_{NM})$ . Due to this effect the Josephson critical current can still be observed even if the thickness of the  $NM$ -layer exceeds  $1 \mu\text{m}$ . [15]

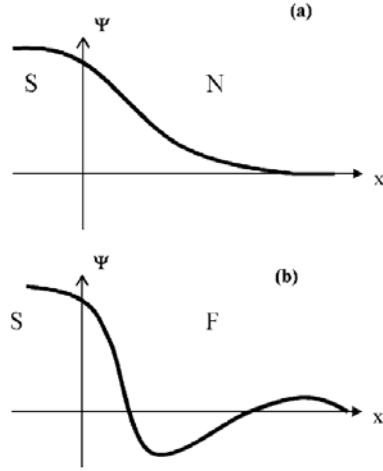


**Figure 2.3:** Schematic behavior of the superconducting order parameter near the (a) superconductor-normal metal and (b) superconductor-ferromagnet interfaces. The continuity of the order parameter at the interface implies the absence of the potential barrier. [2]

Now, replacing the normal metallic layer  $NM$  in an  $NM/S$  structure by a metallic ferromagnetic layer  $F$ , one comes to basically the same effect: The pair wave function from  $S$  penetrates into  $F$  and makes the  $F$ -layer superconducting. But the penetration depth into the ferromagnet is drastically reduced as contrasted to the  $NM$  layer given by the correlation length from the characteristic rate,  $\xi_F = \sqrt{D_F/2h}$  in the dirty limit with the diffusion coefficient of the ferromagnet  $D_F$  and the exchange field in the ferromagnet  $h$ . [31] For example, in strong ferromagnets like Fe, Co and Ni, the length  $\xi_F$  has a typical value of 0.7 nm. A reason for the nearly atomic length scale is that the exchange field  $h$  in the F-layer tends to align the spins of a Cooper pair and this leads to a strong pair breaking effect. However, there is another important difference in comparison with the normal metals, in addition to a faster decay of the superconducting condensate in the ferromagnet. Since in the  $F$ -layer the spin-up and spin-down bands are split by the exchange field  $h$ , the electrons of a Cooper pair at the Fermi energy have necessarily different  $k$ -vectors for the up and



down spins. The physical picture of the proximity effect in a ferromagnetic conductor is therefore very similar to the FFLO effect. [26, 27] For simplicity, we first consider the situation in which spin is a good quantum number without spin-orbit interaction. Imagine a Cooper pair being transported across an  $S/F$  interface with its electron momenta aligned with the normal interface. Upon entering the  $F$  region, where the pair is not an eigenstate, it becomes an evanescent state, decaying exponentially on the length scale. Thus, a Cooper pair in a ferromagnet, the up-spin electron, which defined the spin orientation along the exchange field, decreases its potential energy by  $h$ , while the downspin electron energy increases by the same value. To compensate this energy variation for conservation, the up-spin electron increases its kinetic energy, while the down-spin electron decreases its kinetic energy. As a result the Cooper pair, as shown in Fig. 2.2, entering into a ferromagnetic region results in acquiring a center of mass momentum  $Q=2\Delta P=2h/vF$ . Here, the direction of the modulation wave vector must be perpendicular to the interface, because only this orientation provides a uniform order parameter in the superconductor. Combining the two pairs into a singlet combination we find that the overall effect of the exchange field in the  $F$  region on a singlet Cooper pair is to give it a spatial modulation, as shown in Fig. 2.3 (b). Hence if the wave function of the pair in a superconductor is  $\Phi(x_1-x_2)$ , where  $x_1$  and  $x_2$  are the coordinates of the two electrons in a ferromagnet the wave function becomes  $\cos[Q(x_1+x_2)] \Phi(x_1-x_2)$ . This simply establishes the physical origin of the oscillations. [28]

Superconducting/ferromagnet systems are in some ways analogous to the nonuniform superconducting state. The Cooper pair wave function extends from superconductor to ferromagnetic with damped oscillatory behavior. This leads to oscillations of the electron density of states, a nonmonotonic dependence of the critical temperature of  $F/S$  multilayers and bilayers on the ferromagnet layer thickness,

and the realization of “ $\pi$ ” Josephson junctions in  $S/F/S$  systems. Spin-valve behavior in complex  $F/S$  structures gives another example of the interesting interplay between magnetism and superconductivity, an effect that is promising for potential applications. There are many effects behind this pairing amplitude oscillation. We shall discuss some effects later.

In contrast to the proximity effect, the reverse effect, namely, the uniform magnetization into the superconductor is also possible. Theoretically, the induced magnetic moment of conduction electrons in the  $S$  layer at distances of the order of the Cooper pair size,  $\xi_s$ , from the  $F/S$  interface should exactly compensate the moment of conduction electrons in the  $F$  layer. This effect is called the inverse proximity effect. [32] Qualitatively, the physical origin of the ferromagnetism in the  $S$  layer can be explained by the spin-up electrons (the majority spins in the  $F$ -layer) residing with a higher probability in the  $F$  layer, and the spin down electrons, due to superconducting correlations, with a higher probability in the  $S$  layer. Thus, the magnetic moment in the  $S$  layer should be oriented antiparallel to the magnetization of conduction electrons in the  $F$  layer, as shown in Fig. 2.4. But experimental observation of this state is difficult. Only recently confirmed experiments have studied this state with the nuclear magnetic resonance (NMR) measurement in  $\text{Pd}_{1-x}\text{Fe}_x/\text{V}/\text{Pd}_{1-x}\text{Fe}_x$  and  $\text{Ni}/\text{V}/\text{Ni}$  heterostructures [33] and with the polar Kerr effect measurement using zero-area-loop Sagnac magnetometer in  $\text{Pb}/\text{Ni}$  and  $\text{Al}/(\text{Co-Pd})$  bilayers system. [34]

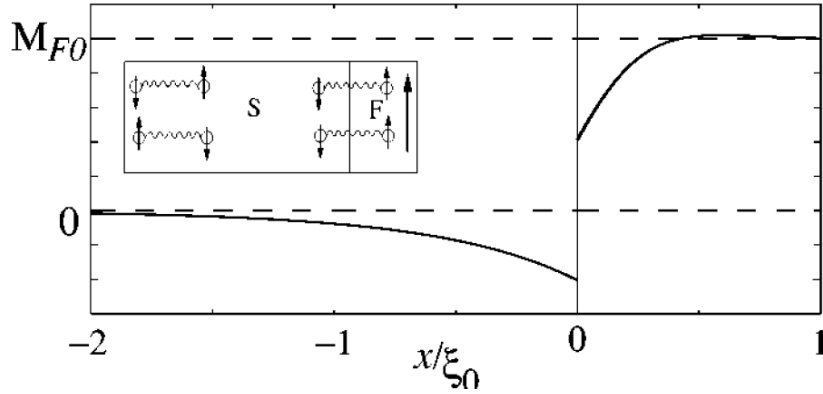


**Figure 2.4:** Spatial dependence of the magnetization in the  $F/S$  system. Inset: Schematic view of the inverse proximity effect in a  $F/S$  system. [16]

## 2.4 Oscillatory superconducting temperature in $F/S$ layered structure



In the  $F/S$  layered system, the damped oscillatory behavior of the superconducting order parameter in ferromagnet may produce commensurability effects between the period of the order parameter oscillation and the thickness of a  $F$  and  $S$  layer. It may be easier to achieve experimental observation by fabricating artificially hybrid layered  $F/S$  structures in different configuration as shown in Fig. 2.5. These structures lead to oscillations of the superconducting transition temperature in  $F/S$  bilayers as well as trilayers and multilayers system. Actually there are qualitatively differences of physical behaviors between various layered structures.

[17]

The magnetic coherence length, which determines the oscillation length and the penetration depth of the pair amplitude in  $F$ , is given by  $\xi_F^{ex} = \frac{\hbar v_F}{2E_{ex}} (\xi_F < l_F)$  in the

clean limit, and  $\xi_F^{ex} = \sqrt{\frac{\hbar D_F}{2E_{ex}}}$  ( $\xi_F > l_F$ ) in the dirty limit, where  $D_F$  is the diffusion constant,  $v_F$  the Fermi velocity and  $l_F$  the mean free path in the  $F$ . [18,35] In such a case, we are able to study the properties of superconducting electrons under the influence of exchanging field, since we can change the relative strengths of two competing orderings by varying the layer thickness.

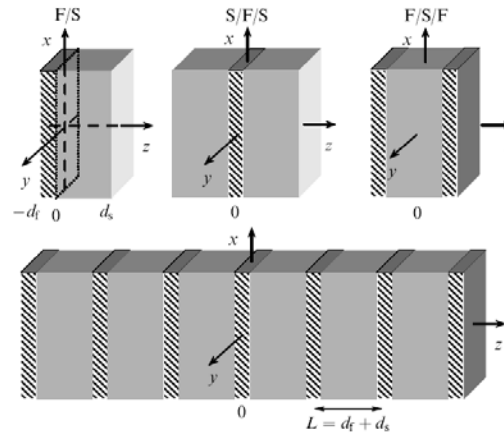


**Figure 2.5:** Multilayered  $F/S$  systems that have been studied in experiments: bilayers, trilayers and superlattices. [17]

Thus, most of the predicted phenomena in proximity effect found experimentally are based on the oscillatory superconducting wavefunction. For example, behaviors of the critical temperature versus thickness of magnetic or superconductor layer are the sign of the order parameter changes in the ferromagnet. In 1964 Hauser, Theurer, and Werthamer [36] first investigated the proximity effect in  $F/S$  layer systems by studying the reduction of the superconducting transition temperature  $T_C$  in  $Pb/X$  systems in which  $X$  denoted various types of materials; ferromagnetic Fe, Ni, and Gd, antiferromagnetic Cr and dilute magnetic alloys like 1% Fe in Mo or 2.9% Gd in Pb. If the thickness of a superconducting layer was smaller than a critical one, the proximity effect totally suppressed the superconducting transition. In the beginning,

they tried to interpret theoretically their results in terms of the proximity effect. The methods were ignoring the fact that used metals were ferromagnetic and another hypothesis that iron has an effective electron-electron interaction as shown in the solid curve and dashed line, respectively. In Fig. 2.6, both methods were above the data curve and in disagreement with the measurements. In the best fit, they concluded that the ferromagnetism of the iron played an important role in determining the sandwich transition temperature, and it was necessary to combine the proximity effect with the Abrikosov-Gor'kov theory, in order to better agreement with the data in Fig. 2.6. According to the result, the depression of the transition temperature is identical when the iron thickness was larger than 1.5 nm.

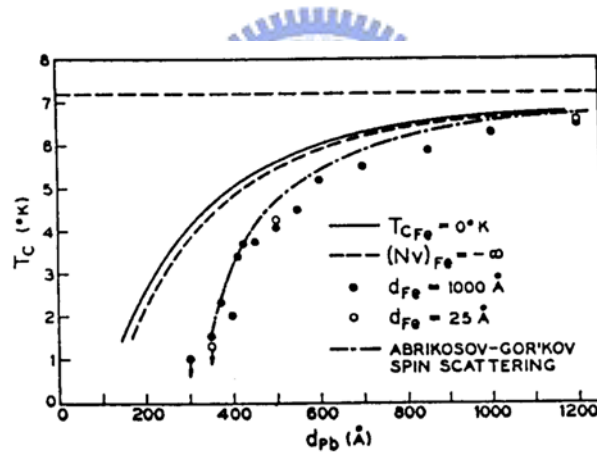


**Figure 2.6:** Transition temperature for glass-Pb-Fe sandwiches with a constant iron film thickness of 100 nm. The solid line represents a fit ignored the fact that the used metals are ferromagnetic. The effective electron-electron interaction for Fe has been taken into account in the dashed line. In the lower curve the proximity effect is combined with the Abrikosov-Gor'kov theory and is in fair agreement with the data. [36]

Much interest in  $F/S$  proximity effects has been aroused since the theoretical work of Radovic *et al.* [37] and the experimental results of Wong *et al.* [38], who studied the  $T_C$  dependence of V/Fe multilayers as a function of the Fe thickness for

different fixed V thicknesses as shown in Fig. 2.7. It can be seen that  $T_C$  decreases rapidly with the iron thickness increasing. They also noticed that an upturn of  $T_C$  at large  $d_{Fe}$  for some V-thicknesses. This was the first indication on the nonmonotonic variation of  $T_C$  versus the F layer thickness. The peculiarities in the  $T_C(d_{Fe})$ -dependence in the V/Fe system could be explained by the existence of the oscillatory transition from 0- to  $\pi$ -Josephson coupling between two superconducting layers separated through ferromagnetic layers. Radovic *et al.* concluded from their calculations that  $T_C$  could be higher for the system with  $\pi$ -coupling rather than for the system with the phase difference equal to 0.

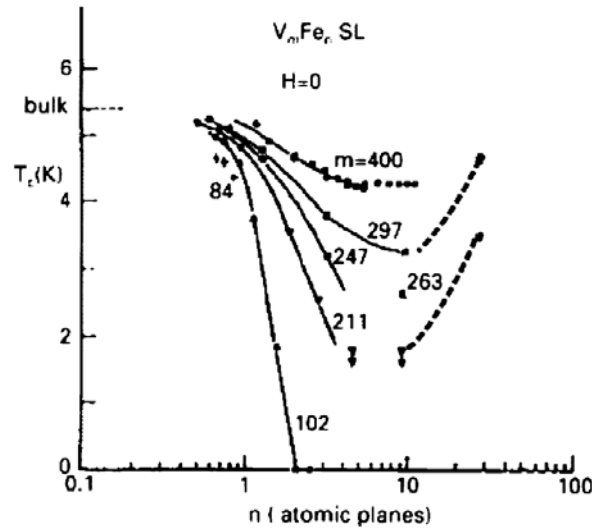


**Figure 2.7:** Superconducting transition temperature of  $V_mFe_n$  superlattices. [38].

Therefore, several experiments attempted to observe nonmonotonic behavior of the transition temperature in  $S/F$  layered system. However, in subsequent experiments of Koorevaar *et al.* [39], no oscillatory behavior of  $T_C$  was found in V/Fe system. The transition-metal ferromagnets, such as Fe, have a strongly itinerant character of the magnetic moment that is very sensitive to the local coordination. In thin Fe layers, the magnetism may strongly decrease and even vanish. The best choice was to use the rare-earth ferromagnetic metal with localized magnetic moments. Two groups have

studied Nb/Gd multilayers. Strunk *et al* [40] observed a step-like behavior of  $T_C$  as a function of the Gd thickness for the samples prepared by molecular beam epitaxy (MBE) technique (Fig. 2.8). They explained the step-like behavior of  $T_C$  in terms of the Gd layers by changing of the magnetic state. It was found that due to initial island growth, long-range magnetic order occurred above  $d_{Gd} = 2$  nm. However, Jiang *et al.* [41] clearly observed oscillatory behavior of  $T_C$  for the Nb/Gd multilayers at larger thickness of Gd prepared by the sputtering technique (Fig. 2.9). They concluded that the obtained results provided the first experimental evidence for the predicted  $\pi$ -phase shift in  $F/S$  multilayers. An increase of  $T_C$  implied the transition from the 0 phase to the  $\pi$  phase. As a result, the experimental results from different groups were contradictory. In particular, the rapid initial decrease in  $T_C$  with an increase in  $d_F$  was replaced by the subsequent plateau, but in other experiments with same systems the plateau was preceded by an oscillating behavior of  $T_C$ .

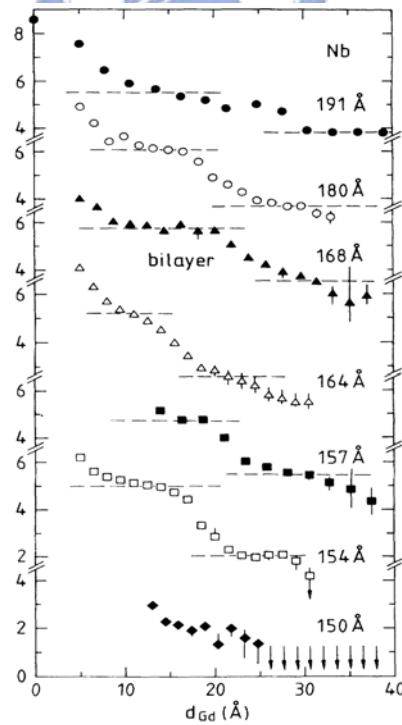


**Figure 2.8:** Resistively determined transition temperature  $T_C$  as a function of  $d_{Gd}$  in several series of MBE triple Nb/Gd layers that have been prepared in a single evaporation run. [40]

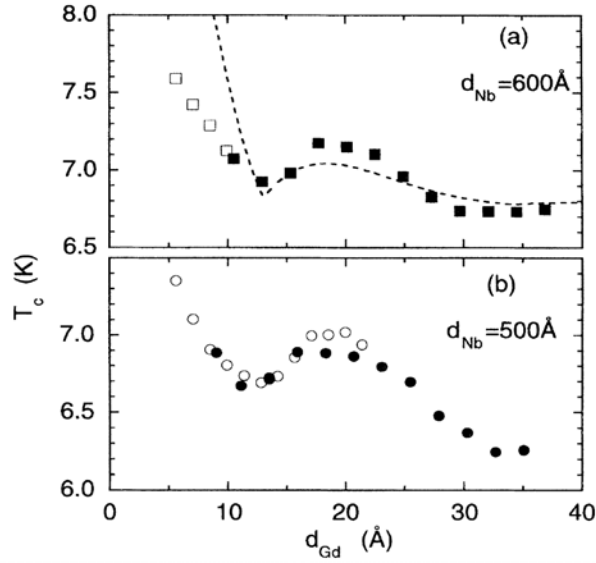


**Figure 2.9:** Superconducting transition temperature  $T_C$  versus  $d_{Gd}$  in sputtered Nb/Gd multilayers with (a)  $d_{Nb} = 60 \text{ nm}$  and (b)  $50 \text{ nm}$ . Different symbols correspond to different sample series. Dashed line in (a) is a fit by Radovic's theory. [41]

The other unusual behavior observed by Mühge *et al* [42, 43] who studied  $T_C$  dependence on the Fe thickness  $d_{Fe}$  with fixed  $d_{Nb}$  for Fe/Nb/Fe trilayers prepared by sputtering. The non-monotonic  $T_C$  behavior (Fig. 2.10) was very similar to that in Nb/Gd multilayers reported by Jiang *et al.* [41] The explanations related to  $0$  to  $\pi$  phase transition could not be used in this case because in the Fe/Nb/Fe trilayers only one superconducting layer existed while for the  $\pi$ -junction to occur it was necessary to have at least two superconducting layers. According to their results, there was a magnetically dead layer close to the Nb/Fe interface with the thickness  $0.7 \text{ nm}$  which resulted in the  $T_C(d_{Fe})$  sharply drops up to  $0.7 \text{ nm}$ . It was concluded that non-monotonic  $T_C$ -behavior occurred in this system due to the strong modification of the properties of magnetically dead Fe layer coupled with the onset of ferromagnetic order.



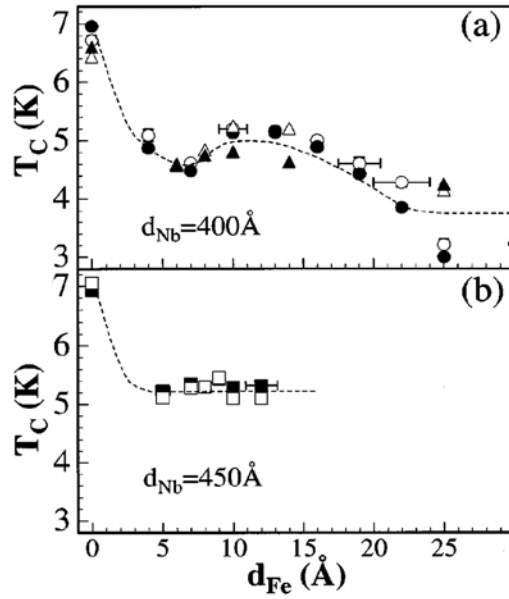


**Figure 2.10:** Superconducting transition temperature  $T_c$  as a function of  $d_{Fe}$  as determined by ac susceptibility solid symbols and resistivity opened symbols measurements. The triangles, circles, and squares correspond to different sample sets. The dashed lines are guide for the eyes. [42]

For MBE samples the thickness of the magnetically dead Fe layer was smaller than 0.5 nm but a step-like behavior of  $T_c$  versus Fe layer thickness (Fig. 2.11) was observed. [44] A comparative analysis of sample preparations showed that the molecular beam epitaxy grown samples did not reveal  $T_c$  oscillations, whereas magnetron sputtered samples did. [45] This difference might be attributed to the appearance of a magnetically “dead” interdiffused layer at the  $F/S$  interface and initial island growth of the ferromagnetic layers, which played an important role for the molecular beam epitaxy grown sample.

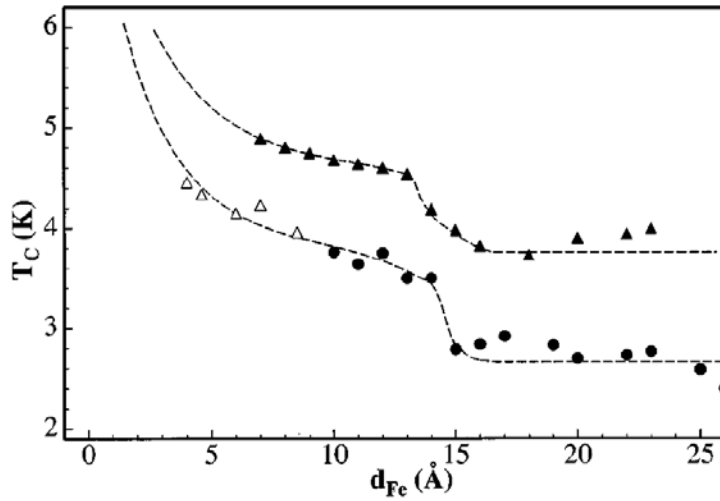


**Figure 2.11:** Superconducting transition temperature  $T_c$  versus  $d_{Fe}$  for three series of samples. The broken lines are guides for the eye. [44]

All of these controversial results listed above made it necessary to consider the transport property at  $F/S$  interface. Aarts *et al* [46] were the first to study interface transparency in order to understand the pair-breaking mechanism in  $Fe/V_{1-x}Fe_x$  multilayer system. They used the V-Fe alloy with different Fe composition to continuously change the average magnetic moment in the ferromagnetic layer. They presented experimental evidence that the transmission coefficient of the  $F/S$  interface for the Cooper pairs could be restricted by the average magnetic moment in the ferromagnetic material. Later Lazar *et al.* experimentally studied the Fe/Pb/Fe system which had a much smaller intermixed layer at the interface. [47] According to their report, the inconsistency between the oscillating  $T_c(d_{Fe})$  behavior and Radvoic's model [48] with an assumption of highly transparent interface could be solved by reducing interface transparency from Tagirov's model [35] (Fig. 2.12). It implied that the discontinuity in the pairing wave function actually occurred in real systems. The result might be caused by quantum mechanical reflection of the conduction electrons

at the interface due to electron energy band mismatch.

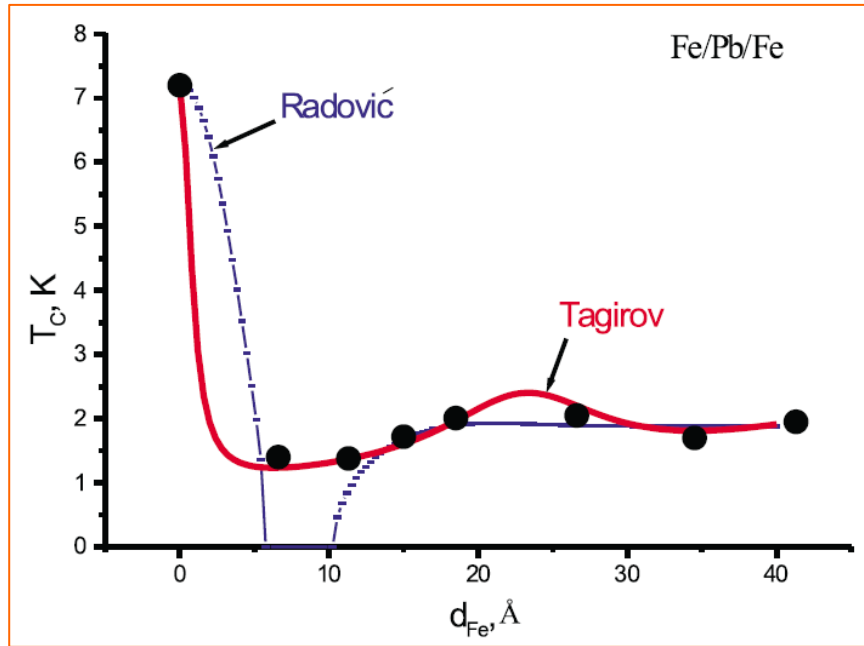


**Figure 2.12:** Dependence of the superconducting transition temperature on the thickness of the Fe layer as determined by resistivity measurements. The dashed and solid lines are the best fits using the theory by Radović *et al.* and the theory by Tagirov, respectively. [47]

Recently, the interface transparency has been included in the analysis of the interface quality and considered to play a dominant role in the boundary condition in layered structure. For the  $F/S$  bilayers, even though the transitions between 0 and  $\pi$  phases are impossible, the proximity effect at interface can still lead to a nonmonotonic dependence of  $T_c$  on the  $F$  layer thickness. Fominov *et al.* [49] performed a detailed analysis of the nonmonotonic critical temperature dependence of  $F/S$  bilayers for arbitrary interface transparency and compared the results of different approximations with exact numerical calculations. Such model was used to analyze experimental result by fitting the behavior of the superconducting critical temperature  $T_c$  depended on ferromagnetic thickness with finite interface transparency in Nb/ $\text{Co}_{60}\text{Fe}_{40}$ , Nb/Ni, and Nb/ $\text{Cu}_{40}\text{Ni}_{60}$  bilayers. [50] In Fig. 2.13, the parameter  $\gamma_b$

characterizes the interfacial transparency, which can be obtained by being treated it as a fittable value in terms of the interface resistance. This important parameter can help to understand which boundary condition is suitable at interface. The model of proximity effect which considered interface transparency have also successful explained the  $T_C$  behavior with weak ferromagnet, such as Nb/Pd<sub>81</sub>Ni<sub>19</sub> bilayers fabricated by sputtering system in Fig. 2.14. [51] Moreover, this fitting procedure even could describe the reentrant behavior for Nb/Cu<sub>1-x</sub>Ni<sub>x</sub> bilayers that fabricated in a wedge-shaped sample in order to obtain a series of varying Cu<sub>1-x</sub>Ni<sub>x</sub> thickness in Fig. 2.15 [52]. However, the interfacial transparency is still difficult in direct measurement but can be obtained through the fitting parameter.

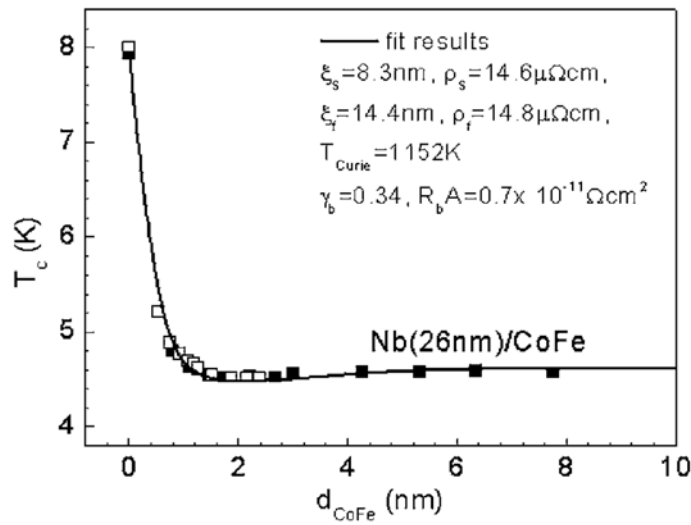


**Figure 2.13:**  $T_C$  of Nb (26 nm)/Co<sub>60</sub>Fe<sub>40</sub> bilayers as a function of  $d_{\text{CoFe}}$ . The different symbols mean two different sets of data. The solid line is a fit. [50]

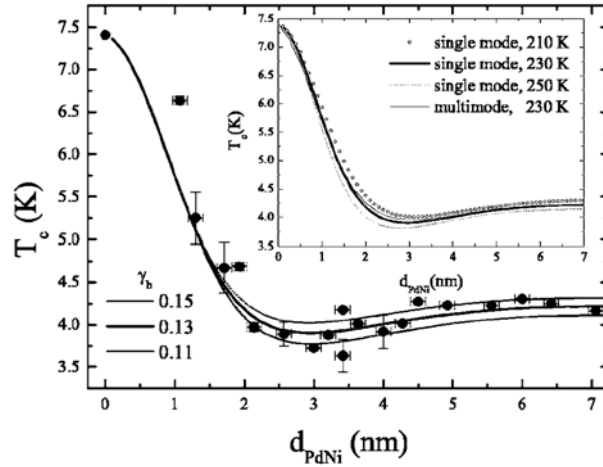


**Figure 2.14:** Critical temperature  $T_C$  versus PdNi thickness  $d_{\text{PdNi}}$  in Nb/Pd<sub>0.81</sub>Ni<sub>0.19</sub> bilayers with constant Nb thickness  $d_{\text{Nb}}=14$  nm. Different lines are the theoretical fit in the single-mode approximation for different values of  $\gamma_b$ . Inset: comparison between the single-mode and the multimode calculations. [51]

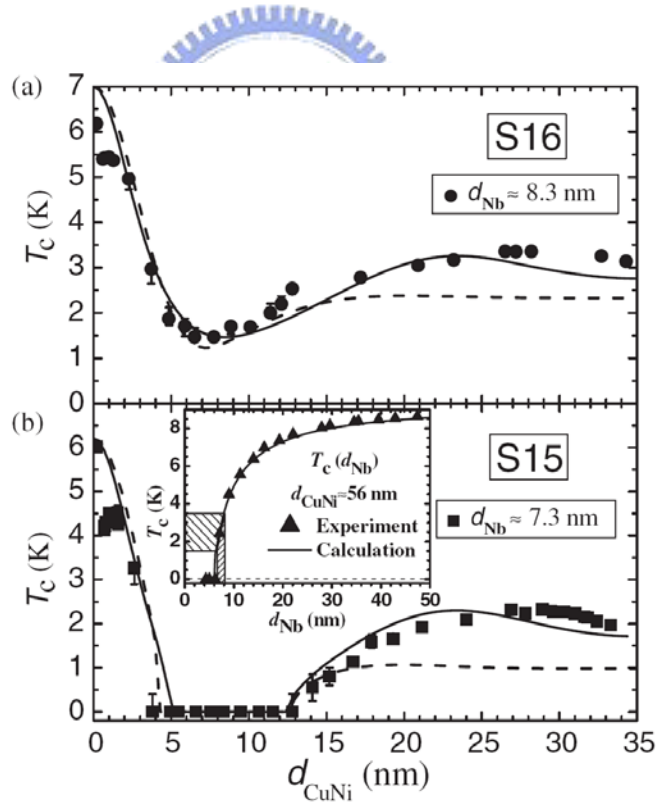


**Figure 2.15:** Nonmonotonous  $T_C(d_F)$  dependence for Nb/Cu<sub>41</sub>Ni<sub>59</sub> bilayers: (a)  $d_{\text{Nb}} = 8.3$  nm; (b)  $d_{\text{Nb}} = 7.3$  nm. The solid and dashed lines are theoretical curves for the clean and dirty cases, respectively. The inset shows  $T_C(d_{\text{Nb}})$  for a top layer Cu<sub>41</sub>Ni<sub>59</sub> of constant thickness with the solid line calculated for the clean case. [52]

## 2.5 Superconductor-Ferromagnet-Superconductor $\pi$ junction

In the previous literatures, the thickness dependence of the critical temperature  $T_C$  indicates a qualitatively different behavior between various layered structures but is based on proximity effect at interface. Using weak ferromagnetic layers is advantageous to achieving appropriate exchange energy in a suitable window of experimental phase space. It is considered as an unambiguous proof of  $\pi$  phase shift when the formation of current perpendicular to plan (CPP) Josephson junction with ferromagnetic barriers ( $S/F/S$ ) measurement by Ryazanov, *et al.* [53] For the same reason, in Josephson junctions with an  $S/F/S$  structure, where the insulating barrier of a conventional tunnel junction is replaced by a ferromagnetic layer, the condensate function may change sign when crossing the  $F$ -layer, this junction which leads to so-called  $\pi$ -type coupling of the two  $S$ -layers. The  $\text{Cu}_x\text{Ni}_{1-x}$  alloy used in Ryazanov's experiments has a Curie temperature 20–30 K and results in a small exchange field, which provides the strong nonmonotonic temperature dependence of  $I_C$ .

The  $\pi$  state in  $S/F/S$  Josephson junctions can be described by the anomalous current-phase relation  $I_s = I_c \sin(\varphi + \pi) = -I_c \sin \varphi$  with negative critical current. The Josephson critical current  $I_C$  in  $S/F/S$  junction would change sign from positive to negative corresponding to a phase shift of  $\pi$  in the Josephson ground state and, in turn there is a damped oscillatory dependence of the singular pair wavefunction in the  $F$  layer. Therefore, at certain ferromagnetic layer thicknesses the superconducting pairing function at two sides of the ferromagnetic layer has opposite phases, i.e. the phase difference is equal to  $\pi$ , as shown in Fig. 2.16. The physical origin of the oscillations is the exchange splitting of spin-up and spin-down electron subbands in  $F$ .

Recently, experiments by Ryazanov *et al.* (2006) have reported the first experimental observation of the two-node thickness dependence of the critical current in Josephson junction with  $F$  layer thickness up to 7 nm. [54] In Fig 2.17, nodes of the critical current correspond to the transition into the  $\pi$  state and back into the conventional 0 state. This means that now it is also possible to fabricate the  $\pi$  junctions with a  $10^4$  times higher critical current. A natural explanation for such strong thickness dependence is the magnetic scattering effect, which is inherent to ferromagnetic alloys. The phase sensitive experiments are also performed by using dc SQUID [55]. If the dc SQUID consists of a  $\pi$  junction and a 0 junction, a spontaneous phase shift of the diffraction pattern is observed. Recently, Bauer *et al.* have measured the magnetization of a mesoscopic superconducting loop containing a PdNi ferromagnetic  $\pi$  junction with the micro-Hall sensor technique [56]. The results provided a direct evidence of spontaneous current induced by the  $\pi$  junction.

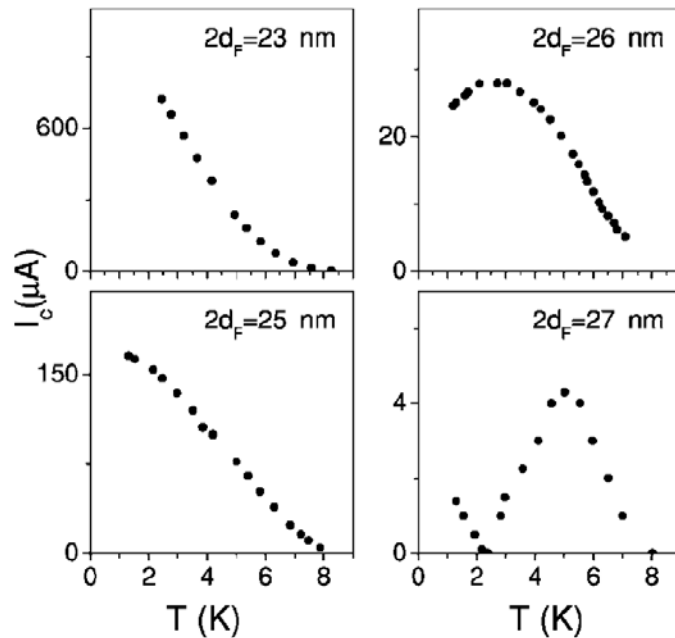


**Figure 2.16:** Critical current  $I_C$  as a function of temperature for  $\text{Cu}_{0.48}\text{Ni}_{0.52}$  junctions with different  $F$  layer thicknesses  $2d_F$ . The temperature mediated transition between the 0 and  $\pi$  phase occurs when the thickness of the  $F$  layer is 27 nm. [53]

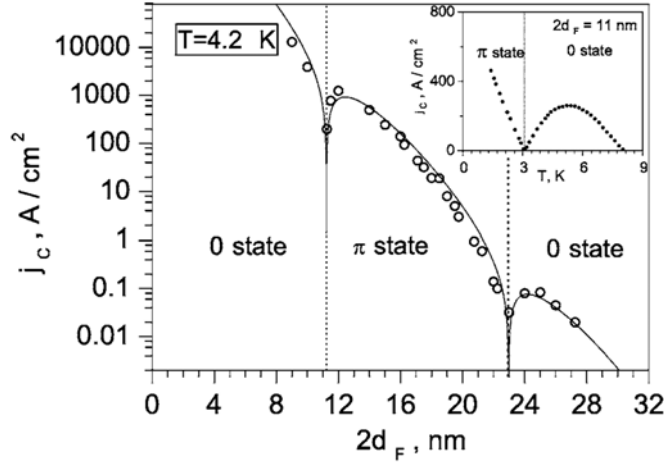


**Figure 2.17:** Critical current  $I_C$  at  $T=4.2$  K of  $\text{Cu}_{0.47}\text{Ni}_{0.53}$  junctions as a function of the  $F$  layer thickness. Two  $0-\pi$  transitions are revealed. The solid line is theoretical fit taking into account the presence of magnetic scattering. The inset shows the temperature mediated  $0-\pi$  transition for a  $F$  layer thickness of 11 nm. [54]

## 2.6 Density of states oscillations

Superconductivity creates a gap in the electronic density of states (DOS) near the Fermi energy  $E_F$ . The induced superconductivity in  $N/S$  structures decreases DOS at  $E_F$  near the interface. However in the  $F/S$  structure, the damped oscillatory dependence of the Cooper pair wave function in a ferromagnet suggests that similar behavior may be expected for the DOS variation due to the proximity effect.

Indeed, the DOS  $N(\varepsilon)$ , where  $\varepsilon=E-E_F$  is the energy calculated from the Fermi energy, is directly related to the normal Green's function in the ferromagnet  $G_f(x,\omega)$  [57]. In the dirty limit, the DOS of the Fermi energy in a ferromagnet can be obtained by

$$N_F(\varepsilon = 0) \approx N(0) \left[ 1 - \frac{1}{2} \exp\left(-\frac{2x}{\xi_F}\right) \cos\left(\frac{2x}{\xi_F}\right) \right] \quad (2.18)$$

at the distance  $x > \xi_F$ , where  $N(0)$  is the DOS of the ferromagnetic metal. Thus, at



certain distances the DOS at the Fermi energy may be higher than that in the absence of superconductor. This is in contradiction with the proximity effect in  $S/NM$  systems. The result of the proximity effect on the DOS is generally measured by tunneling spectroscopy experiments. The differential conductance of a tunnel junction as a function of voltage  $V$  is proportional to the DOS at energy  $eV$ . This is based on the fact that sweeping the voltage changes the difference in the chemical potentials between the normal metal and superconductor separated by an insulator. The conduction is a tunneling process from the occupied states of one material to the empty levels of the other which is dependent on the number of the available states. Kontos *et al.* [58] are the first to measure DOS with planar-tunneling spectroscopy in  $Al/Al_2O_3/PdNi/Nb$  junctions ( $F/S$  bilayers). In order to increase the penetration length of the Cooper pair inside the ferromagnet, the PdNi is used to reduce exchange energy. As shown in Fig. 2.18, the DOS decreases inside the gap characterizing a normal BCS-like behavior for a 50 Å thick PdNi layer. However, for a 75 Å thick PdNi layer, the DOS becomes larger than its normal state value. They observe spatial oscillations of electron density of state for ferromagnets of different thicknesses from tunneling spectroscopy. The transition from a normal to an inverted DOS is analogous to the transition from a 0-state to a  $\pi$ -state in a Josephson junction.

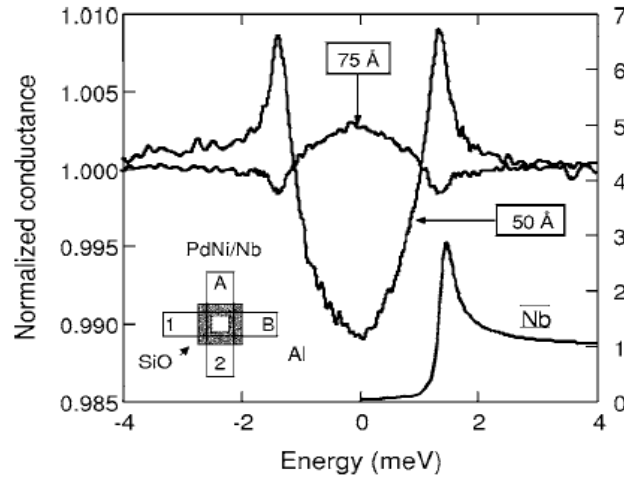


**Figure 2.18:** The differential conductance for two Al/Al<sub>2</sub>O<sub>3</sub>/PdNi/Nb junctions with two different thicknesses ferromagnetic PdNi. Tunnel junction areas were defined by the 50 nm thick SiO<sub>2</sub> evaporated through masks. [58]

## 2.7 Ferromagnet-Superconductor-Ferromagnet spin-valve sandwiches

Recently, researchers observed that the strong proximity effect of superconductor/metallic ferromagnet structures can lead to the phenomenon of spin-orientation dependent superconductivity in *F/S/F* spin valve sandwiches; see Fig. 2.19. The parallel orientation of the magnetic moments is more harmful for superconductivity due to the presence of the nonzero averaged exchange field acting on the surface of the superconductor. This effect has been experimentally observed [59, 60] in a Cu<sub>1-x</sub>Ni<sub>x</sub>/Nb/Cu<sub>1-x</sub>Ni<sub>x</sub> system, where a weak ferromagnet has been used because it is less devastating to superconductivity. The largest difference in  $T_C$  observed between the antiparallel (AP) and parallel (P) states of the *F*-layer mutual magnetizations is only 6 mK when  $T_C$  is 2.8 K. In 2006, Birge *et al.* have measured

the superconducting transition temperature  $T_C$  of Ni/Nb/Ni trilayers with the magnetizations of the two outer Ni layers are parallel (P) and antiparallel (AP). [61] The largest difference  $\Delta T_C$  occurs when the Nb thickness is just above the critical thickness at which superconductivity disappears completely. As shown in Fig. 2.20, they have observed a difference  $\Delta T_C$  between the P and AP states as large as 41 mK. A significant increase is over earlier results in samples with higher  $T_C$  and with a CuNi alloy in place of the Ni. Their result also demonstrates that strong elemental ferromagnets are promising candidates for future investigation of ferromagnet/superconductor heterostructures.

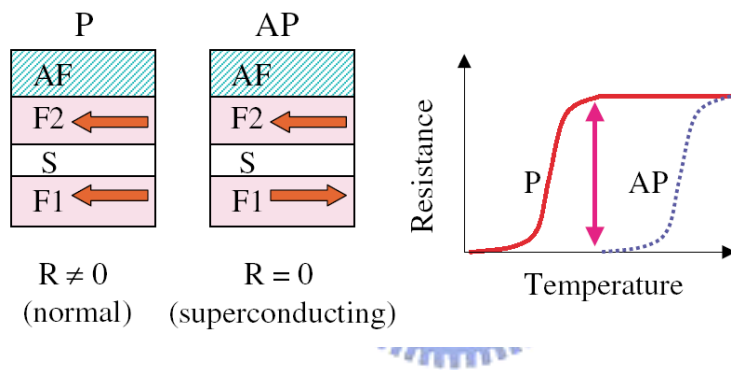


**Figure 2.19:** Schematic structure of a  $F/S/F/AF$  proximity switch device. [59]

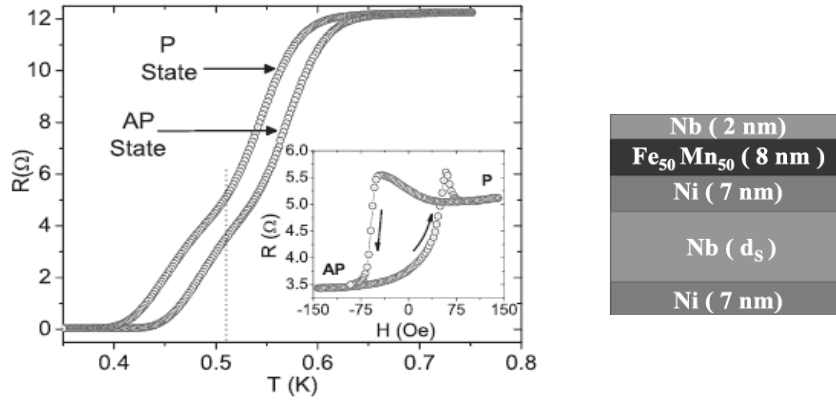


**Figure 2.20:** Resistance vs temperature for the P and AP states of a  $d_s = 17$  nm sample measured in 100 Oe. Two distinct transitions are observed, with  $\Delta T_C = 28$  mK. Inset: Resistance vs applied field at  $T = 0.51$  K (dotted line in main graph). [61]

However, the experimentally observed magnitude of change in  $T_C$  for  $F1/S/F2$  spin valve structures has been 2 orders of magnitude smaller than the expected value from calculations. Thus, the asymmetry of interface transparency caused by different boundaries between  $F1/S$  and  $S/F2$  is also considered to account for the discrepancy. [62] Moodera *et al.* have studied the spin valve effect in fully epitaxial bcc-Fe/V/Fe heterostructures. [63] In Fig. 2.21, the transition temperature is spin dependent in the presence of the proximity effect and infinite magnetoresistance with clear remanence state is obtained. They conclude that the intrinsic interface impedance is revealed as a result of the band symmetry mismatch. The absence of  $\Delta 2$  Bloch states at the Fermi level in the Fe spin majority channel results in symmetry mismatch and leads to spin selectivity and reduced transparency at the interface.

Thus, the  $T_C$  shift, which depends on the magnetization orientation of a superconducting spin-valve system, gives another example of the interesting effect. The interface transparency is an important factor again, controlling the spin-valve

effect in  $F/S/F$  structure. Experimental observation of the  $T_C$  behavior is difficult to realize the transport characteristic at interface with current in the plane, because the interface property and competition between the exchange energy and the superconducting condensation energy are extremely sensitive.

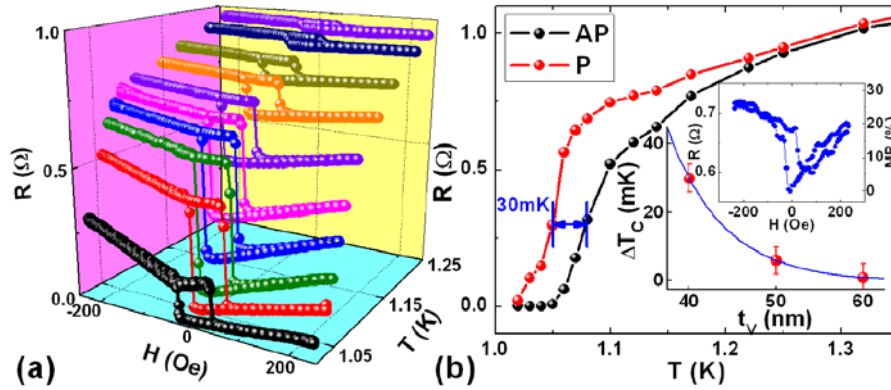


**Figure 2.21:** (a) Superconducting spin valve effect in the structure (in nm): MgO (10)/Fe(6)/V(40)/Fe(6)/CoO, and the sample is fully submerged in superfluid He4 which has infinitely thermal conductivity to avoid heating complications. (b) Superconducting transition of the same sample in its spin P and AP configurations. Inset: Thickness dependence of the  $S$  spin valve effect; solid line is only for visual guidance. Example of the MR loop with 50 nm V is also shown. [63]

## References:

1. P. Grunberg, R. Schreiber, Y. Pang, M.B. Brodsky, C.H. Sowers, Phys. Rev. Lett. **57** (1986) 2442.
2. M. N. Baibich, J. M. Broto, A. Fert, F. Nguyen van Dau, F. Petro, P. Etienne, G. Creuzet, A. Friederich, J. Chazeles, Phys. Rev. Lett. **61** (1988) 2472.
3. C. Kittel, *Introduction to Solid State Physics* (Wiley, New York, 1986), p.144.
4. N. W. Ashcroft, and N. D. Mermin, *Solid State Physics*, (Brooks/Cole, 1976).
5. H. E. Stanley, *Introduction to Phase Transition and Critical Phenomena*, (Oxford University Press, New York, 1971).
6. J. Linder, M. Zareyan, and A. Sudbø, Phys.Rev. B **79**, 064514 (2009).
7. C. L. Chien, and D. H. Reich, J. Magn. Magn, Mater. **200**, 83 (1999).
8. M. Tinkham, *Introduction to Superconductivity* (McGraw-Hill, New York, 1975).
9. J. Bass and W. P Pratt Jr, J. Phys.: Condens. Matter **19**, 183201 (2007).
10. T. Valet and A. Fert, Phys. Rev. B **48**, 7099 (1993).
11. P. M. Levy, *Solid State Physics Series vol 47, ed D Turnbull and HEhrenreich* (New York: Academic 1994) p 367.
12. W. P. Pratt, S. F. Lee, J. M. Slaughter, R. Loloee, P. A. Schroeder and J. Bass Phys. Rev. Lett. **66**, 3060 (1991).
13. J. Bass and W. P. Pratt, Jr., J. Magn. Magn, Mater. **200**, 274 (1999).
14. S. Takahashi and S. Maekawa, Journal of the Physical Society of Japan Vol. **77**, No. 3, 031009 (2008).
15. M. Faure, A. I. Buzdin, A. A. Golubov and M. Y. Kupriyanov Phys. Rev. B **73**, 064505 (2006).
16. F. S. Bergeret, A. F. Volkov and K. B. Efetov Rev. Mod. Phys. **77**, 1321 (2005).

17. Yu. A. Izyumov, Yu. N. Proshin, and M. G. Khusainov, *Phys. Usp.* **45**, 109 (2002).
18. A. I. Buzdin. *Rev. Mod. Phys.* **77**, 935 (2005).
19. V. L. Ginzburg, *Zh. Eksp. Teor. Fiz.* **31**, 202–214, (1956) [*Sov. Phys. JETP* **4**, 153–161 (1957)].
20. M. B. Maple and Ø. Fisher, *Superconductivity in Ternary Compounds II, Topics in Current Physics* (Springer-Verlag, Berlin 1982).
21. K.-H. Müller and V. N. Narozhnyi, *Rep. Prog. Phys.* **64**, 943–1008 (2001).
22. P. W. Anderson, ,and H. Suhl, *Phys. Rev.* **116**, 898–900 (1959).
23. L. N. Bulaevskii, A. I. Buzdin, M. L. Kulić, and S. V. Panjukov, *Adv. Phys.* **34**, 175–261 (1985).
24. S. S. Saxena, , P. Agarwal, K. Ahilan, F. M. Grosche, R. K. W. Haselwimmer, M. J. Steiner, E. Pugh, I. R. Walker, S. R. Julian, P. Monthoux, G. G. Lonzarich, A. Huxley, I. Sheikin, D. Braithwaite, and J. Flouquet, *Nature (London)* **406**, 587–592 (2000).
25. D. Aoki, A. Huxley, E. Ressouche, D. Braithwaite, J. Flouquet, J.-P. Brison, E. Lhotel, and C. Paulsen, *Nature (London)* **413**, 613–616 (2001).
26. P. Fulde and R. A. Ferrel, *Phys. Rev.* **135**, A550 (1964).
27. A. I. Larkin and Y. N. Ovchinnikov, *Sov. Phys. JETP.* **20**, 762 (1965).
28. E. A. Demler, G. B. Arnold, and M. R. Beasley, *Phys. Rev. B* **55**, 15174 (1997).
29. P. G. de Gennes, *Superconductivity of Metals and Alloys* (Benjamin, New York, 1966).
30. G. Deutscher, *Rev. Mod. Phys.* **77**, 109 (2005).
31. H. Zabel and S.D Bader, *Magnetic Heterostructures: Advances and Perspectives in Spinstructures and Spintransport* (Springer Tracts in Modern, Physics, 2007).
32. F. S. Bergeret, A. F. Volkov, and K. B. Efetov, *Phys. Rev. B* **69**, 174504 (2004).
33. R. I. Salikhov, I. A. Garifullin, N. N. Garif'yanov, L. R. Tagirov K. Theis-Brohl, K. Westerholt, and H. Zabel, *Phys. Rev. L* **102**, 087003 (2009).

34. Jing Xia, V. Shelukhin, M. Karpovski, A. Kapitulnik, and A. Palevski, Phys. Rev. L **102**, 087004 (2009).
35. L. R. Tagirov, Physica **307C**, 145 (1998).
36. J. J. Hauser, H.C. Theuerer, and N.R. Werthamer, Phys. Rev **142**, 118 (1964).
37. Z. Radovic, A. I. Buzdin, and J. R. Clem, Phys. Rev. B **44**, 759(1991).
38. H. K. Wong, B. Y. Jin, H. q. Yang, J. B. Ketterson, and J. E. Hilliard, Journal of Low Temp. Physics, Vol **63**, Nos.3/4, (1986).
39. P. Koorevaar, Y. Suzuki, R. Coehoorn, and J. Aarts, Phys. Rev. B **49**, 441(1994).
40. C. Strunk, C. Sürgers, U. Paschen, and H. v. Lohneysen, Phys. Rev. B **49**, (1994).
41. J. S. Jiang, D. Davidovic, D. H. Reich, and C. L. Chien, Phys. Rev. Lett. **74**, 314 (1995).
42. Th. Müuhge, N. N. Garifyanov, Yu. V. Goryunov, G. G. Khaliullin, L. R Tagirov, K. Westerholt, I. A. Garifullin, and H. Zabel, Phys. Rev. Lett. **77**, 1857 (1996).
43. Th. Mühge, K. Westerholt, H. Zabel, N. N. Garifyanov, Yu. V. Goryunov, I. A. Garifullin, and G. G. Khaliullin, Tagirov, K. Westerholt, and, Phys. Rev. B. 8945, **55** (1997).
44. Th. Müuhge, K. Theis-Nrohl, K. Westerholt, H. Zabel, N. N. Garifyanov, Phys. Rev. B **57**, 5071 (1998).
45. A. S. Sidorenko, V. I. Zdravkov, A. A. Prepelitsa, C. Helbig, Y. Luo, S. Gsell, M. Schreck, S. Klimm, S. Horn, L. R. Tagirov, and R. Tidecks, Ann. Phys. **12**, 37 (2003).
46. J. Aarts, J. M. E. Geers, E. Bru'ck, A. A. Golubov\*, and R. Coehoorn, Phys. Rev. B **56**, 2779 (1997).
47. L. Lazar, K. Westerholt, H. Zabel, L. R. Tagirov, Yu. V. Goryunov. N. N. Garifyanov, and I. A. Garifullin. Phys. Rev. B **61**, 3711 (2000).
48. Z. Radovic', M. Ledvij, L. Dobrosavljevic'-Grujic', A. I. Buzdin, and J. R. Clem,



- Phys. Rev. B **44**, 759 (1991).
49. Y. V. Fominov, N. M. Chtchelkatechev, and A. A. Golubov, Phys. Rev. B **66**, 014507 (2002).
  50. J. Kim, Jun Hyung Kwon, K. Char, and Hyeonjin Doh, Phys. Rev. B **72**, 014518 (2005).
  51. C. Cirillo, A. Rusanov, C. Bell, and J. Aarts, Phys. Rev. B **75**, 174510 (2007).
  52. V. Zdravkov, A. Sidorenko, G. Obermeier, S. Gsell, M. Schreck, C. Müller, S. Horn, R. Tidecks, and L. R. Tagirov, Phys. Rev. Lett. **97**, 057004 (2006).
  53. V. V. Ryazanov, V. A. Oboznov, A. Yu. Rusanov, A. V Veretennikov, A. A. Golubov, and J. Aarts, Phys. Rev. Lett. **86**, 2427 (2001).
  54. V. A. Oboznov, V. V. Bol'ginov, A. K. Feofanov, V. V. Ryazanov, and A. I. Buzdin, Phys. Rev. Lett. **96**, 197003 (2006).
  55. W. Guichard, M. Aprili, O. Bourgeois, T. Kontos, J. Lesueur, and P. Gandit, Phys. Rev. Lett. **90**, 167001 (2003)
  56. A. Bauer, J. Bentner, M. Aprili, and M. L. Della Rocca, Phys. Rev. Lett. **92**, 217001 (2004).
  57. A. Abrikosov, A., L. P. Gor'kov, and I. E. Dzyaloshinski, *Methods of Quantum Field Theory in Statistical Physics* (Dover, New York, 1975).
  58. T. Kontos, M. Aprili, J. Lesueur, and X. Grison, Phys. Rev. Lett. **86**, 304 (2001)
  59. J. Y. Gu, C.-Y. You, J. S. Jiang, J. Pearson, Ya. B. Bazaliy, and S. D. Bader, Phys. Rev. Lett. **89**, 267001 (2002).
  60. A. Potenza and C. H. Marrows, Phys. Rev. B **71**, 180503(R) (2005).
  61. Ion C. Moraru, W. P. Pratt, Jr., and Norman O. Birge, Phys. Rev. Lett **98**, 037004 (2006).
  62. P. Cadden-Zimansky, Ya. B. Bazaliy, L. M. Litvak, J. S. Jiang, J. Pearson, J. Y. Gu, Chun-Yeol You, M. R. Beasley, Phys. Rev. Lett. **77**, 184501 (2008)
  63. Guo-Xing Miao, Ana V. Ramos, and Jagadeesh S. Moodera<sup>1</sup>, Phys. Rev. Lett **101**, 137001 (2008)

# Chapter 3

## Experimental Techniques and Measurement System

### 3.1 The sputtering system

We fabricated several series of  $\text{Nb}_x\text{Ti}_{1-x}/\text{Co}$ ,  $\text{Nb}/\text{Co}$ ,  $\text{Nb}/\text{Fe}$ ,  $\text{Nb}/\text{Ni}$  and  $\text{Nb}/\text{Cu}_x\text{Ni}_{1-x}$  trilayer and multilayer samples by dc magnetron sputtering onto Si (100) substrates. The system was evacuated using a cryopump which provided a high pumping power equipped with no oil vapor contamination. The system was first roughly pumped to 0.02 torr with a mechanical pump which had an oil trap and then pumped to  $< 2 \times 10^{-7}$  torr with the cryopump. The sputtering gas came from a cylinder of ultrahigh purity Ar (99.999%) and was further purified by passing through a liquid  $\text{N}_2$  cold trap. It was held at approximately 100 K to freeze out impurities such as water vapor and others, as shown in Fig. 3.1. Then, deposition was made under the pressure of 1 m Torr with high purity Ar sputtering gas, and the temperature of the substrate was between  $20^\circ\text{C}$  and  $30^\circ\text{C}$  during fabrication of the CPP and CIP samples.

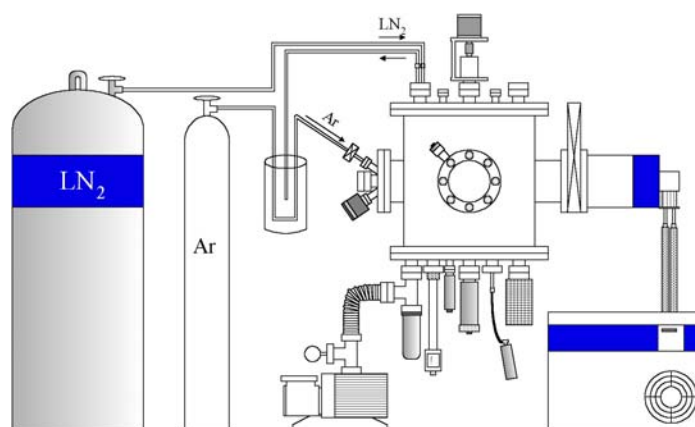


**Figure 3.1:** The schematic view of the sputtering system.

To obtain samples with comparable quality for different  $F$  and  $S$  layer thicknesses, up to twelve different CIP samples and eight different CPP samples were fabricated in the same run to minimize deviation in uncontrolled preparation conditions. The substrates were (100) oriented silicon crystal wafers, cleaned in acetone, and then were given a final ultrasonic rinse in alcohol. The CIP-type samples, in which current flows in the plane, were produced by mechanical masks as shown in Fig. 3.2. The metal mask divided the sample into two parts for transport and magnetization measurements.

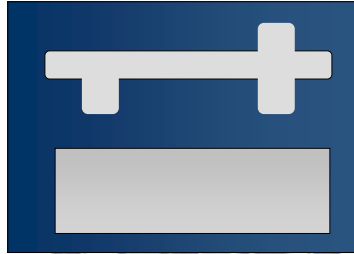


**Figure 3.2:** Metal mask of CIP-type sample to produce a 4-terminal device for transport measurements and a rectangular film for magnetization measurement.

For the CPP-type samples with current perpendicular to the plane, the substrates were held in circular stainless steel plate which was located about 7 cm above the sources. Up to eight samples can be mounted on holders which can be rotated above the sputtering sources, as seen in Fig 3.3 (a). The CPP samples were sputtered using multiple-sequence mechanical masks which required three contact metal masks in different shapes. Figure 3.3 (b) shows our multiple mask system, which is rotated to expose the Si substrate sequentially. The samples are covered with mask by the rotary plate of masks which is connected with a linear-rotary feedthrough. The mask plate accommodating three different shapes could be changed without opening the vacuum chamber so that the interfaces between the superconductor and ferromagnetic layer

would not be contaminated.

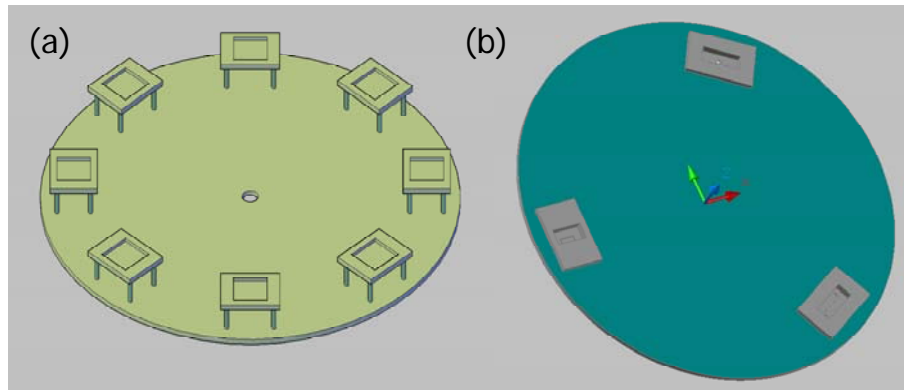


**Figure 3.3:** (a) Top view of CPP samples plate (b) Bottom view of CPP masks plate.

The CPP sample design was illustrated in Fig. 3.4. They were made by depositing a Nb strip on the substrate first, unloaded the bottom strip mask, changed to the multilayer mask, depositing the multilayer film, and finally a similar sequence for the top Nb strip perpendicular to the first one. Each strip was approximately 150 nm thick in order to become a superconductor at 4.2 K. They could be both used as a current and as a voltage lead. In this procedure, the exposure times of both the bottom Nb and the multilayer surface were less than 3 minutes. Our targets were bought from commercial companies (Silicon Development International Corporation A Technology Materials Company, SDIC). Depending on the materials, one needs to pre-sputter for several minutes in order to eliminate oxide layers formed in the targets during exposure to the atmosphere. For instance, Nb requires a minimum of 20-30 minutes for good quality superconducting properties and needs even more time for new target.

Furthermore, we had another special design in which the sputtered multilayer was sandwiched between circular superconducting electrodes. There were several advantages using this sample construction with circular superconducting leads. First,

it eliminated Joule heating in the current leads to make it have stably thermal condition at 4.2 K. Secondly, it kept the resistance of the SQUID circuit small so that we could achieve high precision measurement of resistance. Thirdly and the most importantly, the superconducting circular leads provided equipotential surfaces at the top and bottom of the CPP sample, thus allowing uniform current through the whole multilayer sample when the circular CPP sample is in the superconducting state.

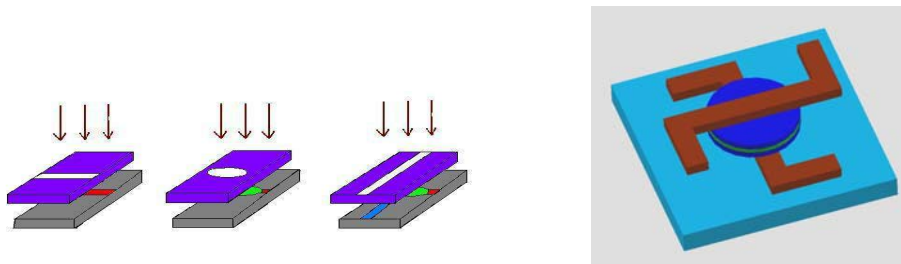


**Figure 3.4:** Geometry of a current perpendicular to plane sample on a substrate. The middle part of the circular shape is the multilayer.

## 3.2 Magnetic property measurement (SQUID)

The Superconducting Quantum Interference Device (SQUID) is one of the most important parts for a standard technique in detecting small magnetic flux nowadays. We use a commercial Quantum Design MPMS (Magnetic Property Measurement System) to measure magnetization of sample.

### 3.2.1 Josephson Effect: SQUID

The device was made of a superconducting loop with one or two Josephson junctions for RF SQUID and DC SQUID, respectively. The junction consisted of two superconductors separated by thin insulation layer as a weak link. As shown in Fig.

3.5, if this  $S/I/S$  junction was placed in an external magnetic field parallel to the plane, a screening current would be generated close to the surfaces. This current circulated within a surface of thickness  $\lambda$  and had to cross the weak link. [1] The critical current density across the junction would be smaller than typical critical currents for single specimens, because the paired electrons must cross a gap of nonsuperconducting material. Josephson made a remarkable prediction that superconducting tunnel current should be determined by the change in phase of the order parameter across the junction,  $\Delta\varphi$ . By using gauge invariance with the value of an applied vector potential to relate the phase of the order parameter, the tunneling current in the presence of a magnetic field should have the form, [2,3]

$$I_s = I_C \sin \Delta\varphi \quad (1).$$

Here the critical current  $I_C$  is the maximum supercurrent that the junction can support. If a voltage difference  $V$  is maintained across the junction, the phase difference  $\Delta\varphi$  would evolve according to

$$d(\Delta\varphi)/dt = 2eV/\hbar, \quad (2)$$

so that the current would be an alternating current of amplitude  $I_C$ . This is the basic effect for the dc and ac Josephson effects. It is clear now that the effects are much more general through various weak links such as  $S/I/S$ ,  $S/NM/S$ ,  $S/F/S$ , and  $S$ -c- $S$  junctions, where the  $S$ ,  $I$ ,  $NM$ ,  $F$  and  $c$  denote superconductor, insulator, normal metal, ferromagnet, and constriction, respectively. [2]

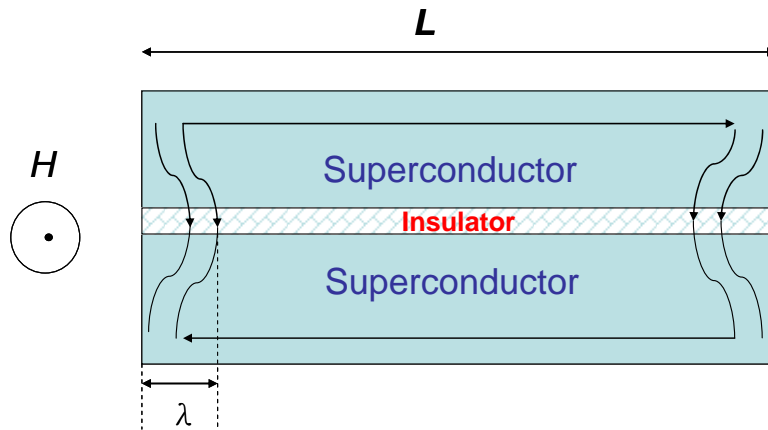


**Figure 3.5:** Tunnel Josephson junction in a magnetic field  $H$ . The distribution of the screening supercurrent is shown by lines with arrows.

A DC SQUID has two Josephson junctions  $a$  and  $b$  in parallel in a superconducting loop as shown in Fig. 3.6. This device can be utilized in sensitive magnetometers. A dc magnetic field applied through a superconducting circuit containing two junctions causes the maximum supercurrent to show interference effects as a function of magnetic field intensity. It is based on the dc Josephson Effect. When a small amount of external flux is applied to the superconducting loop, the screening currents would generate the magnetic field to cancel this applied external flux. Thus, when the current in any one of the branches exceeds the critical current for the Josephson junction, the superconducting ring becomes resistive and a voltage appears across the junction. [4, 5]

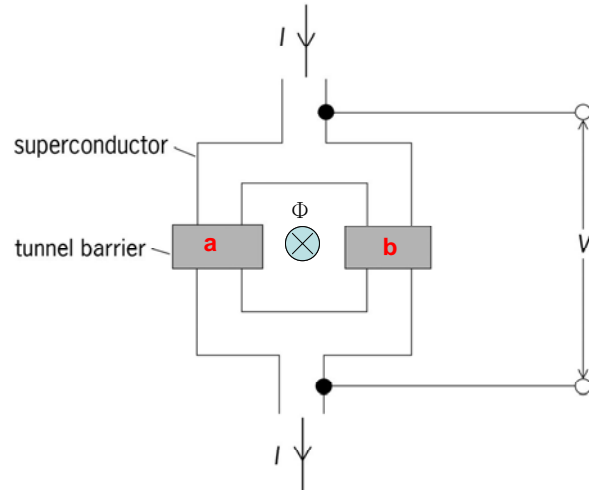


**Figure 3.6:** Superconducting interferometer with two Josephson junctions, a and b, are connected in parallel. The interior of the SQUID loop is threaded by a magnetic flux  $\Phi$ . [2]

We need to know that the maximum zero-voltage current  $I_{max}$  through the device, which depends on the total magnetic flux  $\Phi$  enclosed in the SQUID loop. The current through the junction a is

$$I_a = I_C \sin \varphi_a, \quad (3)$$

and through the junction b,

$$I_b = I_C \sin \varphi_b, \quad (4)$$

where  $\varphi_a - \varphi_b = 2\pi\Phi / \Phi_0$ , and  $\Phi_0 = \pi\hbar c / e$  is the magnetic flux quantum.

The total current is the sum of  $I_a$  and  $I_b$ :

$$I = I_C (\sin \varphi_a + \sin \varphi_b). \quad (5)$$

If the magnetic flux in the SQUID is an integer number of the flux quantum, the maximum current of the device is [1,6]

$$I_{max} = 2I_C |\cos(\pi\Phi / \Phi_0)|. \quad (6)$$

Thus the critical current oscillates with a function of the applied flux as illustrated in Fig. 3.7.



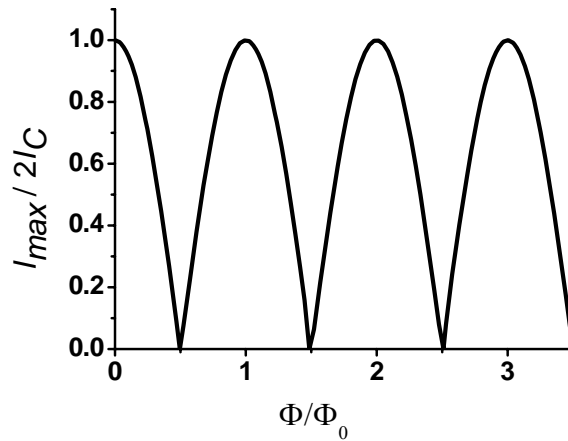


**Figure 3.7:** Dependence of the maximum supercurrent through the two-junction interferometer on the total magnetic flux through its interior.

If the input current is more than  $I_C$ , the SQUID would operate in the resistive mode and the SQUID voltage,  $V_S$ , as a function of the applied flux  $\Phi$ , is sinusoidal with the period of a flux quantum  $\Phi_0$  as shown in Fig. 3.8. The SQUID is a linear response to the applied flux through the flux-locked loop mode, where an addition modulated applied flux is used to maintain the voltage at an extreme in the  $V_S$  versus  $\Phi$  curve.

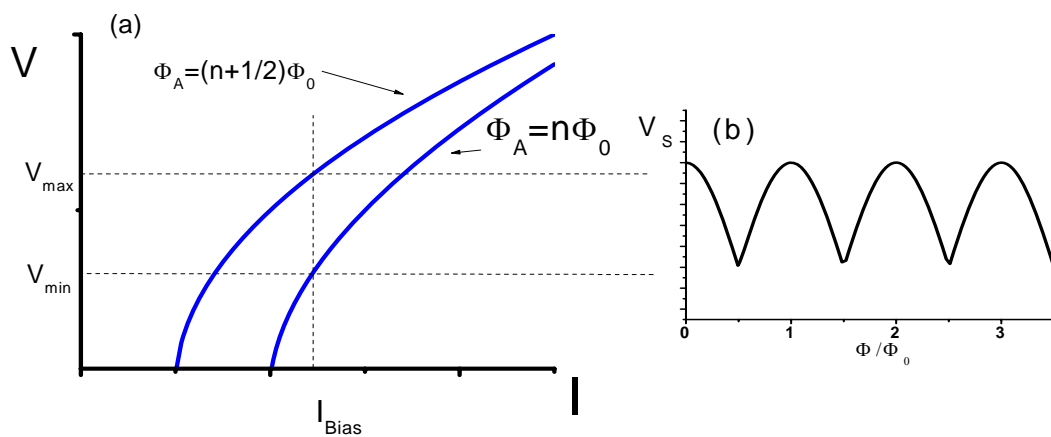


**Figure 3.8:** (a) V-I characteristic curve of dc SQUID with integer and half integer flux quantum,  $\Phi$ , of applied flux. (b) To bias the SQUID above the critical current with applying an external flux results in a sinusoidal behavior of the  $V_S$  versus  $\Phi$ .

### 3.2.2 Magnetic measurement

For all our magnetic measurements, we used a MPMS XL5 system with the magnetic moment resolution of  $10^{-7}$  emu. MPMS XL includes amplifier control electronics, sensing pick-up loops, and specially designed filtering with computer control. (see Fig. 3.9 [7]) The temperature control system regulates the sample in the range of 1.8-400 K and the maximum magnetic field using the superconducting magnet is  $\pm 5$  T.

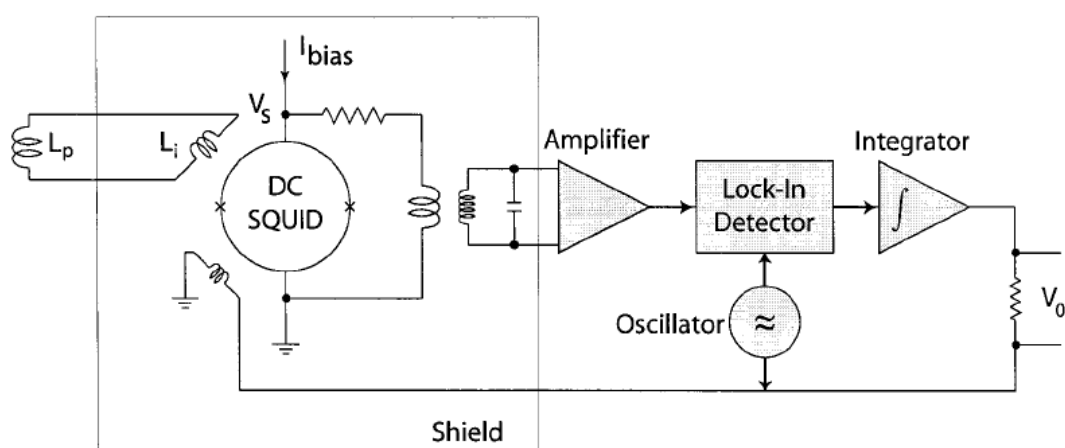


**Figure 3.9:** The superconducting pick-up coil couples the external flux to the input terminal of the SQUID. [7]

The sample is usually placed in a straw, tied by cotton thread, and the straw is attached to the sample rod. The measurement is performed by moving the sample vertically through superconducting detection coils. The detection coils consist of superconducting wire wrapped in a second-order gradiometer configuration, The orientation of coil 2 and 3 are opposite to that of coil 1 and 4 to reduce the spacing gradient ( $\partial H / \partial Z$ ) and the higher order gradient ( $\partial^2 H / \partial^2 Z$ ) of the magnetic field as shown in Fig. 3.10. [7, 8] The signal of coils induced by the magnetic moment of the

sample is inductively coupled to the SQUID by an input coil. So the current variations in the detection coils produce corresponding variations in the SQUID output voltage, which are proportional to the net magnetic moment of the sample as a linear flux-to-voltage convert. Before measurements, there is a function in the MPMS to ensure that the sample measurement path is symmetric with respect to the pick-up coil that couples to the SQUID and positioned at the center of the magnet. Fig. 3.10 illustrates the typical response as a function of the position of the sample with respect to the center of the gradiometer. We can then get the magnetic moment of sample by fitting the SQUID response curve. Moreover, the procedure of demagnetization for weak signal of a sample is necessary due to the large remnant field in the superconducting magnet.

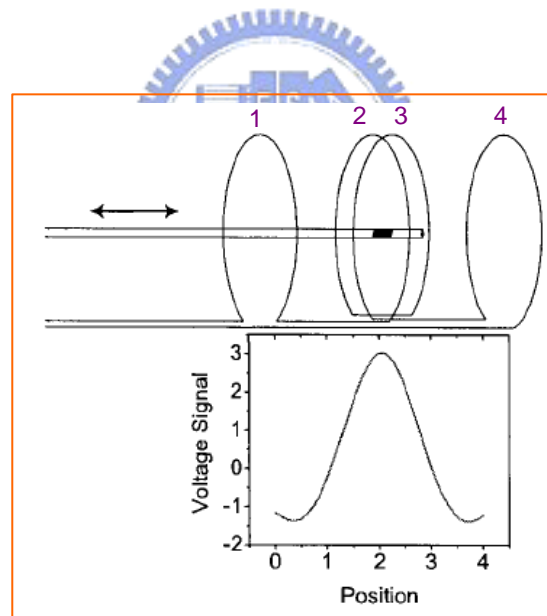


**Figure 3.10:** Voltage signal profile when a magnetic sample is moved through a detection pick-up coils. [7]

### 3.3 CPP with low resistance measurement

Presumably, the CPP (current flowing perpendicular to the plane) resistance measurement in metallic multilayer can give fundamental information of the transport properties. To study giant magnetoresistance (GMR) in magnetic multilayers, it is easier to analyze the CPP resistance by using two-channel series resistance model than the CIP one. [9,10] Moreover, the CIP measurement always gives zero resistance in the  $F/S$  multilayers unless we drive the samples to normal state by warming or applying magnetic fields. Consequently, we can quantitatively analyze the interface and bulk contributions by using CPP resistance measurement.

In general, for a sample with a constant resistivity, the resistance depends on the geometry of the sample  $l/A$ , where  $l$  is the length parallel to current and  $A$  is the cross-sectional area. A typical structure of our CIP sample is  $l=10\text{ mm}$  in the plane of the layer and  $1\text{ }\mu\text{m}$  thick in the direction of layer growth. If the current flows along the plane of the layers, we would obtain  $l/A=10^3\text{ mm}^{-1}$ , whereas for CPP one we would obtain  $l/A=10^{-3}\text{ mm}^{-1}$ . The resistance of CPP is one million times smaller than that of CIP for the same sample just simply because of its measurement geometry (see Fig. 3.11). Our CPP sample consists of a bottom  $S$  strip, the multilayer of interest, and a top  $S$  strip as shown in Fig 3.4. The effective CPP resistance is the area of the circular electrode with diameter about 3 mm to ensure the uniformity of current density. Thus, CPP samples have currents flowing perpendicular to the several nm-thick layers, with resistance as small as a few n $\Omega$ . A typical current of 100 mA yields  $10^{-9}\sim 10^{-10}$  volt, which requires special techniques for precision measurement.

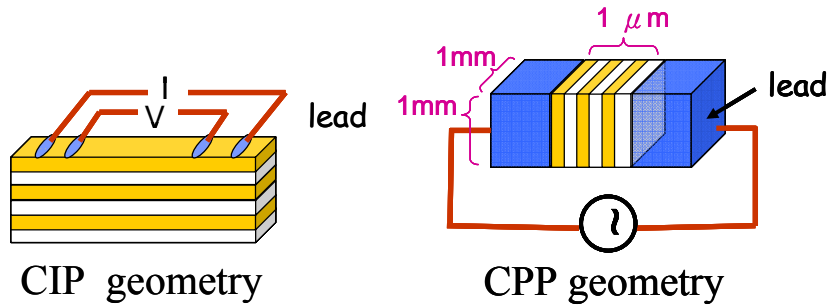


**Figure 3.11:** Cross section of a CIP and CPP structure with current traveling in the plane and perpendicular to the plane, respectively.

A very useful application for the SQUID's sensitivity to small changes in magnetic flux is its ability to detect extremely small resistance. A schematic drawing of the circuit is shown in Fig. 3.12 with the multilayered structure incorporated as part of a SQUID-based picovolt meter which balances a low temperature potentiometer by supplying a current into a reference resistor. [11,12] The DC currents which pass into the Nb strips are provided up to 100 mA from a battery-powered source and give voltage bias much less than the Nb superconductor energy-gap voltage. At our CPP measuring temperature of 4.2 K as shown in Fig. 3.13, the Nb strip and circular electrode remained superconducting, and thus ensured a uniform current distribution. The effective sample areas  $A$  for both normal and superconducting Nb are thus the same. The circular  $S$  electrodes ensure uniform measuring current throughout the whole multilayer sample. According to Ref. [13], since our circular Nb electrode defines the effective sample area, the ratio of sample's thickness divided by the width, about  $3 \times 10^{-4}$  ( $1 \text{ } \mu\text{m}/3.4 \text{ mm}$ ), can make fringing currents negligible. The resulting resistance  $R_T$  due to the 3.4 mm diameter circular area and the thickness, ranging from 20 nm to about 1 mm is less than 10 nV. This small resistance was measured by a

superconducting quantum interference device (SQUID) based picovolt meter and a battery-powered dc current source. The small CPP resistance  $R \approx 10^{-8} \Omega$  of our samples was measured by a SQUID based picovolt meter. [14] The low noise DC current is provided to the unknown sample resistance. Furthermore, the signal can be detected by the SQUID through the inductor connected in parallel and the SQUID electronic supplies a current to the reference resistor ( $30 \mu\Omega$ ). When the circuit is balanced, the voltage across the sample would be equal to the one across the reference resistance. Thus, the ratio of the resistance is the inverse of the current ratio at balance. Therefore, the CPP resistance of the metallic multilayers can be measured by using a bridge circuit with SQUID device detector to balance the voltage  $V$  between the samples against a current  $I$  that pass through a reference resistance used to amplify the signal to  $10^8$ . The total thickness of the CPP samples and the diameter  $W$  of circular electrode were checked with a stylus surface profiler. The deviation of thicknesses was found to be within 5% of the intended values. The small gap between the contact masks and the substrates resulted in rounded edge of the films. This edge effect contributes to the largest systematic error in this experiment. The uncertainty in the unit area total resistance  $AR_T$  of our multilayer samples was dominated by the uncertainty in  $A = \pi(W/2)^2$ , which is about 10% for the  $S$  samples and 15% for the  $NM$  samples.

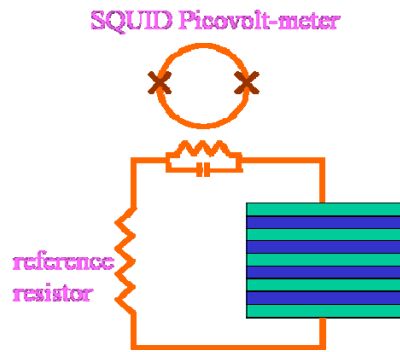


**Figure 3.12:** Simplified circuit for the precision measurement with SQUID based picovolt meter.

We use two steps to get minimum contact resistance in which the superconducting solder joints to the Nb strips at leads of  $I$  and  $V$ . First a thin layer of In is put on by ultrasonic soldering to break through the oxide on the Nb surface. Then the superconducting wire is soldered on with Ostalloy 158 which has a low melting point about 343 K and a superconducting transition temperature around 9 K with alloy of bismuth, tin, lead, and cadmium. The bond between Ostalloy 158 and Nb by In is strong and useful for soldering items which can not be subjected to high temperature. Because, in the four-terminal measurement, there is no current flowing in the voltage circuit at balance, so the thin layer of In resistance does not produce any voltage drop. The sample is placed inside a small superconducting magnetic coil that produces a field (up to 800 Oe) in the layer plane, perpendicular to the current direction. The magnet was hand-wound by NbTi superconducting wires with Cu cladding and potted with epoxy to prevent any wire movement. To reduce field fluctuation due to the high frequency noise produced by the Kepco's bipolar BOP dc power supplies, we added a small piece of thick Cu wire as a resistor between the magnet leads to increase the circuit time constant. [15] A pure lead sheet of  $T_C=7$  K

are wrapped outside the magnet's supporting rods as superconducting magnetic shields to protect the SQUID from magnetic fields. At our measuring temperature of 4.2 K, the 150 nm-thick Nb strip and circular electrode remain superconducting, thus ensuring a uniform current distribution.

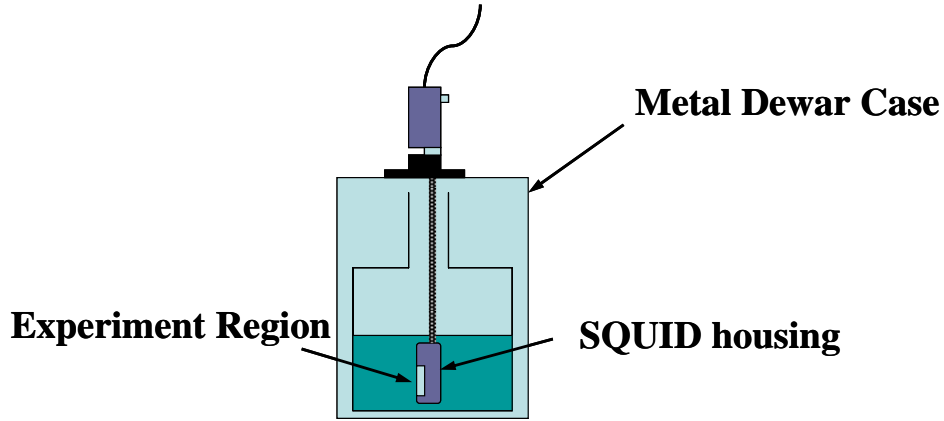


**Figure 3.13:** CPP sample measured by by a superconducting quantum interference device (SQUID) based picovolt meter at 4.2 K.

In a homogeneous sample with a uniform current distribution, the resistivity is the quantity to be used for comparison between different bulk materials. For CPP samples, since the interfaces are two dimensional, the equivalent quantity is the product of resistance and effective area. As shown in Fig. 3.14, if we write the conductance per unit area as  $1/R_\alpha$  and consider the conduction in parallel with perpendicular transport, then the total conductance  $1/R_b$  of a boundary can be described as

$$\frac{1}{R_b} = \sum_i \delta A_i \left( \frac{1}{R_\alpha} \right) = \frac{A}{R_\alpha} \quad (7)$$

by summing over the total sample area  $A$ . Thus, the interface resistance per unit area in equation (7) is  $R_\alpha = AR_b$ , representing the sample area times the boundary resistance.  $AR_b$  is the useful quantity for comparing between different materials with CPP transport.



In the present experiment, the influence of the conventional superconducting proximity effect on our perpendicular measurement was insignificant. Clearly, this effect arose from the presence of the Nb electrodes. If the sample was a nonmagnetic normal metal, the system might become superconducting below some temperatures due to the Cooper pairs could penetrate through *NM*. For example, a 2.8  $\mu\text{m}$  film of Ag beside Nb layer became superconducting at  $\sim 1.6$  K [16]. However, the *F/S* multilayer could kill the proximity effect because of the pair-breaking effect of the ferromagnetic such as Co, Fe and Ni. Therefore, the bottom and the top of the multilayer was always *F* film in our CPP samples. Each sample had *N* *F/S* repeated bilayers plus one layer of *F*, indicated as  $[F(d_F)/S(d_S)]_N/F(d_F)$ , where thickness was in nm,  $d_{F,(S)}$  was the thickness of the *F* and *S* layers.

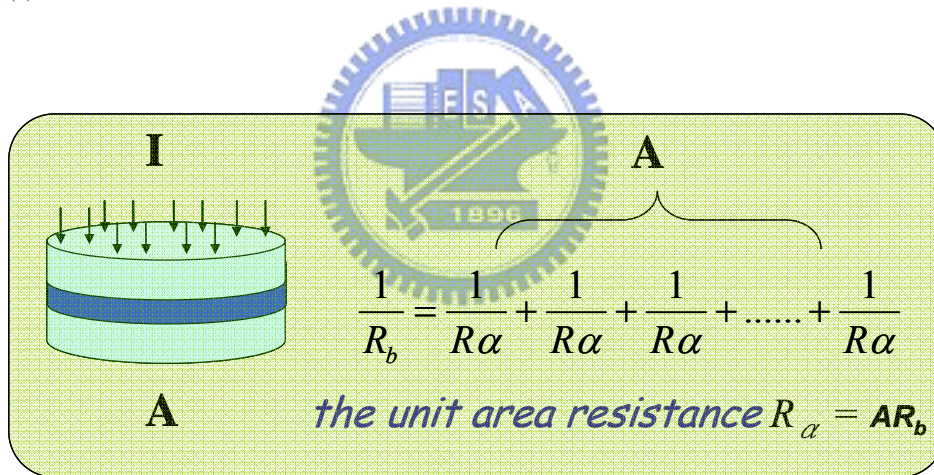


**Figure 3.14:** Interface resistance representing the sample area  $A$  times the boundary resistance  $R_b$  in the CPP sample.

### 3.4 Electric property measurement with CIP structure

All of the CIP resistivity measurements in our study were performed in the Quantum Design physical property measurement system (PPMS). The PPMS can provide an experimental environment in the temperature range of 1.9 to 400 K and magnetic field of 9T by low noise bi-polar power supply. In the DC Resistivity option, the current range is from 5 nA to 5 mA and voltage sensitivity is 20 nV. Moreover, the option of AC Transport measurement system (ACT) contains a precision current source and voltage detector providing four different types of automated, electrical transport measurements: AC resistivity, five-wire Hall effect,  $I$ - $V$  curve, and critical current.

The critical temperature  $T_C$  and the critical field  $H_{c2}$  are resistively measured by a standard four-probe technique with the current larger than 1 mA. The geometry for the measured sample is 5 mm long and 1 mm wide between the voltage contact pads, as shown in Fig. 3.15. The current density is about  $2 \times 10^2$  A/cm<sup>2</sup> for layer thickness of 500 nm. We defined the  $T_C$  as the temperature at which the resistance of the samples reached 90% of the normal state resistance at 10 K. In the  $H_{c2}$  measurement, we take advantage of Horizontal Rotator to obtain information about angular dependence of upper critical field with high angular resolution 0.0045°.

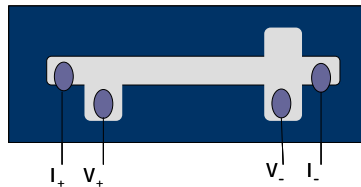


**Figure 3.15:** A 4-terminal device for transport measurement in the CIP sample.

## References:

1. P. Müller and A. V. Ustinov, *The physics of Superconductors*, (Springer, New York, 1997).
2. M. Tinkham, *Introduction to Superconductivity* (McGraw-Hill, New York, 1975).
3. N. W. Ashcroft, and N. D. Mermin, *Solid State Physics*, (Brooks/Cole, 1976).
4. E. du Trémolet de Lacheisserie, D. Gignoux, and M. Schlenker, *Magnetism: Materials and Applications*, Vol. 2, (Springer, 2005).
5. J. Clarke and A. I. Braginski, *The SQUID handbook*, Vol. 1, 2nd Ed., (Wiley-Vch 2004).
6. C. Kittel, *Introduction to Solid State Physics* (Wiley, New York, 1986), p.144.
7. I. C. Moraru, *Proximity Effect in Ferromagnet/Superconductor Hybrid Systems*, (Ph. D thesis, Michigan State University, 2006 ).
8. Ulrich Weiss, *Encyclopedia of Physical Science and Technology* **16**, 211 (1998).
9. J. Bass and W. P. Pratt, Jr., *J. Magn. Magn. Mater.* **200**, 274 (1999).
10. T. Valet and A. Fert, *Phys. Rev. B* **48**, 7099 (1993).
11. J. M. Slaughter, W. P. Pratt, Jr., and P. A. Schroeder, *Rev. of Sci. Instr.* **60**, 127 (1989).
12. D. Edmunds, W. Pratt, and J. Rowlands, *Rev. of Sci. Instr.* **51**, 1516 (1980).
13. S. F. Lee, Q. Yang, P. Holody, R. Loloee, J. H. Hetherington, S. Mahmood, B. Ikegami, K. Vigen, L. L. Henry, P. A. Schroeder, W. P. Pratt, Jr., and J. Bass. *Phys. Rev. B* **21**, 15426 (1995).
14. J. M. Slaughter, W. P. Pratt, Jr., and P. A. Schroeder, *Rev. Sci. Instrum.* **60**, 127 (1989).
15. S. F. Lee, *Perpendicular Resistance and Magnetoresistance of Co/Ag Multilayers*, (Ph. D thesis, Michigan State University, 1994 ).

16. J. M. Slaughter, J. Bass, W. P. Pratt, Jr., P. A. Schroeder, and H. Sato. *Jpn. J. Appl. Phys.* **26**, Suppl. 26-3, 1451 (1987).



# Chapter 4

## Theoretic Description for Data Analysis

### 4.1 Radovic's Theory: single-mode approximation

Because of the possibility for engineering heterogeneous superconductor-ferromagnet metallic systems, studies of their antagonistic orderings and mutual influence with alternately stacked  $S$  and  $F$  layers are of considerable interest. These  $F/S$  heterostructures may exhibit phenomena such as coexistence of superconductivity and magnetism, reentrant behavior, and oscillation of the critical current with temperature in the absence of an external magnetic field. In the theoretic work, Radović *et al.* only study the influence of the ferromagnet on the superconductivity in  $F/S$  superlattice, with the magnetic ordering being unperturbed by the proximity of  $S$  layers. [1, 2] The exchange field in the ferromagnet tends to polarize the conduction electron spins, thus breaking the Cooper pairs, which penetrate from the superconducting order parameter in the vicinity of an  $F/S$  interface. [3] As a consequence, the superlattice transition temperature  $T_C$  becomes much lower than the superconductor's bulk transition temperature  $T_{CS}$  and the phase transition can become of first order. They also found that below a certain critical thickness of  $S$  layers there is no superconductivity at all, even for short-period superlattice with thin  $F$  layers. In addition to these destructive consequences of the  $F/S$  proximity effect, a nonmonotonic oscillatory variation of  $T_C$  with  $F$  layer thickness, related to “ $\pi$ -contact” superconducting interferometer, was observed. [4] On the characteristic ground-state configurations, the phase difference between two neighboring  $S$  layers can be not only  $\varphi=0$ , as is always the case in superconductor-normal-metal superlattice, but also  $\varphi=\pi$ ,

as in the case [5] of  $S/F/S$  Josephson junction. Or it can take intermediate values,  $0 < \varphi < \pi$ , depending on the superlattice characteristics.

To study the normal to superconducting state transition, Radović *et al* model the behavior of an  $F/S$  superlattice by assuming a position- and temperature-independent exchange field in the  $F$  layers. Assuming both metals are dirty [5], they use Usadel's [7] dirty-limit version of the quasiclassical theory of superconductivity to derive the boundary conditions that connect the quasiclassical propagation near magnetically active interfaces. [8, 9]

Using Usadel's equation, the quasiclassical theory can be reduced to the linear equation between the order parameter  $\Delta(x)$  and the pair amplitude  $F(x, \omega)$  as follows:

$$-\frac{\hbar D_S}{2} \frac{d^2 F_S(x, \omega)}{dx^2} = \Delta_S(x) - \hbar|\omega| F_S(x, \omega) \quad (4.1)$$

$$-\frac{\hbar D_F}{2} \frac{d^2 F_F(x, \omega)}{dx^2} = -(\hbar|\omega| + iI) \text{sgn } \omega F_F(x, \omega) = 0 \quad (4.2)$$

Where  $D_{S, (F)}$  are the diffusion coefficients in the superconductor and ferromagnet,  $I$  is the exchange energy, and  $\omega$  is the Matsubara frequency given by  $\hbar\omega = \pi kT(2n+1)$  with integer  $n$ . For one  $S$  layer embedded between two  $F$  layers, the condensate of pairs can be given by  $F(x, \omega)$ . The Gorkov's Green function integrates over energy and averages over the Fermi surface with the Matsubara frequency  $\omega$ . Near the second-order phase transition at  $H_{c2}(T)$  we have for the  $S$  layer and  $F$  layer, respectively, [1]

$$\begin{aligned} \Pi^2 F_S &= -K_S^2 F_S, \\ \Pi^2 F_F &= +K_F^2 F_F, \end{aligned} \quad (4.3)$$

where  $\Pi = \nabla + 2\pi i \mathbf{A}/\Phi_0$  is the gauge-invariant gradient with vector potential  $\mathbf{A}$  and flux quantum  $\Phi_0$ . The propagation momentum  $K_S$  corresponds to the effective pair breaking parameter  $\rho(t)$  by

$$\rho(t) = \xi_s^2 K_S^2(t) / 2 \quad (4.4)$$

with the reduced temperature  $t=T_C/T_{CS}$  and the bulk critical temperature  $T_{CS}$ . The  $S$  coherence length is given by  $\xi_S = (\hbar D_S/2\pi k_B T_C)^{1/2}$  with the diffusion coefficient  $D_S$  and the Boltzmann constant  $k_B$ . On the other hand, it relates to the Ginzburg–Landau coherence length via  $\xi_{GL}(T) = \xi_S(1-T/T_{CS})^{-1/2}$ . The characteristic inverse length is given by

$$K_F = \sqrt{\frac{2(\pi K_B T + iE_{ex})}{\hbar D_{FM}}} \quad (4.5)$$

where  $E_{ex}$  is the exchange energy and  $D_{FM} = v_F \ell_{FM}/3$  is the diffusion constant in the  $F$  layer with the Fermi velocity  $v_F$  and the mean-free-path  $\ell_{FM}$ . In the case of strong ferromagnets  $E_{ex} \gg K_B T_{CS}$ ,  $K_F$  can be taken as temperature independent and Eq. 4.5 becomes

$$K_F = \sqrt{\frac{2iE_{ex}}{\hbar D_{FM}}} = \frac{2(1+i)}{\xi_F} \quad (4.6)$$

The penetration length of the superconducting pair function in the  $F$  layer is introduced as:

$$\xi_F = \sqrt{\frac{4\hbar D_{FM}}{E_{ex}}} \quad (4.7)$$

Within the single-mode approximation of Eq. (4.1) for  $F_S$  and Eq. (4.2) for  $F_F$ , the reduced temperature is connected to the pair-breaking parameter by

$$\ln t = \Psi\left(\frac{1}{2}\right) - \text{Re} \Psi\left(\frac{1}{2} + \frac{\rho}{t}\right), \quad (4.8)$$

where  $\text{Re}\Psi$  represents the real part of the digamma function.  $\rho$  can be obtained by the boundary conditions, [10]

$$\left. \frac{dF_{SC}}{dx} \right|_{bd} = \eta \left. \frac{dF_{FM}}{dx} \right|_{bd}, \quad (4.9)$$

$$F_{SC} = F_{FM} \quad (4.10)$$

with the  $\eta$  as a phenomenological parameter characterizing the  $F/S$  interface. In the

dirty limit,  $\eta = \sigma_{FM}/\sigma_{SC}$  is the ratio of the normal state conductivities of the  $F$  and  $S$  layers to influence the propagation momentum at the interface. Equation (4.10) implies a high quantum mechanical transparency of the  $F/S$  interface, that the probability of transport at interface is equal, as represented by  $|F_S|^2 = |F_F|^2$ . Moreover, the absence of the pairing function current through the outer surface of the trilayer implies that at  $x = \pm (d_S/2 + d_F)$  for the  $F/S/F$  trilayer system

$$\frac{dF_F}{dx} = 0. \quad (4.11)$$

Using the boundary conditions (4.9), (4.10), and (4.11) in Equations (4.4) and (4.8) the equation for computing  $K_S d_S$  can be derived:

$$K_{sc} d_{sc} \tan\left(\frac{K_{sc} d_{sc}}{2}\right) = \frac{2(1+i) d_{sc}}{\varepsilon \varepsilon_{sc}} \tanh\left[2(1+i) \frac{d_{FM}}{\varepsilon_{FM}}\right] \quad (4.12)$$

with  $\varepsilon = \xi_{FM}/\eta \xi_{SC}$ . The numerical results show the  $T_C$  behavior of  $F/S$  is very sensitive to the ferromagnet influence. For typical values of parameters  $D_S$ ,  $D_F$ ,  $T_{CS}$  and  $\eta$ , Fig. 4.1 illustrates the result by the example  $\varepsilon = 1$  for the strong magnet influence.

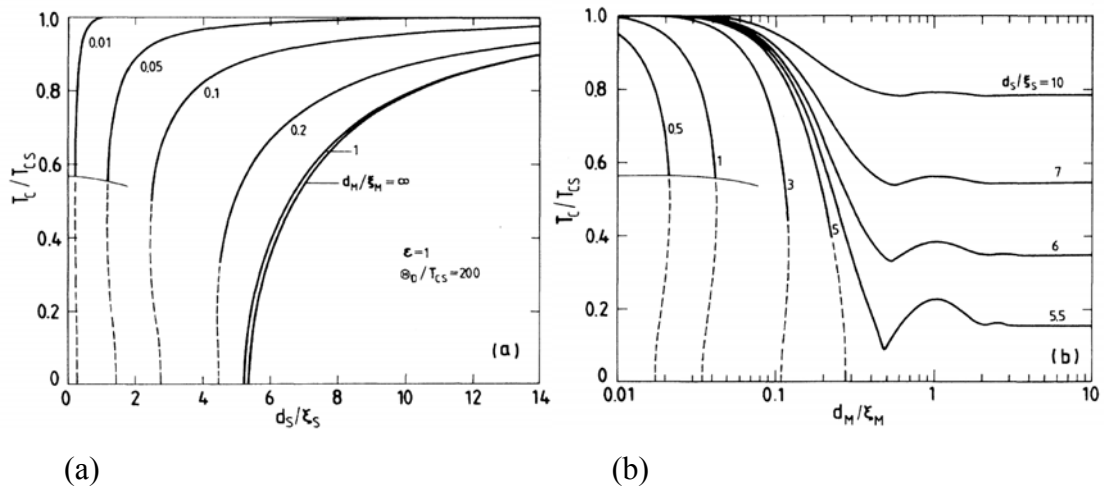


**Figure 4.1:** The reduced transition temperature as a function of the reduced (a) S film thickness and (b)  $F$  film thickness for  $\varepsilon=10$ . The tricritical points  $T^*/T_{CS}$  are shown as thin curves. Dashed curves show solutions that are physically unstable. [2]



For relatively thin  $S$  and  $F$  layers,  $T_C$  decreases rapidly with decreasing  $d_S/\xi_S$  as shown in Fig. 4.1 (a), or increasing  $d_F/\xi_F$  as in Fig. 4.1 (b). For a given  $d_F/\xi_F$ , the superconductivity persists only for  $d_S$  larger than a certain critical thickness  $d_{crit}$ . Moreover, below the tricritical temperature  $T^*$ , the  $T_C$  curves become doubly valued, but the solutions are physically unstable as shown the dashed curves in Fig. 4.1.

For thicker  $S$  layers and  $d_F/\xi_F \sim 1$ , significant oscillations arise on the  $T_C$  versus  $d_F/\xi_F$  curves. In the region of strong oscillations new ground states appear with finite phase difference  $\varphi \neq 0$  between neighboring  $S$  layers, which is never the case for  $S/NM$  superlattices. On the whole transition curve, the states with 0 phase and with  $\pi$  phase are dominant. As shown in Fig. 4.2, the interchange of their stability domain is due to the interplay of two oscillating  $T_C$  curves. Although the transition between the 0 and  $\pi$  phase is continuous, the intervals of  $d_F/\xi_F$  corresponding to  $0 < \varphi < \pi$  are very narrow.

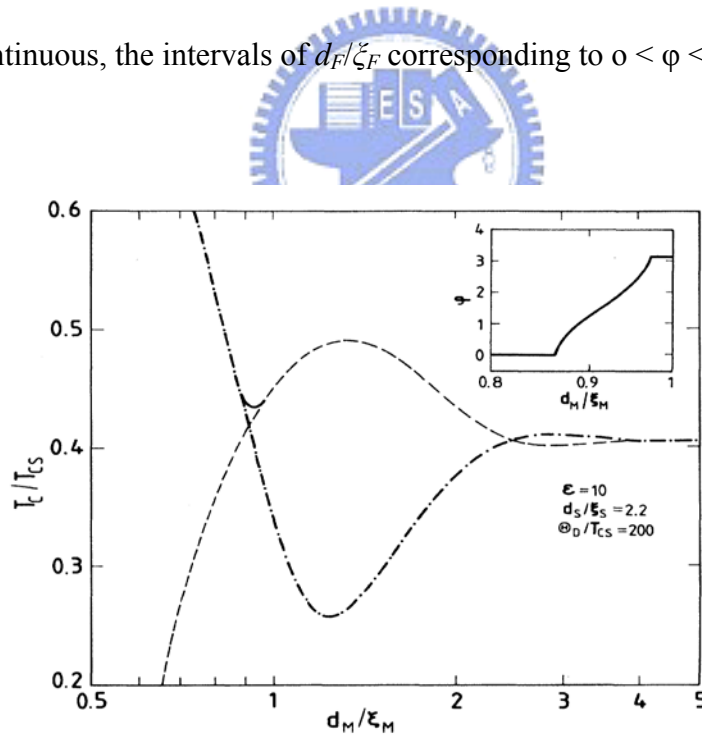


**Figure 4.2:** The calculation for the phase difference  $\varphi=0$ , dot-dashed line, and  $\varphi=\pi$ , dashed line. The ground state oscillations where  $0 < \varphi < \pi$ , solid line. Inset: ground state  $\varphi$  vs  $d_F/\xi_F$ . [2]

Figure 4.3 [11] shows the spatial variation of the real part of the pairing wavefunction near the interface. At the  $S$  side the  $\text{Re}F_S$  decreases slightly as the interface is approached; however, when crossing the interface the derivative of function decreases by a factor  $\eta$ , giving a steep decrease of  $F_F$  at the  $F$  side of the interface. At larger distances from the interface,  $F_F$  exhibits the oscillatory behavior with a change of sign at  $d_F \sim 0.5\zeta_F$ . This is achieved by the assumption that the pairing function is continuous at the interface, i.e. assuming a perfectly transparency interface.

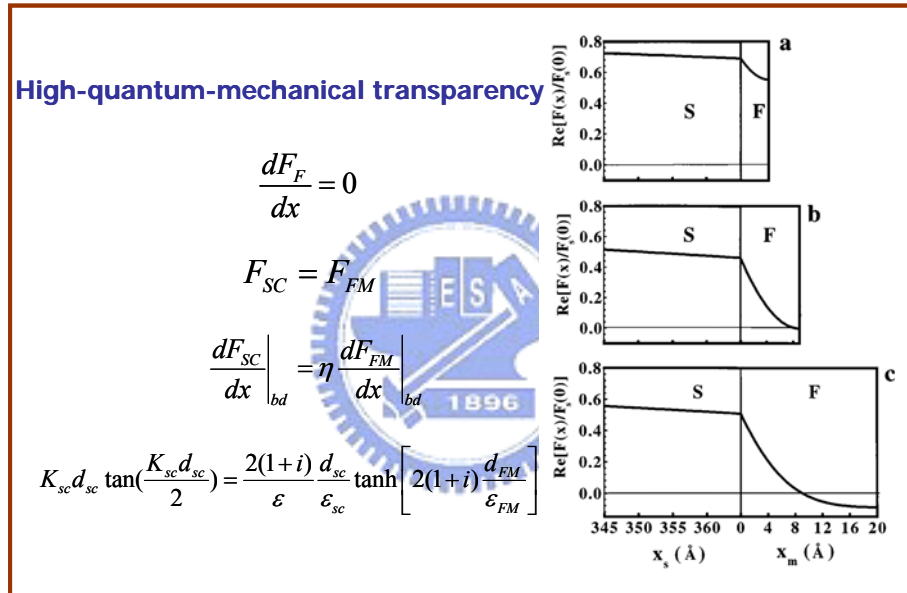


**Figure 4.3:** Spatial variation of the real part of the pairing function near the interface in the models by Radovic' *et al* with  $d_{pb}=730 \text{ \AA}$  and  $d_{Fe}=4 \text{ \AA}$  (a),  $9 \text{ \AA}$  (b), and  $20 \text{ \AA}$  (c) with the parameters  $\zeta_S=170 \text{ \AA}$ ,  $\zeta_F=16 \text{ \AA}$ , and  $\varepsilon=3.4$ . [11]

## 4.2 Tagirov's Theory

Considering with imperfect interface, Aarts *et al.* was the first to discuss the important role of the interface transparency and present experimental evidence of the intrinsically reduced interface transparency in the  $V/V_{1-x}\text{Fe}_x$  multilayer system. [12] They analyzed their experimental results using the boundary conditions in the dirty limit for the  $F/S$  interface, which have been developed by Tagirov *et al.*, with the finite transparency taken into account. [13] The first boundary condition is the same as Equation 4.9, which ensures the continuity of the electric current associated with the charged quasiparticles crossing the interface. The second boundary equation is replaced by

$$-D_F (n_F \cdot \nabla F_F) = \frac{V_F T_m}{2} (F_S - F_F), \quad (4.13)$$

where  $n_F$  is the unit vector perpendicular to the interface and  $T_m$  is the dimensionless interface transparency parameter. ( $T_m \in [0, \infty]$ ). The key qualitative difference between the boundary condition Eq. 4.10, used by Radovic *et al.* [2], and Eq. 4.13, is that the latter allows a jump of the anomalous Green function at interface. Using this boundary condition and taking renormalization of the diffusion coefficient in the  $F$  layer into account, we may obtain a new equation for finite transparency

$$K_S d_S \tan(K_S d_S) = \frac{3d_S}{l_s} \frac{N_F v_F}{N_S v_S} \frac{\tanh(k_F d_F)}{i\xi_F k_F + \tanh(k_F d_F)}. \quad (4.14)$$

Here  $N_F$  and  $N_S$  is the density of states of the conduction electrons at the Fermi level in the ferromagnetic and superconducting layer, respectively. The numerical results and parameters are given in Fig. 4.4. It is clear to observe that the main difference between the behavior of the pairing function within the perfect interface transparency assumption and the Tagirov's model is the defined jump of the  $F$ -function at the interface.

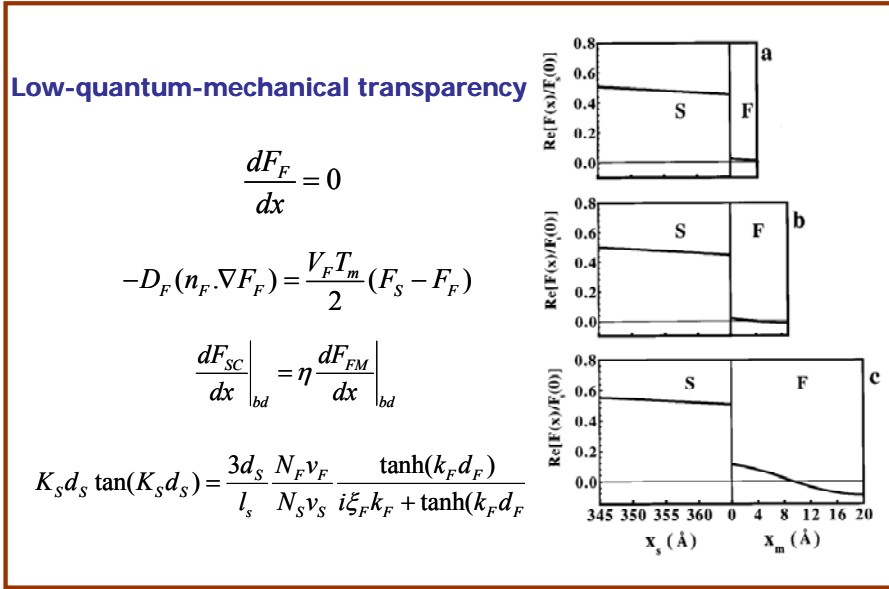


**Figure 4.4:** Spatial variation of the real part of the pairing function near the interface in the model by Tagirov with  $d_{pb}=730$  Å and  $d_{Fe}=4$  Å (a), 9 Å (b), and 20 Å (c) with the parameters  $\zeta_S=170$  Å,  $\zeta_F=7.7$  Å,  $l_s=15$  Å,  $N_F v_F / N_S v_S=1.3$  and  $T_m=0.4$ . [13]

### 4.3 Fominov's Theory: single-mode and multi-mode solution

In Section 4.2, according to the Tagirov's theory, the transparency  $T_m$  entering in the proximity theory may vary within the range  $[0, \infty]$ . However, it is unsuitable to compare it with the quantum mechanical transmission coefficient obtained via  $S/F$  tunneling or point contact spectroscopy, which lies in the range  $[0, 1]$ . Therefore, Fominov *et al.* [14] study the critical temperature of  $F/S$  bilayers by choosing a more general theory valid at arbitrary temperature with quasiclassical approach. [15] Near  $T_C$  the quasiclassical equations become linear with the help of the single-model approximation, the way which is argued to be qualitatively reasonable in a wide region of parameters. Moreover, they also study an exact solution of the linearized quasiclassical equation when this method fails.

### 4.3.1 single-mode solution

In the dirty limit conditions, the critical temperature  $T_C$  of the bilayer is calculated within the framework of the linearized Usadel equation for the  $S$  and  $F$  layers. Fig. 4.5 shows the domain of  $0 < x < d_s$  and  $-d_f < x < 0$  which are occupied by the  $S$  and  $F$  metal, respectively. Near  $T_C$  the normal Green function is  $G = \text{sgn} \omega_n$ , and the Usadel equations for the anomalous function  $F$  take the form

$$\xi_S^2 \pi T_{CS} \frac{d^2 F_S}{dx^2} - |\omega_n| F_S + \Delta = 0, \quad 0 < x < d_s \quad (4.14)$$

$$\xi_F^2 \pi T_{CS} \frac{d^2 F_F}{dx^2} - (|\omega_n| + iE_{ex} \text{sgn} \omega_n) F_F = 0, \quad -d_f < x < 0 \quad (4.15)$$

$$\Delta \ln \frac{T_{CS}}{T} = \pi T \sum_n \left( \frac{\Delta}{|\omega_n|} - F \right) \quad (4.16)$$

Here the pairing potential  $\Delta$  is nonzero only in the  $S$  part.  $\xi_S = \sqrt{D_S / 2\pi T_{CS}}$  and  $\xi_F = \sqrt{D_F / 2\pi T_{CS}}$  are the coherence lengths, while the diffusion constants  $D_{S,F}$  can be expressed via the Fermi velocity and the mean free path by  $D_F = Vl/3$ . The other parameters are already described in Section 4.1.

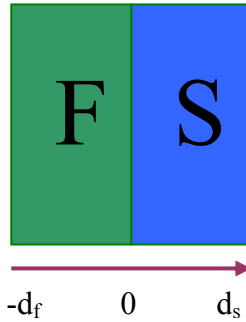


**Figure 4.5:**  $SF$  bilayer. The  $F$  and  $S$  layers occupy the regions  $-d_f < x < 0$  and  $0 < x < d_s$ , respectively.

At the outer surfaces of the bilayer, Eq. (4.14) to (4.16) must be supplemented with boundary conditions at the outer surfaces of the bilayer,

$$\frac{dF_S(d_S)}{dx} = \frac{dF_F(-d_F)}{dx} = 0, \quad (4.17)$$

as well as at the  $SF$  boundary, [16]

$$\xi_S \frac{dF_S(0)}{dx} = \gamma \xi_F^* \frac{dF_F(0)}{dx}, \quad \gamma = \frac{\rho_S \xi_S}{\rho_F \xi_F^*} \quad (4.18)$$

$$\xi_F^* \gamma_b \frac{dF_F(0)}{dx} = [F_S(0) - F_F(0)], \quad \gamma_b = \frac{R_b A}{\rho_F \xi_F^*} \quad (4.19)$$

Here  $R_b$  is the resistance of the  $SF$  boundary, and  $A$  is its area. The parameter  $\gamma$  is a measure of the strength of the proximity effect between the  $S$  and  $F$  metals while  $\gamma_b$  describes the effect of the interface transparency  $T_{tran}$ , define as:

$$\gamma_b = \frac{2}{3} \frac{\ell_F}{\xi_F^*} \frac{1 - T_{tran}}{T_{tran}}. \quad (4.20)$$

$T_{tran}$  is 0 for the completely reflecting interface, large resistance of the barrier  $R_b$ . It is equal to one for a completely transparent interface. It is useful to compare this definition to the  $T_m$  present in Tagirov's model as discussed in Section 4.2 by the expression:

$$T_m = \frac{T_{tran}}{1 - T_{tran}}, \quad (4.21)$$

where the  $T_m$  can vary between zero, negligible transparency and infinity, perfect interface. It is important to note that the boundary condition (4.19) determines a jump of the pairing function at the interface, and this characteristic is similar to the Eq. (4.13) developed by Tagirov. However, it is in contrast with Radovic's picture, in which the pairing wavefunction varies continuously due to the perfect boundary assumption.

The Usadel equation in the  $F$  layer is readily solved,

$$F_f = C(\omega_n) \cosh(k_f[x + d_f]), \quad k_f = \frac{1}{\xi_f} \sqrt{\frac{|\omega_n| + iE_{ex} \operatorname{sgn} \omega_n}{\pi T_{cS}}}. \quad (4.22)$$

And the boundary condition at  $x=0$  can be written in closed form with respect to  $F_S$ :

$$\xi_S \frac{dF_S(0)}{dx} = \frac{\gamma}{\gamma_b + B_f(v)} F_S(0), \quad B_f = [K_f \xi_f \tanh(K_f d_f)]^{-1} \quad (4.23)$$

This boundary condition is complex. In the single-model approximation, the critical temperature of the bilayer is then determined by the equation

$$\ln\left(\frac{T_{cS}}{T_c}\right) = \psi\left(\frac{1}{2} + \frac{\Omega^2 T_{cS}}{2 T_c}\right) - \psi\left(\frac{1}{2}\right) \quad (4.24)$$

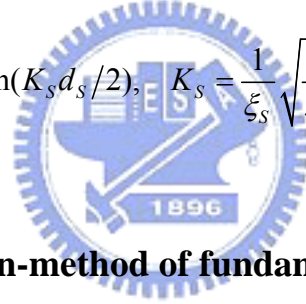
where  $\psi$  is the digamma function.  $\Omega$  can be derived from the boundary conditions of matching the pairing function at  $x=0$ , as given by

$$\Omega \tan\left(\Omega \frac{d_S}{\xi_S}\right) = W(\omega_n), \quad \omega_n = \pi T_c (2n+1) \quad (4.25)$$

with

$$W(\omega_n) = \gamma \frac{A_S (\gamma_b + \text{Re } B_F) + \gamma}{A_S |\gamma_b + B_F|^2 + \gamma (\gamma_b + \text{Re } B_F)}, \quad (4.26)$$

$$A_S = K_S \xi_S \tanh(K_S d_S / 2), \quad K_S = \frac{1}{\xi_S} \sqrt{\frac{\omega_n}{\pi K_B T_{cS}}} \quad (4.27)$$



### 4.3.2 multi-mode solution-method of fundamental solution

According to Fominov's report, the single-mode approximation is correct only if the parameters are such that  $W$  can be considered  $\omega_n$  independent. Although this method is popular, it is often used without considering the limits of its applicability. An example for this limitation is the case when  $\gamma_b \gg |B_f|$ , hence  $W = \gamma/\gamma_b$ . The condition can be written in a simpler form,  $\sqrt{E_{ex}/\pi T_{cS}} \gg 1/\gamma_b$  as one of experimentally relevant cases. The single-model approximation implies that one takes the only real root  $\Omega$  of Eq. (4.24). An exact method for solving the problem is obtained when the imaginary roots are taken into account. Thus, there is infinite number of solution in a multi-mode method. The parameters are determined by the

self-consistency equation:

$$\ln\left(\frac{T_{CS}}{T_C}\right) = \psi\left(\frac{1}{2} + \frac{\Omega_0^2}{2} \frac{T_{CS}}{T_C}\right) - \psi\left(\frac{1}{2}\right),$$

$$\ln\left(\frac{T_{CS}}{T_C}\right) = \psi\left(\frac{1}{2} + \frac{\Omega_m^2}{2} \frac{T_{CS}}{T_C}\right) - \psi\left(\frac{1}{2}\right), \quad m = 1, 2, \dots \quad (4.28)$$

Numerically, it is complicated to solve this matrix equation. Fominov developed the fundamental solution  $G(x, y; \omega_n)$ , which is also called the Green's function, to satisfy the same equation, but with the delta function "source",

$$\xi_s^2 \pi T_{CS} \frac{d^2 G(x, y)}{dx^2} - \omega_n G(x, y) = -\delta(x - y), \quad (4.29)$$

$$\xi_s \frac{dG(0, y)}{dx} = W(\omega_n) G(0, y), \quad \frac{dG(d_s, y)}{dx} = 0 \quad (4.30)$$

This equation can be expressed in an operator form:

$$\Delta(x) \ln \frac{T_{CS}}{T_C} = 2\pi T_C \sum_{\omega_n > 0} \left[ \frac{\Delta(x)}{\omega_n} - \int_0^{d_s} G(x, y; \omega_n) \Delta(y) dy \right] = \hat{L} \Delta. \quad (4.31)$$

Then the condition that Eq. (4.31) has a nontrivial solution with respect to  $\Delta$  is expressed by the equation

$$\det(\hat{L} - \hat{1} \ln \frac{T_{CS}}{T_C}) = 0. \quad (4.32)$$

This critical temperature  $T_C$  is determined as the largest solution of this equation.

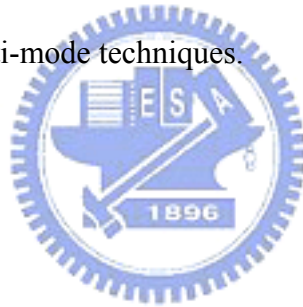
Numerically, the operator  $\hat{L}$  becomes a finite matrix by putting equations (4.31) and (4.32) on a spatial grid.

In the general case, as shown in the Fig. 4.6, there are three characteristic types of  $T_C(d_f)$  behavior: (1) At a large enough  $\gamma_b$ ,  $T_C$  decays nonmonotonically to a finite value exhibiting a minimum at a particular  $d_f$ . (2) At a moderate  $\gamma_b$ ,  $T_C$  demonstrates a reentrant behavior which makes  $T_C$  vanish in a certain interval of  $d_f$  and is finite otherwise. (3) At a small enough  $\gamma_b$ ,  $T_C$  decays monotonically, vanishing at finite  $d_f$ . These characteristics can be explained by the fact that the suppression of superconductivity by a dirty ferromagnet is only due to the effective  $F$  layer with a thickness on order of  $\lambda_{ex}$ , adjacent to the interface. The wavelength of the oscillations



$\lambda_{\text{ex}}$  is the layer of explored and felt by quasiparticles entering from the  $S$  side due to the proximity effect.

The single-mode approximation is a popular method widely used in the literature for calculating the critical temperature of  $FS$  bilayers and multilayers. However, the condition of its validity is limited according to Fomonov's report. In order to estimate the actual accuracy in the single-mode approximation, we compare single-mode and multi-mode methods in the Fig. 4.6. In the general case, the results of the single-mode and multi-mode methods are close. However, when  $\gamma_b < 0.1$ , they are quantitatively and qualitatively different, the single-mode method somewhat underestimates the minimum value of  $T_C$  and overestimates the amplitude of  $T_C$  oscillation. Thus the single-mode approximation can be used for quick estimates, but reliable results should be obtained by one of the multi-mode techniques.



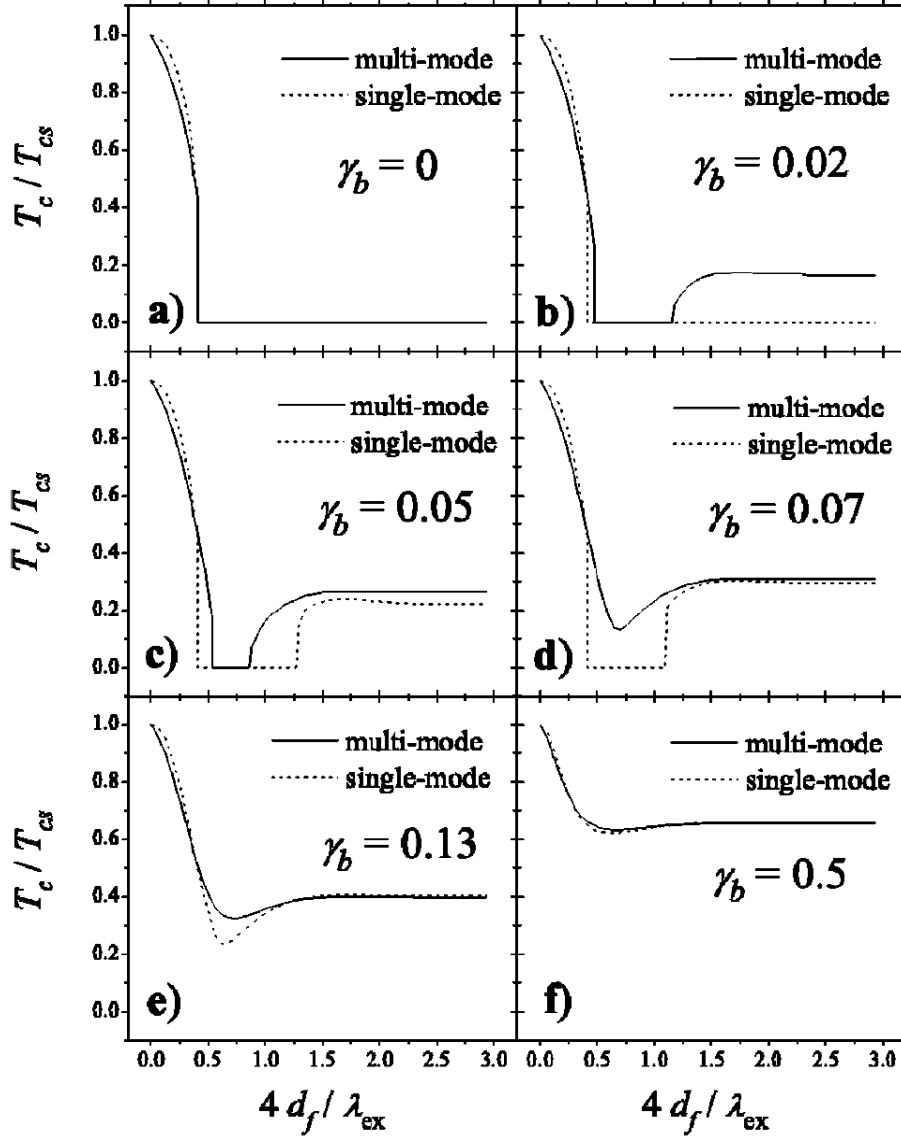


**Figure 4.6:** Comparison between single- and multimode methods. Generally speaking, the results of the single-mode and multimode methods are close: (a) and (f). However, at some parameters are different: (b), (c), (c), (d), and (e). [14]

Based on the interference of quasiparticles in the ferromagnet, the thickness of the  $F$  layer, at which the minimum of  $T_c(d_f)$  occurs, can be estimated from qualitative arguments. [14] According to Feynman's interpretation of quantum mechanics, [17] the quasiparticle wave function may be represented as a sum of wave amplitudes over all classical trajectories. Consider a point  $x$  inside the  $F$  layer, as shown in Fig. 4.7.

The anomalous wave function of correlated quasiparticles, which characterizes superconductivity, is equivalent to the anomalous Green function  $F(x)$ . We sum over trajectories that (i) start and end at the point  $x$ , and (ii) change the type of the quasiparticle converting an electron into a hole, or vice versa through the Andreev reflection.

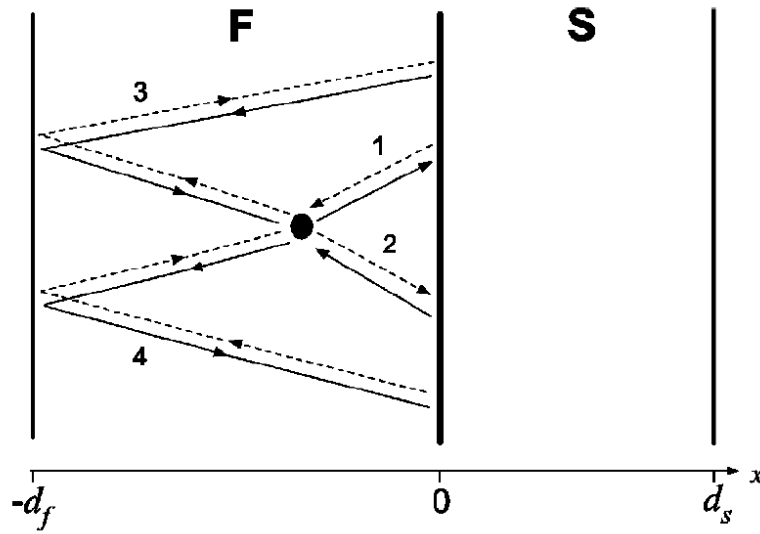


**Figure 4.7:** Four types of trajectories contributing in the sense of Feynman's path integral to the anomalous wave function of correlated quasiparticles in the ferromagnetic region. The solid lines correspond to electrons, and the dashed lines to holes; the arrows indicate the direction of the velocity. [14]

Hence, there are four kinds of trajectories that should be taken into account. In Fig 4.7, the trajectory 1 and 2 start in the direction toward the  $FS$  interface as an electron and as a hole, respectively, experiencing the Andreev reflection and returning to the point  $x$ . The other two trajectories denoted 3 and 4 start in the direction away from the interface, experiencing normal reflection at the outer surface of the  $F$  layer, moving toward the  $FS$  interface, experiencing the Andreev reflection there, and

finally returning to the point  $x$ . The corresponding actions can be represented as:

$$S_1 = -Qx - \alpha,$$

$$S_2 = Qx - \alpha,$$

$$S_3 = -Q(2d_f + x) - \alpha,$$

and

$$S_4 = Q(2d_f + x) - \alpha. \quad (4.33)$$

Where  $Q$  is the difference between the wave numbers of the electron and the hole, and  $\alpha = \arccos(E/\Delta)$  is the phase of the Andreev reflection. Here, we assume that the ferromagnet is strong, the  $FS$  interface is ideal, and consider the clean limit first:

$$Q = K_e - K_h = \sqrt{2m(E + E_{ex} + \mu)} - \sqrt{2m(-E - E_{ex} + \mu)} \approx 2E_{ex}/v, \quad (4.34)$$

where  $E$  is the quasiparticle energy,  $\mu$  is the Fermi energy, and  $v$  is the Fermi velocity.

Thus the anomalous wave function of the quasiparticles is

$$F(x) \propto \sum_{n=1}^4 \exp(iS_n) \propto \cos(Qd_f) \cos(Q[d_f + x]). \quad (4.35)$$

The suppression of  $Tc$  by the ferromagnet is determined by the value of the wave function at the  $F/S$  interface:  $F(0) \propto \cos^2(Qd_f)$ . The minimum of  $Tc$  corresponds to the minimum value of  $F(0)$  which is achieved at  $d_f = \pi/2Q$ . In the dirty limit the above expression for  $Q$  is replaced by

$$Q = \sqrt{\frac{E_{ex}}{D_f}} \equiv \frac{2\pi}{\lambda_{ex}} \quad (4.36)$$

Thus, the minimum of  $Tc(d_f)$  in terms of the wavelength of the oscillations takes place at:

$$d_{f \min} = \frac{\pi}{2} \sqrt{\frac{D_f}{E_{ex}}} \equiv \frac{\lambda_{ex}}{4}. \quad (4.37)$$

For the bilayer of  $Nb/Cu_{0.43}Ni_{0.57}$ , the calculation obtains  $d_{f \min} \sim 7$  nm, whereas the

experimental value is 5 nm [14]. Thus the qualitative estimate is phenomenologically related to  $d_{\min} = 0.7\pi\xi_F^{\text{dirty}}/2$ . It is possible to estimate  $\xi_F^{\text{dirty}}$  directly from the position value of the minimum in  $T_C(d_f)$  curve. The way is examined in Nb/Pd<sub>0.86</sub>Ni<sub>0.14</sub> [18] and Nb/Pd<sub>0.81</sub>Ni<sub>0.19</sub> bilayer system [19] has been proven valid by obtaining reasonable quantity.

## 4.4 Global Fit

In this section, we will describe the detail of Global Fit procedure which is used to simultaneously fit different sets of results with same parameters in the CPP measurement. Assume we have  $l$  common unknowns,  $c_1, c_2 \dots c_l$ , in different sets of data. We want to fit these sets of data simultaneously to get the unknowns. Each set of data can be described by a theoretical relation  $y = Y(x)$ , where  $y$  and  $x$  are experimentally measurable quantities. The unknowns  $c_1, c_2 \dots c_l$  appear in the coefficients of the  $x$ 's.  $Y$  must be linear in  $c$ 's to do this global fit the way we describe here. In set  $p$  we have  $n(p)$  pairs of data  $(x_i, y_i)$ , each of which is theoretically related to  $y_i = Y(x_i, c_1, c_2, \dots, c_l, p)$ . The deviation of the measured  $y_i$  from the theoretical value is given by

$$y_i - Y(x_i, c_1, \dots, c_l, p). \quad (4.38)$$

The root mean square  $\chi^2(p)$  for this set of data is then

$$\chi^2 = \sum_{i=1}^{n(p)} [y_i(p) - Y(x_i, c_1, c_2, \dots, c_l, p)]^2. \quad (4.39)$$

Since each set has same unknown parameter, we can do a global fit to all sets of data and minimize  $\chi_{\text{tot}}^2 = \sum_p \chi^2(p)$ .

We limit the calculation to the case that all functions of  $Y$  are linear in the  $c$ 's.

Thus we can write  $Y(x_i, c_1, \dots, c_l, p) = \sum_{k=1}^l c_k \cdot g_k(x_i, p)$ , where  $g_k(x_i, p)$  are functions of  $x_i$  in different sets  $p$ . Note that if there is a constant term independent of the  $c$ 's on the right side, we can move it to the left and redefine the  $Y$ 's. We have now,

$$\chi_{tot}^2 = \sum_p \sum_{i=1}^{n(p)} [y_i(p) - Y(x_i, c_1, \dots, c_l, p)], \quad (4.40)$$

where  $C^*$  denotes all  $l$  unknowns. To get the best values  $c^*$  for all the unknowns, we minimize  $\chi^2(p)$  with respect to the  $c$ 's:

$$\begin{aligned} \frac{\partial \chi^2}{\partial c_j} &= 0 \\ &= -2 \sum_p \sum_{i=1}^{n(p)} [y_i(p) - Y(x_i, c_1, \dots, c_l, p)] \times g_j(x_i, p) \\ &= -2 \sum_p \sum_{i=1}^{n(p)} \left[ y_i(p) \times g_j(x_i, p) - g_j(x_i, p) \cdot \sum_{k=1}^l c_k^* \times g_k(x_i, p) \right] \end{aligned} \quad (4.41)$$

Define the data vector

$$U_j = \sum_p \sum_{i=1}^{n(p)} y_i(p) \times g_j(x_i, p) \quad (4.42)$$

and the symmetric matrix

$$M_{jk} = \sum_p \sum_{i=1}^{n(p)} g_j(x_i, p) \times g_k(x_i, p). \quad (4.43)$$

We then write  $U_j = \sum_{k=1}^l M_{jk} \cdot C_k^*$ .

The best fit values for the unknown are solved by  $C^* = M^{-1} \cdot U$ .  $M^{-1}$  is known as the “error matrix”. Its diagonal elements are the squares of the errors, and the off-diagonal elements are the covariance, which are the correlations between the best fit value  $C^*$ . The degree of freedom,  $d_{free}$ , equal the number of the data points minus the number of unknown parameters in the fit. Thus, all of the uncertainties can be adjusted by  $M^{-1} \sqrt{\chi^2 / d_{free}}$ . The global fit has been performed by computer program in Mathematica, which can be modified for different numbers of unknowns and different sets of data.

## 4.5 Andreev reflection and the Blonder, Tinkham, and Klapwijk model

While discussing  $F/S$  transport property, spin effects play an important role in the Andreev reflection at the  $F/S$  interface. The behavior occurring at a clean and metallic  $N/S$  interface is a conversion of normal currents to superconducting currents, as was first proposed by Andreev. [20] The opening of a superconducting gap,  $\Delta$ , at the Fermi energy, and the decrease in population of quasiparticles, make  $S$  a low carrier system for spin transport. At voltages lower than the energy gap  $\Delta$ , there are no available quasiparticle states in the superconductor. However, currents can flow through the sample in response to a small voltage less than  $\Delta$  through the Andreev reflection in the metallic junction. As shown in Figure 4.8, a spin-up electron injected from a normal metal is retroreflected at the interface as a spin-down hole in order to

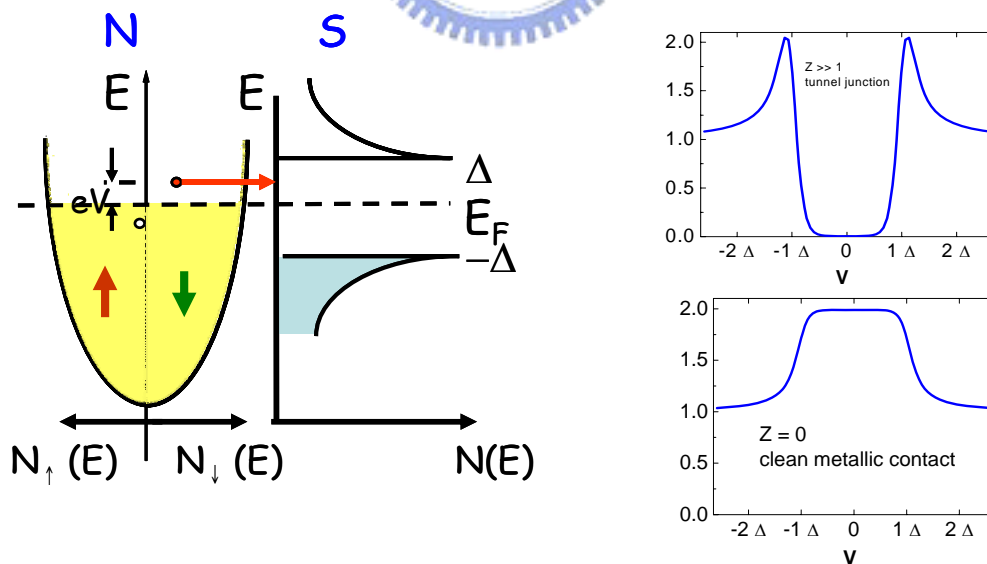


**Figure 4.8:** (a) Schematic diagram of energy versus momentum of a normal metal-superconductor contact (b) the conductance versus voltage for metallic contact (down) and tunnel junction (up) in  $NM/F$  structure.

form a Cooper pair in the superconductor. [21] In this process, the superconducting conductance at bias voltage smaller than  $\Delta$  is twice the normal state conductance value.

In a previous report, Blonder, Tinkham and Klapwijk (BTK) proposed a theory for the  $I$ - $V$  curves of  $NM/S$  microconstriction contact in which the contact diameter is smaller than the mean free path within the ballistic regime. [22] The calculation describes the crossover from metallic behavior with a perfect transparent interface to tunnel junction with an insulating barrier.

The BTK model is calculated within the Bogoliubov equations to treat the transmission and reflection of quasiparticle at the  $NM/S$  interface. The Bogoliubov formalism can be described as a two-element column vector:

$$\Psi(x,t) = f(x,t) |e\rangle + g(x,t) |h\rangle = \begin{pmatrix} f(x,t) \\ g(x,t) \end{pmatrix} \quad (4.44)$$

Here, the quasiparticle is considered as the two base-states “electron-like” and “hole-like”, denoted as  $|e\rangle$  and  $|h\rangle$ , respectively.  $f(x,t)$  and  $g(x,t)$  are the probability amplitudes of the quasi-particle in  $|e\rangle$  and  $|h\rangle$ , respectively. In the calculation of Bogoliubov equation, the Andreev reflection proceeds as the presence of interface barrier. In the Fig 4.9, consider that an electron incident on the interface from the normal state with energy  $E > \Delta$ , as indicated by the arrow at the state labeled 0, while the outgoing particles are located at points 6, 5, 4, and 2, respectively. Here, the excitations at  $\pm k^+$  are predominantly electronlike, whereas those at  $\pm k^-$  are predominantly holelike.



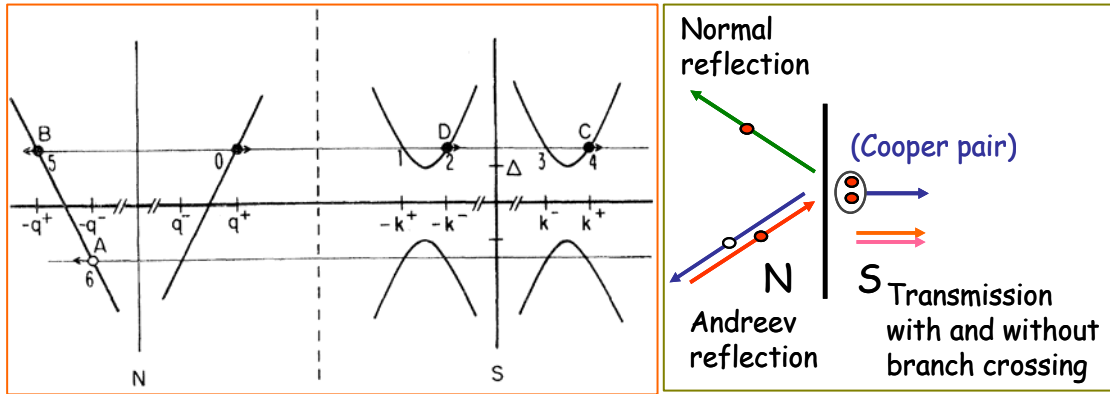


**Figure 4.9:** Schematic diagram of energy vs momentum at an  $NM$ - $S$  interface. The open circles denote holes, the closed circles electrons, and the arrow point in the direction of the group velocity. The figure in the right hand side simply describes the process of transmitted and reflected electron at  $F/S$  interface. [21]

By matching the slope and the value of the wave functions across the interface, BTK model considers the probabilities  $A(E)$ ,  $B(E)$ ,  $C(E)$ , and  $D(E)$  for four processes.  $A(E)$  is the probability of Andreev reflection as a hole on the other side of the Fermi surface, while  $B(E)$  is the probability of ordinary reflection.  $C(E)$  is the probability of transmission through the interface with a wave vector on the same side of the Fermi surface (i.e.,  $q^+ \rightarrow k^+$  in Fig. 4.8), while the probability of transmission in  $D(E)$  is crossing through the Fermi surface (i.e.,  $q^+ \rightarrow -k^-$  in Fig. 4.8). Table 4.1 lists these transmission and reflection as functions of energy and barrier strength by solving the Bogoliugov equation with suitable boundary condition. According to the conservation of probability, it is important to require that

$$A(E) + B(E) + C(E) + D(E) = 1. \quad (4.45)$$

It is useful to simplify the expression for energies below the gap, where there are no transmitted quasiparticles and that  $C=D=0$ . The barrier strength is dimensionless described as  $Z=H \delta(x)/\hbar v_F$ , where the repulsive potential  $H \delta(x)$  located at the interface represents the effect of the oxide layer such as in a point contact

measurement. The significant transmission coefficient in the normal state is simply  $(1+Z^2)^{-1}$ , and corresponding reflection coefficient is  $Z^2/(1+Z^2)$ .

Because the current must be conserved, it can be calculated in any plane. Under ballistic assumption without scattering, it is convenient to do so on the  $N$  side of the interface, where all current is carried by single particles, not supercurrent. We consider the current inside the metal and separate it into the right-flowing part ( $S$  to  $NM$ ) and left-flowing part ( $NM$  to  $S$ ). When a voltage is applied, it causes an energy shift between  $NM$  and  $S$ , described by the shift of the equilibrium Fermi-Dirac distribution in the 1D model. Thus, the incident current from the  $NM$ -side can be obtained by integrating the distribution over  $E$  given by

$$eA \int v(E) \rho(E) [1 + A(E) - B(E)] f(E - eV) dE, \quad (4.46) \quad [N \rightarrow S]$$

where  $v$  and  $\rho$  are the electron velocity and density of states of the normal metal, respectively. While the current coming in from  $S$ -side is given by

$$eA \int v(E) \rho(E) [1 + A(E) - B(E)] f(E) dE. \quad (4.47) \quad [S \rightarrow N]$$

We can simply obtain the total current as

$$I = eA \int v(E) \rho(E) [1 + A(E) - B(E)] [f(E - eV) - f(E)] dE. \quad (4.48)$$

Thus, the conductance is obtained by taking derivative of the bias voltage:

$$G_{NS} = \frac{dI}{dV} = e^2 A v \rho \int [1 + A(E) - B(E)] f'(E - eV) dE. \quad (4.42)$$

Furthermore, it can be normalized as

$$G_{NS} = -(1 + Z^2) \int [1 + A(E) - B(E)] f'(E - eV) dE. \quad (4.49)$$

**TABLE II.** Transmission and reflection coefficients.  $A$  gives the probability of Andreev reflection (i.e., reflection with branch crossing),  $B$  of ordinary reflection,  $C$  of transmission without branch crossing, and  $D$  of transmission with branch crossing (see text). ( $\gamma^2 = [u_0^2 + Z^2(u_0^2 - v_0^2)]^2$ ,  $u_0^2 = 1 - v_0^2 = \frac{1}{2} \{ 1 + [(E^2 - \Delta^2)/E^2]^{1/2} \}$ , and  $N_s(E) = (u_0^2 - v_0^2)^{-1}$ .)

	$A$	$B$	$C$	$D$
Normal state	0	$\frac{Z^2}{1+Z^2}$	$\frac{1}{1+Z^2}$	0
General form				
$E < \Delta$	$\frac{\Delta^2}{E^2 + (\Delta^2 - E^2)(1 + 2Z^2)^2}$	$1 - A$	0	0
$E > \Delta$	$\frac{u_0^2 v_0^2}{\gamma^2}$	$\frac{(u_0^2 - v_0^2)^2 Z^2 (1 + Z^2)}{\gamma^2}$	$\frac{u_0^2 (u_0^2 - v_0^2) (1 + Z^2)}{\gamma^2}$	$\frac{v_0^2 (u_0^2 - v_0^2) Z^2}{\gamma^2}$
No barrier ( $Z = 0$ )				
$E < \Delta$	1	0	0	0
$E > \Delta$	$v_0^2 / u_0^2$	0	$1 - A$	0
Strong barrier [ $Z^2(u^2 - v^2) \gg 1$ ]				
$E < \Delta$	$\frac{\Delta^2}{4Z^2(\Delta^2 - E^2)}$	$1 - A$	0	0
$E > \Delta$	$\frac{u_0^2 v_0^2}{Z^4(u_0^2 - v_0^2)^2}$	$1 - \frac{1}{Z^2(u_0^2 - v_0^2)}$	$\frac{u_0^2}{Z^2(u_0^2 - v_0^2)}$	$\frac{v_0^2}{Z^2(u_0^2 - v_0^2)}$

**Table 4.1:** Transmission and reflection coefficients.  $A$  gives the probability of Andreev reflection,  $B$  of normal reflection probability,  $C$  of transmission probability without branch crossing,  $D$  of transmission probability with branch crossing. [21]

Since the Andreev reflection is spin-dependent behavior, in fully spin-polarized metals that all carries have the same spin and the Andreev reflection would be totally suppressed. The spin polarization can be probed based on the fact that the subgap conductance drops from twice the normal-state conductance value to a small value for highly polarized metal (see Fig. 4.10). Consequently, the spin-up and spin-down bands of electron in a ferromagnet are involved in this process. The major influence of spin polarization in a ferromagnet on the conductance of the  $F/S$  interface has been first demonstrated by de Jong and Beenakker (1995) theoretically. [22] Subsequent experiments of spin polarization with Andreev point-contact spectroscopy permit us to measure the spin polarization by a modified BTK model. [23] In general, the current is divided into an unpolarized part,  $P$ , and a completely polarized part,  $1 - P$ , given by [24, 25]

$$I = I_u + I_p = (1-P)I + PI. \quad (4.50)$$

The spin polarization can be simply obtained in the absence of the interface scattering by the zero-bias conductance and the normal state conductance through the relation,

$$\frac{G_0}{G_N} = 2(1-P) \quad (4.51)$$

where  $G_N$  is the normal state conductance,  $G_0$  the zero-bias conductance and  $P$  the spin polarization. However, the interpretation of the Andreev reflection data on the conductance of the  $F/S$  interface is complicated. There are many investigations going on such as studies of band-structure effect [22], Fermi velocity mismatch of metals [26], and spectra broadening effect [27], etc. These investigations allow us to achieve a reliable determination of spin polarization.

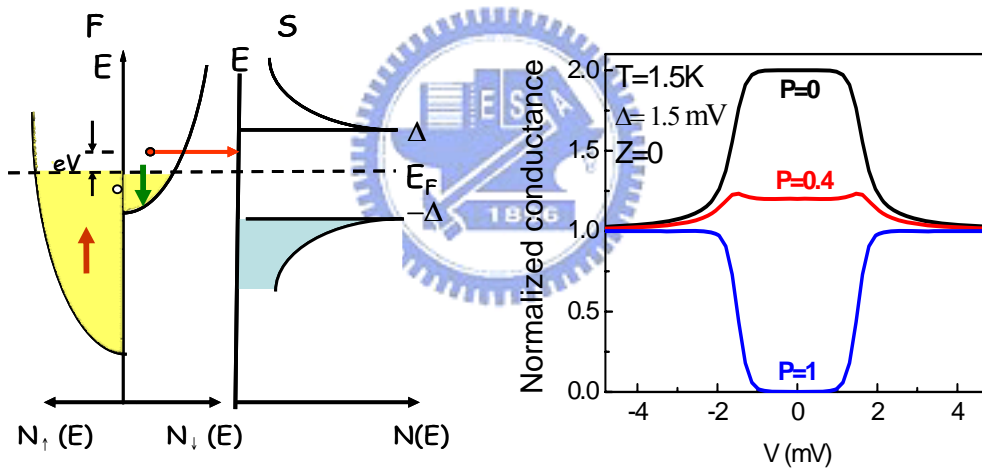


**Figure 4.10:** (a) Schematic diagram of energy versus momentum of a ferromagnet-superconductor contact (b) the conductance versus voltage for metallic contact with different polarization of ferromagnet in  $F/S$  structure.

## References:

1. Z. Radović, L. Dobrosavljević -Grujić, A.I. Buzdin, and J.R. Clem, Phys. Rev. B **38**, 2388 (1988).
2. Z. Radović, M. Ledvij, L. Dobrosavljević -Grujić, A.I. Buzdin, and J. R. Clem, Phys. Rev. B **44**, 759 (1991).
3. P. G. de Gennes and G. Darma, J. Appl. Phys. **34**, 1380 (1963).
4. V. V. Ryazanov, V. A. Oboznov, A. Yu. Rusanov, A. V Veretennikov, A. A. Golubov, and J. Aarts, Phys. Rev. Lett. **86**, 2427 (2001).
5. L. N. Bulaevskii, V. V. Kuzii, and A. A. Sobyenin, JETP Lett. **25**, 290 (1977).
6. V. G. Kogan, Phys. Rev. B **32**, 139 (1985).
7. K. Usadel, Phys. Rev. Lett. **25**, 507 (1970).
8. A. Millis, D. Rainer, and J. A. Sauls, Phys. Rev. B **38**, 4504 (1988).
9. T. Tokuyasu, J. A. Sauls, and D. Rainer, Phys. Rev. B **38**, 8823 (1988).
10. A. G. Ivanov, M. Yu. Kurprianov, K. K. Likharev, S. V. Meriakri, and O. V. Snigirev, Sov. J. Low Temp. Phys. **7**, 274 (1981).
11. L. Lazar, K. Westerholt, H. Zabel, and L. R. Tagirov. Phys. Rev. B. **61**, 3711 (2000).
12. J. Aarts, J. M. E. Geers, E. Bruck, A. A. Golubov, and R. Coehoorn, Phys. Rev. B **56**, 2779 (1997).
13. L. R. Tagirov, Physica **307C**, 145 (1998).
14. Ya. V. Fominov, N. M. Chtchelkatchev, and A. A. Golubov, Phys. Rev. B **66**, 014507 (2002).
15. A. I. Larkin and Yu. N. Ovchinnikov, in *Nonequilibrium Superconductivity*, edited by D. N. Langenberg and A. I. Larkin (Elsevier, New York, 1986), p. 530, and references therein.
16. M. Yu. Kupriyanov and V. F. Lukichev, Sov. Phys. JEPT **67**, 1163 (1988).

17. R. P. Feynman and A. R. Hibbs, *Quantum Mechanics and Path Integrals* (McGraw-Hill, New York, 1965).
18. C. Cirillo, S. L. Prischepa, M. Salvato, and C. Attanasio, Phys. Rev. B **72**, 144511 (2005).
19. C. Cirillo, A. Rusanov, C. Bell, and J. Aarts, Phys. Rev. B **75**, 174510 (2007).
20. A. F. Andreev, Zh. Eksp. Teor. Fiz. **46**, 1823 (1964) [Sov. Phys. JETP **19**, 1228 (1964)].
21. G. E. Blonder, M. Tinkham, and T. M. Klapwijk, Phys. Rev. B **25**, 4515 (1982).
22. M. J. M. de Jong and C. W. J. Beenakker, Phys. Rev. Lett. **74**, 1657 (1995).
23. R. J. Soulen, J. Byers, M. S. Osofsky, B. Nadgorny, T. Ambrose, S. F. Cheng, P. Broussard, C. T. Tanaka, J. Nowak, J. S. Moodera, et al., Science **282**, 85 (1998).
24. G. J. Strijkers, Y. Ji, F. Y. Yang, C. L. Chien, and J. M. Byers, Phys. Rev. B **63**, 104510 (2001).
25. I. I. Mazin, A. A. Golubov, and B. Nadgorny, J. Appl. Phys. **89**, 7576 (2001).
26. P. Chalsani, S. K. Upadhyay, O. Ozatay, and R. A. Buhrman, Phys. Rev. B **75**, 094417 (2007).
27. T. W. Chiang, Y. H. Chiu, S. Y. Huang, S. F. Lee, J. J. Liang, H. Jaffrès, J. M. George, and A. Lemaitre, J. Appl. Phys. **105**, 07C507 (2009).

# Chapter 5

## Results and Discussion-Conventional Ferromagnet: Co/Nb<sub>x</sub>Ti<sub>1-x</sub> System

Almost every physical phenomenon mentioned in the previous chapters is related to the interaction between superconductivity and magnetism which occurs at the boundary of  $F/S$  structures. In order to study the transport properties, it is important to understand the influence of interfaces. The main idea of this series of samples is to study electric transport properties between strong ferromagnet and different superconductor alloys. In this section, the dependence of critical temperature,  $T_C$ , on the superconductor thickness for the  $F/S$  trilayers with strong ferromagnet Co and three kinds of superconductors, Nb, Nb<sub>0.6</sub>Ti<sub>0.4</sub>, and Nb<sub>0.4</sub>Ti<sub>0.6</sub>, are studied by the electrical resistivity measurement. For a fixed Co layer thickness, the behavior of  $T_C$  with decreasing  $S$  layer thickness can be described in terms of pair breaking by the proximity effect. By current perpendicular to plan measurement, quantitative analysis of the interface resistance between  $F$  and  $S$  both in the superconducting state and in the normal state is firstly presented by one-band series-resistance model. In comparison with three kinds of superconductor alloys, the interface resistance follows the Pippard model with partial quenching of Andreev reflection due to impurities in the superconductor. Moreover, the interface transparency in terms of the ratio between interface resistance and various physical quantities are discussed.

## 5.1 Thickness dependence of superconducting transition temperature in Co/*S* trilayers with $S = \text{Nb}, \text{Nb}_{0.4}\text{Ti}_{0.6},$ and $\text{Nb}_{0.6}\text{Ti}_{0.4}.$

In this section, the dependence of transition temperature on the superconductor thickness for Co/*S* trilayers is discussed. Deposition was done under 1 mTorr Ar gas, with 0.05 nm/s rate for Co and 0.12 nm/s for Nb and  $\text{Nb}_x\text{Ti}_{1-x}$ . Twelve samples were fabricated in the same run. Nb and Co can form alloys at high temperature, but they should be immiscible around room temperature. [1] Series of samples of Nb/Co bilayers and Co/Nb/Co trilayers as well as  $\text{Nb}_x\text{Ti}_{1-x}$ /Co bilayers and Co/ $\text{Nb}_x\text{Ti}_{1-x}$ /Co trilayers were prepared for the present study. The thickness of the Co layer for both systems was kept to 2 nm and that of the *S* layers ranged from 20 to 300 nm for the former and from 10 to 100 nm for the latter. We checked the structure of our multilayers with low angle and high angle  $\theta$ - $2\theta$  x-ray scans. X-ray diffraction showed crystalline structures of bcc (110) for Nb and fcc (111) or hcp (0001) for thick Co, not distinguishable from theta-two theta scan. Our data confirmed that sputtered multilayers were polycrystalline. [2, 3]

The superconducting transition temperatures were determined by the electrical resistivity as well as magnetic susceptibility. Both results show the same  $d_S$  dependence of  $T_C$ . With decreasing  $d_S$ ,  $T_C$  shows a continuous reduction down to a critical thickness  $d_S^{crit}$ , below which superconductivity vanishes. Single *S* layers of comparable thickness showed only minor  $T_C$  depressions due to disorder as shown in Fig. 5.1 (a), (b) and (c). However, the decrease in  $T_C$  with decreasing Nb layer thickness is clearly seen for the Co/Nb/Co trilayers and that of Co/Nb bilayers with



$d_{Co}=2$  nm as a function of Nb layer thickness in Figure 5.1. In much the same way, the thickness dependent  $T_C$  of Co/  $Nb_{0.4}Ti_{0.6}/Co$  and Co/  $Nb_{0.6}Ti_{0.4}/Co$  trilayers with  $d_{Co}=2$  nm decrease sharply when the thickness of  $S$  is smaller than 50 nm. The decrease in  $T_C$  results from the depression of the amplitude of the Cooper pair wavefunction. The pair-breaking effect near the  $F/S$  boundary is due to the strong exchange field  $E_{ex}$  in Co. Here we observed that the  $T_C$  showed a monotonically rapid decrease with decreasing  $Nb_xTi_{1-x}$  thickness for the case of bilayers and trilayers structure. The experimental data can be fitted by theoretical model related to the proximity effect, as will be discussed in detail in the next section. In Figure 5.1, the solid lines are fitted by the model proposed by Radovic' *et al.* [4] It can be seen that the experimental points are well described by this model, and the  $T_C$  value decreases with decreasing  $Nb_xTi_{1-x}$  thickness down to the critical thickness  $d_{crit}$ , where the superconductivity vanished.



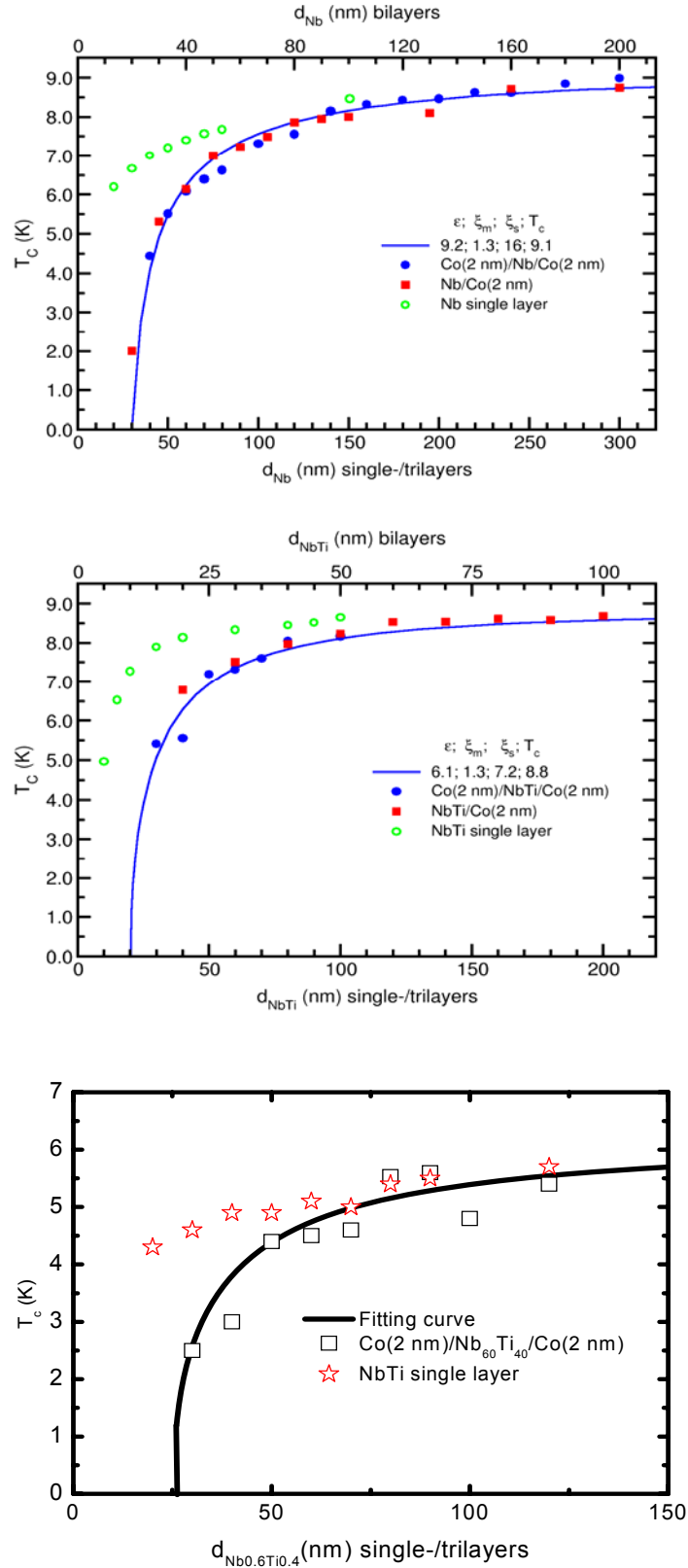


**Figure 5.1:** Dependence of the superconducting transition temperature on the thickness of the (a) Nb, (b) Nb<sub>0.4</sub>Ti<sub>0.6</sub> and (c) Nb<sub>0.6</sub>Ti<sub>0.4</sub> contained layers. The solid curves are obtained by fitting Eq. (1).

## 5.2 Theoretical fitting in term of Radovic's model

A microscopic theoretical model for the interpretation of experimental results with  $F/S$  trilayers has been proposed by Radović *et al.* The detail of theoretical model is presented in Chapter 4. The reduced  $T_C$  with decreasing  $d_S$  is associated with the pair-breaking effect within the single-mode approximation. In the framework of this model, the  $T_C$  is given by Eq. (4.8). The effective pair-breaking parameter,  $\rho^*(T)$  can be calculated in Eq. (4.12) by Usadel's equation for the pair amplitude  $F_S$  in the superconductor by making use of the boundary condition from Eqs 4.9 to 4.11. [5] This condition implies a high-quantum-mechanical transparency of the  $F/S$  interface. The diffusion coefficient  $D_F$  of Co can be estimated in terms of the low-temperature conductivity  $\sigma$  and the coefficient of the electronic specific heat  $\gamma$  from the Pippard relation [6]

$$v_F l = (\pi k_B / e^2)^2 (\sigma / \gamma). \quad (5.1)$$

For a single-Co film prepared at conditions identical to the Co layer in our layered structures, the low-temperature resistivity was determined to be  $\rho = 7 \times 10^{-8} \Omega \text{ cm}$ . Using  $\gamma = 4.73 \times 10^{-3} \text{ J/K}^2 \text{ mole}$  for Co [7] the diffusion coefficient is derived from  $D_F = 5 \text{ cm}^2/\text{s}$ . From the spin splitting energy  $2I_0 = 1.55 \text{ eV}$  [8], the penetration depth of the superconducting pairing function in Co is estimated to be  $\xi_F = 1.3 \text{ nm}$ .

The experimental results can be fitted well by equation (4.12) in terms of the Radovic's model shown as the solid curves in Fig. 5.1. We can extract a critical thickness  $d_{Nb}^{crit} = 30 \text{ nm}$  by extrapolating the fit to  $T_C = 0$ . The parameters for the calculation are  $T_C = 9.1 \text{ K}$ ,  $\xi_S = 16 \text{ nm}$ , and  $\varepsilon = 9.2$  ( $\eta = 0.01$ ). For comparison, the superconductor coherence length deduced from the temperature-dependent upper-critical field measurement  $H_{c2\perp}(T)$  is  $\xi_S = 12 \text{ nm}$ . [3] This value is smaller than

the fitted result from proximity effect and should be a result of pair breaking effect.

The bulk resistivities at 10 K measured on sputtered single film of  $\text{Nb}_{0.4}\text{Ti}_{0.6}$  and  $\text{Nb}_{0.6}\text{Ti}_{0.4}$  were  $40 \mu\Omega \text{ cm}$  and  $80 \mu\Omega \text{ cm}$ , respectively, with errors of about 10 %. The residual resistance ratios (RRR) were larger than 2 for Nb,  $\sim 1.25$  for  $\text{Nb}_{0.4}\text{Ti}_{0.6}$  and less than 1.06 for  $\text{Nb}_{0.6}\text{Ti}_{0.4}$  films, indicating the quality of our  $\text{Nb}_{0.6}\text{Ti}_{0.4}$  films is not as good as the others. The electron mean free paths estimated from these resistivities were 4.7 nm for pure Nb, 0.9 nm for  $\text{Nb}_{0.4}\text{Ti}_{0.6}$ , and 0.5 nm for  $\text{Nb}_{0.6}\text{Ti}_{0.4}$  with an assumption that the product  $\langle \rho l \rangle = 3.75 \times 10^{-6} \mu\Omega \text{ cm}^2$  remained unchanged. [9, 10] Moreover, the bulk  $\text{Nb}_x\text{Ti}_{1-x}$  have  $T_c = 8.8$  and 7.0 K for  $x = 0.4$  and 0.6, respectively. In the same strategy, the critical thickness for the case of Co/  $\text{Nb}_{40}\text{Ti}_{60}$ , and Co/ $\text{Nb}_{60}\text{Ti}_{40}$  trilayers are  $d_{\text{Nb}_{40}\text{Ti}_{60}}^{\text{crit}} \approx 20 \text{ nm}$  and  $d_{\text{Nb}_{60}\text{Ti}_{40}}^{\text{crit}} \approx 27 \text{ nm}$ , respectively, when deduced from fitted results, as the solid lines in the Fig. 5.1 (b) and (c) show. Here, the data are within the range of  $d_s^{\text{crit}} / \xi_s \geq 2$ ; this ensures the usage of the single-mode approximation, since higher-order modes are substantially short-range modes and strongly damped at  $d_s > \xi_s$ . [5]

We looked up the literature and found that the large resistivity and low  $T_C$  are most likely due to the structure variation as explaining following. Although the critical temperature peaks towards the niobium-rich side of the compositions, i.e. in the range 50-70 at.% Nb, The most widely used superconducting materials are based on Nb-Ti alloys with Ti contents ranging from 46-50 weight % Ti. These alloys of Nb and Ti have both high strength and ductility and can be processed to achieve high critical current densities that make them ideal candidates for magnet and applications. Nb-Ti based superconductors are commercially produced in long uniform lengths and cost significantly less to produce than other superconductors. [11] The main drawbacks of this material are a low critical temperature, typically requiring cooling

by liquid helium, and a low upper critical field which limits the applied field at which they can be used to below 12 T.

The variations of  $T_C$ ,  $\rho_n$  and the upper critical field  $H_{c2}$  as a function of alloy composition are plotted in Figure 5.2. The data were adapted from [11] and [12]. The critical temperature shows a mild variation between pure Nb (9.23 K) and Nb50Ti50 (8.5 K), with a weak peak at about Nb70Ti30 (9.8 K). Addition of Ti is more potent at reducing  $T_C$  for alloys with Ti content above 50 mass%. The critical temperature drops continuously over this range with increasing Ti content. The rate of resistivity increase is concave upward, tending towards the Mott localization limit ( $> 100 \mu\Omega$  cm) for more than 70 at%Ti. Thin-films were used to show that these trends continue for higher Ti content [13], where bulk samples are difficult to make, as shown in the Fig 5.3. Resistivity increases with increase in Ti content. The resistivity of the thin film is found to be larger than typical values found in the corresponding bulk alloy as much as  $20 \mu\Omega$  cm. Except near the endpoints (pure Nb or pure Ti) where higher resistivity ratios can be obtained, residual resistivity ratios of these alloys are close to 1. (see Fig. 5.3)

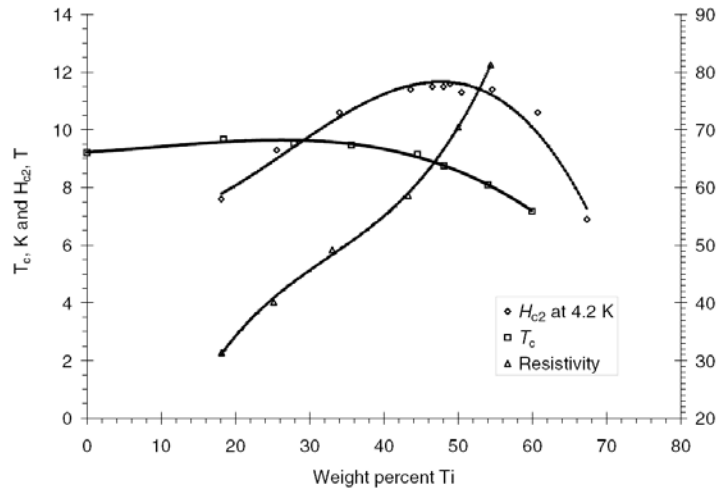


**Figure 5.2:** The variation in  $H_{c2}$  at 4.2 K,  $T_C$  and resistivity are plotted as a function of the mass fraction of Ti across the binary Nb-Ti alloy system.  $H_{c2}$  is defined as the linear extrapolation of the high field pinning force to zero. [11]

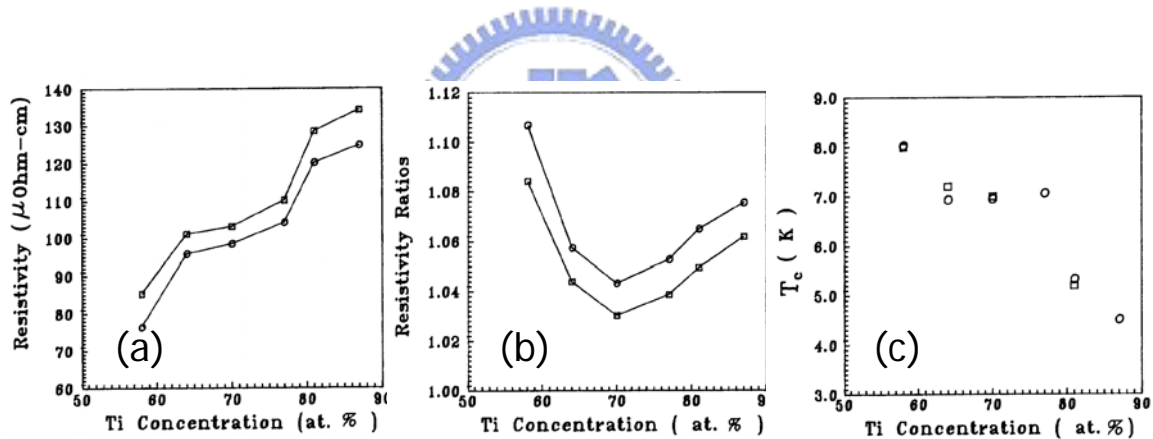


**Figure 5.3:** (a) Variation in resistivity as a function of Ti content in Nb-Ti films for 300 K and 10 K, respectively. (b) Variation in resistivity ratios with Ti content in Nb-Ti films for 300K/77K and 300K/10K, respectively. (c) Variation in  $T_C$  with Ti content in Nb-Ti films. [13]

The upper critical field at 4.2 K exhibits a broad dome-like curve in the range of 40 weight % Ti to 60 weight % Ti with a maximum of about 11.6 T at a composition of 44 weight % Ti. The peak results from a balance of the trends for the resistivity and critical temperature, where the zero-temperature value can be predicted by

$$\mu_0 H_{c2}(0) = 3.11 \times 10^3 \rho \gamma T_C. \quad (5.2)$$

The above equation is an extension of the Ginzburg–Landau theory [14]. The value of  $H_c$  is linked to  $T_C$  via the condensation energy of the superconducting state and the scattering value of  $\rho$ . Thus, the reason for this  $H_{c2}$  behavior is basically from the anomalous increase in the normal-state resistivity. This increase in  $\rho_n$  is more than compensating for the slight decrease in  $\gamma$ , the electronic specific heat coefficient, and  $T_C$ , resulting in an enhancement of the upper critical fields  $H_{c2}$  for Ti-rich alloys.

The atomic volume difference between Ti and Nb is only about 2 % resulting in a isomorphous system where the  $\beta$  phase has a body-centered cubic structure with a lattice parameter of approximately 0.3285 nm. An important property of the Nb-Ti phase diagram, shown in the Figure 5.4, is that the  $\beta$  phase starts to decompose only well below the melting temperature. [11] The  $\beta$  phase is favored at high temperature, and can be retained by quenching to room temperature. Many  $\beta$  alloys are good superconductors [15], as would be expected from the high transition temperatures of V, Nb and Ta. The other stable  $\alpha$  phase in this system is the titanium rich phase which has a low solubility and low-temperature hexagonal close-packed (HCP) structure. The low Nb content of the  $\alpha$ -Ti phase suggests that  $\alpha$ -Ti precipitates should have a low  $T_C$  (approaching the 0.39 K  $T_C$  of pure Ti) and should be non-superconducting under practical operating conditions. The alpha phase is only stable below 882 °C (at atmospheric pressure) and for the alloy composition range of interest Ti is only stable below 570 °C to 600 °C. In Figure 5.4 the widely used high temperature phase boundaries of Hansen *et al.* [16] are combined with the calculated low temperature boundaries of Kaufman *et al.* [17] modified by Moffat and Kattner [18] to provide a composite equilibrium phase diagram that generally reflects production experience. The competition between these phases and the incipient phase transition of a quenched  $\beta$  alloy to  $\alpha+\beta$  is the origin of many observed physical properties of Nb–Ti

alloy. Thus at room temperature and below, the standard alloy consists of metastable  $\beta$  phase and any phase transition is latent.

In the previous report, the resistivity increases with increasing in Ti content. In our system, even though the  $T_C$  decreases with increase resistivity following the expected tendency, the resistivity of  $\text{Nb}_{0.6}\text{Ti}_{0.4}$  is larger than  $\text{Nb}_{0.4}\text{Ti}_{0.6}$ . A. Main *et al.* reported that the incipient instability of the  $\beta$ -phase (bcc lattice) in the Ti rich composition region resulting in the dynamical fluctuation of the diffuse phase ( $\omega$ -phase) and leads to the anomalous increase in the resistivity. [13] In our system, this increase in the resistivity may be due to the stress developed in the film between substrate or ferromagnet layer which influenced the instability in the direction of relieving it in favor of a structural transformation. Another possibility is that the increase in resistivity is due to the small grain size of our polycrystalline films.

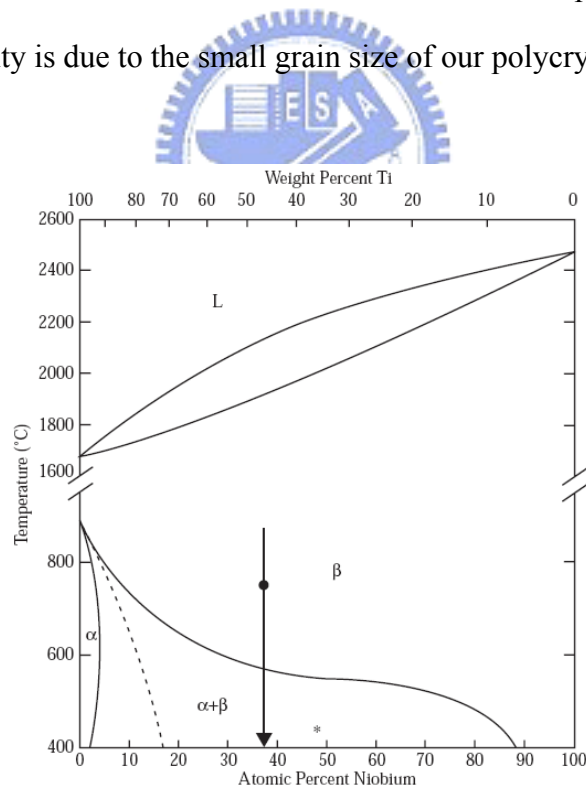


**Figure 5.4:** A hybrid equilibrium phase diagram for Nb-Ti combining the experimentally determined high temperature phase boundaries of Hansen et al [16] with the calculated low temperature phase boundaries of Kaufman and Bernstein [17] modified by Moffat and Kattner. [18] Also shown is the martensite transformation curve (Ms) of Moffat and Larbalestier. [19]



## 5.3 The behavior of upper critical field for Co/Nb

### multilayers

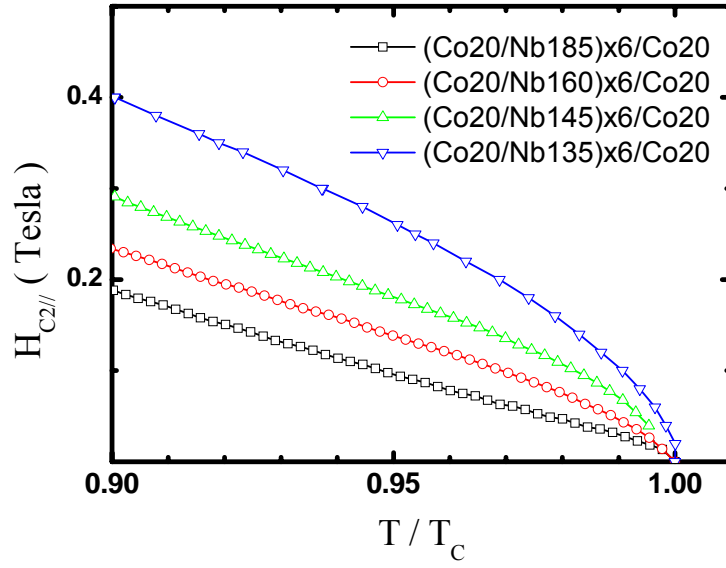
In the  $H_{c2}$  measurement, As the thickness of an S layer is reduced, the temperature dependence of  $H_{c2}$  changes from three-dimensional (3D) behavior to two-dimensional (2D) one. This dimensional crossover is due to the difference of anisotropic coherence lengths parallel and perpendicular to the film. From the Ginzburg-Landau (G-L) theory,  $H_{c2}$  for layered S/F structures can be written as

$$H_{c2\parallel}(T) = \frac{\phi_0}{2\pi} \frac{1}{\xi_{\parallel}(T)\xi_{\perp}(T)}, \quad H_{c2\perp}(T) = \frac{\phi_0}{2\pi} \frac{1}{\xi_{\parallel}^2(T)}, \quad (5.3)$$

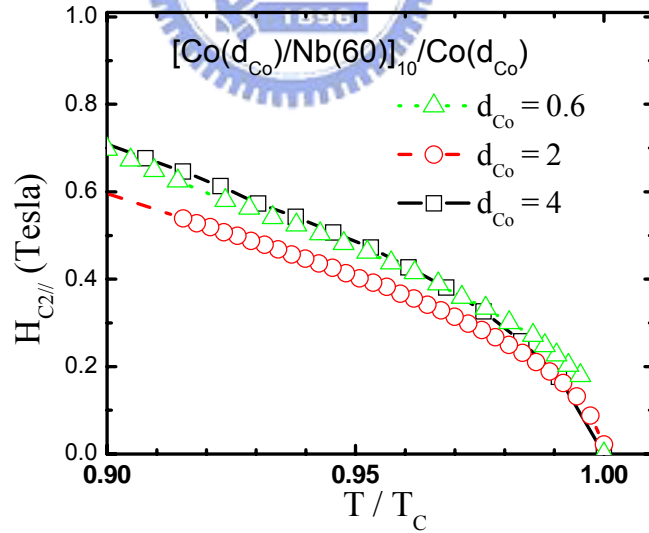
where  $H_{c2\parallel}$  and  $H_{c2\perp}$  are upper critical fields with applied field parallel and perpendicular to layer planes, respectively,  $\phi_0$  is the flux quantum, and  $\xi$ 's are G-L coherence lengths. Near  $T_C$ ,  $\xi(T)$  has  $(1-T/T_C)^{-1/2}$  temperature dependence and diverges at  $T_C$ . When the wavefunction of one S layer is restricted by the adjacent F layers, the maximum  $\xi_{\perp}(T)$  is limited by the layer thickness plus penetration depths into F layers and becomes constant near  $T_C$ . Thus, though for a 3D superconductor,  $H_{c2} \propto (1-T/T_C)$  for all field directions, for a 2D superconductor,  $H_{c2\parallel} \propto \sqrt{1-T/T_C}$ , and  $H_{c2\perp} \propto (1-T/T_C)$ . When the S layer thickness is reduced, the dependence of  $H_{c2\parallel}(T)$  on temperature changes from 3D to 2D, i.e., from a linear to some square-root dependence.

Figure 5.5 shows  $H_{c2\parallel}$  versus reduced temperature,  $T/T_C$ , for a series of  $[\text{Co}(d_{\text{Co}})/\text{Nb}(d_{\text{Nb}})]_N/\text{Co}(d_{\text{Co}})$  samples with fixed  $d_{\text{Co}} = 20\text{nm}$  and bilayer numbers  $N = 6$ . A clear separation between 2D and 3D behavior is not seen but only a gradual transition from 2D to 3D behaviors as  $d_{\text{Nb}}$  increases from 145 to 185 nm. All  $H_{c2\perp}$  versus temperature behaved linearly as expected.

When the Nb layer is in the 2D regime and the Co thickness is reduced, as shown in Figure 5.6, multilayers with  $d_{\text{Co}}$  as thin as 0.6 nm still shows 2D behavior. This indicates our nominal 0.6 nm Co is magnetically ordered and is capable of separating the S wavefunctions.



**Figure 5.5:** Upper critical field,  $H_{c2||}$ , versus reduced temperature for series of multilayers  $[\text{Co}(20\text{nm})/\text{Nb}(d_S)]_6/\text{Co}(20\text{nm})$ , with  $d_S = 135, 145, 160,$  and  $185$  nm.



**Figure 5.6:** Upper critical field,  $H_{c2||}$ , versus reduced temperature for series of multilayers  $[\text{Co}(d_F)/\text{Nb}(60)]_{10}/\text{Co}(d_F)$ , with  $d_F = 0.6, 2,$  and  $4$  nm.

Another criterion to determine the difference between 2D and 3D behaviors is

the dependence of upper critical field on the angle of external field to the surface. For a 3D, Josephson coupled superconductor, from the Lawrence-Doniach equation [20]

we have  $\left[ \frac{H_{c2}(\theta) \sin \theta}{H_{c2\perp}} \right]^2 + \left[ \frac{H_{c2}(\theta) \cos \theta}{H_{c2\parallel}} \right]^2 = 1$ . But for a 2D superconductor film,

Tinkham pointed out that, [21]  $\left| \frac{H_{c2}(\theta) \sin \theta}{H_{c2\perp}} \right| + \left[ \frac{H_{c2}(\theta) \cos \theta}{H_{c2\parallel}} \right]^2 = 1$ . From these two

equations, we can see that the slope of upper critical field versus field angle is continuous for 3D behavior, but discontinuous for 2D one around  $\theta=0$ . This has been observed in Nb/CuMn multilayers [22] and high  $T_C$   $\text{Bi}_2\text{Sr}_2\text{CaCu}_2\text{O}_8$  materials.[23]

The angular dependence of upper critical field was measured at 4 K for selected samples. The parallel upper critical field can change very sharply, with angle variation of less than 0.1 degree, when field is parallel to the layer plane. This also indicates the above-presented parallel upper critical field could very well be under-estimated. Figure 5.7 shows our results on  $H_{c2}$  versus angle. We found that samples all have a cusp shape when the thickness of Nb is less than 136 nm, with discontinuous slopes at  $\theta = 0$ . The bell shape, with continuous slope, applies to samples thicker than 160 nm. This agrees with the result from  $H_{c2}$  versus temperature behavior.

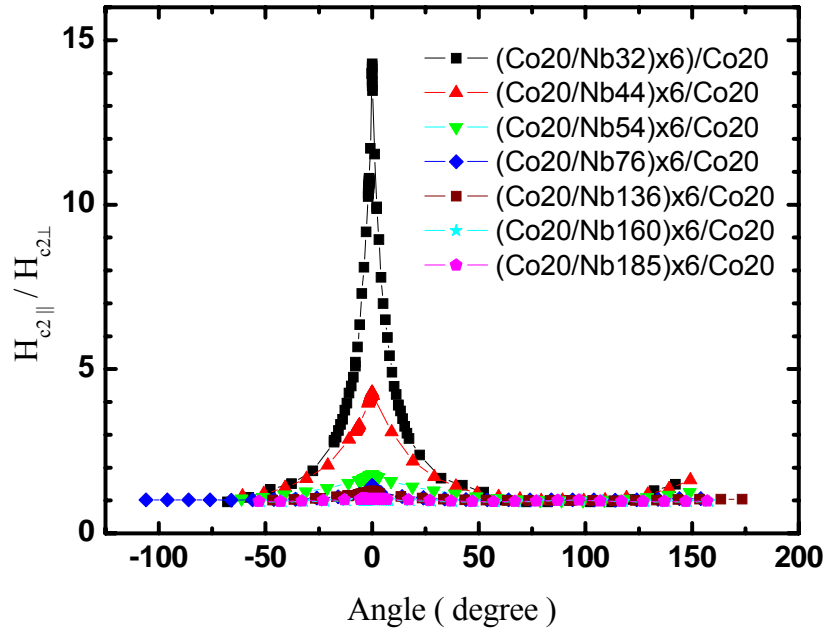


**Figure 5.7:** Angular dependence of upper critical field of a series of samples.

## 5.4 The result of CPP measurement for $\text{Co/Nb}_x\text{Ti}_{1-x}$ multilayers

The CPP resistance measurement in metallic multilayer thin films is known to give fundamental information of the transport properties. For the study of giant magnetoresistance (GMR), the CPP resistance was analyzed by two-channel series resistance model to quantitatively separate the interface and bulk contributions. [24, 25] In the  $F/S$  multilayers we studied here, the current in plane (CIP) standard four-point measurement always gave zero resistance unless the samples were driven to normal state by warming and applying magnetic fields or currents larger than the critical values. For the deposition, 99.99% pure Co and Nb were used as sources. The deposition rates for CPP sample were 0.7 nm/s for Co and 1.1 nm/s for Nb.

Simple planar multilayers were also made for magnetization measurements, which were performed at 10 K using a SQUID magnetometer. The resistivities at 10 K measured on thick Nb and Co films no less than 500 nm were 8 and 7  $\mu\Omega$  cm, respectively, with an error of around 10%. Figure 5.8 shows the hysteresis loop of a multilayer  $[\text{Co} (20)/\text{Nb} (30)/\text{Co} (2)/\text{Nb} (30)]_5/\text{Co} (20)$ , with all numbers in nm. When the direction of the external field was reversed, the 20 nm Co layers switched around 620 Oe and the magnetization changed roughly 12/13 of the total variation. Around  $\pm 250$  Oe, the 2 nm layers started to rotate and reached saturation. Thus, the magnetization rotation in different layers can be distinguished.

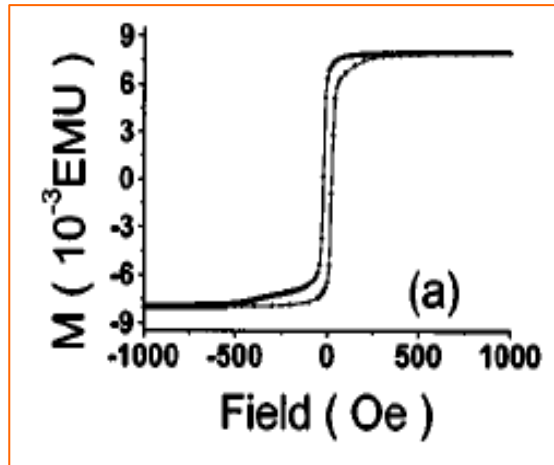


**Figure 5.8:** Hysteresis curves measured at 10 K of [Co (20)/Nb (30)/Co (2)/Nb (30)]<sub>5</sub>/Co (20) multilayers with all numbers in nm.

We fabricated similar samples [Co (20)/Nb (*t*)/Co (2)/Nb (*t*)]<sub>10</sub>/Co (20) for CPP magnetoresistance measurement. Figure 5.9 shows the CPP resistance versus the magnetic field of two similar samples of Fig. 5.8 with the Nb thickness fixed at 20 and 80 nm, respectively. There is no change in resistance within our experimental uncertainty of 0.1%.

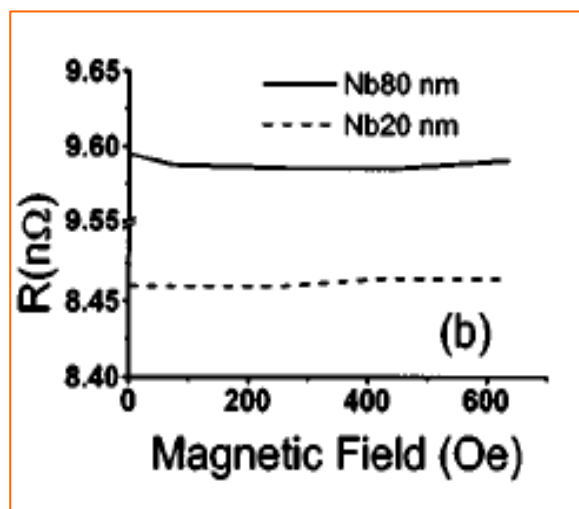


**Figure 5.9:** CPP resistance vs magnetic field of two samples [Co (20)/Nb (*t*)/Co (2)/Nb (*t*)]<sub>10</sub>/Co (20) with Nb thicknesses of 20 and 80 nm, respectively.

Our sputtered bulk Nb has a superconducting transition temperature of  $T_C = 9.2$  K. For thin Nb films,  $T_C$  decreases with a decrease in thickness due to finite size effect. When Nb films are sandwiched between Co, we found from our CIP results in Fig 5.1 that there is a critical thickness of 30 nm, below which no superconducting transition could be found. We make series of samples with the Nb thickness fixed at 20 and 80 nm. When the Nb thickness is 20 nm we have normal metal  $F/NM$  multilayers. When Nb is 80 nm, we have  $F/S$  multilayers.

Parkin reported antiferromagnetic coupling of Co through 0.9 nm of Nb, but no further coupling for larger thicknesses. [26, 27] Theory predicts that  $F$  could couple through  $S$  layers. However the conditions required are that coupling must exist when  $S$  is in its normal state and that the interface roughness must be small. [28] The large coherence length of Nb plus the proximity effect of Co makes the thickness required for Nb to be superconducting very large. Thus we do not expect any magnetoresistance when Nb is superconducting as the experimental result shown in Fig. 5.9. The absence of MR when Nb is normal indicates that the spin diffusion length is short in Nb. Park *et al.* [29] reported a  $25_{-5}^{\infty}$  nm of this length. Our result implies that it is even shorter in our samples. The absence of Giant magnetoresistance indicated that there was no spin memory across Nb layers. For Nb in  $NM$  state, bulk Nb was reported to have long spin diffusion length. Strong spin mixing was present at the Nb/Cu interface. [30] According to the fact, our results suggest that there is strong spin mixing at the Co/Nb interface. As the spin up and spin down electron channels cannot be distinguished from the electric transport, we shall apply a one-band model to describe our CPP data. For systematic analysis, a series of samples with Nb thicknesses fixed at 20 and 80 nm, Co fixed at 20 nm, and an increasing number of bilayers were made. We found the CPP resistance is linearly proportional to the

number of bilayers for both Nb thicknesses, as shown in Fig. 5.10. Linear least square fits to individual sets of data and a simultaneous global fit to both sets gave best-fit values of the coefficients to the equation  $AR_T=C_1+C_2N$ , listed in Table 5.1.

		$C_1$	$C_2$
Individual fit	Nb80	$6.9\pm 1.1$	$7.9\pm 0.2$
	Nb20	$0.6\pm 1.9$	$7.4\pm 0.3$
Global fit	Nb80	$7.7\pm 0.2$	$7.7\pm 0.2$
	Nb20		$6.5\pm 0.2$

**Table 5.1:** Linear least-square fits to the two sets of data in Figure 5.10. The fits are independent of the model.

#### 5.4.1 Two parameters Global Fit for Co/Nb multilayers

According to the one-band model, the linear behavior of  $AR$  vs  $N$  in Fig. 5.10 permits us to write

$$AR_T = 2AR_{Co/Nb(S)} + \rho_{Co}t_{Co} + N(\rho_{Co}t_{Co} + \rho_{Nb}t_{Nb} + 2AR_{Co/Nb(NM)}) \quad (5.4)$$

for normal Nb and

$$AR_T = 2AR_{Co/Nb(S)} + \rho_{Co}t_{Co} + N(\rho_{Co}t_{Co} + 2AR_{Co/Nb(S)}) \quad (5.5)$$

for superconducting Nb. Here  $R_T$  is the measured total resistance of multilayers,  $t$  the thickness,  $\rho$  the resistivity, and  $R_{Co/Nb(NM),(S)}$  the interface resistance between  $NM$  and  $S$  Nb, and Co layers. Here we assumed that all  $S/F$  and  $F/S$  interface resistance is identical, the same as for  $NM/F$  and  $F/NM$ , however we always write  $2AR$  for one pair of interfaces. Strictly speaking, the resistivity of Co can also be different when the Nb layer in the multilayer is  $NM$  or  $S$ , we do not consider this possibility here since we have  $S$  electrodes. For an individual fit to the data set of Nb=80 nm as shown the

dashed line in Fig 5.8, our model gives  $C_1=C_2=2AR_{\text{Co/Nb}(S)}+\rho_{\text{Co}}t_{\text{Co}}$ . From Table 5.1, we see  $C_1$  and  $C_2$  for this set are within mutual uncertainty. Another way to analyze this set of data according to our model is to plot  $AR_T$  vs  $N+1$  and force the best fit to go through the origin. The result of doing this is a slope of  $7.8\pm 0.1$  f $\Omega$  m<sup>2</sup>, again within the uncertainty of the above numbers. For Nb=20 nm, the intercept  $C_1$  should be the same as for Nb=80 nm. However, the  $N=1$  data point is clearly much lower than the expected linear behavior, resulting in  $C_1$  being too small and  $C_2$  too big. Since the two sets of data share the same parameter, we performed a global fit to all the data simultaneously which is presented as the solid lines in Figure 5.10. Using the bulk resistivities at 10 K for Co and normal Nb layers, we extracted  $2AR_{\text{Co/Nb}(NM)}=3.5\pm 0.7$  f $\Omega$  m<sup>2</sup> and  $2AR_{\text{Co/Nb}(S)}=6.3\pm 0.9$  f $\Omega$  m<sup>2</sup>. The latter value is within experimental error of that reported by the Michigan State University group.

[31]

In the case of  $F/S$  tunnel junction and point contact experiments, fitting the whole  $I-V$  (or  $dI/dV-V$ ) spectrum above and below the Fermi energy is important to determine the barrier strength  $Z$  and the polarization  $P$  of the  $F$  metal. In our CPP setup, the drop in voltage across the sample is at most 1 nV for a constant measuring current of 100 mA, six orders of magnitude smaller than the  $S$  Fermi energy of several mV. To drive the metallic contact CPP samples into normal state would require another experimental setup. Since all of our samples have been made *in situ* in a vacuum chamber, there is no barrier at the interfaces, that is, all our samples have  $Z$  close to zero. Although we cannot drive each individual  $S$  sample normal by high enough current density, we can do it by warming the sample or, as in the present study, we can compare different samples with various Nb thicknesses to get the  $F/S$  and  $F/NM$  unit area interface resistance. In the  $F/S$  point contact experiment, resistance is of the order 1–100  $\Omega$  and the contact area was estimated to have a diameter of 4–60



nm.[32] This corresponds to  $AR=1-3 \text{ f}\Omega \text{ m}^2$ , which agrees well with our values.

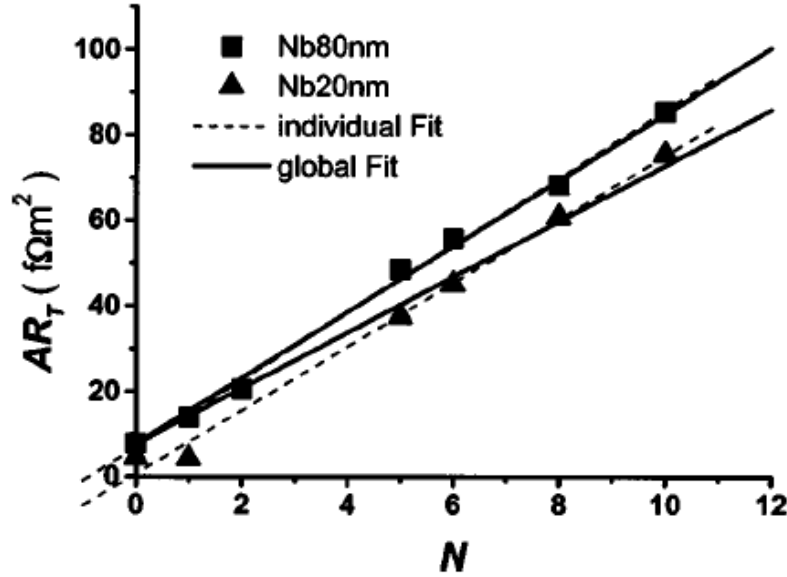


**Figure 5.10:** Unit area resistance,  $AR_T$  vs  $N$  number of bilayers for two sets of samples with Nb thicknesses fixed at 20 and 80 nm, respectively. The dashed lines are linear least-square fits to individual sets. The solid lines are global fits to two sets of data simultaneously.

The theoretical models used to explain metallic  $F/S$  point contacts results were based on the BTK model as described in Chapter 4. The BTK model solved the Bogoliubov equations for a  $NM/S$  interface in the ballistic regime. It was modified for the  $F/S$  interface by dividing the current into polarized and unpolarized parts. [32, 33] For our large area CPP case, a diffusive regime model should be applicable. From the relation [34]

$$(R_{F/S}R_{F/NM})/R_{F/NM} = P^2/(1-P^2) \quad (5.6)$$

for the diffusive regime in the  $F$  layer and infinite thick  $S$  layer, we deduced  $P=(66\pm 12)\%$  for Co. This is large compared to most values found in tunnel junction and point contact experiments ( $<45\%$ ). We suggest that normal conductance at high

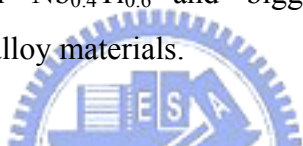
bias in those cases involves all states above the Fermi energy. This would enhance the weight of the unpolarized part of the current, thus reducing the  $P$  derived.

Unlike spin-resolved photoemission, which measures the  $P$  of the electronic density of states (DOS), our measurements determine transport  $P$ . As in the tunnel junction and point contact cases,  $P$  derived this way is related to the weighted average of the DOS, and is not sensitive to the sign of intrinsic polarization. In our analysis, the use of bulk resistivities of Nb and Co to obtain the interface resistance is not justified. More data that include various Nb and Co thicknesses are needed to treat the resistivities as fitting parameters as well, which is presented in the next section.

#### 5.4.2 Two parameters Global Fit for Co/Nb<sub>0.4</sub>Ti<sub>0.6</sub> and Co/Nb<sub>0.6</sub>Ti<sub>0.4</sub> multilayers

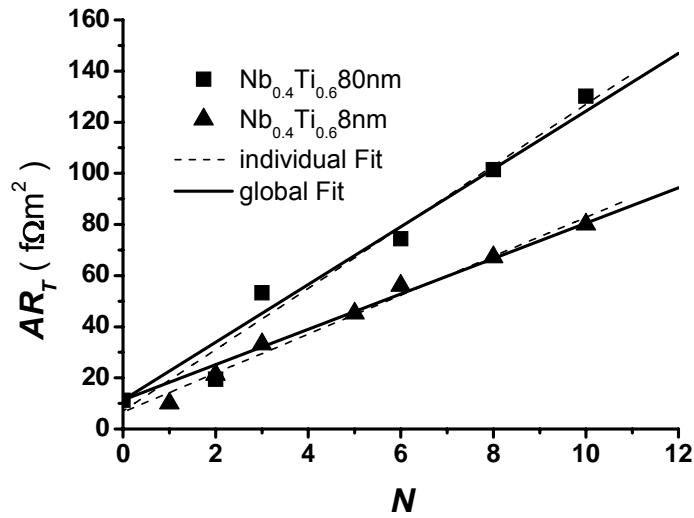
In the Co/Nb<sub>0.4</sub>Ti<sub>0.6</sub> multilayers, the Nb<sub>0.4</sub>Ti<sub>0.6</sub> normal layer thickness was chosen 8 nm and superconducting thickness was 80 nm. The CPP resistance was also linearly proportional to the number of bilayers. Plots of the product of sample area  $A$  and total resistance  $R$  against bilayer number  $N$  are given in Fig. 5.10 for Co/ Nb<sub>0.4</sub>Ti<sub>0.6</sub> multilayers. The dash lines in Fig. 5.11 are least-squares fits to each set of data. According to a one-band model, the linear behavior of  $AR$  against  $N$  are described by Eqs. (5.4) and (5.5) with  $R_{F/S(NM),(S)}$ 's represent the interface resistances between Co and Nb<sub>(x)</sub>Ti<sub>(1-x)</sub> layers for normal and superconducting states, respectively. For an individual fit to the data set of Nb<sub>0.4</sub>Ti<sub>0.6</sub>=80 nm, we can write  $AR_T = C_1 + C_2N$  with  $C_1 = C_2 = 2AR_{Co/Nb_{0.4}Ti_{0.6}(S)} + \rho_{Co}t_{Co}$ . In Table 5.2, we also see the value of  $C_1$  and  $C_2$  are within mutual uncertainties. Because of the two sets of data share the same parameter, we can perform a global fit to all data simultaneously. This gives  $C_1 = C_2 = 11.3 \pm 1.3 f\Omega m^2$  for Nb<sub>0.4</sub>Ti<sub>0.6</sub>=80 nm,  $C_1 = 11.3 \pm 1.3 f\Omega m^2$  and  $C_2 = 6.9 \pm 0.6 f\Omega m^2$  for Nb<sub>0.4</sub>Ti<sub>0.6</sub>=8 nm. Used the bulk resistivities at 10 K for Co and normal Nb<sub>0.4</sub>Ti<sub>0.6</sub> layers, we extracted  $2AR_{Co/Nb_{0.4}Ti_{0.6}(S)} = 9.9 \pm 1.3 f\Omega m^2$  and  $2AR_{Co/Nb_{0.4}Ti_{0.6}(NM)} = 2.3 \pm 0.8 f\Omega m^2$ .

Figure 5.11 shows a plot of  $AR_T$  versus  $N$  for  $Nb_{0.6}Ti_{0.4}$ . The  $Nb_{0.6}Ti_{0.4}$  normal layer thickness was chosen 15 nm and superconducting thickness was 80 nm according to the phase diagram in Fig. 5.1 (c). The linear behavior also permitted us to use the above equations. The  $S$  electrodes in these sets were pure Nb because it had higher  $T_C$ . The lines of individual fit intercept the ordinate axes at non-zero values, which represent the Co/Nb interface resistance plus  $\rho_{Co}t_{Co}$ . But in Table 5.2, we see  $C_1$  from  $Nb_{0.6}Ti_{0.4}=15$  nm and from  $Nb_{0.6}Ti_{0.4}=80$  nm individual fits are different. To get the quantitative analysis, we also performed a global fit to both sets of data simultaneously. When we put in the bulk resistivities at 10 K for normal  $Nb_{0.6}Ti_{0.4}$  layers and the Co/Nb interface resistance we have presented, the best value for  $2AR_{Co/Nb_{0.6}Ti_{0.4}(S)}$  is  $22.6 \pm 1.7 f\Omega m^2$  and for  $2AR_{Co/Nb_{0.6}Ti_{0.4}(NM)}$  is  $5.6 \pm 1.5 f\Omega m^2$  derived from the fit. When superconducting layer was composed of alternating 0.5 nm thick layers of Nb and Ti,  $2AR_{Co/NbTi} = 12.4 \pm 0.7 f\Omega m^2$  was reported in the literature. [35] We have smaller value in  $Nb_{0.4}Ti_{0.6}$  and bigger value in  $Nb_{0.6}Ti_{0.4}$  when superconductor layer is NbTi alloy materials.



	Individual fit				Global fit			
	$Nb_{40}Ti_{60}$		$Nb_{60}Ti_{40}$		$Nb_{40}Ti_{60}$		$Nb_{60}Ti_{40}$	
	80 nm	8 nm	80 nm	15 nm	80 nm	8 nm	80 nm	15 nm
$C_1$	$7.0 \pm 1.4$	$6.6 \pm 0.5$	$13.8 \pm 1.7$	$6.4 \pm 1.1$	$11.3 \pm 1.3$		$7.7 \pm 0.6$	
$C_2$	$12 \pm 1.0$	$7.6 \pm 0.4$	$22.9 \pm 1.4$	$19.6 \pm 0.6$	$11.3 \pm 1.3$	$6.9 \pm 0.6$	$24 \pm 1.7$	$19 \pm 0.9$

**Table 5.2:** Linear least-square fits to the two sets of data in Figure 5.11 and Figure 5.12. The fits are independent of the model.



**Figure 5.11:** Unit area resistance,  $AR_T$  versus bilayer number  $N$  of two sets of samples with  $Nb_{0.4}Ti_{0.6}$  thicknesses fixed at 8nm and 80nm, respectively. The dashed lines are linear least square fits to individual sets. Solid lines are global fit to two sets of data simultaneously.

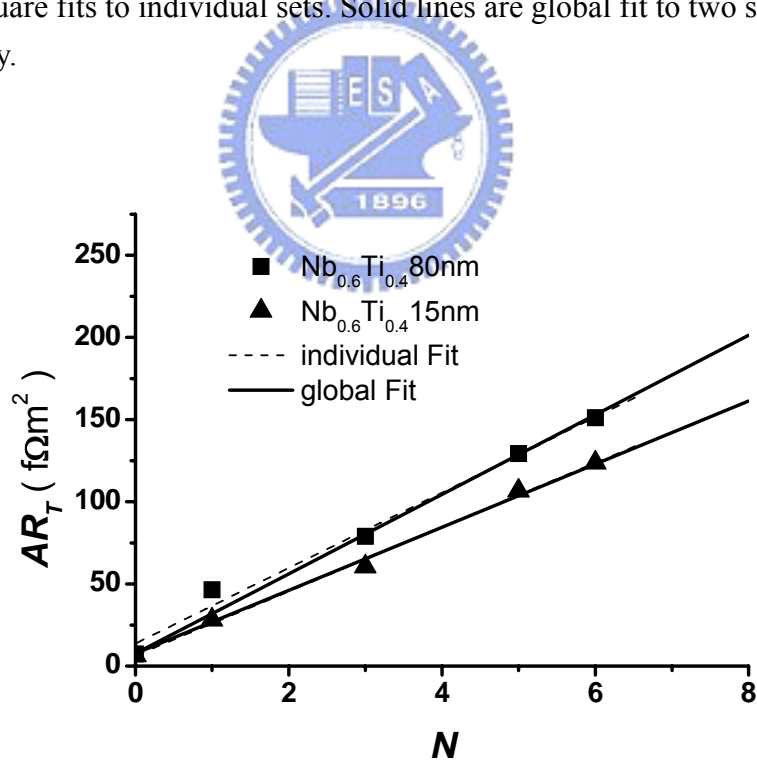


**Figure 5.12:** Unit area resistance,  $AR_T$  versus bilayer number  $N$  of two sets of samples with  $Nb_{0.6}Ti_{0.4}$  thicknesses fixed at 15nm and 80nm, respectively. The dashed lines are linear least square fits to individual sets. Solid lines are global fit to two sets of data simultaneously.

### 5.4.3 Four parameters Global Fit for Co/Nb multilayers

In the analysis of section 5.3.1, the use of bulk resistivities of Nb and Co to obtain the interface resistance may cause the deviation of interface resistance. More data that include various Nb and Co thicknesses are needed to treat the resistivities as fitting parameters. In this section, we report a more appropriate model for the  $F/S$  multilayer case. The thicknesses were chosen by the phase diagram of Fig. 5.1. Below the  $d_{\text{Nb}}^{\text{crit}}$ , no superconducting transition was found down to 1.8 K.

Two more series of CPP samples were made for each  $S$  material. We use  $t$  to indicate that the thickness is fixed in the series of samples and  $d$  when the thickness is varied. For Nb, the total four series are:

1. Co(20)/[Nb(20)/Co(20)] $_N$  with  $t_{\text{Nb}}$  fixed at 20 nm ( $< d_{\text{Nb}}^{\text{crit}}$ ) for normal state,  $t_{\text{Co}}$  fixed at 20 nm, and the numbers of bilayers were varied;
2. Co(20)/[Nb(80)/Co(20)] $_N$  with  $t_{\text{Nb}}$  fixed at 80 nm ( $> d_{\text{Nb}}^{\text{crit}}$ ) for superconducting state,  $t_{\text{Co}}$  fixed at 20 nm, and the numbers of bilayers were varied;
3. Co( $d_{\text{Co}}$ )/[Nb(20)/Co( $d_{\text{Co}}$ )] $_6$  with  $t_{\text{Nb}}$  fixed at 20 nm, 6 bilayers, and varying Co thickness;
4. Co(20)/[Nb( $d_{\text{Nb}}$ )/Co(20)] $_6$  with  $t_{\text{Co}}$  fixed at 20 nm, 6 bilayers, and varying Nb thickness but smaller than  $d_{\text{Nb}}^{\text{crit}}$ .

The first and second series have been discussed in Section 5.4.1. Each series of samples can be individually fitted with the model as the first way of analyzing our data. But results for the same quantity from different series are different. The second way is that we can apply the bulk resistivities of Nb and Co at 10 K to derive the two interface resistances as parameters from all series, as in section 5.4.1 of two parameters Global Fit. The third way is that we treat all resistivities and the interface resistances as fitting parameters to perform four-parameter global fit.

Figure 5.10 (a) presents the plots of  $AR_T$  against bilayer number  $N$  for the first two series of samples.  $AR_T$  is linearly proportional to the number of bilayer for Nb both in normal and superconducting states. We can write out Eq. (5.4) and Eq. (5.5) explicitly

to a general form for such linear behavior as

$$AR_T = 2AR_{F/S(S)} + \rho_F t_F + N(\rho_F t_F + \rho_S t_S + 2AR_{F/S(NM)}) \quad (5.7)$$

for normal Nb and

$$AR_T = 2AR_{F/S(S)} + \rho_F t_F + N(\rho_F t_F + 2AR_{F/S(S)}) \quad (5.8)$$

for superconducting Nb. Here  $R_T$  is the measured total resistance of multilayers,  $t$ 's are the thicknesses,  $\rho$ 's are the resistivities, and  $AR_{F/S(NM),(S)}$ 's are the interface resistances between normal state Nb and Co layers; and superconducting state Nb and Co layers, respectively. Since there is a mutual deviation using the individual fits, we add two series of samples and then examine whether we can perform global fitting procedure without using bulk resistivities.

Figure 5.13 (b) and (c) show the  $AR_T$  behavior of the Co/Nb multilayers as functions of Co and Nb thickness, respectively, with  $d_{Nb}$  smaller than  $d_{Nb}^{crit}$  and  $N=6$ . The dash lines show the individual fit results. The CPP resistance is linearly proportional to the thickness for both varied Co and Nb thickness ranges. With the one-band model, the linear behavior of  $AR_T$  versus thickness can be explicitly written as

$$AR_T = 2AR_{F/S(S)} + 12AR_{F/S(NM)} + 6\rho_S t_S + 7\rho_F d_F, \quad (5.9)$$

for varying Co thickness ( $d_F$ ) with Nb thickness fixed at 20 nm and

$$AR_T = 2AR_{F/S(S)} + 12AR_{F/S(NM)} + 6\rho_S d_S + 7\rho_F t_F, \quad (5.10)$$

for varying Nb thickness ( $d_{Nb}$ ) with Co thickness fixed at 20 nm. The individual linear least square fits of  $AR_T$  versus  $d_{Co}$  and  $d_{Nb}$  samples yield a slope  $\rho_{Co}$  of  $5.4 \pm 0.4 \mu\Omega \text{ cm}$  and the other slope  $\rho_{Nb}$  of  $17 \pm 2 \mu\Omega \text{ cm}$ , respectively. If we calculate interface resistance by putting the best fit values of resistivities from the slopes into Eq (5.9) and Eq (5.10), we find  $AR_{Co/Nb(S)} = 5.8 \pm 1.3 \text{ f}\Omega \text{ m}^2$  and  $AR_{Co/Nb(NM)} = 3.4 \pm 1.2 \text{ f}\Omega \text{ m}^2$  differing from the previously calculated values using bulk resistivities of Nb and Co. Therefore, we perform a four-parameter global fit to all the data simultaneously. The four parameters are  $2AR_{Co/Nb(S)}$ ,  $2AR_{Co/Nb(NM)}$ ,  $\rho_{Nb}$ , and  $\rho_{Co}$ . Accordingly, we can rewrite

Eq. (5.7) as  $AR_T = g_1 + Ng_2 + (N+1)t_{Co}g_3 + Nt_{Nb}g_4,$

Eq. (5.8) as  $AR_T = (N+1)g_1 + (N+1)t_{Co}g_3,$

Eq. (5.9) as  $AR_T = g_1 + 6g_2 + 7d_{Co}g_3 + 6t_{Nb}g_4,$

and

$$\text{Eq (5.10) as } AR_T = g_1 + 6g_2 + 7t_{Co}g_3 + 6d_{Nb}g_4.$$

Here  $g_1$  is  $2AR_{Co/Nb(S)}$ ,  $g_2$  is  $2AR_{Co/Nb(NM)}$ ,  $g_3$  is  $\rho_{Co}$ , and  $g_4$  is  $\rho_{Nb}$ . The solid lines in Fig. 5.13 (a), (b), and (c) are global fits for four parameters to all the data simultaneously. We list the best fit values in Table 5.3. The interface resistance  $2AR_{Co/Nb} = 6.7 \pm 0.3 f\Omega m^2$  for pure Nb in superconducting state is within the mutual experimental error of that reported by the Michigan State University group. [35]

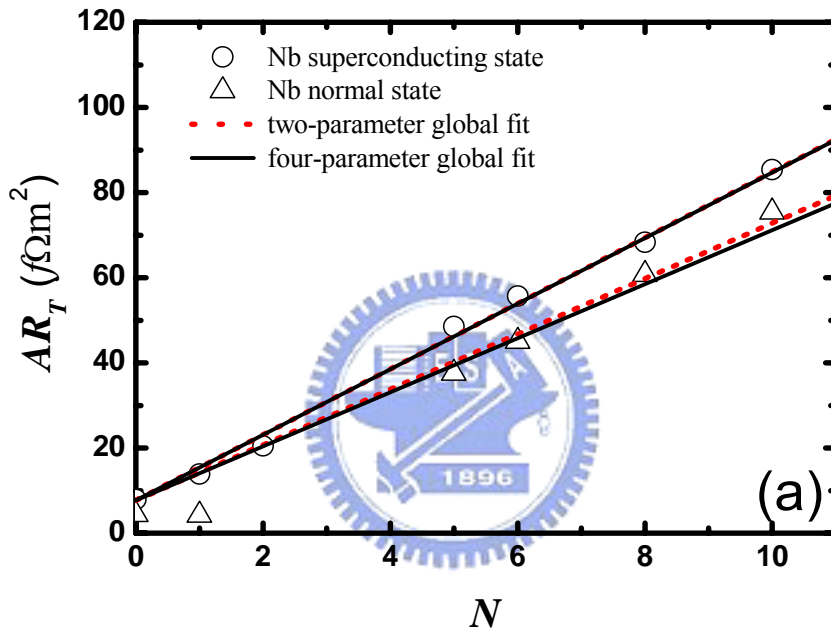


**Figure 5.13:** (a) Specific resistance  $AR_T$  vs bilayers number  $N$  of two sets of samples with Nb thicknesses fixed at 15 and 80 nm, respectively. The dot lines and solid lines are global fit for two and four parameters, respectively.

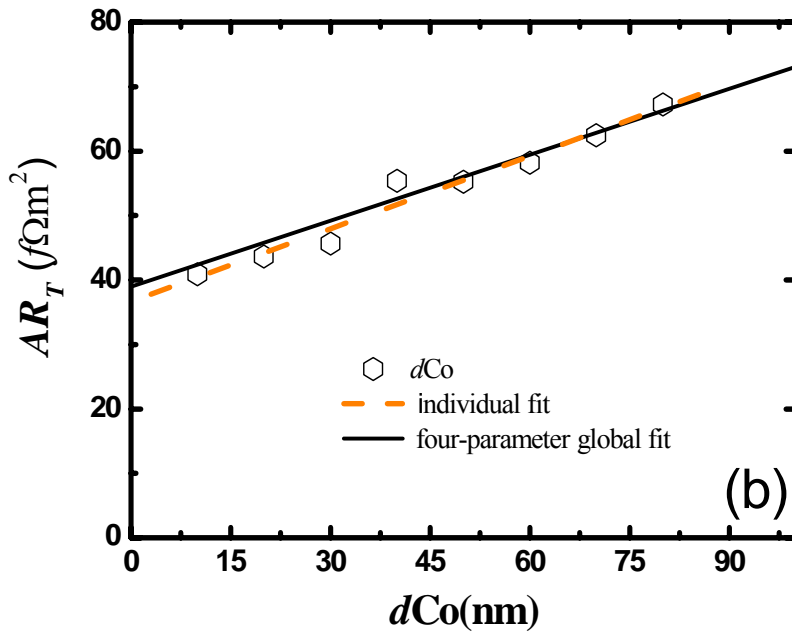


**Figure 5.13:** (b) Specific resistance  $AR_T$  vs Co thickness with Nb thickness fixed at 15 nm and  $N = 6$ . The dot lines and solid lines are global fit for four parameters.

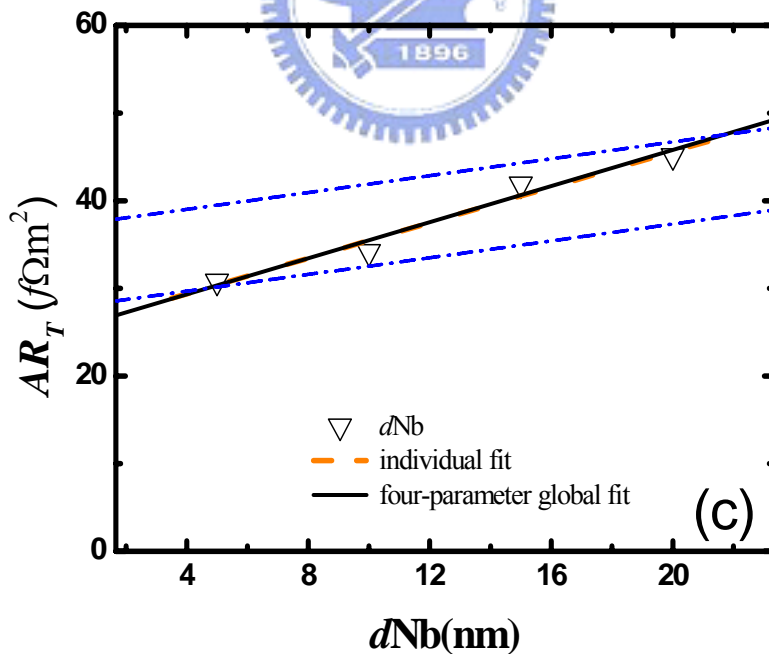


**Figure 5.13:** (c) Specific resistance  $AR_T$  vs Nb thickness with Co thickness fixed at 20 nm and  $N = 6$ . The dot lines are linear least squares fit to individual sets. The solid lines are global fit for four parameters to the data simultaneously. The dot-dashed lines used the bulk CIP resistivities as the slope and the two interface resistances from two- and four-parameter fits as upper and lower limits, respectively.



## 5.5. The result of CPP measurement for Co/Nb<sub>0.4</sub>Ti<sub>0.6</sub> and Co/Nb<sub>0.6</sub>Ti<sub>0.4</sub> multilayers with four parameter Global Fit and comparison

In comparison to the Co/Nb system, we also fabricated several series of Co/Nb<sub>0.6</sub>Ti<sub>0.4</sub>, and Co/Nb<sub>0.4</sub>Ti<sub>0.6</sub> CPP multilayer samples. For the deposition, 99.99% pure Co and Nb<sub>0.6</sub>Ti<sub>0.4</sub>, and 99.97% Nb<sub>0.4</sub>Ti<sub>0.6</sub> alloy targets were used as sources. The deposition rates for CPP samples were 0.7 nm/s for Co, 1.1 nm/s for Nb<sub>0.6</sub>Ti<sub>0.4</sub>, and 1.0nm/s for Nb<sub>0.4</sub>Ti<sub>0.6</sub>, respectively. The linear behavior of CPP resistance is reproduced when we use either Nb<sub>0.4</sub>Ti<sub>0.6</sub> or Nb<sub>0.6</sub>Ti<sub>0.4</sub> as a superconducting metal with  $t_{\text{Co}} = 20$  nm. When Nb<sub>x</sub>Ti<sub>1-x</sub> films were sandwiched between Co, we deduced  $d_{\text{Nb}_{0.4}\text{Ti}_{0.6}}^{\text{crit}} \approx 20$  nm and  $d_{\text{Nb}_{0.6}\text{Ti}_{0.4}}^{\text{crit}} \approx 27$  nm from fitting the  $T_c$  versus  $S$  thickness data according to the Radovic's model in the Figs. 5.1 (b) and (c). Detailed analysis has been presented in Section 5.1. We varied the Co and Nb<sub>0.4</sub>Ti<sub>0.6</sub> thickness while the numbers of bilayers were fixed at 6 to treat CPP resistivities as fitting parameters to all data. These parameters, as shown in Table 5.3, yielding the solid lines in Figure 5.14(a), (b), and (c) provide a satisfactory prediction in comparison with experimental data.

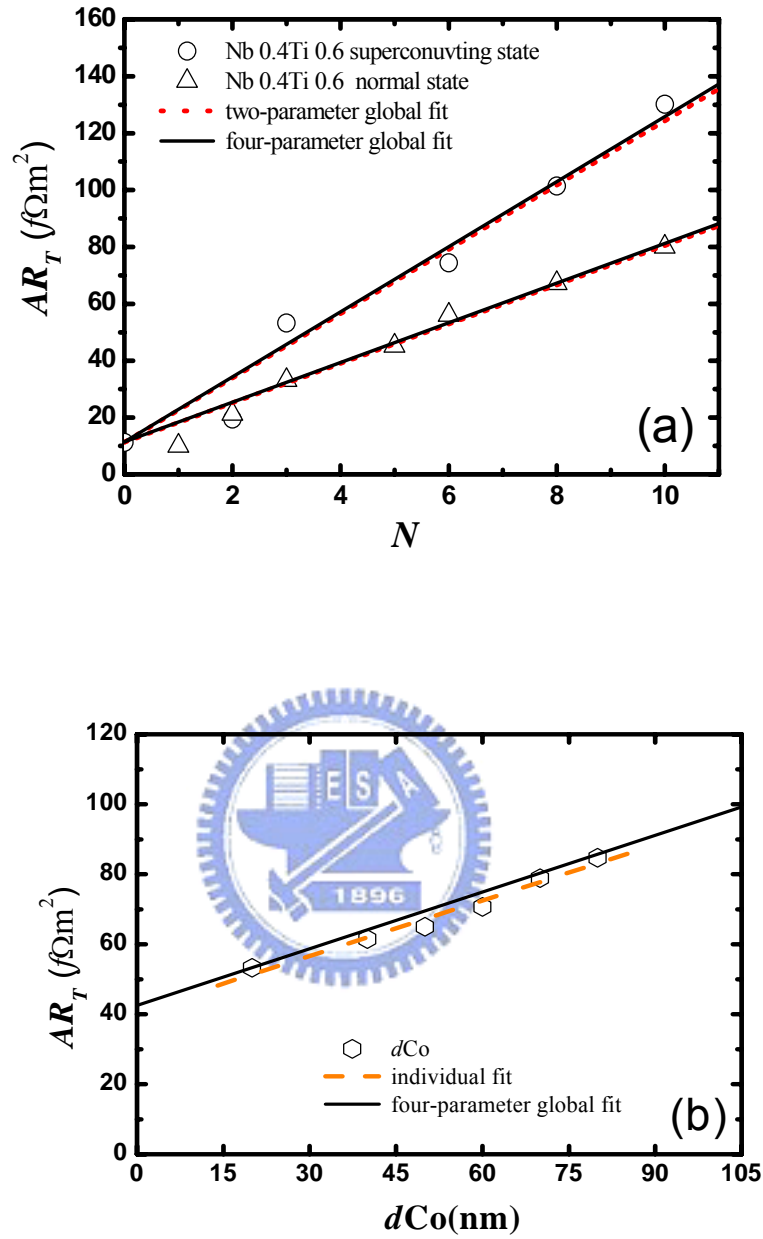


**Figure 5.14:** Data for Co/Nb<sub>0.4</sub>Ti<sub>0.6</sub> multilayers. (a) Unit area resistance,  $AR_T$ , plotted against bilayer number  $N$  of two sets of samples with Nb<sub>0.4</sub>Ti<sub>0.6</sub> thickness fixed at 8 nm and 80 nm, respectively. The dot lines are fits for two parameters. (b)  $AR_T$  versus Co thickness with Nb<sub>0.4</sub>Ti<sub>0.6</sub> thickness fixed at 8 nm and  $N = 6$ . The dashed lines are linear least square fits to individual sets. The solid lines in (a) and (b) are global fits for four parameters to the data simultaneously.

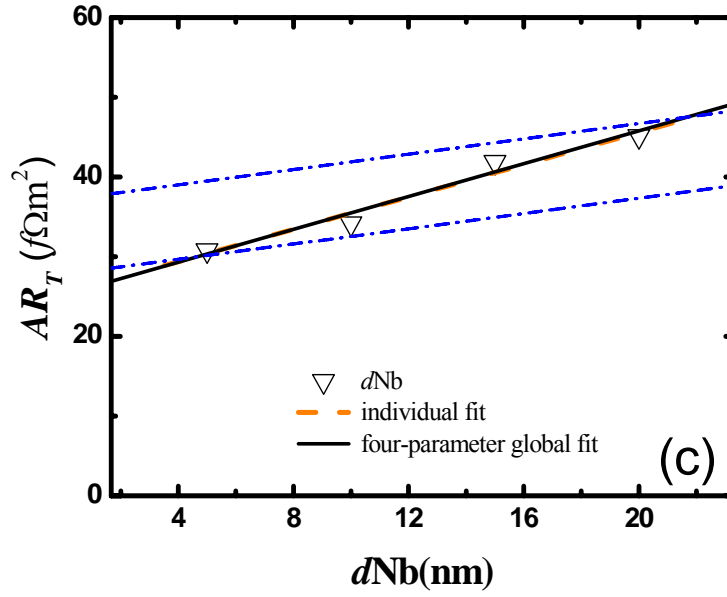


**Figure 5.14:** (c)  $AR_T$  versus  $Nb_{0.4}Ti_{0.6}$  thickness with Co thickness fixed at 20 nm and  $N = 6$ . The dashed lines are linear least square fits to individual sets. The dot-dashed lines used the bulk CIP resistivities as the slope and the two interface resistances from two- and four-parameter fits as upper and lower limits, respectively. The solid lines in (c) are global fits for four parameters to the data simultaneously.

For the  $Co/Nb_{0.6}Ti_{0.4}$  multilayers case, we got the interface resistances of  $Co/Nb_{0.6}Ti_{0.4}$  in normal state and in superconducting state, as well as the CPP resistivities of Co and of  $Nb_{0.6}Ti_{0.4}$  again from two-parameter fit and four-parameter global fit. The best results of the calculations are shown as dotted lines for the two-parameter fit in Fig. 5.15 (a), as dashed lines for individual fits for (b) and (c), and as solid lines for the four-parameter global fits. These parameters are summarized in Table 5.3 and the analysis of data will be discussed later. The interface resistance  $2AR_{F/S(S)} = 12.4 \pm 0.7 \text{ f}\Omega \text{ m}^2$  for  $Co/Nb_{0.5}Ti_{0.5}$  in superconducting state was reported by the Michigan State University group with resistivity  $\sim 57 \mu\Omega \text{ cm}$ . [31] Our results scale with their numbers well.

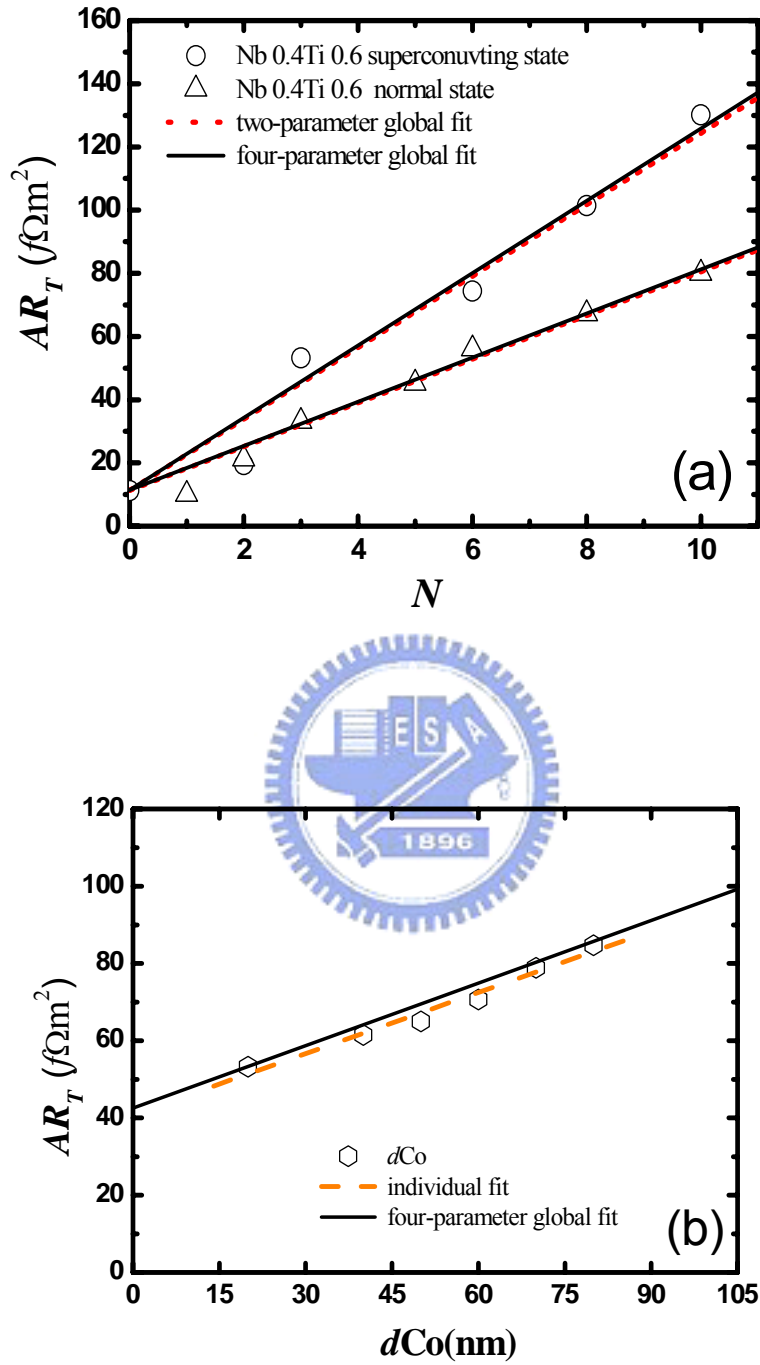


**Figure 5.15:** Data for Co/Nb<sub>0.6</sub>Ti<sub>0.4</sub> multilayers. (a) Unit area resistance,  $AR_T$ , plotted against bilayer number  $N$  of two sets of samples with Nb<sub>0.6</sub>Ti<sub>0.4</sub> thickness fixed at 15 nm and 80 nm, respectively. The dot lines are fits for two parameters. (b)  $AR_T$  versus Co thickness with Nb<sub>0.6</sub>Ti<sub>0.4</sub> thickness fixed at 15 nm and  $N = 6$ . The solid lines in (a) and (b) are global fits for four parameters to the data simultaneously.

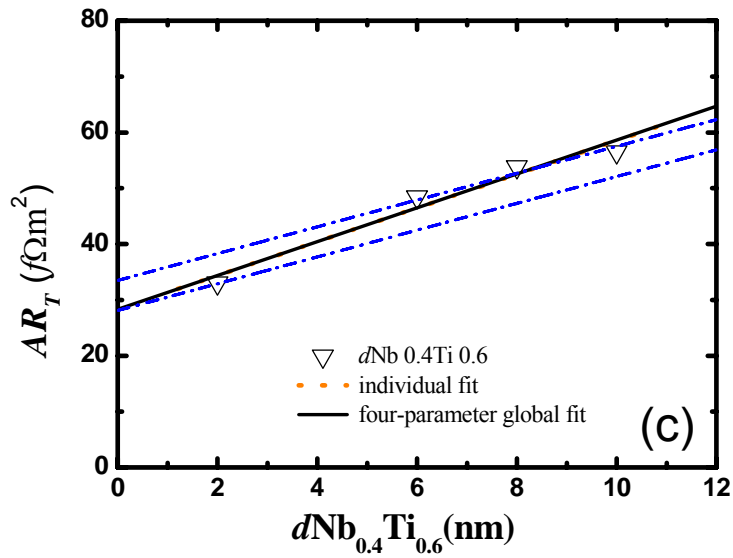


**Figure 5.15:** (c)  $AR_T$  versus  $\text{Nb}_{0.6}\text{Ti}_{0.4}$  thickness with Co thickness fixed at 20 nm and  $N = 6$ . The dashed lines are linear least square fits to individual sets. The dot-dashed lines used the bulk CIP resistivities as the slope and the two interface resistances from two- and four-parameters fits as upper and lower limits, respectively. The solid lines in (c) are global fits for four parameters to the data simultaneously.

Co/Nb multilayer				
	$\rho_{\text{Co}} (\mu\Omega \text{ cm})$	$\rho_{\text{Nb}} (\mu\Omega \text{ cm})$	$2AR_S (\text{f}\Omega \text{ m}^2)$	$2AR_{NM} (\text{f}\Omega \text{ m}^2)$
Two parameter	7 <sup>a</sup>	8 <sup>a</sup>	6.3±0.9	3.5±0.7
Four parameter	4.9±0.6	17±2	6.7±0.3	1.9±0.5
Co/Nb <sub>0.4</sub> Ti <sub>0.6</sub> multilayer				
	$\rho_{\text{Co}} (\mu\Omega \text{ cm})$	$\rho_{\text{Nb}_{0.4}\text{Ti}_{0.6}} (\mu\Omega \text{ cm})$	$2AR_S (\text{f}\Omega \text{ m}^2)$	$2AR_{NM} (\text{f}\Omega \text{ m}^2)$
Two parameter	7 <sup>a</sup>	40 <sup>a</sup>	9.9±0.7	2.3±1.9
Four parameter	7.2±0.4	50±6	9.9±0.2	1.4±0.5
Co/Nb <sub>0.6</sub> Ti <sub>0.4</sub> multilayer				
	$\rho_{\text{Co}} (\mu\Omega \text{ cm})$	$\rho_{\text{Nb}_{0.6}\text{Ti}_{0.4}} (\mu\Omega \text{ cm})$	$2AR_S (\text{f}\Omega \text{ m}^2)$	$2AR_{NM} (\text{f}\Omega \text{ m}^2)$
Two parameter	7 <sup>a</sup>	80 <sup>a</sup>	22.6±1.7	5.6±1.5
Four parameter	6.5±0.6	102±7	22.9±0.2	2.1±0.7

<sup>a</sup>Bulk values measured in 500 nm thick films.

**Table 5.3:** The derived values and parameters of different fitting procedures for the Co/Nb<sub>x</sub>Ti<sub>1-x</sub> multilayers with x=1, 0.6, and 0.4.

In order to compare the interface and the bulk properties in the multilayers, we examine in the following two quantities, which are found in the literature as useful indicators. The relative contributions to CPP resistance can be found in the ratio between the interface resistance  $R_{F/NM}$  and the bulk resistance in  $F$  within a spin-flip length  $l_{sf}^F$  or mean free path  $l$ . For 3d metals, the mean free path  $l$  is about 10 times shorter than the spin-flip length  $l_{sf}^F$  at low temperature. [36, 37] To estimate the contribution of bulk resistance of the ferromagnet within its spin-active part, we choose  $l_{sf}^F$  instead of  $l$ . Thus, the quantity we are interested in is

$$\frac{R_{F/NM}}{R_{sf}^F} = \frac{AR_{F/S(NM)}}{\rho_{\text{Co}} l_{sf}^F}$$

as described in the theoretical work of Ref. [38]. The interface

resistance  $AR_{F/S(NM)}$  from our four-parameter fits are used in the following analysis.

The spin-diffusion length was reported in Ref. [37] for electrodeposited Co  $l_{sf}^F = 59 \pm$

18 nm at 77 K. The spin-diffusion length is an extrinsic quantity. It depends on the elastic mean free path and the spin flip length. The spin diffusion length should be larger in our case because our Co film has smaller resistivity and the measuring temperature was 4.2 K. Thus, we can calculate the upper limits  $R_{F/NM}/R_{sf}^F \approx 0.2$  for Nb/Co,  $R_{F/NM}/R_{sf}^F \approx 0.2$  for Nb<sub>0.6</sub>Ti<sub>0.4</sub>/Co, and  $R_{F/NM}/R_{sf}^F \approx 0.1$  for Nb<sub>0.4</sub>Ti<sub>0.6</sub>/Co, respectively. These ratios mean that the interface resistances are smaller than the relevant bulk resistances. The dominant contribution to the resistance comes from the bulk of Co, and with fair approximation to neglect the interface resistance with  $S$  in the normal state according to the theoretical work of Morten. *et. al.* [38]

However, the  $AR_{F/S(S)}$  interface resistance is found to be larger than  $AR_{F/S(NM)}$  and would give  $R_{F/S}/R_{sf}^F > 0.8$ . The increase in the CPP total resistance with spin injection can be most dramatic if the  $NM$  region is taken to be a superconductor [39], as shown in Figure 5.13, 5.14, and 5.15. This means the interface resistance  $AR_{F/S(S)}$  with the superconductor in the superconducting state has a greater contribution. Therefore, the interface resistance of the  $F/S$  system is larger than that of the  $F/NM$  system with the materials we chose. The spin accumulation is a candidate for causing an additional voltage drop across the interface due to reduced spin transport into  $S$ . When spin-polarized current are injected onto the  $F/S$  interface from  $F$ , spin accumulation is established in the range of the spin diffusion length in  $F$ . In  $S$ , the spin polarized quasiparticle wave function decays because there are no available states. There are reports on conductance by subgap residual density of states and by crossed Andreev reflection [40-42]. However, the longest length scale these phenomena can happen is the superconducting coherence length. Our  $S$  state samples have much larger thickness than  $\xi_S$  at the measuring temperature. In  $F$ , the spin accumulation decays because of spin-orbital scatterings. This causes an additional

voltage drop associated with the interface. In the Giant Magnetoresistance effect in  $F/NM$  multilayers, similar spin accumulation at the interface is responsible for the extra voltage drop. [25] It could be detected by a second  $F$  layer, which is parallel or antiparallel to the first one, placed within spin diffusion length of  $NM$ . In our  $F/S$  multilayers, the  $S$  layers were much larger than the penetration length and we did not observe the spin accumulation effect.

Our quantitative results clearly show that  $R_{F/S}$  is larger than  $R_{F/NM}$  in  $\text{Co/Nb}_x\text{Ti}_{1-x}$  systems, where the  $S$  materials are in the ‘dirty limit’ ( $l < \xi_S$ , see below). Electrons’ wave functions decay exponentially when penetrating from a metal into a superconductor if their excitation energy with respect to the Fermi level is below the superconducting gap. In our CPP setup, the drop in voltage across the sample is at most 10 nano-volt for a maximum constant current of 100 mA, much smaller than the Nb energy gap  $\Delta = 1.76 k_B T_c \sim 1.4$  meV. Current flows through the sample in response to a small applied voltage  $V$  less than  $\Delta$  by means of the Andreev reflection. A spin-up electron from a normal metal is retro-reflected at the interface as a spin-down hole in order to form a Cooper pair in the superconductor. This property makes a distinction between superconducting and normal states. The classical work of Blonder, Tinkham, and Klapwijk (BTK) [43] have described the Andreev reflection and the elastic scattering process at the  $N/S$  interface of a nanocontact. It interpolates between a perfect transparent interface and an insulating barrier at the interface with a barrier strength  $z$  varying from zero to infinity. The Andreev current at  $F/S$  interface is partially suppressed by the exchange splitting of the conduction band in the ferromagnet, and this behavior has been demonstrated theoretically by de Jong and Beenakker [44].



## 5.6 Interface transparency

To study the transport through  $NM/S$  [45] or  $F/S$  [46] bilayers, the Usadel's equation is used in the dirty limit. By considering the coherence length  $\xi_F$  in  $F$  metal, which is determined by exchange energy  $E_{ex}$ , the  $NM/S$  bilayer can be easily adapted to the  $F/S$  case. In the general situation, the exchange energy is much larger than the superconducting gap, and this situation makes  $\xi_F$  virtually independent of temperature. From the current continuity requirement, the boundary conditions for the anomalous Green's functions at interface are derived by Kuprianov and Lukichev. [47] The interface transparency parameter

$$\gamma_B = (AR_{F/S(NM)} / \rho_F \xi_F^*) \quad (5.11)$$

is proportional to the interface resistance when superconductor is in the normal state. The boundary conditions are justified only when the exchange field in the  $F$  is much smaller than the Fermi energy. For strong  $F$  like Co in our case, appropriate boundary conditions for the Usadel's equations need to be worked out. [48] Recently, the quasiclassical formalism, or the Eilenberger's equations, has been employed for the Andreev conductance of  $NM/S$  [49] and  $F/S$  [50] interfaces. Vodopyanov and Tagirov have derived boundary conditions for strong  $F$  case. [50] The quantum mechanical transmission and reflection coefficients for the two spin channels were discussed in the normal and superconducting states. However, the interface transparency was not taken into account.

Perfect transmission coefficient  $T=1$  of the boundary conditions to the Usadel's equations was assumed in the work of Radovic *et al.* [4] Lots of experimental works on the  $F/S$  junctions in the CIP geometry has applied the theory of Radoic *et al.* to the explanation of the data. However, more and more reports have pointed out that the

inconsistency between data and calculation could be traced back to the assumption of continuity of the wave functions at the  $F/S$  interface. Analyses and procedures for fitting experimental results have to take the finite transparency into account. For example, Aarts *et al.* were the first to observe the importance and presented experimental evidence of the intrinsically reduced interface transparency in the  $V/V_x\text{Fe}_{1-x}$  multilayers. [51] They have explained the non-monotonic behavior in  $T_c$  as the competing effects of increasing attenuation depth  $\xi_F$  of the order parameter in the  $F$  material and the decreasing transparency of the  $F/S$  interface for the penetration of Cooper pairs. Lazar *et al.* have fitted their results by introducing interface transparency and pointed out its relation to the angular average of the transmission coefficient. [52] Kim *et al.* [53] have reported the  $F$  layer thickness dependence of the  $T_c$  behaviors in bilayer  $F/S$  structures, determined with CIP resistance measurements. Quantitative analyses were made from these literatures. For example, the interface resistance at the Ni/Nb and  $\text{Cu}_{0.4}\text{Ni}_{0.6}/\text{Nb}$  boundary estimated from the best fit  $\gamma_B$  values were  $2AR \sim 2.4 \text{ f}\Omega \text{ m}^2$  for both Ni and  $\text{Cu}_{0.4}\text{Ni}_{0.6}$ . The estimated values are comparable to our CPP measurements with  $S$  in the normal state. Experimentally,  $\gamma_B$  is usually treated as an adjustable parameter to describe and modify the behavior of critical temperature dependence on the thickness for  $S$  or  $F$ .

We can estimate the interface transparency parameter  $\gamma_B$  without spin-flip scatterings directly from our results. The characteristic spatial scale is given by

$$\xi_F^* = \sqrt{\frac{\hbar D_F}{2\pi K_B T_C}}, \text{ where } D_F = V_F l_F / 3 \text{ is the diffusion constant in } F \text{ layer with the}$$

Fermi velocity  $V_F$  and the mean-free path  $l_F$ . Here,  $\xi_F^*$  is different from  $\xi_F^{\text{ex}}$  which corresponds to the actual penetration depth of the Cooper-pairs in the  $F$ . While  $\xi_F^*$  is the Cooper-pairs penetration depth in normal metal without considering the exchange field. Both diffusion constant and  $\xi_F^{\text{ex}}$  of Co were derived to be

$D_F = 5 \text{ cm}^2 / \text{s}$  and  $\xi_F^{\text{ex}} = 1.2 \text{ nm}$ . [3] These quantities allow us to obtain the following parameters in our  $F/S$  CPP multilayers: characteristic spatial length  $\xi_F^* \approx 8.1 \text{ nm}$  and transparency parameter  $\gamma_B \approx 1.6$  for Co/Nb,  $\xi_F^* \approx 8.3 \text{ nm}$   $\gamma_B \approx 1.2$  for Co/Nb<sub>0.4</sub>Ti<sub>0.6</sub>, and  $\xi_F^* \approx 9.3 \text{ nm}$   $\gamma_B \approx 1.6$  for Co/Nb<sub>0.6</sub>Ti<sub>0.4</sub> when  $S$  is in the normal state. These finite transparency parameters justify the boundary conditions we used to describe the  $T_C$  dependence on  $S$  thicknesses with current parallel to plane by Radovic's model. [3, 4] Numerical studies also showed insignificant discrepancy of the  $T_C(d_S)$  behavior when using the boundary condition of high-quantum-mechanical transparency and of finite transparency introduced by Lazar *et al.* [39] and Tagirov [54] as  $\gamma_B$  is small. For comparison,  $\gamma_B = 0.7$  for Ni/Nb bilayers [53], and  $\gamma_B = 0.5$  and  $1.15$  in CoFe/Au and Au/Nb interface, respectively [55], for CoFe/Au/Nb trilayers, were derived by fitting  $T_C(d_F)$  curves. The given values for  $\gamma_B$  depend on the way by which  $\xi_F^*$  is extracted from the  $T_C$  that may be somewhat different in multilayers or in single films. We know that the transmission coefficient for the Cooper pairs in the  $F/S$  proximity effect theory is close to the smaller one between the transparency coefficients  $T_\downarrow$  for spin-down and  $T_\uparrow$  for spin-up for quasiparticles to form Cooper pairs. [52, 56] But this is not the only mechanism, since from our study the transparency can be varied by adjusting  $x$  as a result of changing compositional disorder or the changing lattice parameter between the Co and Nb <sub>$x$</sub> Ti <sub>$1-x$</sub>  interface. The spin-flip scattering is another mechanism which can lead to a large interface resistance. The interface spin-flips physically come from the following mechanisms: (1) inelastic electron scattering in the intermixed level between the magnetic and non-magnetic layers; (2) the direction of magnetization changed locally near the interface; and (3) spin-orbit scattering at the interface induced by the polarization in magnetic layer. The spin triplet symmetry can also be induced in a

superconductor surrounded by ferromagnets with non-collinear magnetizations and spin flip processes. [57, 58] Thus, the value of interface resistance between the ferromagnet and the superconductor both in normal and superconducting states can provide a lot of physical information in  $F/S$  heterostructures.

## 5.7 Pippard model

Table 5.3 shows that the  $\text{Nb}_{0.6}\text{Ti}_{0.4}$  has the largest resistivity in the normal state, and the largest interface resistance in both superconducting and normal states. According to Pippard's model [59] of partial quenching of Andreev reflection by impurities in the superconductor, the residual  $NM/S$  boundary resistance can be written as:

$$AR = \frac{l_a}{2l_s} \rho_N l_N = \left( \frac{\rho_s l_a}{2\rho_s l_s} \right) (\rho_N l_N), \quad (5.12)$$

where  $l_a = \hbar v_F / 2\Delta = \pi \xi_S / 2$  is the amplitude decay length in  $S$  for the electron evanescent mode from  $NM$ ,  $v_F$  is the Fermi velocity,  $\Delta$  is the superconducting energy gap,  $\xi_S$  is the intrinsic coherence length,  $\rho_0 l_0$  is the product of bulk resistivity  $\rho_0$  and the mean free path  $l_0$ , and  $\rho_s l_s$  is the product of  $\rho_s$  and  $l_s$ , when  $S$  is in the normal state just above  $T_c$ . Since  $\rho l = mv_F / ne^2$  is a constant for each material, the equation shows that  $AR_{NM/S}$  should be proportional to  $\rho_s \xi_S$ . [31] For the case of  $F/S$  interface, we can write the unit area conductance for two independent channels as:  $\frac{1}{AR_{\uparrow(\downarrow)}} = \frac{2l_s}{l_a} \frac{1}{\rho_{\uparrow(\downarrow)} l_{\uparrow(\downarrow)}}$ . The sum of the two spin channel shows that the

same relation holds and the Pippard model can be extended to ferromagnetic materials.

In a prior work [60], the data were compatible with linear dependence on the

resistivity up to at least  $20 \mu\Omega$  cm. Therefore, we want to test the linear dependence of  $AR$  on  $\rho_S l_S$  predicted on Eq. (5.12). The Ginsburg-Landau (GL) coherence length at zero temperature can be written as  $\xi_{GL}(0) = \sqrt{\phi_0 / 2\pi \cdot \beta T_c}$ , where  $\beta = -dH_{c2} / dT$  close to  $T_c$ . We have deduced the  $\xi_{Nb} \approx 12$  nm,  $\xi_{Nb_{0.4}Ti_{0.6}} \sim 4$  nm, and  $\xi_{Nb_{0.6}Ti_{0.4}} \sim 4.5$  nm from the temperature-dependent upper-critical field measurements which will be discussed in the next chapter. [61] In the table 5.4, we list all parameters which needed for Eq. (5.12). We find that the  $AR_{F/S}$  derived from two-parameter fit is indeed proportional to  $\rho_S \xi$ , which conformed very well to Pippard's model. Thus, Eq. (5.12) held for  $\rho_S$  as large as  $80 \mu\Omega$  cm in our  $S$  samples. But the experimental values of  $AR$  in the linear regime were smaller than prediction by Eq. (5.12). Pippard proposed the effect of Fermi surface mismatching between the  $S$  and  $N$  metals of the sandwich as a partial explanation for the discrepancy. [59] The star symbol in Fig. 5.16 shows this linear relation between  $AR_{F/S}$  and  $\rho_S \xi$ . Good agreement between our results and the theory suggests that the scattering centers and the penetration depths of the electron evanescent wave into the superconductors give rise to the interface resistance.

	$2AR_S$ $f\Omega m^2$	$\rho_S$ $\mu\Omega$ cm	$\xi$ nm	$\rho_S l_a$ $f\Omega m^2$	$2AR_N$ $f\Omega m^2$
Co/Nb	$6.3 \pm 0.9$	$\sim 8$	12	1.5	$3.5 \pm 0.7$
Co/Nb <sub>40</sub> Ti <sub>60</sub>	$9.9 \pm 1.3$	$\sim 40$	4	2.5	$2.3 \pm 0.8$
Co/Nb <sub>60</sub> Ti <sub>40</sub>	$22.6 \pm 1.7$	$\sim 80$	4.5	5.7	$5.6 \pm 1.5$

**Table 5.4.** The best derived values (two global fit) and parameters for the Co/Nb, Co/Nb<sub>40</sub>Ti<sub>60</sub>, and Co/Nb<sub>60</sub>Ti<sub>40</sub> multilayers.

Although our two- and four-parameter fit result in different values of  $S$  resistivity, the  $AR_{F/S(S)}$  values of our samples do not change much. The extracted interface resistances Co/Nb<sub>x</sub>Ti<sub>1-x</sub> of our multilayers when the  $S$  materials are in their normal states are much larger than normal metal interface resistances such as Co/Cu and Co/Ag interfaces that had values  $\sim 0.5 \text{ f}\Omega \text{ m}^2$  or smaller. [20] Nb/Cu has been reported to have large interface resistance of  $\sim 1 \text{ f}\Omega \text{ m}^2$ . [30] Whether these large values are due to alloys at the interfaces or the crystalline mismatch (bcc for  $S$  to fcc or hcp for  $F$ ) [62] remains to be investigated. However, the dependence of  $AR_{F/S(S)}$  on  $\rho_s \xi_S$  is inconsistent with a linear behavior using the values of  $AR_{F/S}$  and  $\rho_s$  from four-parameter global fit, as shown in Fig. 5.16. The CPP resistivity of Nb derived from four-parameter global fit is more than twice the CIP bulk value.

The CPP resistance in normal metal multilayers can be described by the theoretical work of Zhang and Levy. [63] For the CPP geometry, the current is constant throughout, while internal electric field varies from one layer to the next. In the CIP case, the voltage drop across the sample is the same but the current density in each layer is different. Zhang and Levy have shown that the CIP resistivity is an average of the conductivities  $\rho_{||} = L / \int_L \sigma_{||}(z) dz$  while the CPP resistivity is the average of the resistivities  $\rho_{\perp} = \int_L \rho_{\perp}(z) dz / L$ , where  $L$  is the total thickness of multilayers. [64] In other words, the total CPP resistance can be thought of as a series of different resistances of length  $d$ . And the average of CPP resistivity removes the length scale by self-averaging. When the mean free path ( $l$ ) is much larger than the thickness ( $d$ ), the  $\rho_{||}$  and the  $\rho_{\perp}$  are the same because the local conductivity is independent of position  $z$ . For large  $d/l$  they are quite different. Notice that when the scattering from the interface is much weaker than that from the bulk,  $\rho_{\perp}$  is always greater than  $\rho_{||}$ , because the resistivity is dominated by the high conductivities layers

for the in-plane geometry. In our case, the thicknesses of normal Nb,  $\text{Nb}_{0.6}\text{Ti}_{0.4}$ , and  $\text{Nb}_{0.4}\text{Ti}_{0.6}$  are between these two limit situations. The  $\rho_{\perp}$  derived from the CPP measurements is larger than the  $\rho_{\parallel}$  with parallel current.

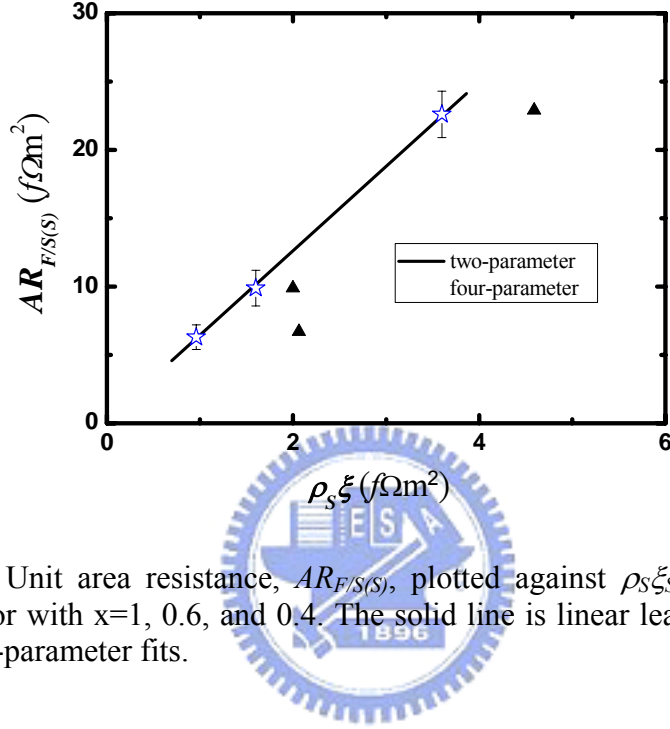


**Figure 5.16:** Unit area resistance,  $AR_{F/S(S)}$ , plotted against  $\rho_S \xi_S$  for alloy  $\text{Nb}_x\text{Ti}_{1-x}$  superconductor with  $x=1, 0.6,$  and  $0.4$ . The solid line is linear least squares fit to the results of two-parameter fits.

The apparently large CPP resistivities for Nb and NbTi alloys derived in the four-parameter global fits could be explained by that the interface resistance  $AR_{F/S(NM)}$  is not constant when the superconductor is in normal state. When layer thicknesses are systematically changed in the narrow window thinner than  $d_{\text{Nb}}^{\text{crit}}$ , thickness fluctuation might increase interface roughness in the thicker samples. By assuming a series resistance model, we attribute part of the extra interface resistance to the CPP resistivity. To verify this assumption, we plot the dot-dashed lines in Figs.5.13(c), 5.14(c), and 5.15 (c) with the bulk CIP resistivities as the slope and the two interface resistances from the two- and four-parameter fits as upper and lower limits, respectively. The thicknesses larger than  $l$  can be fitted by large  $AR_{F/S(NM)}$  ( $\text{Nb} >$

4nm,  $\text{Nb}_{0.4}\text{Ti}_{0.6}$  and  $\text{Nb}_{0.6}\text{Ti}_{0.4}$  ( $>2$  nm), while thinner samples can be fitted by small  $AR_{F/S(NM)}$ . Thus, thickness fluctuation could be a possible explanation for the resistivities discrepancy, while the other NbTi alloys have less deviation. We can modify the global fit by assuming the  $AR_{F/S(NM)}$  is linearly proportional to Nb (NbTi) thickness in the normal state and write  $AR_{F/S(NM)} = a + b d_S$ . The global fit becomes a five-parameter fit. But  $b$  and  $\rho_S$  become strongly dependent and cannot be determined independently. The small thickness range for Nb and NbTi being normal metals prevent us from more detailed studies of the thickness fluctuation. An appropriate model or more experimental data are needed. Another possible reason for the smaller  $AR$  values for thinner Nb (NbTi) samples is the presence of pin-holes. The lack of interfaces through the pin-holes makes the total resistance smaller. Even with the complication for  $\rho_S$  and  $AR_{F/S(NM)}$ , the influence on the extracted values of  $AR_{F/S(S)}$  is small, as shown in Table 5.3.





## References:

1. R. Krishnan, J. Magn. Magn. Mater. **50**, 189 (1985).
2. S. F. Lee, Y. Liou, Y. D. Yao, W. T. Shih, and C. Yu, J. Appl. Phys. **87**, (2000) 5564.
3. J.-J. Liang, S. F. Lee, W. T. Shih, W. L. Chang, C. Yu, and Y. D. Yao, J Appl. Phys. **92**, 2624 (2002).
4. Z. Radovic', L. Dobrosavljevic'-Grujic', A. I. Buzdin, and J. R. Clem, Phys. Rev. B **38**, 2388 (1988).
5. L. Lazar, K. Westerholt, H. Zabel, and L. R. Tagirov. Phys. Rev. B. **61**, 3711 (2000).
6. A. B. Pippard, Rep. Prog. Phys. **23**, 176 (1960).
7. C. Kittel, *Introduction to Solid State Physics* (Wiley, New York, 1986), p.144.
8. W. Clemens, T. Kachel, O. Rader, E. Vescovo, S. Bluigel, C Carbone and W. Eberhardt, Solid State Commun. **81**, 739 (1992).
9. J. Bass, Landolt-Bornstein Numerical Data and Functional Relationships in Science and Technology, New Series, Group III, edited by K. H. Hellwege and J. L. Olsen (Springer, Berlin, 1982), Vol. 15a, p. 1.
10. H. Weber, E. Seidl, C. Laa, E. Schachinger, M. Prohammer, A. Junod, and D. Eckert, Phys. Rev. B **44**, 7585 (1991).
11. P. J. Lee, "Abridged metallurgy of ductile alloy superconductors Wiley Encyclopedia of Electrical and Electronics", Engineering (New York: Wiley 1999).
12. C. M. Meingast, P. J. Lee and D. C. Larbalestier, J. Appl. Phys. **66**, 5962 (1989).
13. A. Mani, L. S. Vaidhyanathan, Y. Hariharan and T. S. Radhakrishnan, Cryogenics **36**, 937 (1966).
14. B. B. Goodman, Rep. Prog. Phys. **49**, 445 (1996).
15. David A Cardwell and David S Ginley, "Handbook of Superconducting

- Materials” (IOP Publishing Ltd 2003).
16. M. Hansen, E. L. Kamen, H. D. Kessler and D. J. McPerson, *J. Metals*, **3** 881 (1951)
  17. P. J. Lee, J. C. McKinnell and D. C. Larbalestier, *Adv. Cryo. Eng. (Materials)*, **36** 287 (1991).
  18. T. S. Kreilick, “*Niobium–Titanium Superconductors Metals Handbook, 10th edn, vol 2, Properties and Selection: Nonferrous Alloys and Special-Purpose Materials*” (Metals Park, OH: ASM International 1990) pp 1043.
  19. D. L. Moffat and D. C. Larbalestier, *The competition between martensite and omega in quenched Ti-Nb alloys, Metallurgical Transactions*, **19A**, pp. 677-1686, (1988).
  20. W.E. Lawrence and S. Doniach, *Proceedings of the 12<sup>th</sup> International Conference on Low-temperature Physics*, edited by E. Kanada (Academic, Kyoto, 1971), p. 361.
  21. M. Tinkham, *Phys. Rev.* **129**, 2413 (1963).
  22. C. Attanasio, C. Coccoresse, L. V. Mercaldo, M. Salvato, L. Maritato, A. N. Lykov, S. L. Prischepa, and C. M. Falco, *Phys. Rev. B* **57**, 6056 (1998).
  23. E. Silva, R. Marcon, R. Fastampa, M. Giura, and S. Sarti, *Physica C* **214**, 175 (1993).
  24. J. Bass and W. P. Pratt, Jr., *J. Magn. Magn. Mater.* **200**, 274 (1999).
  25. T. Valet and A. Fert, *Phys. Rev. B* **48**, 7099 (1993).
  26. S. S. Parkin, *Phys. Rev. Lett.* **67**, 3598 (1991).
  27. S. Y. Huang, S. F. Lee, S. Y. Hsu, and Y. D. Yao, *Phys. Rev. B* **76**, 024521 (2007).
  28. C. A. R. Sa’ de Melo, *Phys. Rev. Lett.* **79**, 1933 (1997).
  29. W. Park, D. V. Baxter, S. Steenwyk, I. Moraru, W. P. Pratt, Jr., and J. Bass, *Phys. Rev. B* **62**, 1178 (2000).
  30. D. V. Baxter, S. D. Steenwyk, J. Bass, and W. P. Pratt, Jr., *J. Appl. Phys.* **85**, 4545

- (1999).
31. C. Fierz, S. F. Lee, J. Bass, W. P. Pratt Jr., and P A Schroeder, *J. Phys. Cond. Matter*: **2**, 9701 (1990).
  32. G. J. Strijkers, Y. Ji, F. Y. Yang, C. L. Chien, and J. M. Byers, *Phys. Rev. B* **63**, 104510 (2001).
  33. G. E. Blonder, M. Tinkham, and T. M. Klapwijk, *Phys. Rev. B* **25**, 4515 (1982).
  34. I. I. Mazin, A. A. Golubov, and B. Nadgorny, *J. Appl. Phys.* **89**, 7576 (2001).
  35. C. Fierz, S. F. Lee, W. P. Pratt, Jr., P. A. Schroder, and J. Bass, *J. Phys.: Condes. Matter* **2**, 1224 (1991).
  36. M. Urech, V. Korenivski, and D. B. Haviland, *J. Magn. Magn. Mater.* **249**, 513 (2002)
  37. L. Piraux, S. Dubois, A. Fert, and L. Belliard, *Eur. Phys. J. B* **4**, 413 (1998).
  38. J. P. Morten, A. Brataas, and W. Belzis, *Phys. Rev. B* **72**, 014510 (2005).
  39. Igor Zutic, J. Fabian, and S. D. Sarma, *Rev. Mod. Phys.* **76**, 323 (2004).
  40. R. Mélin, *Phys. Rev. B* **73**, 174512 (2006).
  41. S. Russo, M. Kroug, T. M. Klapwijk, and A. F. Morpugo, *Phys. Rev. Lett.* **95**, 027002 (2005).
  42. D. Beckmann, H. B. Weber, and H. v. Löhneysen, *Phys. Rev. Lett.* **93**, 197003 (2004).
  43. G. E. Blonder, M. Tinkham, and T. M. Klapwijk, *Phys. Rev. B* **25**, 4515 (1982).
  44. M. J. M. de Jone and C. W. J. Beenakker, *Phys. Rev. Lett.* **74**, 1657 (1995)
  45. S. -K. Yip, *Phys. Rev. B* **52**, 15504 (1995).
  46. Y. V. Fominov, N. M. Chtchelkatechev, and A. A. Golubov, *Phys. Rev. B* **66**, 014507 (2002).
  47. M. Yu. Kuprianov and V. F. Lukichev, *Sov. Phys. JETP* **67**, 1163 (1988).
  48. A. I. Buzdin, *Rev. Mod. Phys.* **77**, 935 (2005).
  49. S. -K. Yip, *Superlattices and Microstructures* **25**, 1213 (1999).
  50. B. P. Vodopyanov and L. R. Tagirov *JETP letters* **77**, 126 (2003); *JETP letters* **78**, 555 (2003).
  51. J. Aarts ,J. M. E. Geers, E. Bruĉk, A. A. Golubov\*, and R. Coehoorn, *Phys. Rev. B* **56**, 2779 (1997).

52. L. Lazar, K. Westerholt, H. Zabel L. R. Tagirov Yu. V. Goryunov, N. N. Garif'yanov, and I. A. Garifullin, *Phys. Rev. B* **61**, 3711 (2000).
53. J. Kim, Jun Hyung Kwon, K. Char, and Hyeonjin Doh, *Phys. Rev. B* **72**, 014518 (2005).
54. L. R. Tagirov, *Physica* **307C**, 145 (1998).
55. J. Kim, Y-J Doh, and K. Char, *Phys. Rev. B* **71**, 214519 (2005).
56. S. K. Upadhyay, A. Palanisami, R. N. Louie, and R. A. Buhrman, *Phys. Rev. Lett.* **81**, 3247 (1998).
57. H. Doh and H. Y. Choi, arXiv:cond-mat/0407149 v1 7 Jul (2004).
58. F. S. Bergeret, A. F. Volkov, and K. B. Efetov, *Phys. Rev. B* **69**, 174504 (2004).
59. A. B. Pippard, *Proc. R. Soc. London, Ser. A* **391**, 255 (1984).
60. G. L. Harding, A. B. Pippard, and J. R. Tomlinson, *Proc. R. Soc. London, Ser. A* **340**, 1 (1974).
61. S. Y. Huang, S. F. Lee, J. C. Huang, G. H. Hwang, and Y. D. Yao, *J. Appl. Phys.* **97**, 10B103 (2005).
62. C. Galinon, K. Tewolde, R. Loloee, W.-C. Chiang, S. Olson, H. Kurt, W. P. Pratt, Jr., J. Bass, P. X. Xu and Ke Xia, and M. Talanana, *Appl. Phys. Lett.* **86**, 182502 (2005).
63. S. Zhang and P. M. Levy, *J. Appl. Phys.* **69**, 4786 (1991).
64. S. Zhang and P. M. Levy, *Phys. Rev. B* **47**, 6776(1993).

## Chapter 6

### Results and Discussion-Conventional

#### Ferromagnet:

### Fe/Nb and Ni/Nb System as Compared with

### Co/Nb System

#### 6.1. Fe/Nb system

There are many controversial experimental results, in Fe/Nb system. For example, the experimental results from Mühge *et al.* [1] found a nonmonotonous dependence of superconducting transition temperature  $T_C$  on Fe layer thickness ( $d_{Fe}$ ). Another research reported by Verbanck *et al.* [2] has demonstrated a sudden drop of  $T_C$  when  $d_{Fe}$  is increased up to 1.5 nm for epitaxial Fe/Nb multilayer systems. However, in studies on coexistence of  $S$  and  $F$ , a thin  $F$  layer, due to the reduction of the exchange energy, shows nonmagnetic behavior. [1, 2] In order to learn the proximity effect between  $S$  and  $F$  in the decoupled regime, we study the critical temperature  $T_C$  and upper critical field  $H_{c2}(T)$  with a constant  $d_{Fe} = 20$  nm, which is much large than the coupled regime of 1.2 nm [2] and a variety of Nb thicknesses. The dependence of  $T_C$  on  $S$  thickness and the temperature dependence of  $H_{c2}(T)$  can be well described by the theory of Radović *et al.* [3] and Ginzburg-Landau theory, respectively. We also compare the Fe/Nb with Co/Nb system of Chapter 5. [4, 5]

### 6.1.1 The behavior of critical temperature for Fe/Nb trilayers

In this section, we report a series of samples as follows: Fe/Nb/Fe trilayers and 6 Fe/Nb repetitions multilayers denoted as  $(\text{Fe/Nb})_6/\text{Fe}$ . The thickness of the Fe layer for both systems was kept 20 nm while that of S layers varied. As shown in Figure 6.1, the good quality and smooth interface could be verified by TEM image. Electrical resistance,  $T_C$ , and  $H_{c2}$  were measured by four-point measurement.

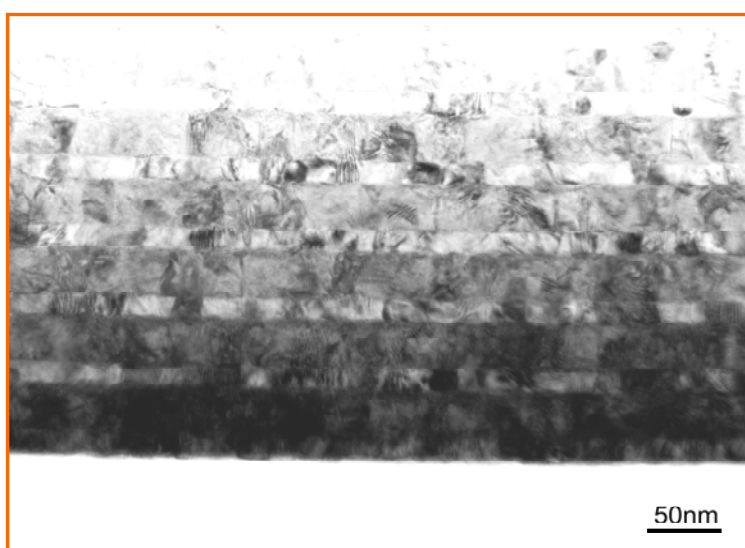


**Figure 6.1:** TEM image of a  $[\text{Fe}(20 \text{ nm})/\text{Nb}(50 \text{ nm})]_6/\text{Fe}(20 \text{ nm})$  multilayer sample.

Simple planar multilayers were also made for measuring temperature and magnetic field dependence of resistivity. X-ray diffraction showed crystalline structure of bcc (110) for Nb and Fe. Higher-order satellite peaks were observed to confirm a good coherence in Fe/Nb multilayer system, as shown in Fig. 6.2.

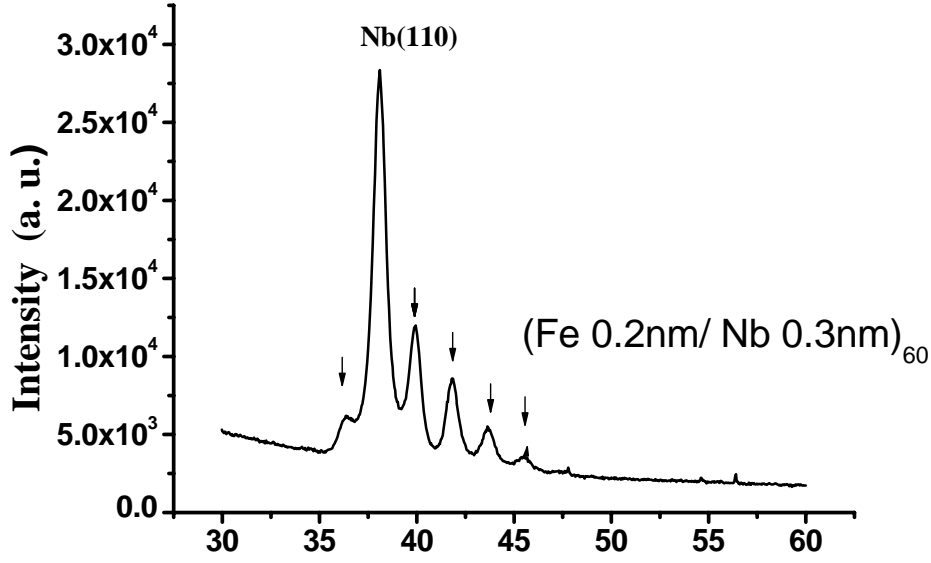


**Figure 6.2:** High-angle x-ray diffraction of  $[\text{Fe}(0.2 \text{ nm})/\text{Nb}(0.3 \text{ nm})]_{60}$  multilayer. Satellite peaks around Nb (110) are indicated by arrows.

Figure 6.3 shows the  $T_C$  as a function of the Nb thickness for the trilayers. With decreasing  $d_{\text{Nb}}$ ,  $T_c$  exhibits a continuous reduction down to a critical thickness  $d_{\text{SC}}^{\text{crit}}$ , below which superconductivity vanishes. We also using Radović's model, a microscopic theoretical model, to interpret the experimental results for  $F/S$  trilayers from Eq. (4.12). [3] The diffusion constant  $D_F$  of Fe can be estimated by the Pippard relation [6] with the low temperature resistivity  $\rho = 6.4 \mu\Omega\text{cm}$  for  $d_{\text{Fe}} = 300 \text{ nm}$  and the coefficient of the electronic specific heat  $\gamma = 4.98 \times 10^{-3} \text{ J}/\text{K}^2\text{mole}$  [7]. The characteristic distance in Fe is derived to  $\xi_{\text{FM}}^{\text{Fe}} = 1.2 \text{ nm}$  from the diffusion coefficient and splitting energy  $I_0 = 1 \text{ eV}$ .  $\xi_{\text{FM}}^{\text{Fe}}$ , for Fe is slightly smaller than  $\xi_{\text{FM}}^{\text{Co}} = 1.3 \text{ nm}$  for Co film (Chapter 5).

The solid line in Figure 6.3 was obtained by fitting Eq. (4.12) to the data with

parameters of  $\varepsilon = 10$  and  $\xi_s = 12$  nm. By extrapolating the fit to  $T_c=0$ , we see that the critical thickness for superconductivity is about  $d_{Nb}^{crit} = 34$  nm. The critical thickness is similar to the  $d_{Nb}^{crit} = 30$  nm for Co/Nb system [4], consistent with stronger pair breaking effect in Fe.

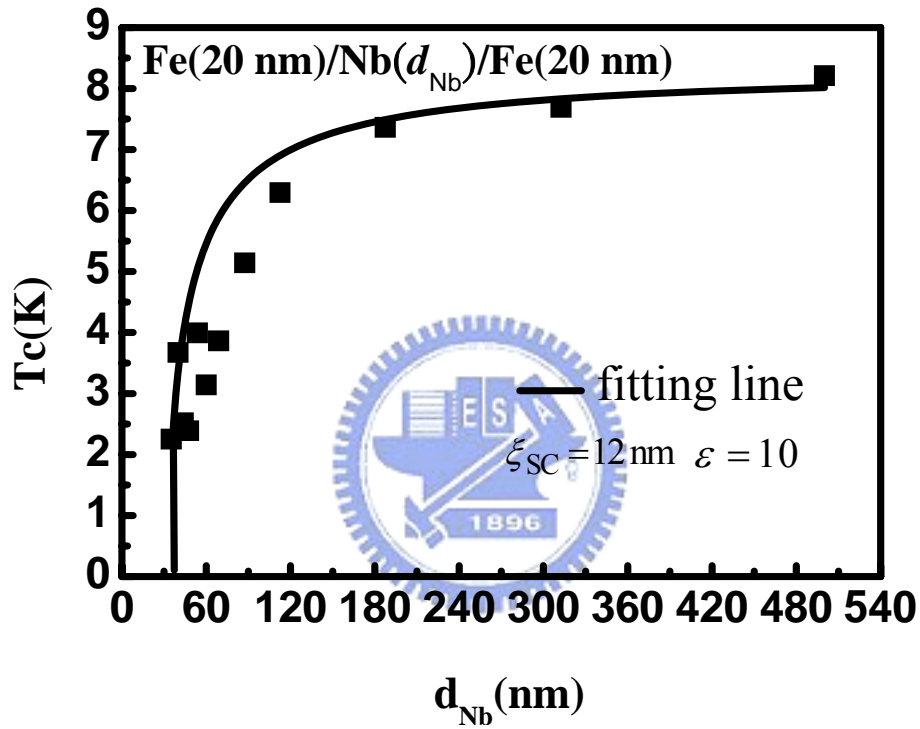


**Figure 6.3:** Dependence of the superconducting transition temperature on the thickness of the Nb layer, the solid line is the best fit with Eq. (4.12).



## 6.1.2 The behavior of upper critical field for Fe/Nb multilayers

We also performed measurements of anisotropic uppercritical field  $H_{c2\parallel}$  and  $H_{c2\perp}$  for Fe/Nb multilayers, where  $H_{c2\parallel}$  and  $H_{c2\perp}$  denote the field parallel and perpendicular to layer planes, respectively. Samples with  $[\text{Fe}(20 \text{ nm})/\text{Nb}(d_s)]_6/\text{Fe}(20 \text{ nm})$  and with  $d_s$  ranging from 500 nm to 20 nm, were systematically measured. Figure 6.4 shows  $H_{c2}$  versus reduced temperature  $t$  for  $d_{\text{Nb}} = 100, 120$  and 140 nm. The solid lines correspond to Ginzburg-Landau (G-L) relation.

By using the G-L formulas for anisotropic superconductors, we can determine the dimensionality. The temperature dependence of the upper critical field can be expressed as follows:

$$H_{c2\parallel}(T) = \frac{\phi_0}{2\pi} \frac{1}{\xi_{\parallel}(T)\xi_{\perp}(T)}, \quad H_{c2\perp}(T) = \frac{\phi_0}{2\pi} \frac{1}{\xi_{\parallel}^2(T)}, \quad (6.1)$$

where  $\xi_{\parallel}$  and  $\xi_{\perp}$  are the temperature dependent coherence lengths, and  $\phi_0$  is the flux quantum. Near  $T_C$ ,  $\xi_{\parallel}(T)$  and  $\xi_{\perp}(T)$  have  $(1-t)^{-1/2}$  temperature dependence. For a 3D superconductor, the relation between  $H_{c2}$  and reduce temperature  $t$  is given by  $H_{c2\parallel}(T) \propto (1-t)$  and  $H_{c2\perp}(T) \propto (1-t)$ . However, in the case of two dimensional (2D) superconductivity, the perpendicular coherence  $\xi_{\perp}$  is limited by the layer thickness and becomes constant near  $T_C$ . In this case, the temperature dependence of  $H_{c2}$  is expressed as  $H_{c2\parallel}(T) \propto (1-t)^{1/2}$  and  $H_{c2\perp}(T) \propto (1-t)$ . The superconducting dimensionality can be investigated by the parallel critical field measurement according to the nonlinear behavior to linear temperature dependence.

In the  $H_{c2}$  measurement, the  $H_{c2}$  is sensitive to the angle between applied

magnetic field and the film plane due to a cusp shape around 0 degree in the 2D sample, that behavior can be described by Tinkham's formula [8]

$$\left| \frac{H_{c2}(\theta) \sin \theta}{H_{c2\perp}} \right| + \left[ \frac{H_{c2}(\theta) \cos \theta}{H_{c2\parallel}} \right]^2 = 1, \quad (6.2)$$

Therefore, the best resolution of the angle is  $0.1^\circ$  has used to carefully measure in order to reduce the deviation.  $H_{c2}$  was defined as the applied field at 90 % point of the residual resistance in the normal state. The applied field was swept at a constant temperature. It can be clearly seen the linear behavior of  $H_{c2\perp}$  for all thickness of Nb. Comparing Figure 6.4(a) with Figure 6.4(c), we find that the dependence of  $H_{c2\parallel}$  on temperature changed gradually from 2D to 3D, i.e., from a square-root dependence to a linear dependence. The extrapolation in Figure 6.4 yields a coherence length  $\xi_{GL}(0) = 10$  nm from the function  $\xi(T) = \sqrt{\phi/2\pi\beta T}$  with  $\beta = -dH_{c2}/dT$ . The superconducting coherence length  $\xi_{sc}$  is related to GL coherence length  $\xi_{GL}$  via  $\xi_{GL}(T) = \pi\xi_{sc}(1-t)^{-1/2}/2$ . This gives  $\xi_{sc} \approx 7$  nm which is the same with the value estimated by  $\xi_{sc} = \sqrt{\hbar D_s/2\pi k_B T} = \sqrt{\xi_{BCS}l/3.4}$  with the electron mean free path  $l$ ; the values were obtained from the product  $\rho l = 3.75 \times 10^{-6} \mu\Omega cm^2$  for bulk Nb. [5]

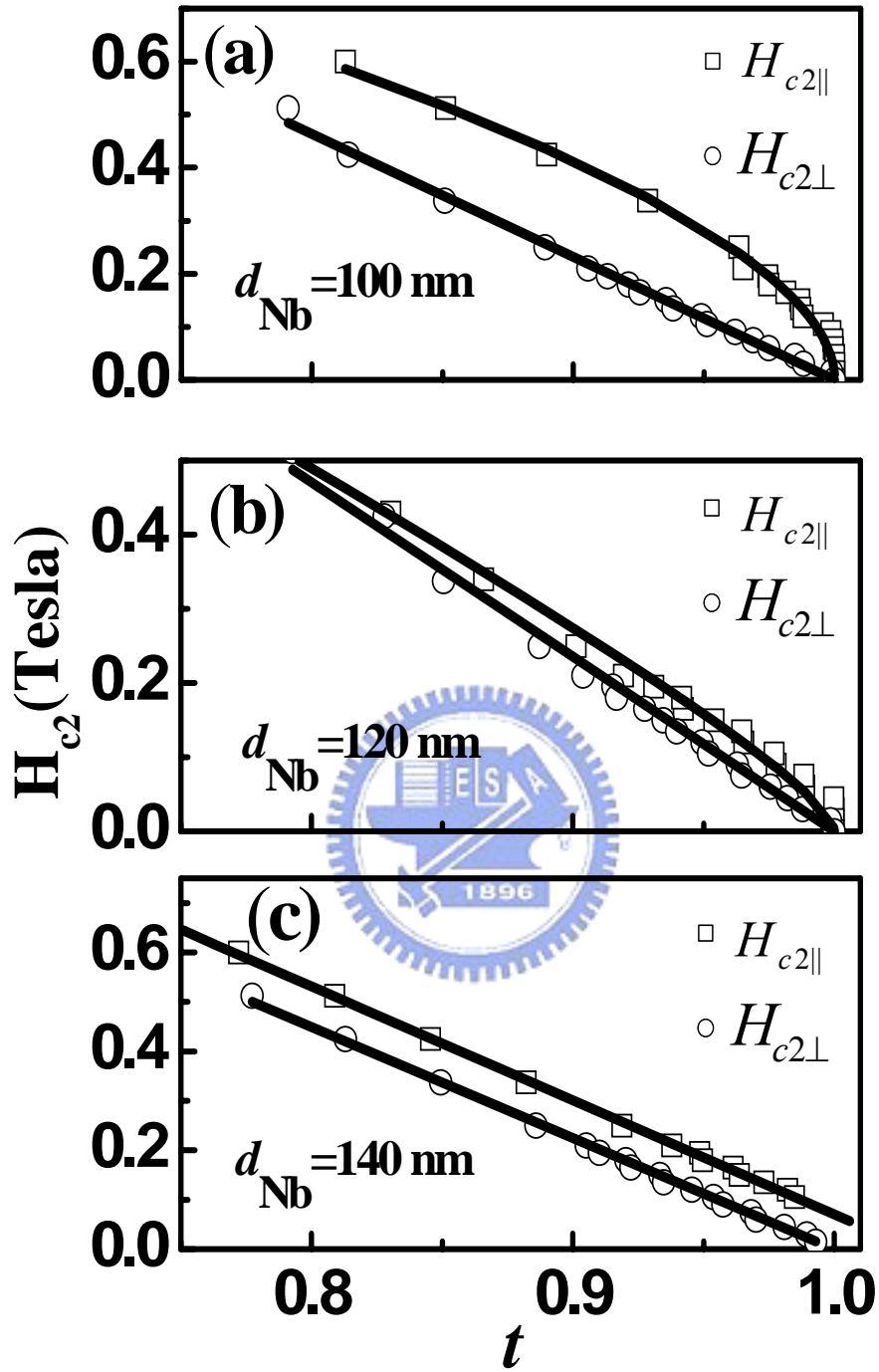


**Figure 6.4:**  $H_{c2}$  versus reduced temperature  $t$  for [Fe (20nm)/Nb ( $d_{\text{Nb}}$ )]<sub>6</sub>/Fe (20nm) multilayers with  $d_{\text{Nb}} = 100$  (a), 120 (b) and 140 nm (c).

### 6.1.3 Fe/Nb interface resistance by CPP measurement

In this section, we investigated the electron transport properties of interface between ferromagnet and superconductor with current flowing perpendicular to plane (CPP) at 4.2 K in Fe/Nb multilayers. When the bulk scattering is negligible in a ballistic contact, the transport properties are directly connected to the probabilities of scattering at the interface. In a ferromagnet with different numbers of spin-up and spin-down conduction channels, only a fraction of the majority channels can be Andreev reflected. However, experimental studies of  $F/S$  contacts in the diffusive limit are more intriguing and are more complex in unconventional proximity effects. [9] The resistance can either decrease or increase when cooling from above the critical temperature of superconductor. [10-12] Transport properties are governed by interplay between spin accumulation close to the interface and the Andreev reflection at the interface.

Each sample has  $N$  Fe/Nb repeated bilayers plus one layer of Fe, indicated as  $(\text{Fe/Nb})_N/\text{Fe}$ . The superconducting energy gap  $\Delta$  of Nb is smaller than the energy of the exchange fields in Fe by several orders of magnitude. Thus, the conventional proximity effect in ferromagnetic metals is negligible. All changes induced by the contact to a superconductor depended on the properties of the interface itself.

From the results of Section 6.1.1, the sputtered bulk Nb has a superconducting transition temperature of  $T_C = 9.2$  K. When Nb films are sandwiched between fixed Fe thickness,  $T_C$  decreases with decreasing Nb thickness. We have deduced the  $d_{\text{Nb}}^{\text{crit}} \approx 34$  nm from the analysis of our experimental data within the Radović's model under the single mode approximation. [13, 14] This means when Nb thickness is thinner than  $d_{\text{Nb}}^{\text{crit}} \approx 34$  nm, Nb is always normal, otherwise the Nb could become

superconductor in Fe/Nb multilayers based on the phase diagram of Fig. 6.3.

In the present CPP experiment, two series of samples were made with Nb thickness fixed at 15 and 80 nm separately, Fe thickness fixed at 20nm, and increasing numbers of bilayers. Plots of the product of the sample area  $A$  and total resistance  $R_T$  against bilayer number  $N$  are given in Fig. 6.5. The unit area CPP resistance  $AR_T$  is linearly proportional to the number of bilayers for both Nb thicknesses. The dash lines in Fig. 6.5 are least-squares fit to each set of data. Shukla *et al.*[15] calculated the interlayer exchange coupling between Fe layers when separated by Nb space layers, using a self-consistent full-potential linear augmented plane-wave (FLAPW) method. They observed an oscillating exchange coupling as a function of Nb spacer thickness with a period of 0.6 nm. However, we found that the Fe layer was not coupled across Nb in the Fe/Nb multilayer thin film with Nb thickness varied from 0.5 nm to 4 nm. [16] Since there is no antiferromagnetic coupling of Fe through Nb film, a one-band model could be applied. Therefore, the linear behavior of AR against  $N$  can be described as

$$AR_T = 2AR_{\text{Fe/Nb}(S)} + \rho_{\text{Fe}}t_{\text{Fe}} + N(\rho_{\text{Fe}}t_{\text{Fe}} + 2AR_{\text{Fe/Nb}(S)}), \quad (6.3)$$

for superconducting Nb and

$$AR_T = 2AR_{\text{Fe/Nb}(S)} + \rho_{\text{Fe}}t_{\text{Fe}} + N(\rho_{\text{Fe}}t_{\text{Fe}} + \rho_{\text{Nb}}t_{\text{Nb}} + 2AR_{\text{Fe/Nb}(NM)}), \quad (6.4)$$

for normal Nb. Here  $t$  is the thickness,  $\rho$  is the resistivity, and  $R_{\text{Fe/Nb}(NM),(S)}$  is the interface resistance between Fe and Nb layers for normal and superconducting states, respectively. According to individual fit, the equation is easy to be simplified as  $AR_T = C_1 + C_2N$  for normal Nb and  $AR_T = (N+1)C_1$  for superconducting Nb, with  $C_1 = 2AR_{\text{Fe/Nb}(S)} + \rho_{\text{Fe}}t_{\text{Fe}}$  and  $C_2 = 2AR_{\text{Fe/Nb}(NM)} + \rho_{\text{Fe}}t_{\text{Fe}} + \rho_{\text{Nb}}t_{\text{Nb}}$ . Similar analysis on Co/Nb multilayers has been presented in Chapter 3. [17] There is mutual uncertainty between  $C_1$  and  $C_2$ . We can perform a global fit to all data simultaneously since the

two sets of data share the same parameters. As shown in Fig. 6.5, the straight line gives  $C_1 = 7.1 \pm 1.3 f\Omega m^2$  and  $C_2 = 5.2 \pm 0.6 f\Omega m^2$ . The specific unit area resistance of one pair of interfaces can be derived to be  $2AR_{Fe/Nb(S)} = 5.9 \pm 0.3 f\Omega m^2$  and  $2AR_{Fe/Nb(NM)} = 2.8 \pm 0.4 f\Omega m^2$  by putting bulk resistivities  $6.2 \mu\Omega cm$  and  $8 \mu\Omega cm$  for 500 nm thick Fe and Nb at 10 K into Eq. (6.6). and Eq. (6.7). From the Pippard's model of partial quenching of Andreev reflection by impurities in the superconductor, the residual ( $S/NM$ ) boundary resistance can be written as  $2AR \propto \rho_s l_a$ , where  $l_a = (\frac{\pi}{2})\xi_s$  is the extinction length in  $S$  of the electron evanescent wave from  $NM$ ,  $\xi_s$  is the intrinsic coherence length in  $S$ , and  $\rho_s$  is the bulk resistivity when  $S$  is in the normal state just above  $T_c$ . [18, 19]

The value  $2AR_{Co/Nb(S)} = 6.3 \pm 0.9 f\Omega m^2$  for Co/Nb multilayer reported in Chapter 5 [17] is close to  $2AR_{Fe/Nb(S)} = 5.9 \pm 0.3 f\Omega m^2$  for Fe/Nb multilayer. This is expected from Pippard's model due to that  $AR$  is only proportional to the coherence length and resistivity in superconductor film.

Instead of using bulk resistivity, we also varied the Fe and Nb thickness while the numbers of bilayers were fixed at 6 and 12, respectively, to treat the CPP resistivities as fitting parameters. The CPP resistance is linearly proportional to the thickness for both Fe layer and Nb layer. Using one-band model, the linear behavior of  $AR$  against thickness can be written as

$$AR_T = 2AR_{Fe/Nb(S)} + 12AR_{Fe/Nb(NM)} + 6\rho_{Nb}t_{Nb} + 7\rho_{Fe}d_{Fe}, \quad (6.5)$$

for varying Fe thickness ( $d_{Fe}$ ) with Nb thickness fixed at 15 nm, and

$$AR_T = 2AR_{Fe/Nb(S)} + 24AR_{Fe/Nb(NM)} + 13\rho_{Fe}t_{Fe} + 12\rho_{Nb}d_{Nb}, \quad (6.6)$$

for varying Nb thickness ( $d_{Nb}$ ) with Fe thickness fixed at 20 nm. As shown in Figure

6.6(a) and (b), individual linear least-square fits of  $AR$  versus  $d_{Fe}$  and  $d_{Nb}$  samples yield a slope  $\rho_{Fe}$  of  $6.2 \mu\Omega cm$  and  $\rho_{Nb}$  of  $12 \mu\Omega cm$ , respectively. However, all the above equations share the same parameters. Therefore, we can perform a global fit to all data simultaneously to reduce the deviation. We can rewrite

$$\text{Eq. (6.3) as } AR_T = g_1 + Ng_2 + (N+1)t_{Fe}g_3 + Nt_{Nb}g_3,$$

$$\text{Eq. (6.4) as } AR_T = (N+1)g_1 + (N+1)t_{Fe}g_3,$$

$$\text{Eq. (6.5) as } AR_T = g_1 + 6g_2 + 7d_{Fe}g_3 + 6t_{Nb}g_3,$$

and

$$\text{Eq (6.6) as } AR_T = g_1 + 12g_2 + 13t_{Fe}g_3 + 6d_{Nb}g_3.$$

Here  $g_1$  is the  $2AR_{Fe/Nb(S)}$ ,  $g_2$  is the  $2AR_{Fe/Nb(NM)}$ ,  $g_3$  is the  $\rho_{Fe}$ , and  $g_4$  is the  $\rho_{Nb}$ . The results in Table 6.1 are two-parameter and four-parameter best fit values by using global fit. From the studies of transport properties of normal metal-superconductor ( $NM/S$ ) structures, it is established that the difference between the superconducting and normal state conductance ( $\delta G = G_{NM/S} - G_{NM/N}$ ) is negative for large  $NM/S$  interface resistance ( $R_{NM/S}$ ) and changes sign with decreasing  $R_{NM/S}$ . [20] In Table 6.1, we can find the  $2AR_{Fe/Nb(S)}$  is larger than  $2AR_{Fe/Nb(NM)}$ . The spin accumulation causes an additional voltage drop across the interface due to reduced spin transport into  $S$ . Therefore, the interface resistance of the  $F/S$  system should be larger than that of the  $F/NM$  system. We also observed that the CPP resistivity of Nb is bigger than bulk resistivity. This probably shows that the conduction electron scattering at grain boundaries is the main scattering process in our sputtered samples.

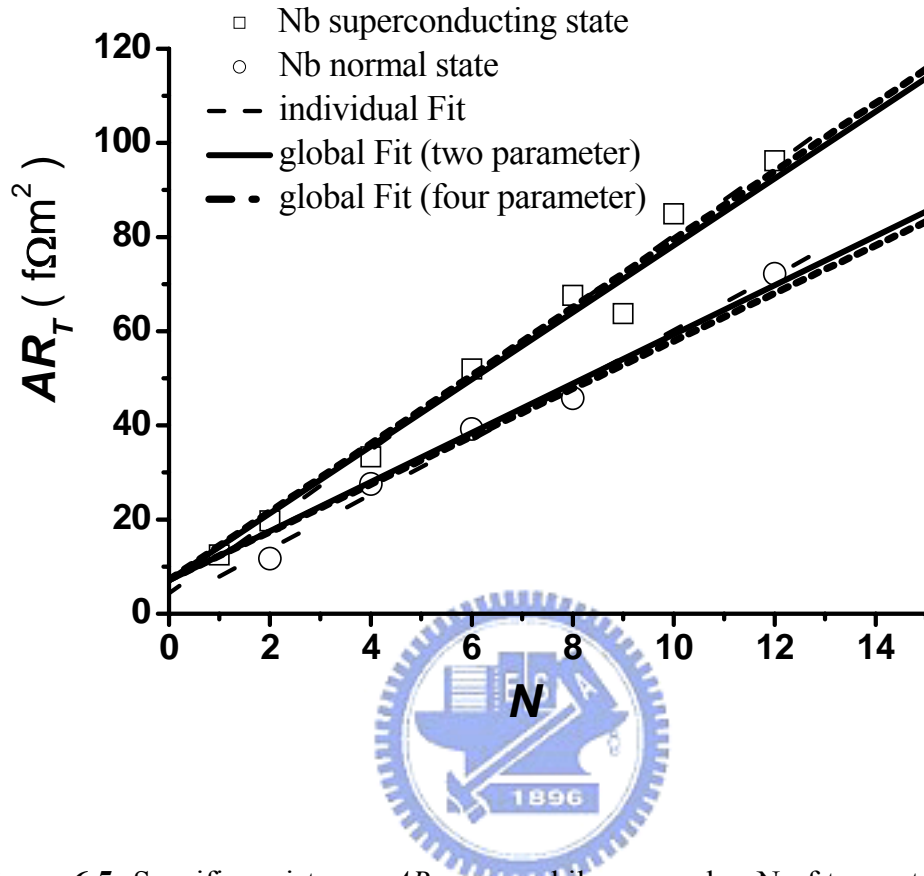


**Figure 6.5:** Specific resistance,  $AR_T$ , versus bilayer number  $N$  of two sets of samples with Nb thicknesses fixed at 15 nm and 80 nm, respectively. The dashed lines are linear least square fits to individual sets. The solid lines are global fit for two parameters and dash dot lines are global fit for four parameters to two sets of data simultaneously.



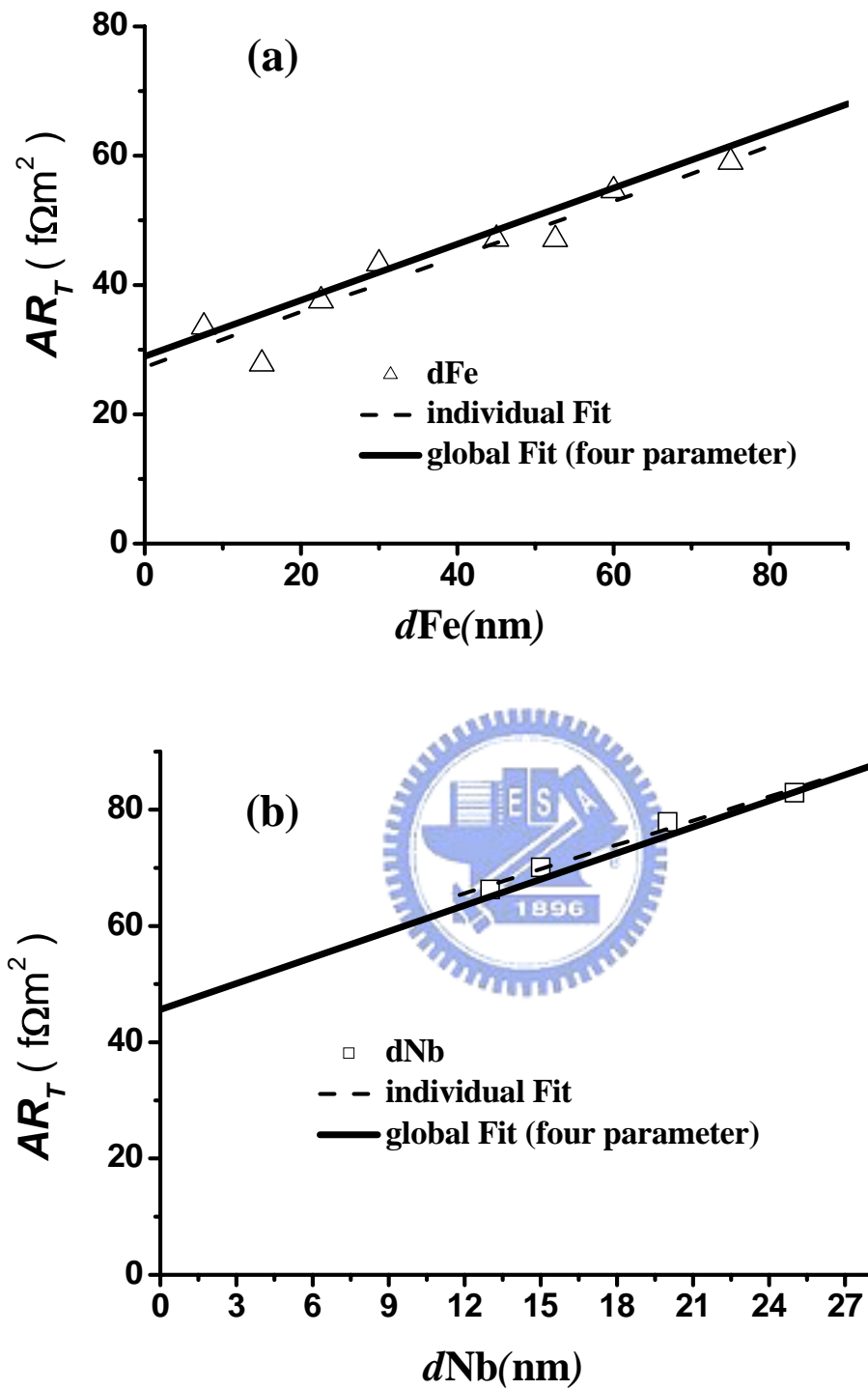


**Figure 6.6:** (a) Specific resistance,  $AR_T$ , versus Fe thickness with Nb thickness fixed at 15 nm and  $N=6$ . (b) Specific resistance,  $AR_T$ , versus Nb thickness with Fe thickness fixed at 20 nm and  $N=12$ . The dashed lines are linear least square fits to individual sets. The solid lines are global fit for four parameters to the data simultaneously.

Global fit	$2AR_S$ ( $f\Omega \text{ m}^2$ )	$2AR_N$ ( $f\Omega \text{ cm}$ )	$\rho_{\text{Fe}}$ ( $\mu\Omega \text{ cm}$ )	$\rho_{\text{Nb}}$ ( $\mu\Omega \text{ cm}$ )
Two parameters	$5.9 \pm 0.3$	$2.8 \pm 0.4$	$6.2 \pm 0.6^{\text{a}}$	$8 \pm 0.9^{\text{a}}$
Four parameters	$6.0 \pm 0.4$	$2.0 \pm 0.9$	$6.2 \pm 0.8$	$12.5 \pm 1.3$

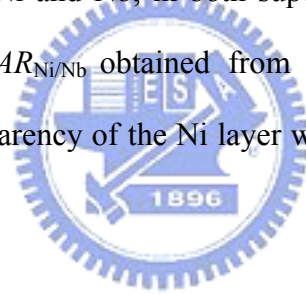
<sup>a</sup>Bulk values measured in 500 nm films.

**Table 6.1:** The best derived values and parameters for the Fe/Nb multilayers



## 6.2 Ni/Nb system

Rich interesting phenomena have been found in hybrids of superconductors ( $S$ ) and ferromagnets ( $F$ ) due to the proximity effect between competing orders in the interface. Many studies have been devoted to investigating both fundamental and applicative aspects of this field. [21] Recently, the unit area interface resistances,  $AR$  (area  $A$  times resistance  $R$ ), for both lattice-matched and lattice-mismatched pairs have become feasible to be calculated with no free parameters. [22] We study the proximity effect between fcc Ni and bcc Nb with mismatched lattice constant about 6.7 %. Current perpendicular to plan (CPP) measurement is used to determine interface resistance between Ni and Nb, in both superconducting and normal states. The quantitative values of  $AR_{\text{Ni/Nb}}$  obtained from the current work allow us to determine the interface transparency of the Ni layer without introducing any arbitrary fitting parameter.



### 6.2.1 The behavior of critical temperature for Ni/Nb trilayers

The details of sample preparation, sample geometry, and measuring techniques are reported in Chapter 3. [23] Figure 6.7 shows the  $T_C$  for Ni/Nb/Ni trilayers as a function of Nb thickness. The resistivities of bulk Nb and Ni, thicker than 500 nm, were 8 and 4  $\mu\Omega$  cm at 10 K. [24] However, the low-temperature resistivity of the film drastically increased with reducing thickness, as shown in the inset of Fig. 6.7. The thickness dependence of pure Ni resistivity could be described by the Fuchs-Sondheimer relation  $\rho(d) = \rho_B \left( 1 + \frac{3l}{8d} \right)$ , where  $\rho_B$  is the bulk resistivity. [25] The fit yields  $\rho_B = 4 \mu\Omega$  cm and the mean free path  $l$  about 180 nm. The  $T_C$  for Ni

(50 nm)/Nb( $d_S$ )/ Ni (50 nm) trilayers as a function of Nb layer thickness is shown in Fig. 6.7. The monotonically rapid reduction in  $T_C$  down to a critical thickness was fitted by Radovic's model. [26]

The spin splitting energy  $I_0 \approx 100$  meV for Ni [27],  $\gamma_F \approx 7.02 \times 10^{-3} J/K^2 \text{mole}$  [28], and  $\xi_F = \sqrt{\frac{4\hbar D_F}{I_0}} \approx 4.1$  nm are input parameters to model  $T_C(d_F)$ . Due to the fact that Ni has smaller splitting energy,  $\xi_F \approx 4.1$  nm is longer than the values  $\xi_{Fe} \sim 1.2$  nm and  $\xi_{Co} \sim 1.3$  nm obtained in Fe/Nb/Fe discussed in Section 6.1.1[29] and Co/Nb/Co [30] trilayer discussed in Chapter 5, respectively. A good fit for  $\xi_S \approx 19$  nm and  $\gamma \approx 0.1$  is shown as a solid line in Fig. 6.7. Moreover, it gives a critical thickness  $d_{\text{crit}}(\text{Ni}) = 45$  nm by extrapolating the fit to  $T_C=0$ .

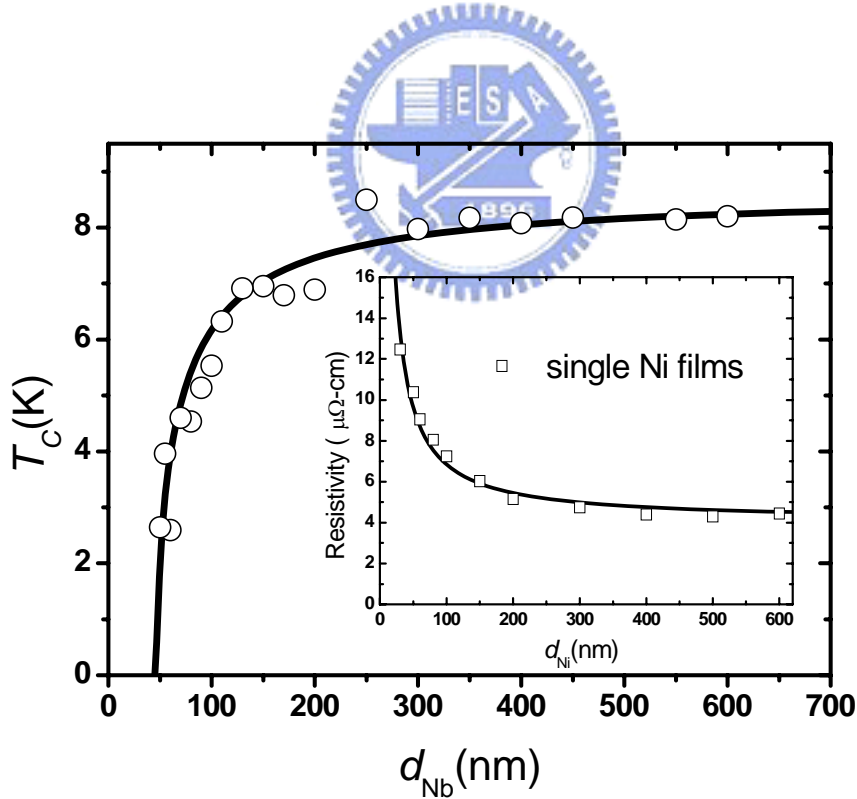


**Figure 6.7:** The superconducting critical temperatures for Ni/Nb/Ni trilayers as a function of  $d_{\text{Nb}}$ . The solid line is obtained from the theoretical fitting with parameters of  $\xi_S = 19$  nm, and  $\gamma = 0.1$ . Inset: thickness dependence of the low temperature resistivity as a function of the single Ni layer fitted by the Fuchs-Sondheimer relation.

## 6.2.2 The behavior of upper critical field for Ni/Nb multilayers

Another parameter to investigate the coupling phenomenon is the upper critical field  $H_{c2}$ , which gives the information on the coherence length and the dimensionality since  $H_{c2}$  reveals the role of the pair-breaking effect. According to the Ginzburg-Landau (G-L) theory, the perpendicular critical magnetic field for a superconducting film with thickness  $d_S$  shows linear temperature dependence,

$$H_{c2\perp} = \frac{\phi_0}{2\pi\xi_{//}^2(0)} \left(1 - \frac{T}{T_c}\right). \quad (6.7)$$

Here  $\phi_0$  is the flux quantum, and  $\xi_{//}(0)$  ( $\xi_{\perp}(0)$ ) is the zero temperature value of the G-L coherence length parallel (perpendicular) to the sample plane. The behavior of the parallel critical field  $H_{c2//}(T)$  can be described by a similar expression where  $\xi_{//}^2$  is replaced by  $\xi_{//}(0) \cdot \xi_{\perp}(0)$ . In the 3-dimensional (3D) regime, the temperature dependence of  $H_{c2//}(T)$  is described by  $H_{c2//} = \frac{\phi_0}{2\pi\xi_{//}(0)\xi_{\perp}(0)} \left(1 - \frac{T}{T_c}\right)$ , while in the 2-dimensional (2D) regime, the perpendicular coherence length  $\xi_{\perp}$  is larger than the thickness of the films, and  $H_{c2//}(T)$  is described by the Tinkham expression [31]

$$H_{c2//} = \frac{\sqrt{12}\phi_0}{2\pi\xi_{//}(0)d_S} \sqrt{\left(1 - \frac{T}{T_c}\right)}. \quad (6.8)$$

Samples with (Ni (50nm)/Nb( $d_S$ ))<sub>6</sub>/Ni (50nm), with  $d_S$  ranging from 20 to 600 nm, were measured. Figure 6.8 shows the temperature dependence of the  $H_{c2//}$  and  $H_{c2\perp}$  for  $d_{Nb}=60, 80, 100,$  and 130 nm. Data for the  $d_{Nb} = 60,$  and 80 are shifted to the left by  $T/T_c = 0.1$  and 0.2;  $d_{Nb} = 130$  nm are shifted to the right by  $T/T_c = 0.1$  in the x-axis for clarity. The solid lines are theoretical curves based on the G-L relation. The  $H_{c2\perp}$  follows a linear behavior for all thicknesses of Nb. It can be clearly seen that a gradual transition occurs from 2D to 3D behaviors as  $d_S$  increases from 100 nm to 130 nm, i.e., from a square-root behavior to a linear relation for the  $H_{c2//}$ . The

extrapolation yields a superconductor coherence length  $\xi_{GL}(0) = 12$  nm from the function  $\xi(0) = \sqrt{\phi/2\pi\beta T}$ , where  $\beta = -dH_{c2}/dT$ .

For comparison with other ferromagnets, the dimension crossover is 120 ~ 140 nm for Nb/Fe [29] and 145 ~ 185 nm for Nb/Co [30]. These values are listed in Table 6.2, confirming that the small crossover thickness is related to the relative weak pair-breaking effect since  $I_0(\text{Co}) > I_0(\text{Fe}) > I_0(\text{Ni})$ . The influence of the pair breaking effect is also observed from different values of critical thickness and related to interfacial transparency in the behavior of  $T_C$  dependence on  $S$  thickness. Detail discussion about critical thickness and interfacial transparency will describe in Chapter 7.

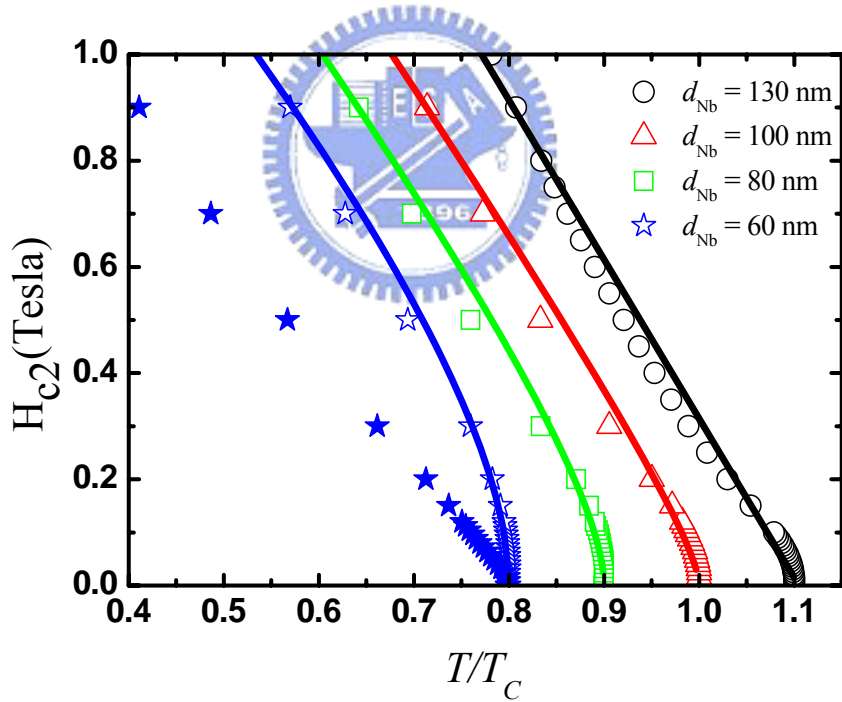


**Figure 6.8:** Temperature dependence of the parallel (open circles, triangles, squares, and stars) and perpendicular (filled stars) upper critical fields for Ni/Nb multilayers with  $d_{\text{Nb}} = 60, 80, 100,$  and  $130$  nm. Data for the  $d_{\text{Nb}} = 60,$  and  $80$  are shifted to the left by  $T/T_C = 0.1$  and  $0.2$ ;  $d_{\text{Nb}} = 130$  nm are shifted to the right by  $T/T_C = 0.1$  for clarity. The lines are least-square fit to describe the 3D to 2D crossover using the Ginzburg-Landau relation.

	Co	Fe	Ni
<b>Dimension crossover</b>	145~185 nm	120~140 nm	100~130 nm

**Table 6.2:** The dimension crossover thickness for Co/Nb, Fe/Nb and Ni/Nb.

### 6.2.3 Ni/Nb Interface resistance by CPP measurement

For CPP measurement, the sample is sandwiched between two circular Nb electrodes in order for the current uniformity to flow through the whole sample. In the insert of Figure 6.9 is the top view of geometry of CPP configuration where the top and bottom Nb strips are used for the four-point measurement. Each Nb strip and circular electrode is 200 nm thick in order to superconduct at the measuring temperature of 4.2 K. The total thickness and sample area  $A$  were verified with a stylus surface profiler.

According to the phase diagram of Fig. 6.7, when Nb thickness was thinner than  $d_{crit}$ , we had  $F/NM$  system; when Nb was thicker, we had  $F/S$  systems. In the present study, four series of CPP samples were made:

1. Ni(58 nm)/[Nb(108 nm)/Ni(58 nm)]<sub>N</sub> with the numbers of bilayers varied for superconducting state Nb;
2. Ni(78 nm)/[Nb(12 nm)/Ni(78 nm)]<sub>N</sub> with the numbers of bilayers varied for normal state Nb;
3. Ni( $d_{Ni}$ )/[Nb(27 nm)/Ni( $d_{Ni}$ )]<sub>7</sub> with 7 bilayers, and various Ni thickness;
4. Ni(78 nm)/[Nb( $d_{Nb}$ )/Ni(78 nm)]<sub>7</sub> with 7 bilayers, and various Nb thickness.

Figure 6.9 presents the total resistance  $AR_T$ , the unit area resistance on multilayer,

versus bilayer number,  $N$ , for the first two series of samples. The  $AR_T$  is linearly proportional to the number of bilayers for Nb both in the normal and superconducting state. Since there is no exchange coupling between Ni through Nb film, a one-band model would be sufficient to describe the linear behavior of  $AR_T$  versus  $N$  as follows

$$AR_T = 2AR_{F/S(S)} + \rho_F t_F + N(\rho_F t_F + \rho_S t_S + 2AR_{F/S(NM)}) \quad (6.9)$$

for normal Nb and

$$AR_T = 2AR_{F/S(S)} + \rho_F t_F + N(\rho_F t_F + 2AR_{F/S(S)}) \quad (6.10)$$

for superconducting Nb. Here  $t$ 's are the thicknesses, and  $AR_{F/S(NM),(S)}$ 's are the interface resistances between Ni and Nb layers for the normal and the superconducting state, respectively. From the series 3 and 4, the CPP resistivities can be determined by measuring the CPP resistance with varying layer thicknesses of Nb and Ni. Figure 6.10 and 6.11 show the  $AR_T$  behavior as a function of Ni and Nb thickness, respectively, for  $d_{\text{Nb}}$  is smaller than  $d_{\text{crit}}(\text{Ni})$  and 7 bilayers. Following Ohm's law, the total resistance is proportional to the thickness. When the Nb and Ni resistivities are independent of the layer thickness, the one-band model gives the linear behavior of  $AR_T$  versus thickness as

$$AR_T = 2AR_{F/S(S)} + 14AR_{F/S(NM)} + 7\rho_S t_S + 8\rho_F d_F, \quad (6.11)$$

for varying Ni thickness with Nb thickness fixed at 27 nm and

$$AR_T = 2AR_{F/S(S)} + 14AR_{F/S(NM)} + 7\rho_S d_S + 8\rho_F t_F, \quad (6.12)$$

for varying Nb thickness with Ni thickness fixed at 78 nm. The individual linear least square fits of  $AR_T$  versus  $d_{\text{Ni}}$  and  $d_{\text{Nb}}$  yield slopes  $\rho_{\text{Ni}}$  of 4.5 and  $\rho_{\text{Nb}}$  of 10  $\mu\Omega$  cm and are plotted as the dashed lines in Figure 6.10 and 6.11, respectively. Even though each series of samples could be individually fitted with the model, there is mutual uncertainty between different sets, as discussed earlier. Since the four sets of data



share the same parameters, we treat all resistivities and the interface resistance as fitting parameters to perform four-parameter global fit in order to reduce the discrepancy of interface resistance. The solid lines in Figures 6.9 to 6.11 are the best global fits for four parameters to all data and give  $\rho_{Ni}=4.2\pm0.3 \mu\Omega \text{ cm}$ ,  $\rho_{Nb}= 11\pm1.0 \mu\Omega \text{ cm}$ ,  $2AR_{Ni/Nb(NM)}=1.5\pm0.4 \text{ f}\Omega \text{ m}^2$ , and  $2AR_{Ni/Nb(S)}= 4.2\pm0.2 \text{ f}\Omega \text{ m}^2$ . The latter value is within experimental error of  $4.8\pm0.6 \text{ f}\Omega \text{ m}^2$  that reported by Fierz *et al.* [32] However, only recently the quality of interface has been added to model the interaction between the  $S$  and  $F$  layers. An important parameter of interface transparency,  $\gamma_b$ , has been used to describe the role of the boundary condition among different layers depending on interface imperfections, Fermi velocities, and band structure mismatch. [33] Here  $\gamma_b$  is defined as the ratio of interface resistance to the product of resistivity and the Cooper pair penetration depth in the  $F$ . It is usually treated as an adjustable parameter due to difficulties in direct measurements. [34] The transparency parameter was then calculated with  $\gamma_b = (AR_{F/S(NM)}/\rho_F\xi_F^*)$  without spin-flip scattering, where  $AR_{F/S(NM)}$  is the unit area resistance at normal state, and  $\rho_F$  is the resistivity of  $F$ .  $\xi_F^* = \sqrt{\frac{\hbar D_F}{2\pi K_B T_C}}$  is the penetration length which corresponds to the actual penetration depth of the Cooper-pairs in the  $F$  without considering the exchange field. We deduced the  $\gamma_b = 2.0$  for Ni/Nb as  $S$  is in the normal state.

When Nb is in the superconducting state, the  $AR_{Ni/Nb(S)}$  is larger than  $AR_{Ni/Nb(NM)}$  in the Ni/Nb system. A spin-up electron injected from a normal metal is retroreflected at the interface as a spin-down hole in order to form a Cooper pair in the  $S$ , which is described as the Andreev reflection. [35] If the normal metal is replaced by  $F$ , the Andreev current at  $S/F$  interface is partially suppressed by the exchange splitting of the conduction band in the ferromagnet. Moreover, the spin accumulation in the boundary of  $F$  leads to an additional voltage drop across the interface due to reduced

spin transport into  $S$ . This accounts for the finding that the interface resistance of Ni/Nb is larger in superconducting state than in the normal state.

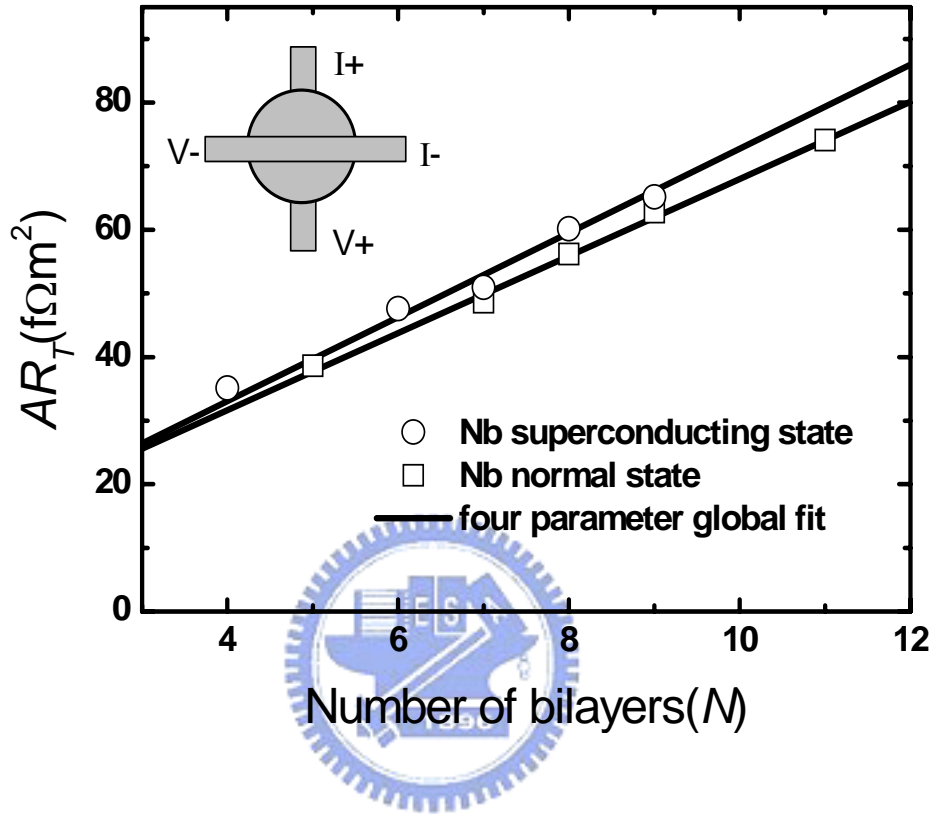


**Figure 6.9:** Unit area resistance,  $AR_T$ , versus bilayer number  $N$  measured at 4.2 K. The two sets of samples have Nb thickness fixed at 12 nm and 108 nm, respectively. The solid lines are global fits for four parameters to the data. Inset: the top view geometry of the current perpendicular to plane (CPP) configuration. Sample is sandwiched between the two circular Nb electrodes. The top and bottom Nb strips are used for the four-point measurement.

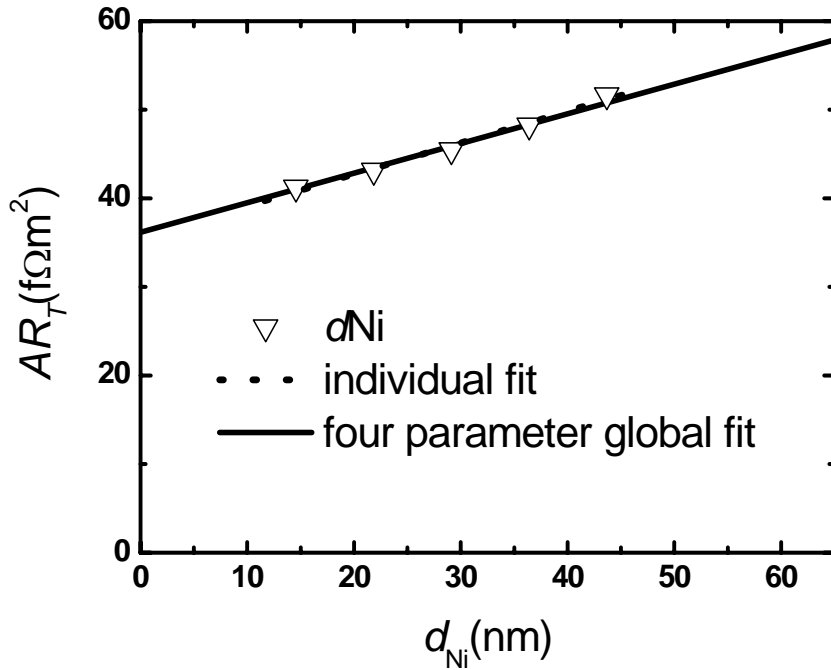


**Figure 6.10:** Unit area resistance,  $AR_T$ , versus Ni thickness with Nb thickness fixed at 27 nm and  $N = 7$  measured at 4.2 K. The dashed-line is linear least-square fit. The solid line is global fit for four parameters to the data.

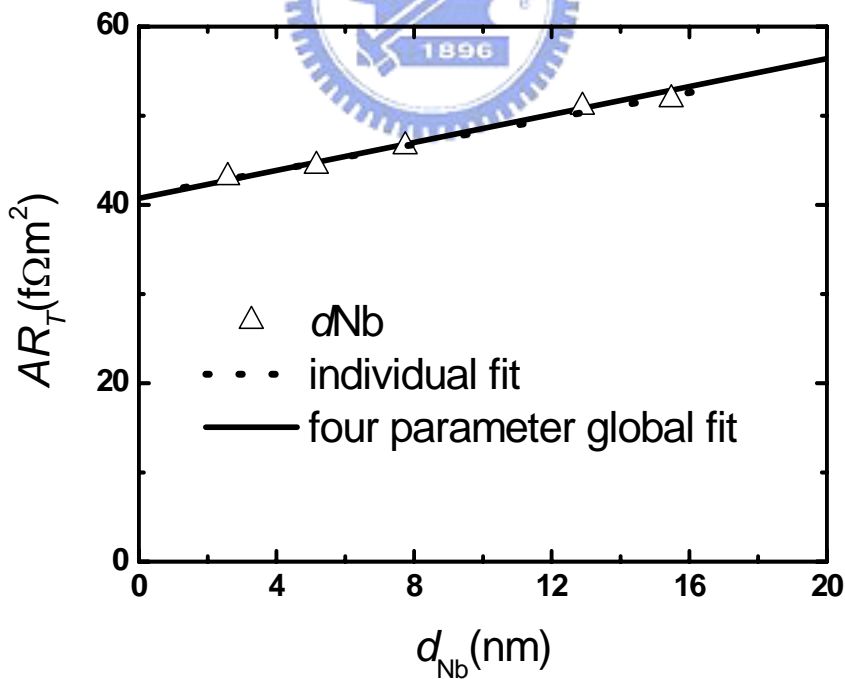


**Figure 6.11:** Unit area resistance,  $AR_T$ , versus Nb thickness with Ni thickness fixed at 78 nm and  $N = 7$  measured at 4.2 K. The dashed-line is linear least-square fit. The solid line is global fit for four parameters to the data.

## 6.3 Co/Nb, Fe/Nb, and Ni/Nb interface resistance calculated by First-Principle calculation

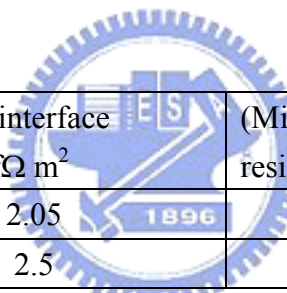
For comparison of interface resistances among different ferromagnets, Table 6.3 shows the interface resistance of Fe/Nb, Co/Nb and Ni/Nb from experimental values in the normal and superconducting state and list the lattice mismatch and lattice structure between  $S$  and  $F$ . When  $S$  is in the normal state, the smallest  $AR_{F/S(NM)}$  surprisingly comes from different lattice structures, bcc of Nb and fcc of Ni. We believe that this small  $AR_{F/S(NM)}$  should result from the less mismatch in lattice constant, even though the difference of interface resistance between Co, Ni and Fe is small. A similar result has also been observed on  $2AR_{Pd/Cu} \approx 0.9$  with 8% lattice mismatch in contrast to  $2AR_{Pd/Ag} \approx 0.7$  and  $2AR_{Pd/Au} \approx 0.5$  with 5 % lattice mismatch. [36] Furthermore, the results of previous reports on the *ab initio* calculation imply that the structure distortion and interface disorder are important for lattice mismatch systems. [37]

	$2AR_S$ ( $f\Omega m^2$ )	$2AR_{NM}$ ( $f\Omega m^2$ )	Lattice structure	Lattice mismatch	Calculation ( $f\Omega m^2$ )
Nb/Fe	$6.0 \pm 0.4$	$2.0 \pm 0.9$	bcc / bcc	$\sim 13.0 \%$	2.20
Nb/Co	$6.7 \pm 0.3$	$1.9 \pm 0.7$	bcc/ bcc(hcp)	$\sim 6 \%$	2.25(A), 1.58(B)
Nb/Ni	$4.2 \pm 0.2$	$1.5 \pm 0.4$	bcc / fcc	$\sim 1 \%$	2.11

**Table 6.3:** The interface resistance in superconducting and normal state for the Fe/Nb, Co/Nb, , and Ni/Nb.

Dr. K. Xia and W. Shuai have studied the Nb(110)/Fe(110), Nb(110)/Ni(111),

and Nb(110)/Co(111) interface resistance by *ab initio* calculation. In the Nb(110)/Fe(110) system, they construct a scattering system using 6x6 supercell Nb bulk and 7x7 Fe bulk for matching the interface. The lattice constants are 3.3 (Nb) and 2.83 (Fe) angstrom. Here they use the bulk potential for calculating the interface resistance. The majority interface resistance is  $2.25 \text{ f}\Omega \text{ m}^2$  and the minority is  $2.12 \text{ f}\Omega \text{ m}^2$ . In the Nb(110)/Co(111) system, here they build the system referring Ref. [38] and construct a unit cell. They deform BCC(110) and FCC(111) structure for matching BCC(110) and FCC(111) interface without considering the relaxation. The potentials are based on the bulk calculation. The lattice constants are 3.3 (Nb) and 3.5 (Co) angstrom. They use two types deformation for the Co/Nb system. One is the best for Nb atom the type A and the other one is for Co atom the typer B, as shown Table 6.4.



Type Nb/Co	(Majority) interface resistance $\text{f}\Omega \text{ m}^2$	(Minority) interface resistance $\text{f}\Omega \text{ m}^2$
A	2.05	2.25
B	2.5	1.58

**Table 6.4:** The interface resistance of Nb/Co by *ab initio* calculation.

For the Nb(110)/Ni(111) system, the configuration is similar to Nb(110)/Co(111). The lattice constants are 3.3 (Nb) and 3.5 (Ni) angstrom for matching interface. Here They only consider one configuration because the real Ni bulk lattice constant is 3.52 angstrom. The mismatch is less than 1%. The majority of the interface resistance is  $2.2 \text{ f}\Omega \text{ m}^2$  and the minority is  $2.0 \text{ f}\Omega \text{ m}^2$ . The results are listed in Table 6.3. These calculation values agree well with those by CPP measurements on sputtered polycrystalline multilayers. We conclude that the influence of the lattice mismatch is found to be more sensitive than the influence of the lattice structure on the interface

resistance when  $S$  is in the normal state.

## 6.4 Transport polarization

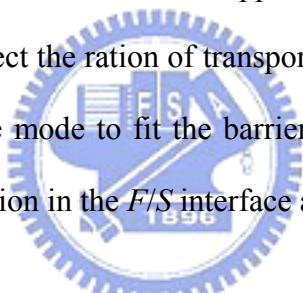
When Nb is in the superconducting state, the  $AR_{F/Nb(S)}$  is larger than  $AR_{F/Nb(NM)}$  (for instance in the Ni/Nb system). The modified BTK theory [39] used to explain the spectrum of metallic  $F/S$  point contact is based on the suppression of Andreev reflection by the spin imbalance of electron density of state in Ferromagnet. In the limit of a clean and ballistic contact, the spin polarization  $P$  is simply related to the conductance at zero bias,  $G(0)$ , and is normalized by the normal-state conductance,  $G(n)$ , as  $G(0)/G(n) = 2(1-P)$ . [40] In contrast, in our CPP samples, the thickness of single layer is smaller than the mean free path, but the number of transverse modes is enormous due to large area. From the theoretical calculation, the interface resistance can be explicitly described as

$$AR_{A/B} = \frac{Ah}{e^2} \left[ \frac{1}{\sum T_{\mu\nu}} - \frac{1}{2} \left( \frac{1}{N_A} + \frac{1}{N_B} \right) \right], \quad (6.13)$$

where  $T_{\mu\nu}$  are the probabilities for eigenstate  $\mu$  in material  $A$  to be transmitted through the interface into the eigenstate  $\nu$  in material  $B$ , and  $e^2/hN_{A(B)}$  is the Shrivin conductance of material  $A(B)$ . [41] Here, no coherent scattering exists between adjacent interfaces along the current direction. The interface transmission can be described as a conductance  $G_{A/B} = e^2/h \sum T_{\mu\nu}$ . [42] Our measurement can be used to derive the transport  $P$  of Ni, about 49 % through the ratio of interface transmission between the superconducting and the normal state, if

$$\frac{(T_{A/B})_S}{(T_{A/B})_N} = \frac{AR_{F/S(N)} + \rho_F \ell_F^{sf} + \rho_S \ell_S^{sf}}{AR_{F/S(S)} + \rho_F \ell_F^{sf}} = 2(1-P) \quad (6.14)$$

is assumed, where  $\ell_{S(F)}^{sf} = \sqrt{l_N \lambda_{sf}} / 6$  is the spin diffusion length and we take  $l_{Nb}^{sf} = 25_{-5}^{+\infty}$  nm and  $\ell_{Ni}^{sf} = 21 \pm 2$  nm for experimental result by CPP-MR using superconducting cross strips and exchange-biased spin valves. [43]  $\ell_{S(F)}^{sf}$  is the dominated length scale in the CPP measurement with current perpendicular to the plane as described in Section 2.1. [44] This value is larger than 46.5 % [45] for Ni foil and 37 % [46] for Ni thin film from the Nb/Ni point contact in the PACR measurement. Table 6.5 list the polarization of Co, Fe and Ni calculated by Eq. 6.21 through the normal and superconducting state interface resistance. We argue that the transport polarization is overestimated due to the assumption of zero barrier strength  $Z$  between interfaces. The Andreev reflection suppressed by spin-polarized metals is not the only mechanism to affect the ration of transport probabilities. More theoretical works on a more approximate mode to fit the barrier strength  $Z$  and distinguish the contribution of spin accumulation in the  $F/S$  interface are needed.



	Co	Fe	Ni
Spin diffusion length	59±18 nm	8.5±1.5 nm	21±2 nm
Transport polarization	0.54 %	0.56 %	0.49 %

**Table 6.5:** The transport polarization of Co, Fe and Ni extracted from interface resistance.

## References:

1. Th. Mühge, N. N. Garif'yanov, Yu. N. Goryunov, G. G. Khaliullin, L. R. Tagirov, K. Westerholt, I. A. Garifullin, and H. Zabel, Phys. Rev. Lett. **77**, 1857 (1996); Phys. Rev. B **55**, 8945 (1997); **57**, 5071 (1998).
2. G. Verbanck, C. D. Potter, V. Metlushko, R. Schad, V. V. Moshchalkov, and Y. Bruynseraede, Phys. Rev. B **57**, 6029 (1998).
3. Z. Radović, L. Dobrosavljević-Grujić, A. I. Buzdin, and J. R. Clem, Phys. Rev. B **38**, 2388 (1988).
4. Jun-Jih Liang, S. F. Lee, W. T. Shih, W. L. Chang, C. Yu, and Y. D. Yao, J. Appl. Phys. **92**, 2624 (2002).
5. S. F. Lee, Y. Liou, Y. D. Yao, W. T. Shih, and C. Yu, J. Appl. Phys. **87**, 5564 (2000).
6. A. B. Pippard, Rep. Prog. Phys. **23**, 176 (1960).
7. C. Kittel, *Introduction to Solid State Physics*, (Wiley, New York, 1986), p. 144.
8. M. Tinkham, *Introduction to Superconductivity*, (McGraw-Hill. New York, 1975).
9. C. J. Lambert and R. Raimondi, J. Phys. Condens. Matter **10**, 901 (1998); A. I. Buzdin, Rev. Mod. Phys. **77**, 935 (2005)
10. V. T. Petrashov, I. A. Sosnin, I. Cox, A. Parsons, and C. Troadec, Phys. Rev. Lett. **83**, 3281 (1999).
11. M. Giroud, H. Courtois, K. Hasselbach, D. Mailly, and B. Pannetier, Phys. Rev. B **58**, R11872 (1998).
12. J. Aumentado and V. Chandrasekhar, Phys. Rev. B **64**, 054505 (2001).
13. Z. Radovic', L. Dobrosavljevic'-Grujic', A. I. Buzdin, and J. R. Clem, Phys. Rev. B **38**, 2388 (1988).
14. S. Y. Huang, S. F. Lee, Jun-Jih Liang, C. Y. Yu K. L. You, T. W. Chiang, S. Y.



- Hsu and Y. D. Yao J. Magn. Mater. **304**, e81 (2006)
15. Nitya Nath Shukla and R. Prasad, Phys. Rev. B. **70**, 014420 (2004)
  16. 游駿毅 中正大學物理系碩士論文 (2003).
  17. S. F. Lee, S. Y. Huang, J. H. Kuo, Y. A. Lin, and Y. D. Yao, J. Appl. Phys. **93**, 8212 (2003).
  18. A. B. Pippard Proc. R. Soc. London, Ser. A **391** 225 (1981).
  19. S. Y. Huang, S. F. Lee, J. C. Huang, G. H. Hwang, and Y. D. Yao J. Appl. Phys. **97**, 10B103 (2005) .
  20. R. Seviour and C. J. Lambert and A. F. Volkov, Phys. Rev. B **58**, 12338 (1998).
  21. A. I. Buzdin, Rev. Mod. Phys. **77**, 935 (2005).
  22. P. C. Xu and K. Xia, Phys. Rev. B **74**, 184206 (2006).
  23. S. Y. Huang, S. F. Lee, S. Y. Hsu, and Y. D. Yao, Phys. Rev. B **76**, 024521 (2007).
  24. 邱昱哲 臺灣大學物理系碩士論文 (2008).
  25. E. H. Sondheimer, Phys. Rev. **80**, 401 (1950).
  26. Z. Radović, M. Ledvij, L. Dobrosavljević-Grujić, A. I. Buzdin, and J. R. Clem, Phys. Rev. B **44**, 759 (1991).
  27. J. W. A. Robinson, S. Piano, G. Burnell, C Bell, and M. G. Blamire, Phys. Rev. **76**, 094522 (2007).
  28. C. Kittel, *Introduction to Solid State Physics* (Wiley, New York, 1986), p. 144.
  29. S. Y. Huang, S. F. Lee, J. J. Liang, C. Y. Yu, K. L. You, T. W. Chiang, S. Y. Hsu, and Y. D. Yao, J. Magn. Mater. **304**, e81-e93 (2006)
  30. J. J. Liang, S. F. Lee, W. T. Shih, W. L. Chang, C. Yu, and Y. D. Yao, J. Appl. Phys. **92**, 2624 (2002).
  31. M. Tinkham, *Introduction to Superconductivity* (McGraw-Hill, New York, 1975).

32. C. Fierz, S. F. Lee, W. P. Pratt, Jr., P. A. Schroder, and J. Bass, *J. Phys.: Condes. Matter* **2**, 1224 (1991).
33. R. Gross et al. (eds.), *Nanoscale Devices - Fundamentals and Applications*, (Springer, 2006), p. 241–249.
34. Ya. V. Fominov, N. M. Chtchelkatchev, and A. A. Golubov, *Phys. Rev. B* **66**, 012507 (2002).
35. G. E. Blonder, M. Tinkham, and T. M. Klapwijk, *Phys. Rev. B* **25**, 4515 (1982)
36. C. Galinon, K. Tewolde, R. Loloee, W.-C. Chiang, S. Olson, H. Kurt, W. P. Pratt, Jr., and J. Bass, *Appl. Phys. Lett.* **86**, 182502 (2005).
37. P. C. Xu and K. Xia, *Phys. Rev. B* **74**, 184206 (2006).
38. H van Leuken, A Loddert and R A. de Groot, *J. Phys.: Condes Matter* **3**, 7651 (1991)
39. G. J. Strijkers, Y. Ji, F. Y. Yang, C. L. Chien, and J. M. Byers, *Phys. Rev. B* **63**, 104510 (2001).
40. R. J. Soulen, Jr., J. M. Byers, M. S. Osofsky, B. Nadgorny, T. Ambrose, S. F. Cheng, P. R. Broussard, C. T. Tanaka, J. Nowak, J. S. Moodera, A. Barry, and J. M. D. Coey, *Science* **282**, 85 (1998).
41. K. Xia, P. J. Kelly, G. E. Bauer, I. Turek, J. Kudrnovsky, and V. Drchal, *Phys. Rev. B* **63**, 064407 (2001).
42. P. X. Xu, K. Kia, M. Zwierzycki, M. Talanana, and P.L.Kely, *Phys. Rev. L* **96**, 176602 (2006).
43. J. Bass and W. P Pratt Jr, *J. Phys.: Condens. Matter* **19**, 183201 (2007).
44. Wen-C. Chiang, C. Ritz, K. Eid, R. Loloee, W. P. Pratt, Jr., and J. Bass, *Phys. Rev. B* **69**, 184425 (2004).
45. R. J. Soulen, J. Byers, M. S. Osofsky, B. Nadgorny, T. Ambrose, S. F. Cheng, P. Broussard, C. T. Tanaka, J. Nowak, J. S. Moodera, et al., *Science* **282**, 85 (1998).

46. Y. Ji, G. J. Strijkers, F. Y. Yang, C. L. Chien, J. M. Byers, A. Anguelouch, Gang Xiao, and A. Gupta, Phys. Rev. L **86**, **5585** (2001).



## Chapter 7

### Results and Discussion-Weak Ferromagnet:

#### $\text{Cu}_{0.5}\text{Ni}_{0.5}/\text{Nb}$ System

Recent discovery of superconductivity with a relatively high transition temperature in the iron-based layered structure has generated tremendous interest in the superconductivity and ferromagnetism fields, though the question of the existence of the ferromagnetic phase in this system is still open. [1] Nevertheless, the coexistence of superconductivity and ferromagnetism has been investigated at the junction of a superconductor ( $S$ ) and a ferromagnet in terms of bilayers, trilayers, and multilayers structure, which have been discussed in Chapter 2. [2] The controversy in such system is that the exchange field in the ferromagnetism is expected to break the time-reversal symmetry of a Cooper pair and suppress superconductivity. The singlet superconductor ( $S$ ) prefers an antiparallel spin orientation to forming Cooper pairs, while the order of ferromagnet ( $F$ ) forces the spins to align in parallel. Because superconductivity and ferromagnetism are two competing orders, their coexistence, as explained by Fulde, Ferrel, Lark, and Ovchinnikov, is only possible in a narrow interval in phase space by proximity effect. [2-4] Recently, advances in the fabrication of artificial  $F/S$  layered structure enable researchers to study this effect from both the fundamental and the applicative aspects when the two interaction orders are spatially separated. In the layered structure, the spatial variation of the superconducting order parameter in the ferromagnet arises from the energy shift between the quasiparticles of the pair caused by the presence of the exchange field  $E_{ex}$ . As a consequence, the superconducting wavefunction not only decays in the  $F$  layer but also oscillates over a length scale, in the direction perpendicular to the interface. Striking effects in the  $F/S$

layered structure include the nonmonotonic oscillation for the dependence of superconducting critical temperature ( $T_C$ ) [5, 6] and critical current ( $I_C$ ) [7-9] on the thickness of the  $F$  layer,  $d_F$ , and even the reentrant superconducting behavior [10, 11]. Various unusual phenomena occur in the CuNi/Nb system due to the oscillation of the  $S$  pairing wave function in  $F$  (see [2, 12] for recent reviews). In order to reliably control ferromagnetic thickness over a large range to study  $S/F/S$  junction, it is essential to have a weak ferromagnetic metal. [7,8] In addition, to study the possibility of quasiparticles mediated coupling in the  $F/S/F$  spin valve structure, the  $S$  layer is expected to be thin. [13-15]

The quality of the interface is important for understanding the coupling mechanism between the  $S$  and the  $F$ . Lately, interfacial transparency  $T_{tran}$ , has been included in the analysis of the interfacial quality and is considered to play a dominant role in the boundary condition in layered structures. While  $T_{tran} = 1$  indicates a perfect interface, the value of  $T_{tran} < 1$  signifies the decrease in the amplitude of the order parameter. It implies that the electrons are apt to be reflected rather than transmitted at the interfaces, which may reduce the strength of the proximity effect [16,17] It is clear that the non-perfect transparency depends on both extrinsic and intrinsic factors such as interface imperfection, Fermi velocities, and band-structure mismatches. By including the interfacial transmission coefficient in the proximity theory, the discrepancy between the experimental results and the theoretical prediction under a perfect interface assumption would be reconciled. Attanasio *et al.* have studied the interfacial transparency for different layered structures, with Nb as a superconductor, Cu, Ag, and Pd as normal metals, and PdNi and Fe as ferromagnetic materials to investigate the effect of the fabrication method on  $T_{tran}$  by sputtering and molecular beam epitaxy. Their results showed that the interfacial transparency was influenced by intrinsic factors related to the microscopic properties of the two metals across the

interface rather than by the fabrication method. [18] Although the interfacial transparency is important both from the theoretical and experimental points of view, it is usually treated as an adjustable parameter  $\gamma_b$ , in terms of the ratio of interface resistance to the product of resistivity and the Cooper pair penetration depth in the  $F$ , due to great difficulties in direct measurements. [15-22]

In this section, we attempt to analyze the  $F/S$  proximity effect accounting for the interfacial transparency both qualitatively and quantitatively. The study reports the proximity effect between a weak ferromagnet ( $F$ ) and a superconductor ( $S$ ) in a sputtered  $\text{Cu}_{0.5}\text{Ni}_{0.5}/\text{Nb}$  layered system. Weak ferromagnetic layers of  $\text{Cu}_{0.5}\text{Ni}_{0.5}$  are essential to achieve appropriate exchange energy in a suitable window of experimental phase space. We deduced superconductor critical thickness, below which superconductivity vanishes, by analyzing the data in terms of proximity theory. High interfacial transparency is derived from the behavior of the superconducting critical temperature as a function of the  $S$  and  $F$  layer thicknesses. Strong pair breaking effect as a result of the high interface quality influences the spatial dimensional crossover and the flux pinning mechanism in the temperature dependence of upper critical magnetic field,  $H_{c2}$ . Using CPP (the current perpendicular to plane measurement) with a series resistor model, the unit area resistance for one pair of  $\text{Cu}_{0.5}\text{Ni}_{0.5}/\text{Nb}$  interface can be extracted when Nb is in the superconducting and normal states by varying its thickness. The interfacial transparency related to the interface resistance is quantitatively discussed. Close correlation between the interfacial transparency and the interface resistance is demonstrated.

## 7.1 The behavior of critical temperature fitted by Radovic's model

Several series of  $\text{Cu}_{0.5}\text{Ni}_{0.5}/\text{Nb}$  trilayers and multilayers samples were fabricated. In order to investigate the proximity effect between Nb and  $\text{Cu}_{50}\text{Ni}_{50}$  in a decoupled regime, we would discuss the series of samples as follows: (1)  $\text{Cu}_{0.5}\text{Ni}_{0.5}/\text{Nb}(d_S)/\text{Cu}_{0.5}\text{Ni}_{0.5}$  trilayers with  $\text{Cu}_{50}\text{Ni}_{50}$  thickness fixed at 50 nm and (2)  $\text{Cu}_{0.5}\text{Ni}_{0.5}/\text{Nb}$  multilayers denoted as  $(\text{Cu}_{0.5}\text{Ni}_{0.5}/\text{Nb}(d_S))_6/\text{Cu}_{0.5}\text{Ni}_{0.5}$  with  $\text{Cu}_{0.5}\text{Ni}_{0.5}$  thickness fixed at 20 nm. The critical temperature  $T_C$  and the critical field  $H_{c2}$  as a function of temperature were resistively measured in a  $^4\text{He}$  cryostat.

The  $T_C$  for  $\text{Cu}_{0.5}\text{Ni}_{0.5}/\text{Nb}(d_S)/\text{Cu}_{0.5}\text{Ni}_{0.5}$  trilayers as a function of  $d_{\text{Nb}}$  are shown in Fig. 7.1. With decreasing  $d_{\text{Nb}}$ ,  $T_C$  exhibited a monotonically rapid reduction down to a critical thickness  $d_{\text{crit}}$ . We first analyzed the behavior of  $T_C(d_S)$  in the framework of the theoretical model developed by Radvoić *et al.* [23] In this way, using the electronic specific heat coefficients  $\gamma(\text{Cu}_{0.5}\text{Ni}_{0.5}) \approx 4.2 \times 10^{-3} \text{ J/K}^2 \text{ mole}$  [24],  $\rho_F \approx 61 \text{ } \mu\Omega \text{ cm}$ , and the spin splitting energy  $I_0 \approx 6 \text{ meV}$ , the  $\text{Cu}_{0.5}\text{Ni}_{0.5}$  coherence length is evaluated to be  $\xi_F = 4.9 \text{ nm}$ . The result of the theoretical simulations obtained for the trilayer system with  $\gamma = 0.1$ ,  $\xi_S = 16 \text{ nm}$ , and  $T_{CS} = 8.7 \text{ K}$  is shown as the solid line in Fig. 7.1. By extrapolating the fit to  $T_C = 0$ , the critical thickness is  $d_{\text{crit}}(\text{Cu}_{0.5}\text{Ni}_{0.5}) = 35 \text{ nm}$ . For the purpose of comparison, the critical thicknesses were about 30 nm and 34 nm for Co/Nb/Co [25] and Fe/Nb/Fe [26] trilayers, respectively. It is found that the critical thickness for the weak ferromagnet is not smaller than those for the strong ferromagnet. For weak magnetic  $\text{V}_{1-x}\text{Fe}_x$  system, the large critical thicknesses have also been observed. [19] We then investigated the physical mechanism that caused this large thickness in the  $\text{Cu}_{0.5}\text{Ni}_{0.5}/\text{Nb}$  system with weak ferromagnet.

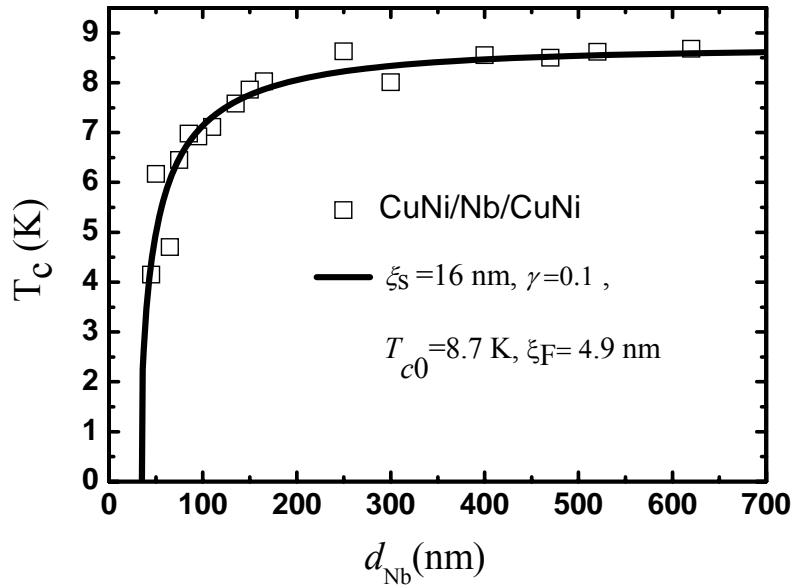


**Figure 7.1:** Superconducting critical temperatures for  $\text{Cu}_{0.5}\text{Ni}_{0.5}/\text{Nb}/\text{Cu}_{0.5}\text{Ni}_{0.5}$  trilayers as a function of  $d_{\text{Nb}}$ . The solid line is obtained from the theoretical fitting with parameters  $\xi_S = 16$  nm,  $\gamma = 0.1$ , and  $T_{c0} = 8.7$  K.

Aarts *et al.* [19] proposed that the behavior of the critical thickness for the  $F/S/F$  case was a function of the parameters  $\gamma$  and  $\gamma_b$ . The parameter  $\gamma_b$  described the quality of the interface barrier. When  $\gamma$  was as small as in our case, the “proximity leak” was large. It required a low barrier (high  $T_r$ , small  $\gamma_b$ ) to increase the critical thickness. Potensa *et al.* [27] reported  $\gamma_b = 0.6$  and Fominov *et al.* obtained a value of 0.3 when fitting the  $T_C$  behavior of CuNi/Nb bilayer data. [28] These values for CuNi/Nb were much smaller than  $\gamma_b = 1.6$  for Co/Nb system obtained from direct interface resistance measurements in Chapter 5. [29] In the next section, we tried to analyze and study the  $F/S$  proximity effect that accounted for the interfacial transparency both qualitatively and quantitatively.



## 7.2 Fitted by Fominov's model in terms of interface transparency

To characterize the properties of the  $F$  films, magnetic moment measurement was performed on a series of  $\text{Cu}_{0.5}\text{Ni}_{0.5}$  single layers using a commercial SQUID magnetometer with magnetic fields applied parallel to the sample surface. Figure 7.2 shows the Curie temperature  $T_{Curie}$  versus the  $\text{Cu}_{0.5}\text{Ni}_{0.5}$  thickness, which was derived from the temperature dependence of the magnetization  $M$  with field-cooled and zero-field-cooled measurement at 30 Oe. The  $T_{Curie}$  was about 80~110 K in agreement with the results reported for bulk samples at this concentration. [30] The saturation magnetization  $M_{sat}$  of  $\text{Cu}_{0.5}\text{Ni}_{0.5}$  estimated from the hysteresis loop at 5 K was about  $0.1 \mu_B/\text{atom}$  as shown in the right inset of Figure 7.2. There was no clear indication of thickness dependence on  $T_{curie}$  and  $M_{sat}$  as  $d_{\text{CuNi}}$  larger than 7 nm.

Based on the weak ferromagnetic nature of  $\text{Cu}_{0.5}\text{Ni}_{0.5}$  ascertained by magnetic measurement and the good quality of the interface verified by the transmission electron microscopy (TEM) image shown in the left inset of Fig. 7.2, the rather large critical thickness for the  $\text{Cu}_{0.5}\text{Ni}_{0.5}/\text{Nb}/\text{Cu}_{0.5}\text{Ni}_{0.5}$  trilayers could be attributed to the high interfacial transparency at the  $F/S$  interface. We know the solid line in Fig. 7.1 could be fitted under a perfect interface assumption developed by Radvoic *et al.* [23], as described in Section 7.1. Although the solid line described well the critical temperature, the approximation of a perfect interface was hardly fulfilled because the Cooper pair with opposite spins could not match the Fermi momentum of the energy-split subbands in a ferromagnet. This mismatch of Fermi vector might reduce the transmission across the interface. The interfacial transparency between two metals with different Fermi energies was a quantum mechanical problem of reflection and

transmission of charge which was carried at the interface. [31]

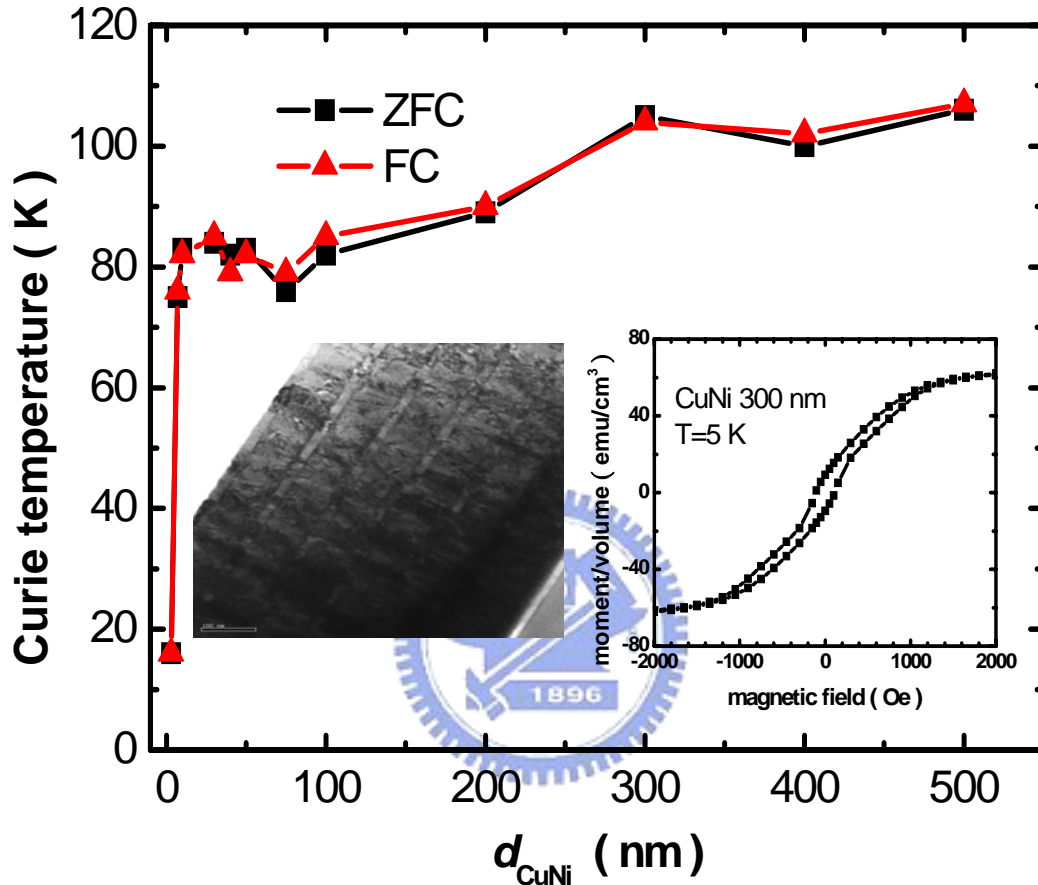


**Figure 7.2:** Curie temperature versus  $\text{Cu}_{0.5}\text{Ni}_{0.5}$  layer thickness. The solid line is meant to guide the eye. Inset (right): magnetic hysteresis loop for  $\text{Cu}_{0.5}\text{Ni}_{0.5}$  thickness of 300 nm at  $T=5$  K. Inset (left): the cross-section TEM image of a  $[\text{Cu}_{0.5}\text{Ni}_{0.5} 20 \text{ nm}/\text{Nb} 100 \text{ nm}]_6/\text{Cu}_{0.5}\text{Ni}_{0.5} 20 \text{ nm}$  multilayer sample.

In order to investigate the microscopic proximity effect of the interface, we adopted a more general theoretical model developed by Fominov *et al.* to analyze the behavior of both  $T_c(d_s)$  and  $T_c(d_f)$ . [17] In the dirty-limit, we extend the Fominov's model from bilayer system to trilayer system by calculating the critical temperature of

superconductor embedded between two Ferromagnet layers within the linearized Usadel equation. The boundary condition for trilayer system is given by

Kupriyanov and Lukichev [32]:

$$\xi_S \frac{dF_S}{dx} \Big|_{\text{if}} = \gamma \xi_F^* \frac{dF_F}{dx} \Big|_{\text{if}}, \quad \gamma = \frac{\rho_S \xi_S}{\rho_F \xi_F^*}, \quad (7.1)$$

$$\xi_F^* \gamma_b \frac{dF_F}{dx} \Big|_{\text{if}} = [F_S(0) - F_F(0)] \Big|_{\text{if}}, \quad \gamma_b = \frac{R_b A}{\rho_F \xi_F^*}. \quad (7.2)$$

Here the physical meaning of  $\gamma$  was the strength of the proximity effect between the  $F$  and  $S$  metals.  $\rho_S$  and  $\rho_F$  were the low temperature residual resistivities of  $S$  in the normal state and  $F$ , respectively.

$$\xi_F^* = \sqrt{\frac{\hbar D_F}{2\pi k_B T_{CS}}} \quad (7.3)$$

was a spatial scale related to the diffusive motion of the Cooper pair in the  $F$  layer without considering the exchange field, where  $k_B$  was the Boltzmann constant.  $A$  was the sample area and  $R_b$  was the normal-state resistance of  $S/F$  boundary. If we wrote the conductance per unit area as  $1/R_\alpha$  and considered the conduction in parallel with perpendicular transport, the total conductance of a boundary could be described as

$$\frac{1}{R_b} = \sum_i \delta A_i \left( \frac{1}{R_\alpha} \right) = \frac{A}{R_\alpha}$$

by summing over the total sample area  $A$ . The value of  $AR_b$  represented the interface resistance per unit area, since in the case of CPP transport the conduction was in parallel. Thus, the interfacial transparency parameter  $\gamma_b$  in Eq. (7.9) was proportional to  $AR_b$ , when the superconductor is in the normal state. It should be essential to note that Radovic's model adopted a boundary condition of high-quantum-mechanical transparency at the  $F/S$  interface, so the pairing function varied continuously at the interface, as indicated by  $F_S = F_F$ . In the present work, the boundary condition implied a jump of the pairing function depending on the magnitude of  $\gamma_b$ . Furthermore, the boundary conditions at the outer surfaces were

$\left. \frac{dF_S}{dx} \right|_{os} = \left. \frac{dF_F}{dx} \right|_{os} = 0$ , accounting for the absence of the pairing function current through the outer surface of the trilayer. In the single-mode approximation, we obtained  $T_c$  as a function of  $d_s$  and  $d_F$  for the  $F/S/F$  trilayer systems in the following form:

$$\Omega_0 \tan(\Omega_0 \frac{d_S}{2\xi_S}) = \gamma \frac{A_S(\gamma_b + \text{Re } B_F) + \gamma}{A_S |\gamma_b + B_F|^2 + \gamma(\gamma_b + \text{Re } B_F)},$$

with

$$B_F = [K_F \xi_F^* \tanh(K_F d_F)]^{-1}, \quad K_F = \frac{1}{\xi_F^*} \sqrt{\frac{|\omega_n| + iE_{ex} \text{sgn } \omega_n}{\pi K_B T_{CS}}},$$

$$A_S = K_S \xi_S \tanh(K_S d_S/2), \quad K_S = \frac{1}{\xi_S} \sqrt{\frac{\omega_n}{\pi K_B T_{CS}}}. \quad (7.4)$$

Practically, only the real root of  $\Omega_0$  was taken into account, while all imaginary roots were neglected. The  $F$  thickness-dependent  $T_C$  was fitted by the previously outlined model, and the results were shown in Fig. 7.3. Most parameters could be derived, except for  $\xi_F^*$ , which is calculated by equation (7.3). The obtained result for  $\xi_F^* = 6$  nm was consistent with the values for the Ni composition of both 0.54 and 0.58 in the literature. [33] The exchange energy  $E_{ex}$  and the interfacial transparency parameter  $\gamma_b$  were taken as free parameters in the fitting. Notice that we first proceeded with the data of  $T_C(d_{CuNi})$  with Nb thickness fixed at 37 nm, (the reason for doing this would be discussed later), and we used the following parameters deduced from experimental measurements to model  $T_C(d_F)$ . For a single 37 nm thick Nb film,  $T_C$  was 7 K and the resistivity was about 300 nΩ m at 10 K. The Nb coherence length  $\xi_S$ , which was related to the Ginzburg-Landa (GL) coherence length  $\xi_{GL}(0)$ , could be determined by upper critical field measurement, as later discussed in Section 7.3.

According to this relation,  $\xi_{GL}(T) = \frac{\pi}{2} \xi_S (1 - \frac{T}{T_C})^{-1/2}$ , we obtained  $\xi_S = 7$  nm.

$T_C$  as a function of  $d_{CuNi}$  is shown in Fig. 7.3. As can be seen, the theoretical fits are rather sensitive to the value of  $\gamma_b$  than that of  $E_{ex}$ . The value of  $E_{ex}$  is determined mostly by this regime that  $T_C$  starts to saturate with respect to  $d_{CuNi}$ , whereas  $\gamma_b$  is used to distinguish the vertical shift of  $T_C$ . Our fitted procedure is similar to previous studies. [17, 20, 33] The optimal value for  $E_{ex}$  is between 80 K and 120 K and for  $\gamma_b$  between 0.2 and 0.4. If we assume  $E_{ex} = k_B T_{Curie}$ , then the value of  $E_{ex}$  is in agreement with the measurement of  $T_{Curie}$  in the single  $Cu_{0.5}Ni_{0.5}$  films, as seen in Fig. 7.2. The nonmonotonic behavior of  $T_C(d_F)$  exhibits a minimum  $T_c$  around 3.3 nm. The occurrence of a minimum of  $T_C(d_F)$  can be qualitatively explained by the interference of quasiparticle wavefunctions in the F layer, which can be either constructive or destructive depending on the  $d_F$ . According to the work of Fominov *et al.* [17],  $\xi_F^{dirty}$  is related to the minimum of  $T_c(d_F)$  by  $d_{min} \approx 0.7\pi\xi_F^{dirty} / 2$ , where  $d_{min}$  is the thickness corresponding to the minimum of  $T_c(d_F)$ . Moreover,  $\xi_F^{dirty}$  related to the exchange energy within the dirty limit denotes the actual decay length of the superconducting Cooper pairs in the F. Notice that  $\xi_F^{dirty}$  should not be confused with  $\xi_F^*$ , for the latter is associated with superconducting diffusion length in the normal metal. Using the value of  $d_{min}$  extracted from Fig. 7.3, we obtained  $\xi_F^{dirty} \approx 3.0$  nm  $<$   $\xi_F^*$  as expected, since  $\xi_F^{dirty}$  is inversely proportional to the square root of the Curie temperature through the exchange energy whereas  $\xi_F^*$  is inversely proportional to that of the superconducting transition temperature. In addition, this result yields  $\lambda_F \approx 2\pi\xi_F^{dirty} = 19$  nm for the oscillation of the anomalous wavefunction in the dirty limit. [17]

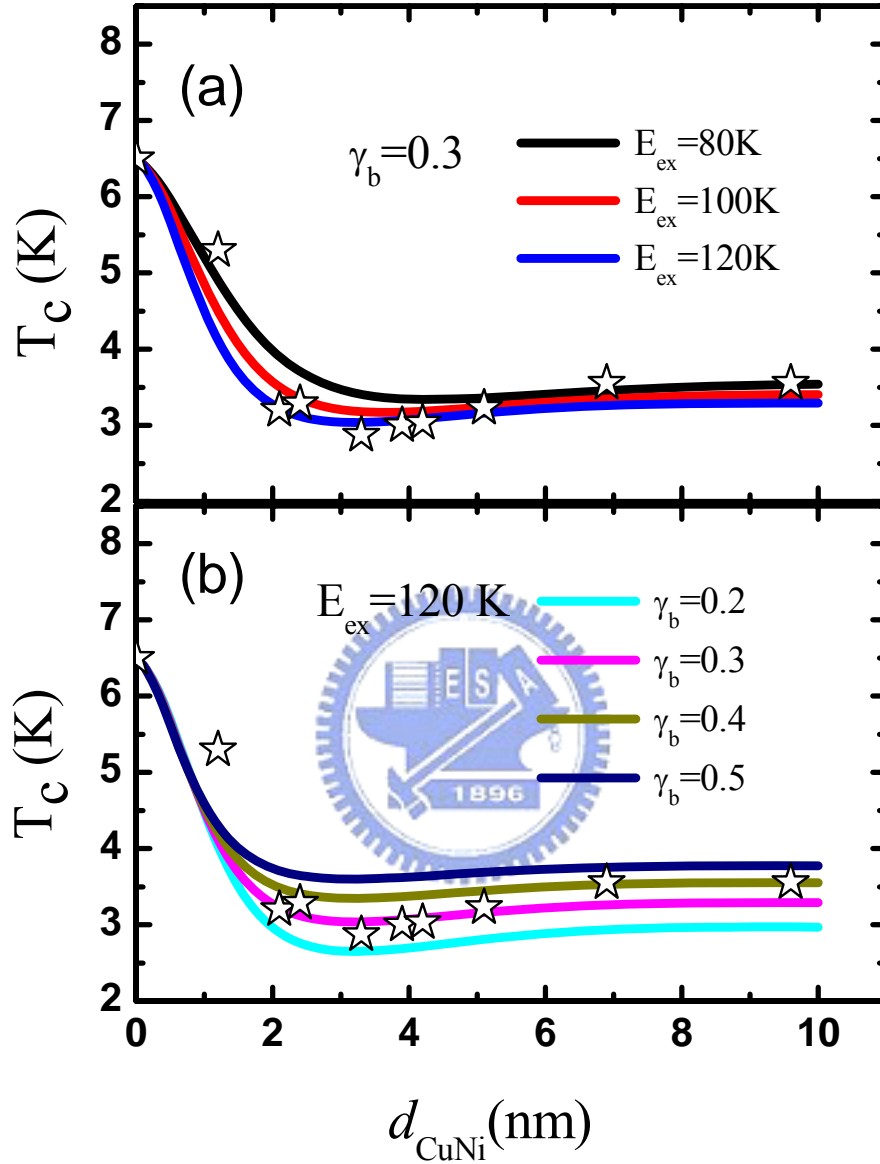


**Figure 7.3:** The superconducting critical temperature versus  $\text{Cu}_{0.5}\text{Ni}_{0.5}$  thickness for  $\text{Cu}_{0.5}\text{Ni}_{0.5}/\text{Nb}/\text{Cu}_{0.5}\text{Ni}_{0.5}$  trilayers with constant Nb thickness  $d_{\text{Nb}} = 37$  nm: (a) different lines are the results of theoretical fit for different values of  $E_{\text{ex}}$  and for  $\gamma_b = 0.3$ , (b) different lines are the results of theoretical fit for different values of  $\gamma_b$  and for  $E_{\text{ex}} = 120$  K.

The behavior of  $T_C(d_S)$  can be characterized with the same set of equations that describes the behavior of  $T_C(d_F)$ . Here, the critical temperature depending on the thickness of a single Nb layer is considered. In Fig. 7.1, the dotted lines are given by the model calculation with fixed parameters  $T_{CS}=8.8$  K,  $\rho_{Nb}=80$  n $\Omega$  m, and  $\rho_{CuNi}=300$  n $\Omega$  m, whereas the values of  $\gamma_b$ ,  $\xi_F^*$ , and  $E_{ex}$  are taken from the  $T_C(d_F)$  fit of Fig. 7.3(b). As can be clearly seen, all calculated curves are able to reproduce the experimental trend of  $T_C(d_S)$  and are comparable to Radovic's model with the perfect transparency assumption. Despite the consistency between the theory and the experimental data, we notice that the effect of a small variation of  $\gamma_b$  is barely distinguishable in the behavior of  $T_C(d_S)$ . As a result, the behavior of  $T_C(d_F)$  should be the key that enables a theoretically quantitative investigation of the interfacial transparency regarding the  $F/S$  proximity effect.

The uncertainty associated with the variation in the measured data of  $T_C(d_S)$  from the fitted curve occurs most obviously in the region of the small  $d_F$  as shown in Figure 7.4, where the  $T_C$  declines due to the pair breaking effect. The discrepancy may imply that some uncontrolled factors in the thinnest films are not considered in the model and that the restriction of the model is caused by the simplified assumption that neglects the imaginary roots of Eq. (7.10). In the theoretical work described by Fominov *et al.*, the single-mode approximation is applicable for  $\gamma_b \gg |B_F|$ , for other cases one should apply the multimode method for the exact solution. This condition can be given in a simpler form as  $\sqrt{E_{ex}/\pi T_C} \gg 1/\gamma_b$  from the view of the experimentally relevant case. [17] When  $T_C(d_F)$  exhibits neither reentrant behavior nor monotonic decay to  $T_C = 0$  at a finite  $d_F$ , but a nonmonotonic decay to a finite  $T_C$  with a minimum at a particular  $d_F$ , the results of the single-mode and multimode methods are quite close, save that the former somewhat underestimates the minimum

value of  $T_c$  [17]. For instance, the single-mode approximation is applied well to the analysis of the Nb/Cu<sub>x</sub>Ni<sub>1-x</sub> bilayer system of  $x= 0.58$  and  $0.54$  with  $\sqrt{E_{ex}/\pi T_C} \approx 2$  and  $1/\gamma_b \approx 1$ , and to the Nb/Pd<sub>0.86</sub>Ni<sub>0.14</sub> system with  $\sqrt{E_{ex}/\pi T_C} \approx 3$  and  $1/\gamma_b \approx 2$  [33] although the requirement is just satisfactory. On the contrary, for the Nb/Pd<sub>0.81</sub>Ni<sub>0.19</sub> bilayers, the condition no longer holds since  $\sqrt{E_{ex}/\pi T_C} (\approx 3) < 1/\gamma_b (\approx 7)$ . Nevertheless, the data are well fitted by the single-mode calculation, and the results indeed provide substantial information about the microscopic parameters related to the proximity effect. [20] For the Cu<sub>0.5</sub>Ni<sub>0.5</sub>/Nb/Cu<sub>0.5</sub>Ni<sub>0.5</sub> trilayers presented in this work, we adopted the single-mode approximation to study the behaviors of  $T_C(d_F)$  as well as that of  $T_C(d_S)$  in spite of  $\sqrt{E_{ex}/\pi T_C} \approx 2$  and  $1/\gamma_b \approx 3$ ; this condition is closer to the need for the limitation. The validity of these proceedings may rest on the fact that the amplitude of the multimode calculation has only a slight reduction in comparison with the single-mode approximation when  $\gamma_b$  is larger than 0.1 [17]. Although there is a minor discrepancy between the calculated curves and the experimental data, it is clearly seen that the  $T_C(d_F)$  dependence cannot be properly described by the larger value of  $\gamma_b$ .

Aarts *et al.* have first discussed the importance of interface transparency and present experimental evidence of the intrinsically reduced interface transparency in the V/V<sub>1-x</sub>Fe<sub>x</sub> multilayer system. [19] Their results show that, for a fixed  $\gamma$ , the critical thickness increases as  $\gamma_b$  decreases. Accordingly,  $\gamma_b < 0.4$  obtained for the Cu<sub>0.5</sub>Ni<sub>0.5</sub>/Nb structure studied in this work reveals a small potential barrier, leading to relatively strong pair-breaking and in turn a larger critical thickness. This factor of high interfacial transparency is in agreement with the result of the critical field  $H_{c2}$  and CPP measurement, which will be discussed in the following section.



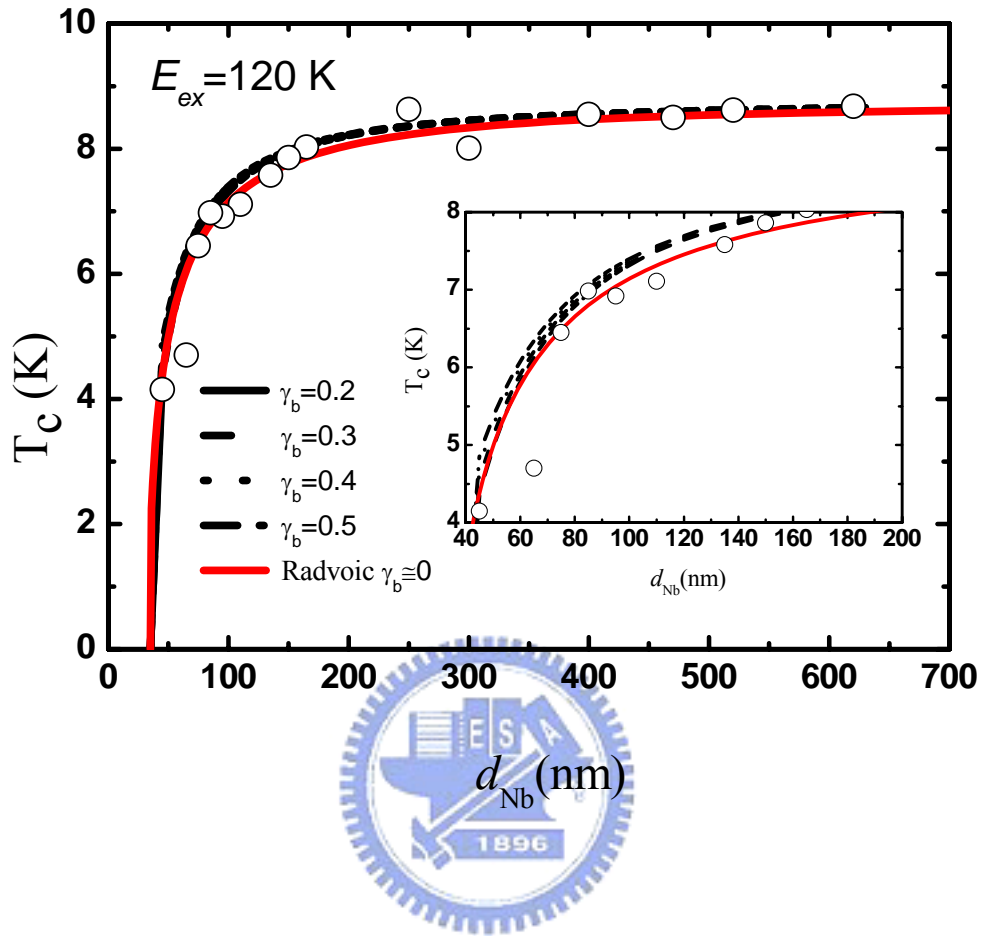


**Figure 7.4:** The superconducting critical temperatures as a function of  $d_{\text{Nb}}$  for  $\text{Cu}_{0.5}\text{Ni}_{0.5}/\text{Nb}/\text{Cu}_{0.5}\text{Ni}_{0.5}$  trilayers with constant  $\text{Cu}_{0.5}\text{Ni}_{0.5}$  thickness  $d_{\text{CuNi}} = 50$  nm. The solid red line is the theoretical fitting with high interfacial transparency assumption. The other different lines are the results of the theoretical calculation for different values of  $\gamma_b$  and for  $E_{\text{ex}} = 120$  K obtained in Figure 3. The inset is an enlargement of the region between 40 nm and 160 nm close to the corner.

## 7.3 Pair breaking ratio by upper critical magnetic field measurement

We also investigate the influence of the interfacial transparency by studying the temperature dependence of the upper critical magnetic field  $H_{c2}(T)$  for  $F/S$  multilayers. The study of  $H_{c2}$  can provide us substantial information on the coherence length and the role of the pair-breaking effect from the occurrence of the dimensionality crossover. To this end, measurement of the temperature-dependent parallel critical field,  $H_{c2//}(T)$ , as well as the perpendicular critical field,  $H_{c2\perp}(T)$ , have been performed. The samples have been prepared with fixed  $d_F = 20$  nm and 6 bilayers, and various  $d_S$  from 50 to 600 nm, denoted as  $[\text{Cu}_{0.5}\text{Ni}_{0.5} (20 \text{ nm})/\text{Nb}(d_S)]_6/\text{Cu}_{0.5}\text{Ni}_{0.5} (20 \text{ nm})$ . The jump of the amplitude of the  $S$  wavefunction at the  $F/S$  boundary is constant on the ground that the  $T_C(d_F)$  is already saturated at  $d_F = 20$  nm, as shown in Fig. 7.3. From the theoretical point of view, the critical field oscillations dependent on the  $F$  layer thickness arising from the different phases between the two adjacent superconductors can be neglected when  $d_S/\xi_S > 2$ . [34] The thicknesses of our samples are well within this regime. Thus we can compare the results obtained from different samples in terms of the barrier quality and exchange force of the  $F$  layer for the  $S$  wavefunction in this system.

According to the Ginzburh-Landau (GL) theory, the temperature dependence of  $H_{c2//}(T)$  for the 3D regime is described with the equation

$$H_{c2//}(T) = \frac{\phi_0}{2\pi\xi_{//}(0)\xi_{\perp}(0)} \left(1 - \frac{T}{T_{CS}}\right). \quad (7.5)$$

While in the 2D regime,  $\xi_{\perp}(T)$  is limited by the layer thickness and  $H_{c2//}(T)$  shows a square-root like behavior by the Tinkham expression [30]

$$H_{c2//}(T) = \frac{\sqrt{12}\phi_0}{2\pi\xi_{//}(0)d_S} \sqrt{\left(1 - \frac{T}{T_{CS}}\right)}. \quad (7.6)$$

The  $\phi_0$  is the flux quantum and  $\xi_{//}(0)$  and  $\xi_{\perp}(0)$  are the GL coherence lengths for fields parallel and perpendicular to the sample plane at 0 K, respectively. Apparently, the dependence of  $H_{c2//}(T)$  on temperature would change from 3D to 2D when the thickness of S film is continuously reduced. On the contrary, the  $H_{c2\perp}(T)$  dependence on temperature always presents a linear relation with arbitrary superconducting thickness, described by [36]

$$H_{c2\perp}(T) = \frac{\phi_0}{2\pi\xi_{//}^2(0)} \left(1 - \frac{T}{T_{CS}}\right). \quad (7.7)$$

Figure 7.4 shows the temperature dependence of the  $H_{c2//}(T)$  and  $H_{c2\perp}(T)$  for  $\text{Cu}_{0.5}\text{Ni}_{0.5}/\text{Nb}$  multilayer samples with  $d_{\text{Nb}}=140, 160,$  and  $180$  nm. The data for  $d_{\text{Nb}}=160$  and  $180$  nm are shifted by 0.05 and 0.1 respectively in the horizontal axis for clarity. The  $H_{c2\perp}(T)$  has a linear behavior and constant slope for all thicknesses of Nb, as expected. The GL coherence length at zero temperature is about 11 nm, which is deduced from the relation  $\xi_{GL}(0) = \sqrt{\phi_0/2\pi\beta T_C}$ , where the slope  $\beta = -dH_{c2}/dT$  is derived from the  $H_{c2\perp}(T)$  curves by a linear least square fit as the dashed line shown in Figure 7.6.

To study the 2D-3D crossover behavior,  $H_{c2//}(T)$  data as the consequence of the GL formulae with anisotropic superconductors have been fitted by  $H_{c2//}(T) = a\sqrt{1-T/T_C} + b(1-T/T_C)$ , a combination of Eqs. (7.12) and (7.13). The results are plotted as solid lines in Fig. 7.4. A gradual transition from 2D to 3D is evolving from square root behavior to a linear relationship, when  $d_S$  increases from 140 nm to 180 nm. In comparison with strong ferromagnetic case reported earlier in Chapter 6, the thickness of two-dimensional to three-dimensional (2D-3D) crossover

takes place at about 120~140 nm in the Nb/Fe [26], and 145~180 nm in the Nb/Co layered structure. The comparable dimensional crossover thickness for this relatively weak ferromagnetic  $\text{Cu}_{0.5}\text{Ni}_{0.5}$  can be attributed to the high interfacial transparency between the  $S$  and the  $F$ . To make a quantitative characterization, we adopt a strategy inspired from earlier reports in which the dimensional crossover temperature was shifted toward a lower value in the system exhibiting high interfacial transparency. [33, 37]

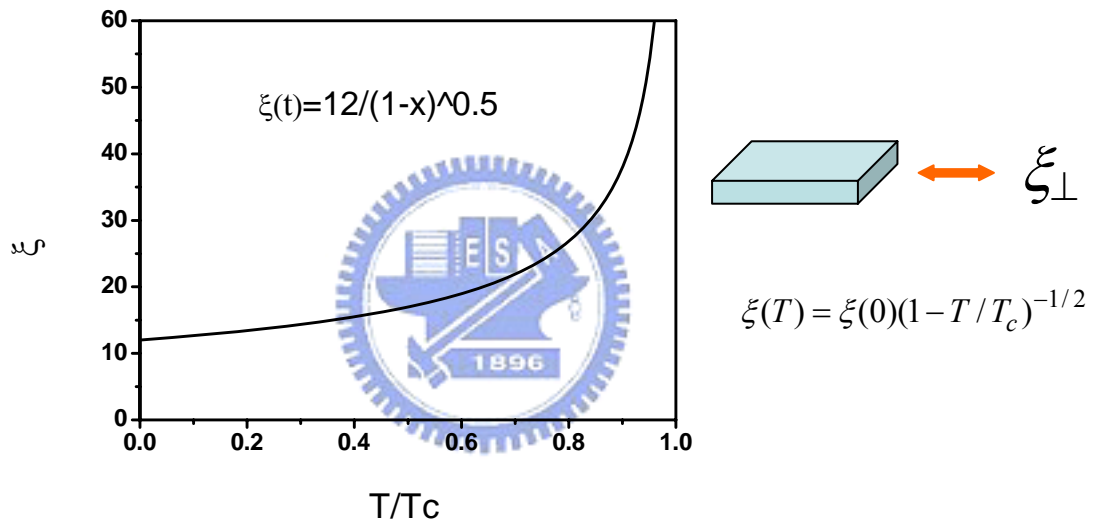


**Figure 7.5:** The superconductor coherence with 12 nm of Nb dependent on the temperature.

For the case of the field perpendicular to the film, the influence of the interface transparency is weak due to the confined in-plane motion of the Cooper pairs. As for the magnetic field parallel to the interface, the Cooper pairs are allowed to move across the interface, that is, they experience the influence of the interface transparency much more strongly. Now we turn to the study of the effect of interface transparency on  $H_{c2//}(T)$ . Since the coherence length  $\xi_{GL}(T)$  has  $(1-T/T_C)^{-1/2}$  dependence, as shown in Figure 7.5,  $H_{c2//}(T)$  behaves like a 3D system at low temperatures due to  $\xi_{\perp}(T) <$

$d_{\text{Nb}}$ . However,  $\xi_{\perp}(T)$  tends to diverge when the temperature is sufficiently close to  $T_c$ , causing  $\xi_{\perp}(T) > d_{\text{Nb}}$ , and 2D behavior is observed [33]. In Figure 7.6,  $H_{c2\parallel}(T)$  for  $d_{\text{Nb}} = 140$  nm at higher temperatures is well described by a GL square-root fit down to  $T/T_c = 0.92$ , whereas at lower temperatures  $H_{c2\parallel}(T)$  exhibits linear behavior. This result could be regarded as single superconducting films with smaller effective thickness  $d_{\text{eff}} = 96$  nm estimated by  $d_{\text{eff}} \approx \xi_{\perp}(T)$  where the superconductivity of Nb is weakened through pair breaking effect at  $F/S$  interface. Consequently, with the introduction of the pair-breaking ratio  $\chi = (d_s - d_{\text{eff}})/d_{\text{eff}}$ , the values of  $\chi$  in different systems are calculated to be  $\chi_{\text{Co}} = 0.31$ ,  $\chi_{\text{Fe}} = 0.28$ , and  $\chi_{\text{CuNi}} = 0.34$  for comparison. Comparable values of  $\chi$  regardless of the thickness in the 2D regime confirm that the higher the transparency of the barrier, the stronger its pair-breaking effect would be. This is consistent with the results of the  $T_c$  measurement.



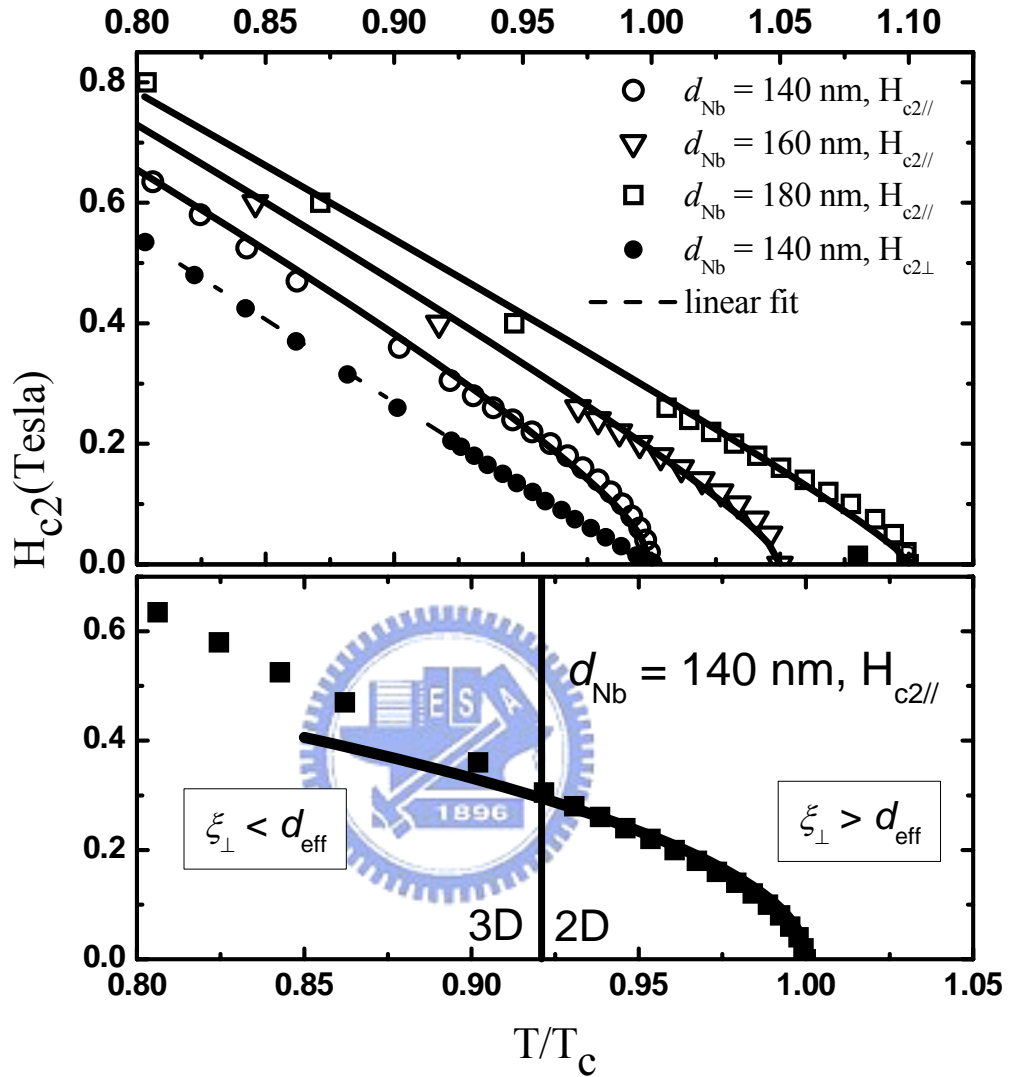


**Figure 7.6:** In the top part, reduced parallel uppercritical fields versus reduced temperature for  $\text{Cu}_{0.5}\text{Ni}_{0.5}/\text{Nb}$  multilayers with  $d_{\text{Nb}}=140, 160,$  and  $180$  nm. Data for the  $d_{\text{Nb}} = 160$  and  $180$  nm are shifted to the right by  $T/T_c=0.05$  and  $0.1$ , respectively, for clarity. The solid lines are least-square fit using the Ginzburg-Landau relation. The filled circle symbol is perpendicular upper critical fields for  $d_{\text{Nb}}=140$  nm and the dashed line is a linear fit. In the down part is parallel upper critical fields as a function of the reduced temperature for the  $\text{Cu}_{0.5}\text{Ni}_{0.5}/\text{Nb}$  multilayers with  $d_{\text{Nb}} = 140$  nm. It can be categorized into two groups according to the 3D and 2D behavior as shown the solid line fitted by Tinkham expression.

## 7.4 Interface resistance by CPP measurement

Since the interface between different metals is never entirely transparent, it screens the proximity effect and is treated as a potential barrier accounting for the lattice mismatches, interface imperfection, the difference of Fermi velocities, and band structures. The interfacial transparency  $T_{tran}$  in the free electron model denotes the projection of Fermi wave vector onto the direction perpendicular to the interface. [19] In this model,  $T_{tran}$  is defined as a parameter to describe the resistance encountered by the electron across the barrier between two metals, given by

$$\gamma_b = \frac{2 \ell_F}{3 \xi_F^*} \frac{1 - T_{tran}}{T_{tran}}. \quad (7.8)$$

The behavior of  $T_C(d_F)$  can be classified into three categories according to the values of  $\gamma_b$  which is proportional to the interface resistance: 1.  $T_C$  decays non-monotonically at a finite interface resistance: 2.  $T_C$  exhibits a reentrant behavior at a moderate interface resistance: 3.  $T_C$  decays monotonically at low enough interface resistance. Practically, the value of  $\gamma_b$  is often deduced from the fitting result because of the difficulty in directly measuring interface resistance. In the conventional transport measurement with current in the plane, CIP provides a direct access to the critical current and critical magnetic field in the  $F/S$  system by driving  $S$  to the normal state. Unfortunately, CIP tends to give zero resistance in this configuration when  $S$  is in the superconducting state. In this section, we present the measurement of interface resistance between Nb and  $\text{Cu}_{0.5}\text{Ni}_{0.5}$  with current perpendicular to plane. That is the information of resistance inaccessible to the CIP configuration.

In order to minimize the deviation in the preparatory condition and obtain comparable physical quality in a specific set, we fabricated 8 different samples in the same deposition run for CPP cases which were achieved by a movable substrate

holder. The construction for CPP samples which required three changes of contact masks in situ to assure clean interfaces was more complicated than that of CIP ones. The deposition conditions used for CPP samples were similar to those used for studying the  $\text{Co/Nb}_x\text{Ti}_{1-x}$  multilayers in Chapter 5. [29]

To analyze quantitatively the interface resistance in the superconducting and normal states, two sets of samples with different numbers of bilayers were made. The  $\text{Cu}_{0.5}\text{Ni}_{0.5}$  thickness was fixed at 50 nm and Nb thicknesses were 15 and 80 nm, respectively. The thickness of Nb was chosen according to the phase diagram of Fig. 7.4. When Nb thickness was thinner than the critical thickness, the  $S$  was in the normal state ( $NM$ ) and we had  $NM/F$  multilayers; otherwise we would obtain  $S/F$  multilayers. Figure 7.7 represents the plot of the product of sample area  $A$  and total resistance  $R_T$  against bilayer number  $N$  for the two series of  $\text{Cu}_{0.5}\text{Ni}_{0.5}/\text{Nb}$  multilayers. The unit area resistance  $AR_T$  is linearly proportional to the number of bilayer for both sets of samples. The fact that the resistance remains the same when an external magnetic field is applied implies that the spin-up and spin-down electron channels cannot be distinguished. As a result, we infer that there is strong spin mixing at the  $\text{Cu}_{0.5}\text{Ni}_{0.5}/\text{Nb}$  interface and in the Nb layer. [38, 39] A one-band model can be applied to analyzing our CPP data. The linear behavior of  $AR_T$  against  $N$  can be explicitly written as

$$AR_T = 2AR_{F/S(S)} + \rho_F t_F + N(\rho_F t_F + \rho_S t_S + 2AR_{F/S(NM)}) \quad (7.9)$$

for normal state Nb and

$$AR_T = 2AR_{F/S(S)} + \rho_F t_F + N(\rho_F t_F + 2AR_{F/S(S)}) \quad (7.10)$$

for superconducting state Nb. Here  $t$ 's are the thicknesses,  $\rho$ 's are the resistivities,  $AR_{F/S(NM)}$ 's is the unit area interface resistances between normal state Nb and  $\text{Cu}_{0.5}\text{Ni}_{0.5}$  layers and  $AR_{F/S(S)}$ 's is the unit area interface resistances between



superconducting state Nb and  $\text{Cu}_{0.5}\text{Ni}_{0.5}$  layers. Recently, theoretical research has asserted that the asymmetry of interface transparency in the  $F/S/F$  structure originates mainly from the unequal interfacial transparencies of the  $F/S$  and  $S/F$ . This asymmetry can be observed from the  $T_c$  dependence on the relative magnetization orientation between two adjacent ferromagnetic layers by varying the  $F$  thicknesses in the  $F1/S/F2$  structure. [40] Even though we assume that interface resistances of the  $S/F$  and  $F/S$  are identical as well as that of  $NM/F$  and  $F/NM$  based on the fact that the  $F$  thickness is the same in all of the CPP multilayer samples, there is still always  $2AR_{F/S(NM)}$  and  $2AR_{F/S(S)}$  for every pair of interfaces in Eqs. (7.9) and (7.10), respectively. In Figure 7.7, the dashed lines are the linear least square fits to individual sets of data. According to the one band model [41], the equations of  $AR_T=C_1+C_2N$  for normal state Nb and  $AR_T= C_1(N+1)$  for superconducting state Nb give  $C_1=2AR_S+\rho_{FF}t_F$  and  $C_2=2AR_{NM}+\rho_{FF}t_F +\rho_{SS}t_S$ , respectively. Each series of samples can be individually fitted with the model to extract the fitting parameters. In this manner, however, the quantities deduced from the fitting are sample series dependent. To overcome this difficulty, global fit is performed to analyze the two sets of data with the same fitting parameters. The results of the two-parameter global fit are shown in Fig. 7.7 as dotted lines.

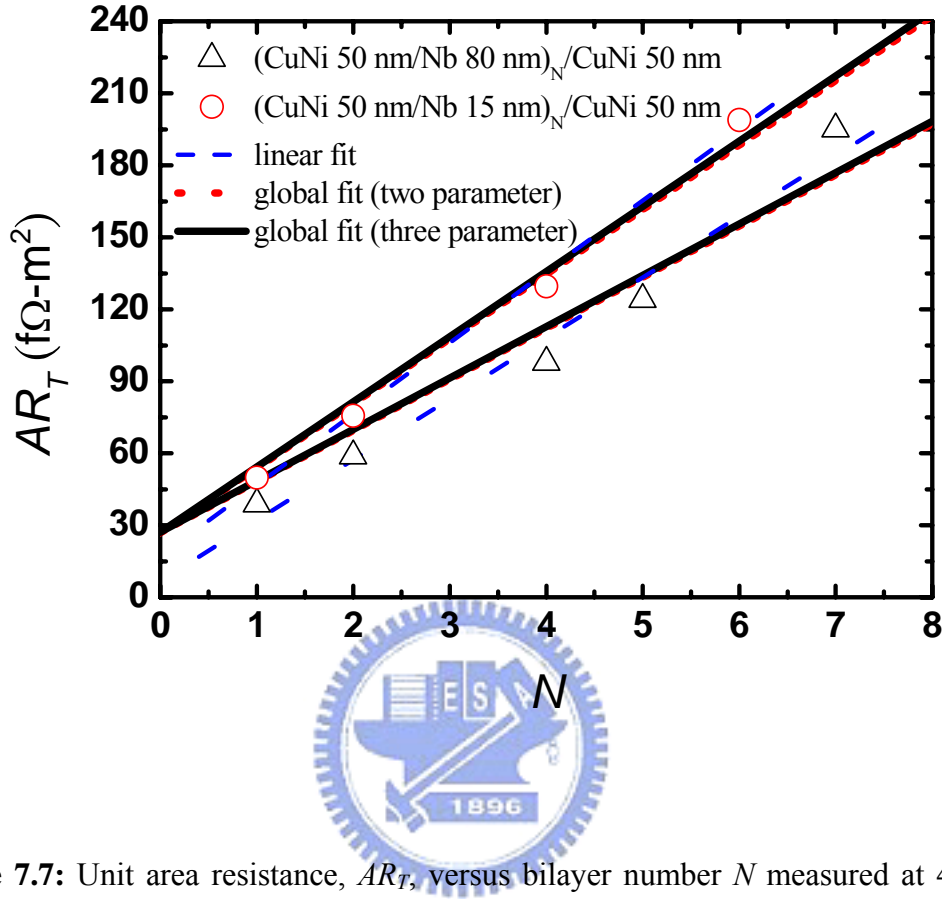


**Figure 7.7:** Unit area resistance,  $AR_T$ , versus bilayer number  $N$  measured at 4.2 K. The two sets of samples have Nb thickness fixed at 80 nm and 15 nm, respectively. The dashed-lines are linear least-square fit. The dotted lines and the solid lines are global fits for two and three parameters, respectively, to the data.

The  $S/F/S$  structure can be seen as a Josephson junction in that superconductor couple weakly through ferromagnetic barrier. It has been shown that the critical current of ferromagnetic Josephson junction,  $I_{Jc}$ , would change sign from positive to negative under certain conditions, in correspondence to a phase shift between two  $S$  layers in the Josephson ground state. [2] This phase change in the Cooper pair wavefunction is induced in the  $F$  layer by the proximity effect. As has been reported,  $I_{Jc}$  exhibited a non-linear  $IV$  characteristic, even for the thickness of the ferromagnet

larger than  $\xi_F^*$ . The largest spacer layer in the literature was 28 nm for CuNi [7, 8], 11 nm for Ni, and 5 nm for Co. [9] In order to normalize the data,  $I_{JC}$  was usually multiplied by  $R_{NM}$  to give the characteristic voltage  $V=I_{JC}R_{NM}$ . Here,  $I_{JC}$  was taken at the point where the  $dV/dI(V)$  increased above the value of zero bias current.  $R_{NM}$  was measured by applying a sufficient large bias current so that the nonlinear part of the current voltage curves could be ignored. Yet, the current was kept small enough to ensure the Nb electrodes remained in the superconducting state. The non-linear  $IV$ -characteristic could be well described by the expression  $V = R\sqrt{I^2 - I_{Jc}^2}$  because a supercurrent can be sustained even through a ferromagnet.

The voltage drop across the sample in the CPP measurements performed for the current study is less than 10 nV for a maximum current of 100 mA provided by the battery-powered DC current source. This voltage is six orders of magnitude smaller than the energy gap 1.4 meV of Nb. Under these circumstances, the measured non-linear  $I-V$  curve can be attributed to the supercurrent in the  $F$  layer. As shown in Fig. 7.8, non-linear  $I-V$  behavior can be observed when the thickness of  $\text{Cu}_{0.5}\text{Ni}_{0.5}$  is less than 40 nm. To characterize the penetration of the supercurrent from the Nb layer into the  $\text{Cu}_{0.5}\text{Ni}_{0.5}$  layer, we introduce a leakage length,  $\delta_s$ , that characterizes the penetration of the supercurrent from the Nb layer into the  $\text{Cu}_{0.5}\text{Ni}_{0.5}$  layer. By fitting the data in which the  $I-V$  characteristic is in the ohmic region, it is found that  $\delta_s \approx 15.8$  nm. This leakage length should be included in the one-band model. Accordingly, the one-band model is revised to

$$AR_T = 2AR_{F/S(S)} + \rho_F t_F - 2\delta_s \rho_F + N(\rho_F t_F + \rho_S t_S + 2AR_{F/S(NM)}) \quad (7.11)$$

for Nb in the normal state and

$$AR_T = 2AR_{F/S(S)} + \rho_F t_F - 2\delta_s \rho_F + N(\rho_F t_F + 2AR_{F/S(S)} - 2\delta_s \rho_F) \quad (7.12)$$

for Nb in the superconducting state. They account for the fact that  $\text{Cu}_{0.5}\text{Ni}_{0.5}$  contributes no resistance within the leakage length. From the results of the two-parameter global fit, the resistance of one-pair interfaces can be obtained by substituting the values of the bulk resistivities of Nb and  $\text{Cu}_{0.5}\text{Ni}_{0.5}$  into Eq. (7.17) and (7.18).

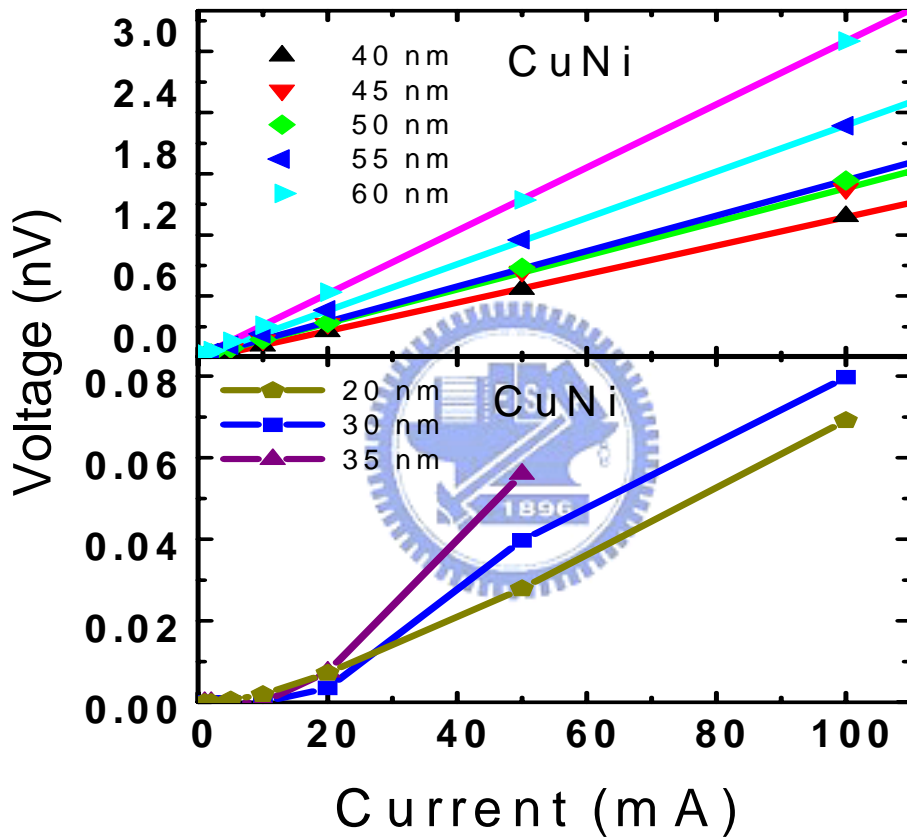


**Figure 7.8:** In the top right side part: the linear  $I-V$  characteristic as a function of  $\text{Cu}_{0.5}\text{Ni}_{0.5}$  thickness for CPP  $\text{Cu}_{0.5}\text{Ni}_{0.5}/\text{Nb}$  multilayer. The different lines are linear least-square fit. In the down right side part: the non-linear  $I-V$  characteristic as a function of  $\text{Cu}_{0.5}\text{Ni}_{0.5}$  thickness for CPP  $\text{Cu}_{0.5}\text{Ni}_{0.5}/\text{Nb}$  multilayer. The solid line is meant to guide the eye.

However, the uncertainty about the deduced interface resistance is found to be

dominated by the large resistivity of  $\text{Cu}_{0.5}\text{Ni}_{0.5}$  alloy. To get through this limitation, the CPP resistivity measurement is carried out by varying the thickness of a single  $\text{Cu}_{0.5}\text{Ni}_{0.5}$  film sandwiched between two Nb strips. The top view geometry for the measurement is illustrated in the inset of Fig. 7.9. The effective area is confined to the overlapped square of the strips. [42] As shown in Fig. 7.9, the unit area CPP resistance,  $AR_T$ , is linearly proportional to the thickness of  $\text{Cu}_{0.5}\text{Ni}_{0.5}$  layer. The individual linear least square fit yields a slope of CPP resistivity  $\rho_{\text{CuNi}} = 380 \pm 20 \text{ n}\Omega \text{ m}$ . This linear behavior can be described by the one-band series-resistor model given by

$$AR_T = 2AR_{F/S(S)} + \rho_F(t_F - 2\delta_S). \quad (7.13)$$

From the best fit, we obtain  $2AR_{\text{CuNi/Nb(S)}} = 19.8 \pm 0.5 \text{ f}\Omega \text{ m}^2$  and  $2AR_{\text{CuNi/Nb(NM)}} = 0.6 \pm 0.1 \text{ f}\Omega \text{ m}^2$ . We also performed a three-parameter global fit to all the three data sets with the same set of parameters. The solid lines in Figure 7.7 and 7.9 are the best global fits with  $\rho_{\text{CuNi}} = 390 \pm 10 \text{ n}\Omega \text{ m}$ ,  $2AR_{\text{CuNi/Nb(S)}} = 19.9 \pm 1.5 \text{ f}\Omega \text{ m}^2$ , and  $2AR_{\text{CuNi/Nb(NM)}} = 0.7 \pm 0.3 \text{ f}\Omega \text{ m}^2$ . Correspondingly, the interfacial transparency parameter  $\gamma_b = \frac{R_b A}{\rho_S \xi_F^*} \approx 0.2$  can be deduced. The small  $\gamma_b$  strongly supports the conclusion of high interfacial transparency between Nb and  $\text{Cu}_{0.5}\text{Ni}_{0.5}$ . This result is consistent with that of  $\gamma_b < 0.4$  from the analysis of the thickness-dependent  $T_C$  and with that of the large pair-breaking ratio  $\chi$  from the behavior of the  $H_{c2}$  dimensional crossover.

It is of interest how the interface resistance changes when  $S$  becomes superconductive. The opening of superconducting gap,  $\Delta$ , at the Fermi energy and the decrease in population of quasiparticles, make  $S$  a low carrier system for spin transport. However, current can flow through the sample in response to a small voltage less than  $\Delta$  by means of the Andreev reflection in the metallic junction. For instance, a spin-up electron injected from a normal metal is retroreflected at the

interface as a spin-down hole in order to form a Cooper pair in the superconductor. [43] On the other hand, the exchange splitting of the conduction band in  $F$  would suppress the Andreev current at  $F/S$  interface and leads to the necessity of the spinless current inside  $S$ . [38] Furthermore, the spin accumulation and spin flipping scattering at the interface bring about additional voltage drop across the interface and a reduction of spin transport into  $S$ . [44] All of the phenomena mentioned above can be responsible for the larger interface resistance of  $\text{Cu}_{0.5}\text{Ni}_{0.5}/\text{Nb}$  in the superconducting state than in the normal state. Since the individual effect on interface resistance cannot be differentiated based on the results obtained here, a quantitative analysis of the distinctive contribution to interface resistance is beyond the scope of this work.

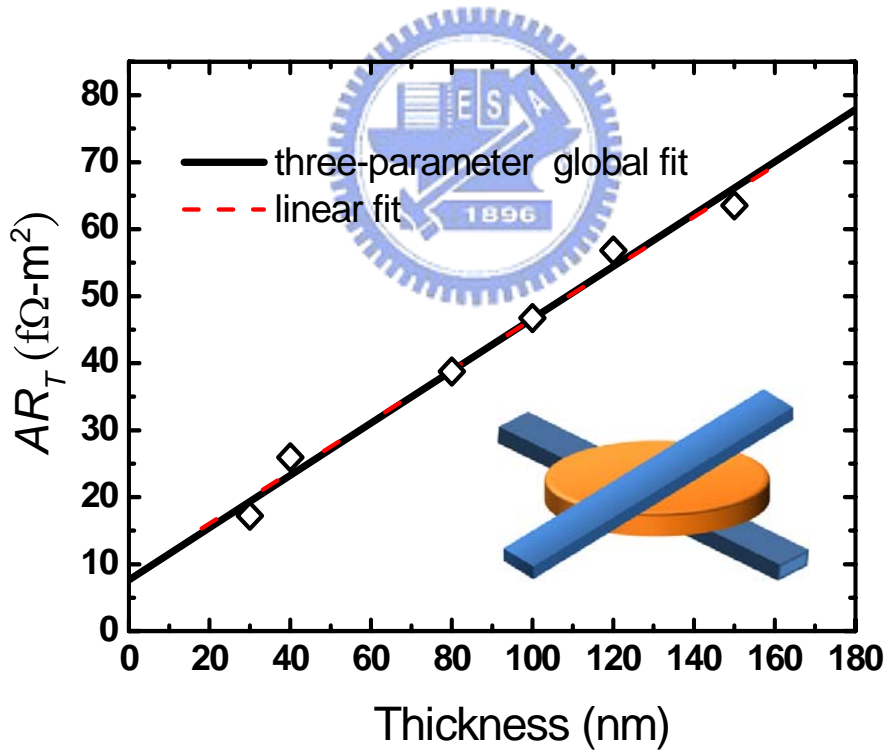


**Figure 7.9:** Unit area resistance,  $AR_T$ , versus  $\text{Cu}_{0.5}\text{Ni}_{0.5}$  thickness measured at 4.2 K. The dashed line is a linear least-square fit. The solid line is a global fit for three parameters to the data. Inset: the top view geometry of the current perpendicular to plane (CPP) configuration for this series sample. Sample is sandwiched between two superconducting electrodes of Nb stripes used for the four-point measurement.

## References:

1. Y. Kamihara,, T. Watanabe , M. Hirano, and H. Hosono, *J. Am. Chem. Soc.* **130**, 3296 (2008).
2. A. I. Buzdin, *Rev. Mod. Phys.* **77**, 935 (2005).
3. P. Fulde and R. A. Ferrel, *Phys. Rev.* **135**, A550 (1964).
4. A. I. Larkin and Y. N. Ovchinnikov, *Sov. Phys. JETP.* **20**, 762 (1965).
5. J. S. Jiang, D. Davidović, D. H. Reich, and C. L. Chien, *Phys. Rev. Lett.* **74**, 314 (1995).
6. I.A. Garifullin, *J. Magn. Magn. Mater.* **240**, 571 (2002).
7. V. V. Ryazanov, V. A. Oboznov, A. Yu. Rusanov, A. V. Veretennikov, A. A. Golubov, and J. Aarts, *Phys. Rev. Lett.* **86**, 2427 (2001).
8. V. A. Oboznov, V. V. Bol'ginov, A. K. Feofanov, V. V. Ryazanov, and A. I. Buzdin, *Phys. Rev. Lett.* **96**, 197003 (2006).
9. J. W. A. Robinson, S. Piano, G. Burnell, C. Bell, and M. G. Blamire, *Phys. Rev. B.* **76**, 094522 (2007).
10. I. A. Garifullin, D. A. Tikhonov, N. N. Garif'yanov, L. Lazar, Yu. V. Goryunov, S. Ya. Khlebnikov, L. R. Tagirov, K. Westerholt, and H. Zabel, *Phys. Rev. B.* **66**, 020505(R) (2002).
11. V. Zdravkov, A. Sidorenko, G. Obermeier, S. Gsell, M. Schreck, C. Müller, S. Horn, R. Tidecks, and L. R. Tagirov, *Phys. Rev. Lett.* **97**, 057004 (2006).
12. I. F. Lyuksyutov and V. L. Pokrovsky, *Adv. Phys.* **54**, 67 (2005).
13. L. R. Tagirov, *Phys. Rev. Lett.* **83**, 2058 (1999).
14. J. Y. Gu, C.-Y. You, J. S. Jiang, J. Pearson, Ya. B. Bazaliy, and S. D. Bader, *Phys. Rev. Lett.* **89**, 267001 (2002).
15. A. Potenza and C. H. Marrows, *Phys. Rev. B.* **71**, 180503(R) (2005).

16. L. R. Tagirov, *Physica C* **307**, 145 (1998).
17. Ya. V. Fominov, N. M. Chtchelkatchev, and A. A. Golubov, *Phys. Rev. B* **66**, 014507 (2002).
18. R. Gross, A. Sidorenko, and L. Tragirov, *Nanoscale Devices-Fundamentals and Applications*, Springer (2004).
19. J. Aarts, J. M. E. Geers, E. Bruck, A. A. Golubov, and R. Coehoorn, *Phys. Rev. B* **56**, 2779 (1997).
20. C. Cirillo, S. L. Prischepa, M. Salvato, and C. Attanasio, *Phys. Rev. B* **72**, 144511 (2005).
21. J. Kim, Jun Hyung Kwon, K. Char, Hyeonjin Doh, and Han-Yong Choi, *Phys. Rev. B* **72**, 014518 (2005).
22. J. Kim, Y-J Doh, and K. Char, *Phys. Rev. B* **71**, 214519 (2005).
23. Z. Radović, L. Dobrosavljević -Grujić, A.I. Buzdin, and J.R. Clem, *Phys. Rev. B* **38**, 2388 (1988).
24. J. W. Loram, and Z. Chen, *J. Phys. F: Met. Phys.* **13**, 1519 (1983).
25. J.-J. Liang, S.F. Lee, W.T. Shih, W.L. Chang, C. Yu, and Y.D. Yao, *J. Appl. Phys.* **92**, 2624 (2002).
26. S.Y. Huang, S.F. Lee, Jun-Jih Liang, C.Y. Yu, K.L. You, T. W. Chiang, S. Y. Hsu, and Y. D. Yao, *J. Magn. Magn. Mater.* **304**, e81 (2006).
27. A. Potenza and C. H. Marrows, *Phys Rev. B* **71**, 180503(R) (2005).
28. Ya. V. Fominov, N. M. Chtchelkatchev, and A. A. Golubov, *Phys. Rev. B* **66**, 014507 (2002).
29. S.-Y. Huang, S. F. Lee, S. Y. Hsu, and Y. D. Yao *Phys. Rev. B* **76**, 024521 (2007).
30. J. W. Loram and Z Chen, *J. Phys F: Met. Phys.* **13**, 1519 (1983).
31. H. Zabel and S.D Bader, *Magnetic Heterostructures: Advances and Perspectives*



- in Spinstructures and Spintransport*, (Springer Tracts in Modern Physics, 2007), p. 251.
32. M. Yu. Kuprianov and V. F. Lukichev, *Sov. Phys. JETP* **67**, 1163 (1988).
  33. A. Angrisani Armenio, C. Cirillo, G. Iannone, S. L. Prischepa, and C. Attanasio, *Phys. Rev. B* **76**, 024515 (2007).
  34. B. Krunavakarn and S. Yoksan, *Physica C* **440**, 25 (2006).
  35. M. Tinkham, *Introduction to Superconductivity*, (McGraw-Hill, New York, 1975).
  36. S. L. Lee, T. M. Chuang, S. Y. Huang, W. L. Chang, and Y. D. Yao, *J. Appl. Phys.* **89**, 7493 (2001).
  37. C. Ciuhu and A. Lodder, *Phys. Rev. B* **64**, 224526 (2001).
  38. F. Taddei, S. Sanvito, J. H. Jefferson, and C. J. Lambert, *Phys. Rev. Lett.* **82**, 4938 (1999).
  39. K. Eid, H. Kurt, W. P. Pratt, Jr., and J. Bass, *Phys. Rev. B* **70**, 100411(R) (2004).
  40. P. Cadden-Zimansky, Ya. B. Bazaliy, L. M. Litvak, J. S. Jiang, J. Pearson, J. Y. Gu, Chun-Yeol You, M. R. Beasley, and S. D. Bader, *Phys. Rev. B* **77**, 18450 (2008).
  41. S. F. Lee, S. Y. Huang, J. H. Kuo, Y. A. Lin, L. K. Lin, and Y. D. Yao, *J. Appl. Phys.* **93**, 8212 (2003).
  42. S.F. Lee, Q. Yang, P. Holody, R. Loloee, J.H. Hetherington, S. Mahmood, B. Ikegami, K. Vigen, L.L. Henry, P.A. Schroeder, W.P. Pratt Jr., and J. Bass, *Phys. Rev. B* **52**, 15426 (1995).
  43. G. E. Blonder, M. Tinkham, and T. M. Klapwijk, *Phys. Rev. B* **25**, 4515 (1982).
  44. S. Takahashi and S. Maekawa, *J. Phy. Soc. Jpn.* **77**, 031009 (2008).

# Chapter 8

## Summary

The proximity effect between a superconductor and ferromagnet produces damped oscillatory behavior of the Cooper pair wave function in the ferromagnet. The proximity effect can couple through the interfaces between the layers where the superconducting and ferromagnetic regions are spatially separated. Superconductivity in such a heterogeneous system is a superposition of the superconductivities of the Bardeen-Cooper-Schrieffer (BCS) type in  $S$  layers and of the Larkin-Ovchinnikov-Fulde-Ferrel (LOFF) type in  $F$  layers. This effect results in a nonmonotonic  $T_C$  behavior depending on the layer thickness, which can be theoretically described by a boundary-value problem for Cooper pair amplitude (Usadel function). This dissertation attempts to quantitatively study the transport property at  $F/S$  interface resulting from the proximity effect.

The samples used in this dissertation were prepared by sputter deposition system. We have designed three different kinds of formation to study the proximity effect in the  $F/S$  layer system including superconductor alloy, strong ferromagnet, and weak ferromagnet. Interface transparency is an important parameter to study the proximity effect, since the quality of the interface transparency would affect the coupling mechanism between the  $S$  and the  $F$ . However, it is usually treated as a fitting parameter for suitable boundary condition associated with the non-monotonic or the monotonic behavior of the superconductor critical temperature  $T_C$  as functions of layer thicknesses. Here, we can quantitatively derive the interface transparency in term of interface resistance for different types of  $F/S$  layer system by CPP measurement and compare to the theoretical parameter of proximity effect from the

fitting procedure for the  $T_C$  behavior.

In Chapter 5, we have experimentally studied the proximity effect in Co/Nb, Co/Nb<sub>0.6</sub>Ti<sub>0.4</sub>, and Co/Nb<sub>0.4</sub>Ti<sub>0.6</sub> trilayer and multilayer samples by the measurement of thickness-dependent superconducting transition temperature. The critical thickness, the superconducting coherence length, and the proximity strength have been deduced from the analysis of experimental data within the framework of the Radovic' model under the single mode approximation. By performing the CPP measurement, we have presented the linear behavior of the CPP resistance in both normal and superconducting states of three different  $S$  materials in  $F/S$  multilayers. The best fits by the one-band model to normal and superconducting states data give quantitative values of interface resistance. The normal state interface resistances are unexpectedly large. These direct measurements of the metallic interface resistance demonstrate that the interface transparency can be extracted and discussed quantitatively. We have also discussed the superconducting state interface resistance with the Pippard model. The  $AR$  between  $S$  and  $F$  is proportional to  $\rho_S l_a$ , which suggesting that the scattering centers and the penetration depths of the electron evanescent wave into the superconductors give rise to the interface resistance that conforms to the Pippard model. These analyses are important in understanding the transport properties between strong ferromagnets and superconductors in the diffusive regime.

In the Fe/Nb and Ni/Nb layer system, we have studied the proximity effect and the superconducting properties of Fe/Nb and Ni/Nb trilayers and multilayers. First, the critical thickness, and the superconducting coherence length are deduced from the analysis of experimental data by analyzing the Nb thickness dependence of  $T_C$  in terms of the Usadel's equation. Secondly, a gradual transition from 2D to 3D superconductivity crossover corresponding to the Ginzburg-Landau relation, determined from the temperature-dependent  $H_{c2}$ , occurs around Nb thickness between

120 and 140 nm for Fe/Nb system, 145 and 185 nm for Co/Nb system, and around 100 and 130 nm for Ni/Nb system . The best fit by the one-band model can derive the absolute value of interface resistance in the diffusive samples within CPP measurement. The unit area resistance of Fe/Nb interface is  $2AR_{\text{Fe/Nb}(NM)}=2.0\pm 0.9 \text{ f}\Omega \text{ m}^2$  for normal Nb and  $2AR_{\text{Fe/Nb}(S)}=6.0\pm 0.4 \text{ f}\Omega \text{ m}^2$  for superconducting Nb with bias voltage much less than the superconducting gap. The unit area resistances of one pair of the Ni/Nb interface are  $4.2\pm 0.2$  and  $1.5\pm 0.4 \text{ f}\Omega \text{ m}^2$  at superconducting and normal Nb states, respectively. The spin accumulation leads to enhanced resistance whereas Andreev reflection can lead to decreased resistance. The diffusive interface resistance between  $F$  and  $S$  should account for the competition between these two mechanisms. The interface transparency parameter and transport polarization can be directly extracted from the interface resistance. The influence of lattice mismatched is found to be important, and proved by the first principal calculation. Our result suggests that the interface resistance is sensitive to the lattice mismatched metal pairs in Nb/Ni, Nb/Fe, and Nb/Co system, and this observation is consistent with the first principle calculation.

For the weak ferromagnetic system as shown in Chapter 7, we have investigated the influence of interfacial transparency on the critical temperature and the upper critical magnetic field in the  $\text{Cu}_{0.5}\text{Ni}_{0.5}/\text{Nb}$  layered system. An analysis of the  $T_c$  dependence of the  $S$  and  $F$  layer thicknesses within the framework of the proximity theory shows that the large  $S$  critical thickness originates from the high transparency of the  $\text{Cu}_{0.5}\text{Ni}_{0.5}/\text{Nb}$  interface. The critical temperature is studied based on the solutions of the Usadel equations subject to the boundary conditions developed by Fominov. We have noticed that the effect of a small variation of  $\gamma_b$  is barely distinguishable in the behavior of  $T_c(d_S)$  but is sensitive to the behavior of  $T_c(d_F)$

which can be achieved more easily by reliably controlling  $F$  thickness over a large range due to weak exchange energy. From the temperature dependence of  $H_{c2}$ , we have found that the rather high interfacial transparency results in a strong pair-breaking effect, which in turn influences the thickness at which the 2D to 3D crossover takes place. In the CPP measurements, the resistance increases linearly with the number of bilayers in both the normal and superconducting states. The interface resistance is then deduced from the best global fit with the one-band model. We have demonstrated that the interfacial transparency ( $\gamma_b \approx 0.2$ ) can be quantitatively extracted from experimental measurements, and that it corresponds to the quantity used in the boundary condition in the microscopic model. With both the qualitative and the quantitative approaches performed in this study, the strong pair-breaking effect in the weak ferromagnetic layer is understood to result from the high interfacial transparency between the  $\text{Cu}_{0.5}\text{Ni}_{0.5}$  and Nb interface.

In this dissertation, the use of current perpendicular measurement to study the  $F/S$  proximity effect can provide important and useful information for understanding complex interfacial transport in  $F/S$  heterostructures. The spin accumulation, the Andreev reflection, spin polarization, lattice mismatch, and interfacial transparency are all included in the interface resistance for the superconducting state or normal state. We can quantitatively analyze the interfacial transport of  $F/S$  heterostructure by CPP measurement.

# Appendix A

## Calculating $T_C$

### A.1 Rodivic's model: $T_C(d_S)$

```
(* ***** *)  
(* Program dsepsln *)  
(* *)  
(* Tc vs ds of PRB61-3711 *)  
(* ***** *)
```



```
Needs["Statistics`NonlinearFit`"];  
SetDirectory["d:"];  
SetDirectory["a"];  
Print["Set current working directory to ",Directory[]];  
Set current working directory to D:\a  
(* dm:thickness of magnetic layer *)  
(* xis:superconducting coherence length *)  
(* xim:penetration depth of Cooper pairs in F layer *)  
(* tc:maximum superconducting transition temperature *)  
(*epsln: *)
```

```
(* ***** *)  
(* input data and parameters *)  
(* ***** *)
```

```
infilename="a.txt";
```

```
dm=20;
```

```
xim=1;
```

```
tc0=8.5;
```

```
thexis=1;
```

```
nk=400;
```

```
incrmk=10.;
```

```
epsln=1;
```

```
nj=200;
```

```
incrmj=10.;
```

```
dsfit=Range[10,700,2];
```

```
(* ***** *)
```

```
(* End of input *)
```

```
(* ***** *)
```

```
plt[x_,y_]:=ListPlot[Thread[Join[{x},{y}]]];
```

```
plt[x_]:=Module[{xtemp,ytemp},
```

```
  If[Length[x]==4,
```

```
    xtemp=Part[x,1];ytemp=Part[x,2];
```

```
    ListPlot[Thread[Join[{xtemp},{ytemp}]]],
```



```

ListPlot[x]]
];
g[z_]:=PolyGamma[z];
thephi:=FindRoot[phi Tan[phi]==rhs,{phi,1+I},MaxIterations->500];
thetc:=FindRoot[Log[tc]==g[0.5]-Re[g[0.5+ rho/tc]],
{tc,0.1,1},MaxIterations->500];
thetcfit:=tc0 tc/.Part[thetc,1];

outfilename=StringJoin[StringDrop[infilename,-3],"fit"];
{dsdata, tcdata}=Transpose[ReadList[infilename, {Number, Number}]];
step=Length[tcdata];
(* dsdata=dsdata 2.5; *)

tcfit=Table[1,{step}];
eps=Table[1,{nj}];
xiss=Table[1,{nk}];
chi=Table[1,{nk},{nj}];

For[k=1,k<=nk,k++,
  xis=thexis+(k-1)/incrmk;
  Part[xiss,k]=xis;
  For[j=1,j<=nj,j++,
    epsilon=epsln+(j-1)/incrmj;
    Part[eps,j]=epsilon;
    For[i=1,i<=step,i++,
      ds=Part[dsdata,i];

```





```

rhs=(1+I)/epsilon ds/xis Tanh[2(1+I)dm/xim];

rho=2 phi^2/(ds/xis)^2/.Part[thephi,1];

Part[tcfit,i]=thetcfit;

];

chi2=Apply[Plus,(tcdata-tcfite)^2];

If[chi2 Reals,Part[chi,k,j]=chi2,Part[chi,k,j]=10^10];

];

];

{mink,minj}=Position[chi,Min[chi]][[1]];

xis=Part[xiss,mink];

epsilon=Part[eps,minj];

Print["xis=", xis, ", epsilon=", epsilon,

", Tc=", tc0, ", xim=", xim, ", chi^2=", Part[chi,mink,minj]];

Print["{k,j}=", mink, ", ", minj];

(* ***** *)

(* Display results *)

(* ***** *)

outfile=OpenWrite[outfilename,FormatType -> OutputForm];

tcfit=dsfit;

step=Length[dsfit];

For[j=1,j<=step,j++,

ds=Part[dsfit,j];

```

```

rhs=(1+I)/epsilon ds/xis Tanh[2(1+I)dm/xim];
rho=2 phi^2/(ds/xis)^2/.Part[thephi,1];
Part[tcfit,j]=thetcfit;
Write[outfile,ds," ",Part[tcfit,j]];
];
Close[outfile];

SetOptions[ListPlot, Frame->True, PlotRange->All, AspectRatio->1.2,
FrameLabel->{"ds (A)", "Tc (K)"}, RotateLabel->True,
PlotJoined False,PlotStyle->PointSize[0.025],DisplayFunction->Identity];
p1=plt[dsdata,tcdata];
SetOptions[ListPlot,PlotStyle->RGBColor[0,0,1],PlotJoined
True,DisplayFunction->Identity];
p2=plt[dsfit,tcfit];
s1=Show[p1,p2,DisplayFunction->${DisplayFunction}];

```



## A.2 Fominov's model: $T_C(d_F)$

```
(* ***** *)
(* Program fominov-dffit *)
(* *)
(* Tc (df) of A. Armonio et. al PRB76-024515 *)
(* ***** *)
```

```
Clear["@"];
```

```
Needs["Statistics`NonlinearFit`"];
```

```
SetDirectory["G:"];

```

```
SetDirectory["df-rb-fitting test different"];

```

```
Print["Set current working directory to ",Directory[]];

```



```
(* ***** *)
```

```
(* input data and parameters *)
```

```
(* ***** *)
```

```
infilename="dCuNi.dat";
```

```
fitex=0; (* "1" for E_ex, "2" for gamma_b, "3" for large range fitting, and "0" for non
of them *)
```

```
ex=80 kb; (* meV *) (* the starting point of E_ex *)
```

```
extend=80 kb; (* the end point of E_ex *)
```

```
increx=1 kb; (* the increment of E_ex *)
```

```
gammab=0.1; (* the starting point of gammab *)
```

```
gaend=0.1; (* the end point of gammab *)
```

```

incrga=0.1; (* the increment of gammab *)

ds=37; (* nm *)

tc0=6.5; (* K *)

rhos=30; (* \mu\Omega cm *)

xis=12; (* nm *)

rhof=60; (* \mu\Omega cm *)

xif=6; (* nm; it's xif* in the paper *)

kb=0.08617; (* meV/K *)

gs=7 10^-4; (* J/K^2 cm^3 *)

vs=2.73 10^7; (* cm/s *)

q=1.60219 10^-19; (* C *)

kj=1.38062 10^-23; (* J/K *)

hbar=6.6262 10^-34/(2 Pi); (* J s *)

(*Get[StringReplace[infilename,"dat"->"pmt"];] (* read input data file *)

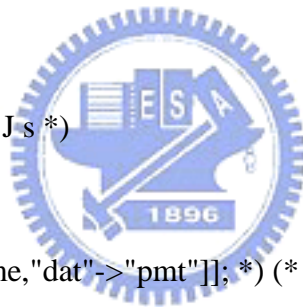
(* end of input *)

rl:=<</win/2007-08/iopas/fominov-dffit;

plt[x_,y_]:=ListPlot[Thread[Join[{x},{y}]]];

plt[x_]:=Module[{xtemp,ytemp},
  If[Length[x]==4,
    xtemp=Part[x,1];ytemp=Part[x,2];
    ListPlot[Thread[Join[{xtemp},{ytemp}]]],
    ListPlot[x]]
];

```



```
g[z_]:=PolyGamma[z];
```

```
theomega:=FindRoot[x Sin[x ds/xis]==rhs Cos[x ds/xis],{x,.5 Pi  
xis/ds},MaxIterations->500];
```

```
thetc:=FindRoot[Log[tc0/y]==g[0.5+0.5 omega^2 tc0/y]-g[0.5],  
{y,tci},MaxIterations->500];
```

```
gamma:=rhos xis/(rhof xif);
```

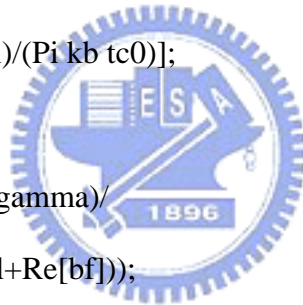
```
ks:=(1/xis)Sqrt[tci/tc0];
```

```
as:=ks xis Tanh[ks ds];
```

```
kf:=(1/xif)Sqrt[(Pi kb tci+I exl)/(Pi kb tc0)];
```

```
bf:=1/(kf xif Tanh[kf df]);
```

```
rhs:=gamma (as(gal+Re[bf])+gamma)/  
(as Abs[gal+bf]^2+gamma(gal+Re[bf]));
```



```
caltc:=Module[{ },
```

```
lf=1/(vs gs rhos) (Pi kj/q)^2;
```

```
dif=vs lf/3;
```

```
xis=Sqrt[hbar dif/(2 Pi kj tc0)] 10^10;
```

```
rhs;
```

```
omega=x/.theomega;
```

```
tc=y/.thetc;
```

```
count=0;
```

```
While[Abs[tci-tc]>0.01,
```

```

count+=1;

tci=tc;

rhs;

If[count>20,x0=0.1];

omega=x/.theomega;

tc=y/.thetc;

];

];

fitloop:=Module[{ },

For[i=1,i<=step,i++,

df=Part[xdata,i];

tci=Part[tcddata,i];

If[tci>tc0,tci=2tc0-tci];

caltc;

Part[tcfite,i]=tc;

];

chi2=Re[Apply[Plus,(tcfite-tcddata)^2]];

Print["E_ex=",ex1,"    ", "gammab=",gal,"    ", "chi2=",chi2];

];

longfitting:=Module[{ },

jmax=1+(exend-ex)/increx;

kmax=1+(gaend-gammab)/incrga;

mchi=Table[10^6,{jmax+1},{kmax+1}];

outname=StringReplace[infilename,"dat"->"log"];

```



```

outfile=OpenWrite[outname,FormatType->OutputForm];
Write[outfile,"E_ex gammab chi2"];
For[j=1,j<=jmax,j++,
gal=gammab;
exl=ex+(j-1)increx;
For[k=1,k<=kmax,k++,
gal=gammab+(k-1)incrga;
fitloop;
Part[mchi,j,k]=chi2;
Write[outfile,exl," ",gal," ",chi2]];
];
Close[outfile];
minchi=Min[mchi];
{{j,k}}=Position[mchi,minchi];
ex=exl-(jmax-j) increx;
gammab=gal-(kmax-k) incrga;
Print[];
Print["Min[chi2]=",minchi," at E_ex=",ex," gammab=",gammab];
];

(* ***** *)

(* Display results *)

(* ***** *)

displ:=Module[{} ,
SetOptions[ListPlot, Frame->True, PlotRange->All, AspectRatio->1.2,
FrameLabel->{"df (nm)", "T_c (K)"}, RotateLabel->True, PlotJoined->False,

```



```

PlotStyle->RGBColor[0,0,1], DisplayFunction->Identity];

p1=plt[xdata,tcdata];

SetOptions[ListPlot, PlotJoined->True,PlotStyle->RGBColor[1,0,0]];

p2=plt[xdata,tcfit];

Show[p1,p2,DisplayFunction->$DisplayFunction,

PlotLabel->FontForm[" ",{"Courier",8}]];

];

(* end of displ *)

(* ***** *)

(* save data *)

(* ***** *)

savedata:=Module[{ },

outx=outy=Range[0.1,Ceiling[Max[xdata]]+5,0.1];

step=Length[outx];

For[i=step,i>0,i--,

df=Part[outx,i];

(* If[i==step,tci=tc0-0.1,tci=Part[outy,i+1]]; *)

If[i==1,tci=tc0-.5,tci=Part[outy,i-1]];

If[tci>tc0,tci=2tc0-tci];

caltc;

Part[outy,i]=tc;

];

outfile=StringReplace[infilename,"dat"->"fit"];

outfile=OpenWrite[outfilename,FormatType->OutputForm];

For[i=1,i<=step,i++,

```





```

Write[outfile,Part[outx,i]," ",Part[outy,i]]
];
Close[outfile];
SetOptions[ListPlot,DisplayFunction->$DisplayFunction];
plt[outx,outy];
];
(* end of save data *)

(* ***** *)

(* Main loop *)

(* ***** *)

{xdata, tcdata}=Transpose[ReadList[infilename, {Number, Number}]];
step=Length[tcdata];
tcfit=Table[1,{step}];
exl=ex;
gal=gammab;
Switch[fitex,
0,fitloop;displ;savdata,
1,For[j=1,j<=11,j++,fitloop;displ;exl+=increx],
2,For[j=1,j<=11,j++,fitloop;displ;gal+=incrga],
3,longfitting];
(* end of main loop *)

```



### A.3 Fominov's model: $T_C(d_S)$

```
(* ***** *)
(* Program fominov-ds *)
(* *)
(* Tc (ds) of A. Armonio et. al PRB76-024515 *)
(* ***** *)
```

```
Clear["@"];
```

```
Needs["Statistics`NonlinearFit`"];
```

```
SetDirectory["M:"];
```

```
SetDirectory["fitting-rb-Tc-CuNi"];

```

```
Print["Set current working directory to ",Directory[]];
```

```
(* ***** *)
```

```
(* input data and parameters *)
```

```
(* ***** *)
```

```
infilename="NbCuNi Tc.dat";
```

```
fitex=0; (* "1" for fitting E_ex, "2" for gamma_b, and "0" for non of them *)
```

```
ex=8.6; (* meV *)
```

```
gammab=0.1;
```

```
df=50; (* nm *)
```

```
(* tc0:=8.8(1-8.78/ds); *) (* K *) tc0=8.8;
```

```
(* rhos=17; (* \mu\Omega cm *) *)
```

```
(* f[x_]:=37.88297/(1+0.00435 x); *) (* rhos *)f[x_]:=8;
```


```
rhof=75; (* \mu\Omega cm *)
```

```

xif=8.3; (* nm; it's xif* in the paper *)
kb=0.08617; (* meV/K *)
gs=7 10^-4; (* J/K^2 cm^3 *)
vs=2.73 10^7; (* cm/s *)
q=1.60219 10^-19; (* C *)
kj=1.38062 10^-23; (* J/K *)
hbar=6.6262 10^-34/(2 Pi); (* J s *)
t[x_]:=9.1789(1-24.858/x); (* tci for estimating thex0 *)
(* theomega fitted in the range (1.7,2.4) Pi xis/ds *)

(*Get[StringReplace[infilename,"dat"->"pmt"]; *) (* read input data file *)
(* end of input *)

```



```

rl:=<<win/2007-08/iopas/fominov-ds;

plt[x_,y_]:=ListPlot[Thread[Join[{x},{y}]]];
plt[x_]:=Module[{xtemp,ytemp},
  If[Length[x]==4,
    xtemp=Part[x,1];ytemp=Part[x,2];
    ListPlot[Thread[Join[{xtemp},{ytemp}]]],
    ListPlot[x]]
];
g[z_]:=PolyGamma[z];
theomega:=FindRoot[x Sin[x ds/xis]==rhs Cos[x ds/xis],{x,1.0 Pi
xis/ds},MaxIterations->500];

```

```
thetc:=FindRoot[Log[tc0/y]==g[0.5+0.5 omega^2 tc0/y]-g[0.5],
  {y,tci},MaxIterations->500];
```

```
(* thex0:=FindRoot[Log[tc0/tci]==g[0.5+0.5 x^2
tc0/tci]-g[0.5],{x,0.01},MaxIterations->500]; *)
```

```
gamma:=rhos xis/(rhof xif);
```

```
ks:=(1/xis)Sqrt[tci/tc0];
```

```
as:=ks xis Tanh[ks ds];
```

```
kf:=(1/xif)Sqrt[(Pi kb tci+I ex)/(Pi kb tc0)];
```

```
bf:=1/(kf xif Tanh[kf df]);
```

```
rhs:=gamma (as(gammab+Re[bf])+gamma)/
(as Abs[gammab+bf]^2+gamma(gammab+Re[bf]));
```

```
caltc:=Module[{ },
```

```
rhos=f[ds];
```

```
lf=1/(vs gs rhos) (Pi kj/q)^2;
```

```
dif=vs lf/3;
```

```
xis=Sqrt[hbar dif/(2 Pi kj tc0)] 10^10;
```

```
rhs;
```

```
(* x0=Abs[x]/.thex0; *)
```

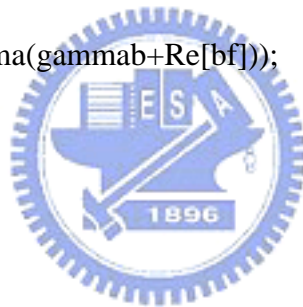
```
omega=x/.theomega;
```

```
tc=y/.thetc;
```

```
count=0;
```

```
While[Abs[tci-tc]>0.01,
```

```
count+=1;
```



```

tci=tc;

rhs;

If[count>20,x0=0.1];

omega=x/.theomega;

tc=y/.thetc;

];

];

(* ***** *)

(* Display results      *)

(* ***** *)

displ:=Module[{ },
SetOptions[ListPlot, Frame->True, PlotRange->All, AspectRatio->1.2,
FrameLabel->{"ds (nm)", "T_c (K)"}, RotateLabel->True, PlotJoined->False,
PlotStyle->RGBColor[0,0,1], DisplayFunction->Identity];

p1=plt[xdata,tldata];

SetOptions[ListPlot, PlotJoined->True,PlotStyle->RGBColor[1,0,0]];

p2=plt[xdata,tcf];

Show[p1,p2,DisplayFunction->${DisplayFunction},
PlotLabel->FontForm[" ",{"Courier",8}]];

];

(* end of displ *)

(* ***** *)

(* save data *)

(* ***** *)

```

```

savedata:=Module[{ },
If[Max[xdata]>20,dx=1.;xstart=Floor[Min[xdata]];xend=Ceiling[Max[xdata]]+1,dx=
0.1;xstart=Min[data];xend=Ceiling[Max[xdata]]];
If[xend<200,outx=outy=Join[Range[xstart,100,1],Range[102,xend+5,2]],
outx=outy=Join[Range[xstart,100,2],Range[105,200,5],Range[210,xend+10,10]]];
step=Length[outx];
For[i=step,i>0,i--,
ds=Part[outx,i];
(* If[i==step,tci=tc0-0.1,tci=Part[outy,i+1]]; *)
tci=t[ds];
If[tci>tc0,tci=2tc0-tci];
caltc;
Part[outy,i]=tc;
];
outfilename=StringReplace[infilename,"dat"->"fit"];
outfile=OpenWrite[outfilename,FormatType->OutputForm];
For[i=1,i<=step,i++,
Write[outfile,Part[outx,i]," ",Part[outy,i]]
];
Close[outfile];
SetOptions[ListPlot,DisplayFunction->$DisplayFunction];
plt[outx,outy];
];
(* end of save data *)

(* ***** *)

```



```

(* Main loop *)
(* ***** *)
{xdata, tcdata}=Transpose[ReadList[infilename, {Number, Number}]];
step=Length[tcdata];
tcfit=Table[1,{step}];
Print["E_ex=",ex,"    ","gamma_b=",gammab];

For[j=1,j<=10,j++,
If[fitex==0,j=10,If[fitex<2,ex+=0.1,gammab+=0.01]];

For[i=1,i<=step,i++,
ds=Part[xdata,i];
tci=t[ds];
If[tci>tc0,tci=2tc0-tci];
caltc;
Part[tcfit,i]=tc;
];

chi2=Re[Apply[Plus,(tcfit-tcdata)^2]];
displ;
If[fitex==0,savedata];
Print["E_ex=",ex,"    ","gammab=",gammab,"    ","chi2=",chi2];
];
(* end of main loop *)

```



## Appendix B

### The Activation Energy in Ni/Nb Layered System

The temperature dependence of  $H_{c2}$  contains the information of the flux pinning mechanism in superconductor, which can be revealed by analyzing the activation energy of the thermally assisted flux flow (TAFF). TAFF can be detected through the resistivity versus temperature curves for different applied fields. The activation energy  $U_0$  is estimated by the Arrhenius law, [1]  $\rho = \rho_0 \exp(-U_0 / k_B T)$ , where  $\rho_0$  is a field-independent pre-exponential factor. For comparison, a monolayer of 240 nm Nb film and a 2D (Cu<sub>50</sub>Ni<sub>50</sub>/Nb) multilayer with the same total Nb thickness have been prepared. Figure 7.7 shows the activation energy of flux flows versus applied field  $H$ . The difference of activation energy between the parallel and perpendicular field are relatively small in the pure Nb film, while for the  $d_{\text{Nb}} = 40$  nm of multilayer sample, the  $U_0$  for parallel field are four times the value for perpendicular field, which implying an easier TAFF due to vertex decoupling across Cu<sub>50</sub>Ni<sub>50</sub> interlayers in 2D system. In the MgB<sub>2</sub>/Mg<sub>2</sub>Si multilayer,  $U_0$  for parallel field are significantly larger than the pure MgB<sub>2</sub> film due to the vortices trapping in the non-superconducting Mg<sub>2</sub>Si layers. [2] Thus, in Figure 7.7, the  $U_0$  for parallel field show the same level of flux pinning between our Cu<sub>50</sub>Ni<sub>50</sub>/Nb multilayer and pure Nb can be attributed to the high interface transparency between Nb and Cu<sub>50</sub>Ni<sub>50</sub>. Therefore, the  $H_{c2}$  measurement provides a lot of useful information such as the strength of pair breaking and flux pinning in studying the proximity effect in  $F/S$  system.



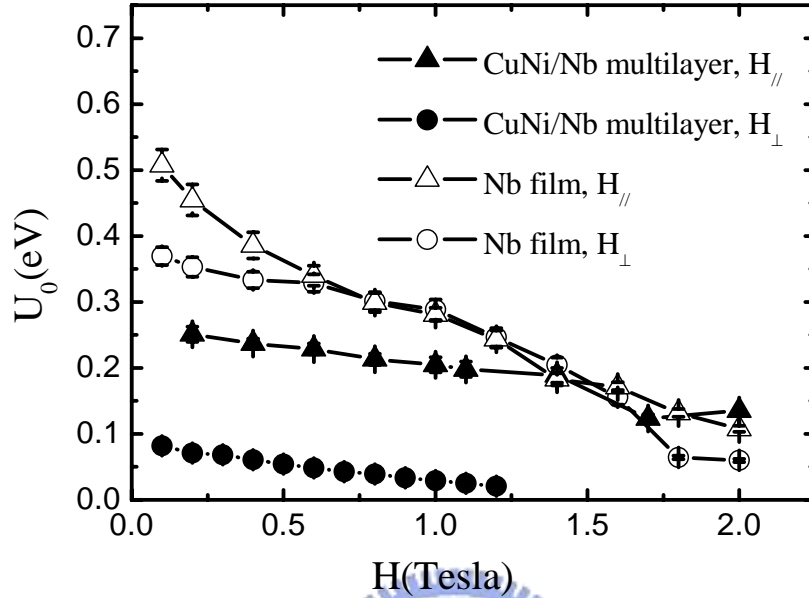


**Figure B.1:** Activation energy  $U_0$  of flux flow versus parallel and perpendicular applied field for  $(\text{Cu}_{50}\text{Ni}_{50}/\text{Nb})_6/\text{Cu}_{50}\text{Ni}_{50}$  multilayer with  $d_{\text{Nb}} = 40$  nm and monolayer Nb with  $d_{\text{Nb}} = 240$  nm. Open symbols are for monolayer and solid symbols for multilayers. Data for parallel field are in triangles and for perpendicular field in circles.

### References:

1. Y. Yeshurun, A. P. Malozemoff, and A. Shaulov, *Rev. Mod. Phys.* **68**, 911 (1996).
2. Y. Zhaoa, S. X. Dou, M. Ionescu, and P. Munroe, *Appl. Phys. Lett* **88**, 012502 (2006).

## List of Publications which have resulted from this Work:

1. S. F. Lee, T. M. Chuang, **S. Y. Huang**, W. L. Chang, and Y. D. Yao  
Two-dimensional to three-dimensional crossover and magnetic penetration depth study in NbTi/Co multilayers, J. Appl. Phys. **89**, 7493 (2001).
2. T. M. Chuang, S. F. Lee, Y. D. Yao, **S. Y. Huang**, W. C. Cheng, and G. R. Huang,  
Anomalous Magnetic Moments in Co/Nb Multilayers, J. Magn. Magn. Mater. **239**, 301 (2002).
3. S. F. Lee, J. J. Liang, T. M. Chuang, **S. Y. Huang**, J. H. Kuo, and Y. D. Yao,  
Paramagnetic Meissner effect depending on superconducting thickness in Co/Nb multilayers cond-mat/0301313, (2003).
4. S. F. Lee, **S. Y. Huang**, J. H. Kuo, Y. A. Lin, L. K. Lin, and Y. D. Yao,  
Quantitative Analysis of Interface Resistance in Co/Nb Multilayers for Normal and Superconducting Nb, J. Appl. Phys. **93**, 8212 (2003); Selected for the May 15, 2003 issue of Virtual Journal of Applications of Superconductivity.
5. **S. Y. Huang**, S. F. Lee, J. C. Huang, J. H. Huang, and Y. D. Yao, Perpendicular interface resistance in Co/Nb(x)Ti(1-x) multilayers for normal and superconducting NbTi alloy with x=0.4, 0.6, J. Appl. Phys. **97**, 10B103 (2005); Selected for the May 15, 2005 issue of Virtual Journal of Applications of Superconductivity.
6. **S. Y. Huang**, S.F. Lee, Jun-Jih Liang, C.Y. Yu, K.L. You, T.W. Chiang, S.Y. Hsu and Y.D. Yao Properties of superconductivity for decoupled ferromagnet/superconductor trilayers and multilayers in Fe/Nb system J. Magn. Mater. **304**, e81-e83 (2006).
7. **S. Y. Huang**, S. F. Lee, C. Y. Yu, S. Y. Hsu, and Y. D. Yao Analysis of diffusive

interface resistance for measurements with perpendicular current in Fe/Nb multilayers J. Appl. Phys. **99**, 08M507 (2006); Selected for the May 1, 2006 issue of Virtual Journal of Applications of Superconductivity.

8. **S. Y. Huang**, S. F. Lee, S. Y. Hsu, and Y. D. Yao, Interface resistance and transparency in ferromagnet/superconductor Co/NbxTi1-x multilayers (x=1, 0.6, and 0.4) Phys. Rev. B **76**, 024521 (2007); Selected for the August 1, 2007 issue of Virtual Journal of Applications of Superconductivity.
9. **S.-Y. Huang**, J. J. Liang, T. C. Tsai, L. K. Lin, M. S. Lin, S. Y. Hsu, and S. F. Lee, Dimensional crossover and flux pinning of decoupled Cu50Ni50/Nb multilayers, J. Appl. Phys. **103**, 07C704 (2008); Selected for February 1, 2008 issue of Virtual Journal of Applications of Superconductivity.
10. **S. Y. Huang**, Y. C. Chiu, J. J. Liang, L. K. Lin, T. C. Tsai, S. Y. Hsu, and S. F. Lee, Analysis of the proximity effect and the interface with perpendicular current in Ni/Nb system J. Appl. Phys. **105**, 07E319 (2009); Selected for the March 15, 2009 issue of Virtual Journal of Applications of Superconductivity.
11. T. W. Chiang, Y. H. Chiu, **S. Y. Huang**, S. F. Lee, J. J. Liang, H. Jaffrès, J. M. George, and A. Lemaitre, Spectra broadening of point-contact Andreev reflection measurement on GaMnAs J. Appl. Phys. **105**, 07C507 (2009)
12. **S. Y. Huang**, J. J. Liang, S. Y. Hsu, L. K. Lin, T. C. Tsai, and S. F. Lee, High interfacial transparency in Cu<sub>0.5</sub>Ni<sub>0.5</sub>/Nb layered systems evidenced by superconducting properties and CPP transport measurements, submitted to Phys. Rev. B

## Award:

1. **Best poster award**, M. S. Lin, S. F. Lee, **S. Y. Huang**, J. J. Liang, T. C. Tsai, M. D. Lin, and Y. D. Yao, "Proximity Effect in Nb/ Cu<sub>50</sub>Ni<sub>50</sub> System", 18<sup>th</sup> Taiwan Association for magnetic Technology, (2006).
2. **Best poster award**, Y. H. Chiu, **S. Y. Huang**, T. W. Chiang, T. C. Tsai, Y. L. Hsu, S. F. Lee, and J. Kwo, "Point Contact Spin Spectroscopy of Ferromagnetic Fe<sub>3</sub>Si epitaxial Films", 18<sup>th</sup> Taiwan Association for magnetic Technology, (2006).
3. **Best poster award**, M. S. Lin, **S. Y. Huang**, S. F. Lee, T. C. Tsai, S. Y. Hsu, J. J. Liang, and Y. D. Yao, "The Proximity Effect in Nb/ Cu<sub>50</sub>Ni<sub>50</sub> System", Taiwan International conference on Superconductivity and the 8<sup>th</sup> Workshop on Low-temperature Physics, (2006).
4. **Best poster award**, T. C. Tsai, **S. Y. Huang**, M. S. Lin, S. Y. Hsu and S. F. Lee, "Dimensional Crossover and The Pinning Mechanism for Decoupled Ferromagnet/Superconductor Multilayers in Cu<sub>50</sub>Ni<sub>50</sub>/Nb system", 19<sup>th</sup> Taiwan Association for magnetic Technology, (2007).
5. **Best Presentation Award**, **S. Y. Huang**, L. K. Lin, T. C. Tsai, J. J. Liang, S. Y. Hsu, Y. D. Yao, and S. F. Lee, "Interface resistance and transparency in ferromagnet/superconductor Co/Nb<sub>x</sub>Ti<sub>1-x</sub> multilayers (x=1, 0.6, and 0.4)", Proceedings of the Third Xiaotu Conference of Science and Engineering with Open Participation (2007).
6. **Best poster award**, **S. Y. Huang**, J. J. Liang, L. K. Lin, T. C. Tsai, S. Y. Hsu, and S. F. Lee, "A strong pair breaking effect in the weak ferromagnet/superconductor heterostructures: Cu<sub>50</sub>Ni<sub>50</sub>/Nb", 20<sup>th</sup> Taiwan

Association for magnetic Technology, (2008).

7. **Best poster award**, Y. C. Chiu, **S. Y. Huang**, L. K. Lin, T. C. Tsai, J. W. Chen, and S. F. Lee, “Analysis of the proximity effect and the interface resistance in Nb/Ni system with current in plane and perpendicular to plan measurements”, Annual Meeting of The Physical Society of Republic of China (2008).

